University of Kentucky
UKnowledge

Theses and Dissertations--Pharmacy College of Pharmacy

2023

New Tools for Biocatalysis: Studies on the Carminomycin 4-O-Methyltransferase DnrK

Elnaz Jalali
University of Kentucky, elnaz.jalali@uky.edu
Author ORCID Identifier:
https://orcid.org/0000-0003-1434-2960
Digital Object Identifier: https://doi.org/10.13023/etd.2023.261

Right click to open a feedback form in a new tab to let us know how this document benefits you.

Recommended Citation
Jalali, Elnaz, "New Tools for Biocatalysis: Studies on the Carminomycin 4-O-Methyltransferase DnrK" (2023). *Theses and Dissertations--Pharmacy*. 154.
https://uknowledge.uky.edu/pharmacy_etds/154

This Doctoral Dissertation is brought to you for free and open access by the College of Pharmacy at UKnowledge. It has been accepted for inclusion in Theses and Dissertations--Pharmacy by an authorized administrator of UKnowledge. For more information, please contact UKnowledge@lsv.uky.edu.

STUDENT AGREEMENT:

I represent that my thesis or dissertation and abstract are my original work. Proper attribution has been given to all outside sources. I understand that I am solely responsible for obtaining any needed copyright permissions. I have obtained needed written permission statement(s) from the owner(s) of each third-party copyrighted matter to be included in my work, allowing electronic distribution (if such use is not permitted by the fair use doctrine) which will be submitted to UKnowledge as Additional File.

I hereby grant to The University of Kentucky and its agents the irrevocable, non-exclusive, and royalty-free license to archive and make accessible my work in whole or in part in all forms of media, now or hereafter known. I agree that the document mentioned above may be made available immediately for worldwide access unless an embargo applies.

I retain all other ownership rights to the copyright of my work. I also retain the right to use in future works (such as articles or books) all or part of my work. I understand that I am free to register the copyright to my work.

REVIEW, APPROVAL AND ACCEPTANCE

The document mentioned above has been reviewed and accepted by the student's advisor, on behalf of the advisory committee, and by the Director of Graduate Studies (DGS), on behalf of the program; we verify that this is the final, approved version of the student's thesis including all changes required by the advisory committee. The undersigned agree to abide by the statements above.

Elnaz Jalali, Student

Jon S. Thorson, Major Professor

David J. Feola, Director of Graduate Studies

NEW TOOLS FOR BIOCATALYSIS: STUDIES ON THE CARMINOMYCIN 4-*O*-METHYLTRANSFERASE DNRK

DISSERTATION

A dissertation submitted in partial fulfillment of the
requirements for the degree of Doctor of Philosophy in the
College of Pharmacy
at the University of Kentucky

By
Elnaz Jalali

Lexington, Kentucky

Director: Dr. Jon S. Thorson, Professor and Associate Dean of Research
of Pharmaceutical Sciences Department

Lexington, Kentucky

2023

Copyright © Elnaz Jalali 2023
0000-0003-1434-2960

ABSTRACT OF DISSERTATION

NEW TOOLS FOR BIOCATALYSIS: STUDIES ON THE CARMINOMYCIN 4-*O*-METHYLTRANSFERASE DNRK

Methyltransferases (MTs) are ubiquitous enzymes commonly involved in biosynthesis and regulation. The fundamental goal of this thesis was to explore the permissive nature of methyltransferases and leverage this unique biocatalytic feature to develop a new platform for chemoselective intramolecular cyclization reactions. To realize this ambitious goal, this thesis project set out to probe the substrate specificity of multiple natural product tailoring enzymes (MTs and glycosyltransferases), identify model substrates common to multiple such tailoring enzymes and subsequently establish multi-enzyme tandem reactions that would set the stage for a subsequent chemoselective intramolecular cyclization reaction. Chapter One highlights current state of the art on enzyme-mediated bioorthogonal technologies in which the key considerations for selecting enzyme catalysts and chemoselective reactions most amenable to bioorthogonal platforms were assessed and reviewed (published in *Curr. Opin. Biotechnol*., 2021). Chapter Two (*manuscript submitted*) describes a comprehensive study on the substrate scope of the carminomycin 4-*O*-MT DnrK, a final enzymatic step in the biosynthesis of daunomycin. This study revealed DnrK as a notably permissive MT and highlighted a functionally and structurally diverse array of validated new DnrK substrates. Bioactivity assays of a select set of the new molecules produced also expanded existing anthraquinone SAR. The third chapter (*manuscript submitted*) is a follow up on the intriguing discovery of DnrK's ability to catalyze *S*- or *N*-alkylation of heteroatom-containing aromatics. This work opens the door to the intriguing possibility of substrate nucleophilicity/reactivity, rather than or in addition to ligand-binding, as potential driver of MT selectivity and also implicates DnrK as a potentially versatile tool for synthetic biology. The final chapter briefly summarizes the range of other tailoring enzymes evaluated and molecules identified that serve as facile complementary substrates for two or more orthogonal tailoring enzymes as a starting point for realizing the vision of bioorthogonal intramolecular cyclization reactions.

KEYWORDS: Biocatalysis, Methyltransferase, *S*-Adenosyl-L-methionine, Natural Product, Bioorthogonal, Chemoselective

Elnaz Jalali

10 April 2023

NEW TOOLS FOR BIOCATALYSIS: STUDIES ON THE CARMINOMYCIN 4-*O*-METHYLTRANSFERASE DNRK

By

Elnaz Jalali

Jon S. Thorson, Ph.D.
Director of Dissertation

David J. Feola, PharmD, Ph.D.
Director of Graduate Studies

To my loving family: Nasrin, Farzan, Faraz and Shahryar

ACKNOWLEDGMENTS

I would like to thank every person that has been a part of my life during my years at the University of Kentucky. A sincere thank you to Dr. Jon S. Thorson for his continued support, encouragement and direction throughout my entire Ph.D. program.

Many thanks are given to my committee members, Dr. Steven Van Lanen, Dr. Jurgen Rohr and Dr. Konstantin V. Korotkov, their expertise, direction and thoughts were critical for the progress of my research goals and dissertation.

Additionally, I also want to thank all the incredible past and present Thorson lab members for their internal collaborations, advice, ideas and support; Dr. Khaled Shaaban, Dr. Larissa Ponomareva, Dr. Rokon Karim, Dr. Tyler Huber, Dr. Aarajana Shrestha, Dr. Erome Hankore, Yixin Xu and Tonya Vance. I would also like to give a special thanks to Dr. Khaled Shaaban for his exceptional experience and ability to teach me various lab techniques imperative to the success of this dissertation.

Additionally, I want to thank the entire University of Kentucky, College of Pharmacy and Pharmaceutical Sciences department notably Dr. David J. Feola and Catina M. Barnes for their continued support and guidance. Lastly, I would like to thank my family for their love and patience throughout this exhausting process. Without them, I would not have been where I am today.

TABLE OF CONTENTS

TABLE OF CONTENTS iv
LIST OF TABLES vi
LIST OF FIGURES vii
Chapter One: Enzyme-mediated bioorthogonal technologies: catalysts, chemoselective reactions and recent methyltransferase applications 1
1.1 Introduction 1
1.2 Desired catalyst properties: The case for methyltransferases 4
1.3 Chemoenzymatic reaction prioritization 6
1.3.1 Modified Huisgen 1,3-dipolar cycloaddition reactions 7
1.3.2 Photoinduced tetrazole-alkene/alkyne cycloaddition reactions 7
1.3.3 Inverse electron-demand Diels–Alder reactions 8
1.4 MT-enabled bioorthoganal applications 8
1.4.1 Representative recent DNA applications 9
1.4.2 Representative recent RNA applications 10
1.4.3 Representative recent protein applications 11
1.4.4 Representative recent natural product and small molecule applications 12
1.5 Conclusions 16
Chapter Two: Biochemical and structural studies of the carminomycin 4-*O*-methyltransferase DnrK 26
2.1 Introduction 26
2.2 Results and discussion 29
2.2.1 DnrK non-native acceptor scope 29
2.2.2 DnrK structure elucidation and relationships to other MTs with similar functions 47
2.2.3 Impact of methylation on the bioactivity of representative model compounds 54
2.3 Conclusions 55
2.4 Materials and methods 57
2.4.1 General materials 57
2.4.2 General methods 58
2.4.3 Protein heterologous production and purification 59
2.4.4 DnrK in vitro assay 59
2.4.5 DnrK kinetics 59
2.4.6 DnrK crystallization and structure elucidation 59
2.4.7 Structure prediction of TcmO 63
2.4.8 4-*O*-Methoxy aranciamycin production and structure elucidation 63
2.4.9 Cancer cell line viability assay 65
2.4.10 Western blot analysis 65
2.4.11 Axolotl embryo tail regeneration assay 66
Supplementary table and figures for Chapter Two 67
References for Chapter Two 85
Appendix for Chapter Two 98
Chapter Three: Broadening the scope of DnrK unnatural acceptors and donors 135
3.1 Introduction 135
3.2 Results and discussion 137

3.3 Conclusions 150
3.4 Experimental procedures 150
3.4.1 General materials and methods 150
3.4.2 Heterologous enzyme production and enzyme purification 152
3.4.3 *In vitro* enzymatic assays 153
3.4.4 Kinetic measurements of DnrK reactions 153
3.4.5 General procedure for the large-scale production of L,L-homocystine 153
3.4.6 General procedure for the large-scale production of *N*-Boc-L,L-homocystine 154
3.4.7 General procedure for disulfide bond reduction, *S*-alkylation and deprotection of Met analogues 155
3.4.8 2-(Methylthio)pyrimidin-4(3*H*)-one and 4-*O*-allyloxycarminomycin production and structure elucidation 158
Supplementary figures for Chapter Three 160
References for Chapter Three 167
Appendix for Chapter Three 173
Chapter Four: Conclusions and Prospectus 231
4.1 Conclusions 231
4.1.1 Develop robust high-throughput MT assays/screens for the discovery of novel MT substrates and to enable MT directed evolution/engineering 232
4.1.2 Robust, scalable, and chromatography-free synthetic method for the synthesis of methionine analogues 233
4.1.3 Establish *in vitro* model systems for tandem chemoselective reactions 233
4.2 Prospectus 236
4.2.1 Develop robust high-throughput MT assays/screens for the discovery of novel MT substrates and to enable MT directed evolution/engineering 236
4.2.2 Robust, scalable, and chromatography-free synthetic method for the synthesis of methionine analogues 236
4.2.3 Establish *in vitro* model systems for tandem chemoselective reactions 237
References for Chapter Four 238

LIST OF TABLES

Table 2.1. Kinetic parameters of DnrK. 30
Table 2.2. Crystal parameters, data collection, and refinement statistics. 62
Table 2.3. NMR spectroscopic data of aranciamycin and 4-*O*-methylaranciamycin 64
Table 3.1. Non-native DnrK acceptors and their putative methylated products. 138
Table 3.2. Kinetic parameters of DnrK with native and non-native substrates. 141
Table 3.3. NMR spectroscopic data of 4-*O*-allyloxycarminomycin 147

LIST OF FIGURES

Figure 1.1. Overview of bioorthogonal strategies used in chemical biology research. 2
Figure 1.2. Key MT and chemoselective bioorthoghonal reactions 5
Figure 1.3. Summary of NPs for which transferase-enable bioorthogonal chemoselective modification and/or MT-enable non-native alkylation 15
Figure 2.1. Overview of DnrK general reaction 27
Figure 2.2. Representative anthracene, tetracene, benz[a]anthracene and related DnrK substrates..... 32
Figure 2.3. Structure elucidation of aranciamycin and DnrK methylated product 4-*O*-methoxyaranciamycin 35
Figure 2.4. Structures of the molecules that were tested but did not turn over with DnrK 37
Figure 2.5. Representative flavones, flavonols, flavanones, isoflavones,coumarins and related DnrK substrates 41
Figure 2.6. Representative 2-quinolones, fused benzoic acid containing natural products and related DnrK substrates 46
Figure 2.7. Polder omit map (mFo-DFc) electron density for the AdoHcy and 4-MeUmb ligands..... 49
Figure 2.8. Ligand binding environment of the 4-MeUmb..... 50
Figure 2.9. Prediction of the TcmO structure output from AlphaFold-multimer run from colabfold..... 51
Figure 2.10. Superposition and alignment of DnrK with TnmH and Predicted model for TcmO..... 52
Figure 2.11. Cut-view through the ligand binding tunnel of DnrK 53
Figure 2.12. Impact of methylation on the bioactivity of representative model agent**s** 56
Figure 2.13. DnrK kinetic parameters for CAR and 4-MeUmb substrates..... 60
Figure 3.1. General DnrK reaction with CAR and non-native DnrK acceptors. 136
Figure 3.2. DnrK kinetic parameters for heteroatom-containing non-native acceptors 141
Figure 3.3. Synthesis steps of S-substituted Met analogues 143
Figure 3.4. Schematic overview and turnover percentage of MAT, MT and MAT/MT reactions 145
Figure 3.5. Dose-response of CAR, DNR and 4-*O*-allyloxycarminomycin against A549 cell line..... 149
Figure 4.1. The proposed chemoenzymatic tandem platform for target NPs 235

Chapter One: Enzyme-mediated bioorthogonal technologies: catalysts, chemoselective reactions and recent methyltransferase applications

1.1 Introduction

A range of innovative chemoselective bioorthogonal/biocompatible conjugation strategies have been developed to enable in situ conjugation of reporters and affinity ligands for molecular tracking and mechanistic studies in cells and even in live animals (**Figure 1.1**).[1–3] Ideally, the chemoselective functional groups employed in such applications must: afford exquisite reactivity/efficiency under physiological conditions; provide notable selectivity/compatibility within the context of living cells and in vivo; lead to conjugated products that are metabolically stable and non-toxic; and not infringe on the native biology to be studied. While, many bioorthogonal/biocompatible conjugation strategies rely on metabolic incorporation of non-native biomolecules synthetically-modified to display a chemoselective group, the use of enzyme-mediated strategies to install the requisite chemoselective functional groups is on the rise.[3-5] This review briefly introduces the catalysts and chemistries most amenable to enzyme-mediated chemoselective functional group installation and highlights recent key technology development and applications of methyltransferase-mediated biorthogonal/biocompatible conjugation.

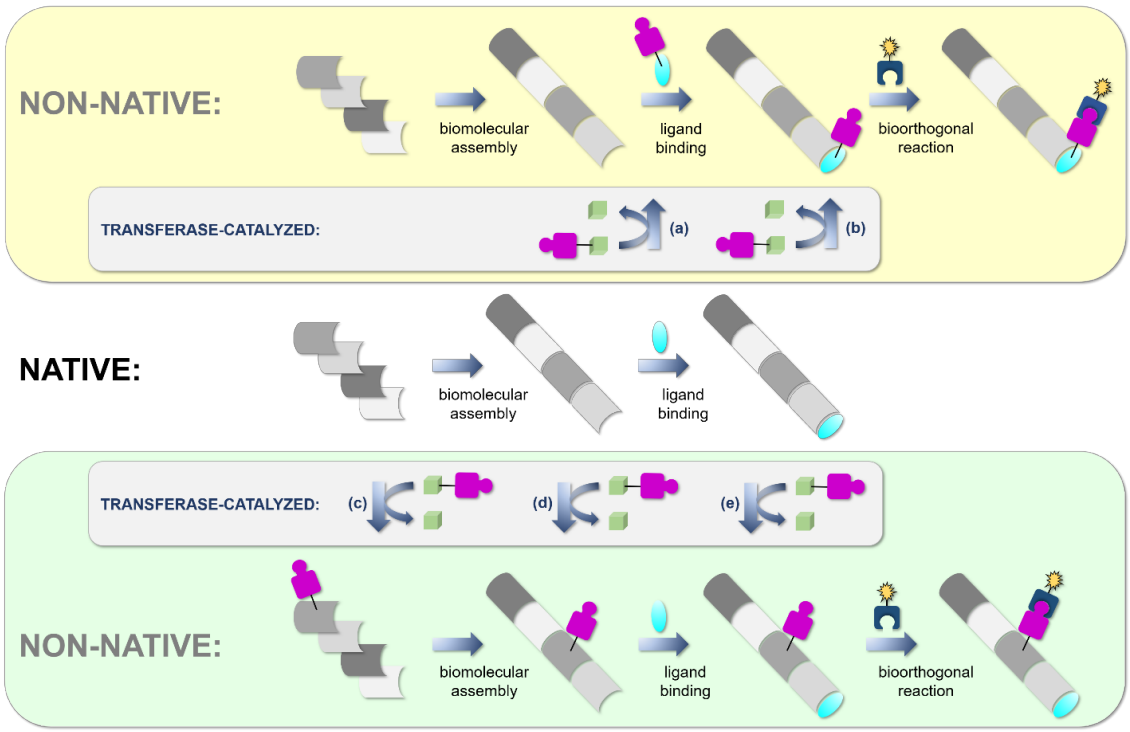

Figure 1.1. Overview of bioorthogonal strategies used in chemical biology research. The center of the figure reflects key steps in native biological systems. Specifically, in the biomolecular assembly step metabolic building blocks (*e.g.*, nucleotides, amino acids, acetate, isoprenes, etc.; represented by grey cylinders) are commonly used to generate functional biopolymers (*e.g.*, RNA, DNA, proteins, lipids, etc.). In the ligand binding step, certain biopolymers (*e.g.*, proteins, RNA or DNA complexes) are able to selectively bind ligands (*e.g.*, hormones, small molecules, metabolites, drugs, etc.; highlighted in light blue). The upper panel (yellow) reflects an application of a ligand analogue (light blue) bearing a bioorthogonal chemoselective 'tag' (purple puzzle shape). This ligand can be tracked in situ via a chemoselective bioorthogonal reaction with a partner reagent (dark blue puzzle piece) commonly appended with a fluorescent reporter or affinity capture ligand (yellow burst). The lower panel (green) reflects an application of a metabolite building block analogue bearing a bioorthogonal chemoselective functional group (purple

puzzle shape). This building block can be tracked in situ via a similar chemoselective labeling strategy using a partner reagent (dark blue puzzle piece) commonly appended with a fluorescent reporter or affinity capture ligand (yellow burst). Transferases are able to introduce bioorthogonal chemoselective functional groups (purple puzzle shape) at many different stages including: modification of the ligand prior to **(a)** or after **(b)** binding to its molecular target as well as modification of metabolic building blocks **(c)** or biopolymers prior to **(d)** or after **(e)** ligand binding. Transferase reactions (grey panels) typically utilize a co-substrate comprised of the transfer group (*e.g.*, alkyl, glycosyl, acyl, etc.) and 'activating group' (*e.g.*, S-adenosylhomocysteine/SAH, nucleotide diphosphate/NDP, coenzyme A/CoA, etc.; represented by the green cube).

1.2 Desired catalyst properties: The case for methyltransferases

There are three key considerations to selecting a catalyst for chemoselective functional group installation-substrate scope, catalyst efficiency, and catalyst abundance. Specifically, an ideal catalyst requires a uniquely balanced *substrate scope* that encompasses target (probe or biomolecule) selectivity with permissivity toward non-native chemoselective group installation. For intracellular applications, such non-native substrates must also be membrane permeable or transported via active/passive transport mechanisms. Catalytic *efficiency* is an essential requirement to enable subsequent rapid reporter conjugation and detection. For in situ applications catalytic turnover ultimately contributes to both probe/assay sensitivity and temporal resolution. Finally, catalyst *abundance* refers to natural/engineered distribution (cellular, tissue and organism) and abundance (protein levels), all of which ultimately influence the range of potential applications. Considering these factors, transferases (Enzyme Commission class 2; EC2) that catalyze macromolecule/metabolite 'tailoring' reactions have typically been favored for chemoselective functional group installation, catalyst development and applications.

Of EC2 transferases, methyltransferases (MTs) are currently the catalysts most favored for chemoselective functional group installation. MTs catalyze the transfer of a methyl group from S-adenosyl- L-methionine (SAM or AdoMet; the 'donor') to a substrate nucleophile (carbon, nitrogen, oxygen or sulfur; the 'acceptor') (**Figure 1.2a**).[6-8] The *substrate scope* of MTs is exceptionally broad and includes macromolecular substrates (DNA, RNA, and proteins) and small molecules (primary and secondary metabolites). MTs are also able to use non-native *S/Se* -alkyl-substituted AdoMet donors to afford non-native

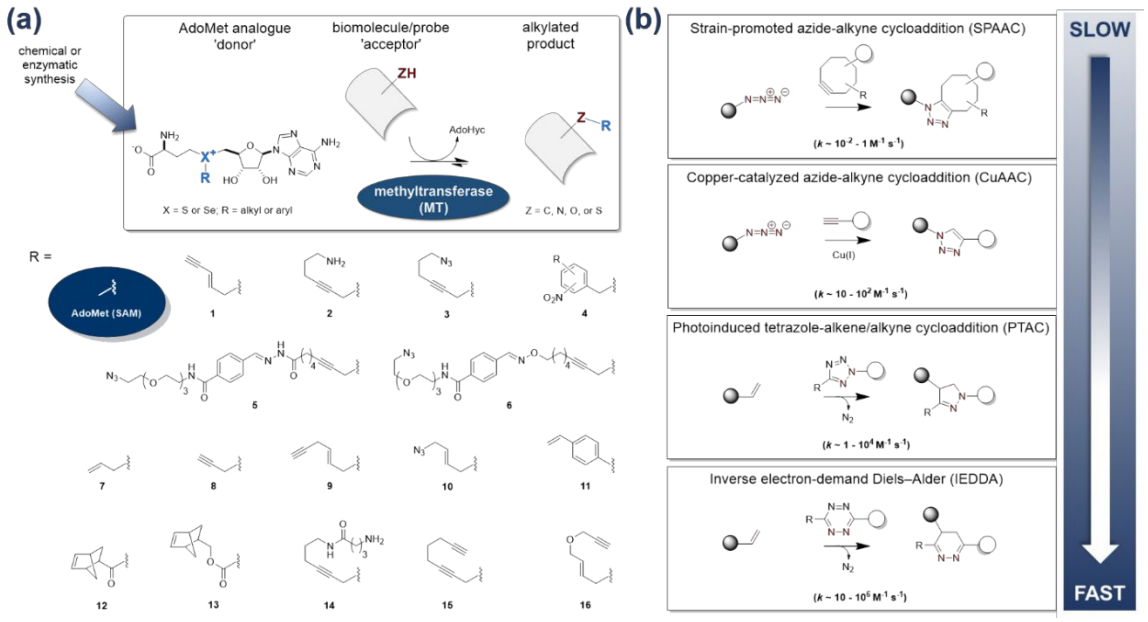

Figure 1.2. (a) The native function of a methyltransferase (MT) is to transfer a methyl group from an *S*-activated AdoMet donor to an acceptor *C*-, *N*-, *O*- or *S*-nucleophile (upper panel). As described in this review, MTs are capable of also using non-native S- or Se-activated alkyl or aryl (light blue) AdoMet analogues and thereby catalyze differential alkylation of target biomolecules. The lower panel highlights the structure of the *S*/*Se*-substituent for representative examples highlighted in this review. **(b)** Chemoselective reactions that fit criteria for transferase-mediated platforms.

alkylation, including *S/Se*-alkyl substituents bearing chemoselective functional groups.[4,7,8] While AdoMet analogues are unsuitable for cell-based studies due to poor uptake and chemical stability, these reagents can be generated in cells from corresponding non-native methionine analogues and ATP via methionine adenosyltransferases (MAT).[9-12] Alternative enzyme-based approaches for non-native AdoMet analogue synthesis[13,14] and new chemically-stable AdoMet isosteric substrates[15] have also been recently reported. MT natural *abundance* and distribution is high and MTs are critical to all walks of life.[4,6-8] Thus, MT-based platforms are anticipated to offer inroads to rich biology and support a vast array of impactful applications. MT catalytic *efficiency* is the perhaps the greatest liability in the context of chemoselective applications. Specifically, the catalytic efficiency for MTs range from ~10 to 7,200 M^{-1} s^{-1} and the corresponding range for AdoMet-producing enzymes is ~145 - 340 M^{-1} s^{-1}.

1.3 Chemoenzymatic reaction prioritization

Chemoselective reaction *efficiency* and *selectivity* are a cornerstone of effective bioorthogonal conjugation platforms.[1-3] Specifically, to be effective, such reactions must proceed at high reaction rates (efficiency) in cellular environments (selectivity). The *molecular properties* (e.g, size, polarity/charge and/or hydrophobicity/hydrophilicity) of the selected non-native chemoselective functional group are also key to selecting chemistries for transferase-mediated platforms. Specifically, these features influence an enzyme's substrate recognition and turnover must thereby align with the selected

transferase's substrate scope. Based on these key parameters, the following chemoselective reactions are considered most amenable to transferase-mediated strategies (**Figure 1.2b**).

1.3.1 Modified Huisgen 1,3-dipolar cycloaddition reactions (CuAAC and SPAAC)[16]

Poor reaction rates limited the synthetic utility of Huisgen 1,3-dipolar cycloaddition prior to the advent of the copper-catalyzed azide-alkyne cycloaddition (CuAAC) reaction by Sharpless and co-workers (often referred as the first conceptual example of 'click' chemistry).[17] Despite favorable reaction rates (10-100 M^{-1} s^{-1}), chemoselectivity and stability of reaction products, the metal dependence of the CuACC reaction limited use in living cells and tissues. To circumvent this liability, Bertozzi and coworkers advanced copper-free strain-promoted azide-alkyne cycloaddition (SPAAC) reactions driven by the ring strain of cyclooctyne reactants such difluorooctyne (DIFO, 0.08 M^{-1} s^{-1}).[18] Alternative constrained reactants and electronic activation strategies led to SPAAC reaction rate improvements of nearly 2-orders in magnitude.[19,20]

1.3.2 Photoinduced tetrazole-alkene/alkyne cycloaddition reactions (PTAC)

This 'photoclick' reaction, first reported by Lin and coworkers, was also inspired by the work of Huisgen.[21] Photo-induced tetrazole cycloreversion to generate short-lived reactive nitrile imine intermediates serves the basis for this reaction. These intermediates rapidly (>50 M^{-1} s^{-1}) undergo 1,3-dipolar cycloaddition reactions with alkynes or alkenes to give fluorescent cyclic pyrazolines. Conceptual advances include optimizing ring strain and electronics, leading to rate improvements of nearly two orders in magnitude.[22,23] While

this method offers exceptional utility for spatial and temporal control in cell/tissue-based applications, the dependence on light may limit in vivo applications.

1.3.3 Inverse electron-demand Diels–Alder reactions (IEDDA)

Unlike a classical Diels–Alder reaction in which an electron-rich diene reacts with an electron-poor dienophile, IEDDA reaction exploit an electron-rich dienophile (alkenes/alkynes) and an electron-poor diene (typically tetrazines).[24] Early IEDDA proof of concept was reported by Fox and coworkers using trans-cyclooctene and tetrazine (>103 M^{-1} s^{-1}). Continued development has focused on tuning reactivity via electronic and steric perturbation to afford rate improvements of over 2 orders in magnitude.[24,25] Photoinduction (photo-IEDDA) and orthogonality, both among exclusive IEDDA reactions and between IEDDA reactions and other chemoselective reactions (*e.g.*, SPAAC and CuAAC), have also been reported.[26,27]

1.4 MT-enabled bioorthoganal applications

Initial work in the field was based on MT-mediated single turnover reactions using aziridine-based AdoMet analogues to give fused AdoMet analogue-acceptor adducts.[28,29] Weinhold and Klimasăuskas were first to demonstrate MT-catalyzed transfer of non-native groups from catalytically-competent AdoMet analogues[30] which set the stage for what they subsequently described as the MT-directed "Transfer of Activated Groups" (mTAG) platform for chemoselective conjugation. This section is limited to recent applications of

MTs in combination with catalytically-competent AdoMet analogues bearing non-native *S*/*Se*-alkyl groups with chemoselective functionality.

1.4.1 Representative recent DNA applications[31]

Building on the mTAG precedent, Neely and collaborators reported DNA adenine-N6 MT M.TaqI-mediated DNA CuAAC using **1** (**Figure 1.2a**) for DNA mapping[32] and a subsequent comparative study of M. TaqI-mediated N-hydroxysuccinimidyl (NHS) ester amide coupling or CuAAC/SPAAC using amine **2** or azide **3**, respectively.[33] These studies revealed SPAAC to outperform CuAAC and amide coupling and also noted DNA decomposition/damage in the CuAAC reactions. Weinhold and co-workers also recently reported the use of a similar M. TaqI-driven strategy with **3** and SPAAC to introduce fluorophores and affinity labels as probe for the study of DNA origami nanostructure folding.[34] Innovative new MT-enabled methods for DNA photocaging open the door to 'reversible' selective modification of DNA as exemplified by the M.TaqI-catalyzed introduction of photocleavable protecting groups (**Figure 1.2a**; **4**).[35,36] This work demonstrated a feasible platform for photoregulation using simple in vitro transcription/translation systems where subtle changes in the photoprotecting group substitution pattern led to modulation of both MT turnover and/or photoreaction efficiency. Rentmeister and coworkers recently extended this platform via the development of new MATs (*Cryptosporidium hominus* MAT and an engineered *Methanocaldococcus jannaschii* thermostable MAT variant) to produce photocaged AdoMet analogues in situ.[12] Neely, Fernandez-Trillo and team also recently put forth tools for an innovative in vitro DNA 'write, remove, rewrite' approach.[37] Specifically, they demonstrated M.TaqI-

mediated and the cytosine-C5 MT M.MpeI-catalyzed installation of a bifunctional DNA tag comprised of a hydrazone-linked **5** or oxime-linked terminal azide **6**. This modification allowed for SPAAC-mediated conjugation and, in the case of the hydrazone-linker, selective hydrolysis in the presence of NH_2OH and chemoselective reinstallation of modifiers via the exposed hydrazide.

1.4.2 Representative recent RNA applications

Rentmeister and colleagues have reported a range of mTAG RNA-based applications in recent years using three fundamental MT model systems – variants of the 5'-cap mRNA adenine-N2 MT trimethylguanosine synthase2 (GlaTgs2),[39-41,44] 5'-cap mRNA gaunine-N7 MT Ecm1 [42-44] and mRNA adenine-N6 MTs and METTL3-14 and METTL16.[45,46] Chemoselective reactions employed in these studies include CuAAC,[41,45,46] SPAAC,[40-44,46] PTAC and IEDDA [39,43,44] using non-native AdoMet analogues (**Figure 1.2a**; **1**, **7-13**). Many of these studies evaluated the impact of mRNA non-native alkylation on RNA processing (primarily reverse transcription) and corresponding MT-catalyzed reactions were conducted in increasingly complex reaction environments (in vitro,[41,44,46] cell lysates[39,40,43] and live cells[45]). Four specific recent advances relating to MT-mediated RNA applications are particularly noteworthy. First, reminiscent to previously reported MT-enabled DNA photocaging (**Figure 1.2a**; **4**), conceptually similar RNA studies were recently reported.[46] Rentmeister and coworkers also demonstrated proof of concept of novel norbornene-based AdoMet co-substrates (*e.g.*, **12**,**13**) for RNA MTs to facilitate downstream IEDDA conjugation reactions.[43] Third, this same team published an innovative study that revealed the ability to use adenine-N2 MT (GlaTgs2 variant) and

gaunine-N7 MT (Ecm1) in tandem, two distinct non-native AdoMet co-substrates **10** and **11**, and subsequent SPAAC and IEDDA to afford selective differential mRNA labeling and FRET.[44] Finally, these researchers also reported a cell-based platform to identify METTL3-METTL14 target sites where the resulting termination of reverse transcription and bioconjugation method facilitated RNA fragment capture and next generation sequencing.[45] Klimašauskas, Vilkaitis and colleagues recently extended these tools to the small-RNA 2'-*O*-MT HEN1 from Arabidopsis thaliana, a duplex-driven MT.[47] Specifically, this work employed amines **2** and **14** (NHS ester amide coupling), azide **3** (CuAAC) and alkyne **15** (CuAAC) as tools to map the sequence/context specificity of HEN1 in vitro.

1.4.3 Representative recent protein applications

A range of diverse strategies have been developed for bioorthgonal chemoselective protein modification.[48] Within this context, the Weinhold group were the first to demonstrate MT-mediated chemoselective protein modification via CuAAC using the *Neurospora crassa* histone 3 lysine 9 N-MT (H3K9) Dim-5 and **1** (**Figure 1.2a**).[49] Luo and coworkers were among the first to advance similar tools for proteomics using oncogenic H3K9 N-MTs as models EuHMT1 (GLP1) and EuHMT2 (G9a). Coined 'bioorthogonal profiling of protein methylation' (BPPM), their proof of concept utilized EuHMT1/2 variants engineered for improved turnover with **10** followed by SPAAC to identify non-histone EuHMT1/2 substrates in cell lysates.[50] The same group used a similar strategy to identify substrates for protein arginine N-MT PRMT3 using a PRMT3 variant (M233G) and **16**.[51] This team extended the concept to living cells via the inclusion of a

MAT (I117A) and H3K9 N-MT (EuHMT1-Y1211A or EuHMT2-Y1154A) engineered to favor **1** followed by CuAAC-based labeling. Referred to as 'clickable chromatin enrichment with parallel DNA sequencing' (CliEn-seq),[52] this proof-of-concept study highlighted MAT-catalyzed intracellular production of **1** from cell-permeable methionine analogues, in situ chromatin modification by engineered EuHMT1/2 and subsequent enrichment of uniquely modified chromatins via CuAAC-enabled capture for sequencing. In vitro functional annotation of two putative lysine N-MTs METTL21A and METTL10 employed similar tactics. Specifically, the use of **8** in cell lysates followed by CuAAC confirmed METTL21A to function as a histone N-MT and revealed METTL10 to EF1A1 lysine 318.[53] Zumbusch and colleagues recently reported an alternative method for conceptually similar cell-based proteomics.[54] In this study, HEK293T and HeLa S3 cells engineered to produce enhanced green fluorescent protein (eGFP)-fusions with 12 protein targets of interest (p53, Akt1, GAPDH, histones H2B, H3, H4; microtubule-associated protein RP/EB family member EB1; Foxo1; and heat shock proteins HSPA1 and HSPA8; valosin-containing protein VCP; and nucleolin) were electroporated with **8**. Subsequent CuAAC-mediated fluorophore conjugation enabled intracellular fluorescence lifetime imaging (FLIM) FRET of each target protein's alkylation state and localization.

*1.4.4 Representative recent natural product and small molecule applications (**Figure 1.3**)*

Transferase-mediated bioactive natural product (NP) chemoselective modification was first demonstrated using the vancomycin glycosyltransferase GtfE and non-native sugars bearing azides and alkoxyamines to afford CuAAC[55] or alkoxyamine-based 'neoglycosylation'[56], respectively. Proof-of concept MT-catalyzed non-native NP

alkylation was first established by Gruber-Khadjawi and colleagues using the novobiocin and coumermycin 8-*C*-MTs NovO and CouO. Using synthetic non-native AdoMet analogues and simple coumarin models, this study demonstrated NovO/CouO-catalyzed 5 non-native 8-*C*-alkyl groups and also highlighted some permissivity toward alternative acceptors. To circumvent limitations associated with synthetic AdoMets within this context, Singh, Thorson and colleagues were the first to develop MAT/MT coupled systems for natural product 'alkylrandomization' using the indolocarbazole rebeccamycin sugar 4'-*O*-MT RebM as a model.[9] This work highlighted the survey of 5 diverse MATs for non-native AdoMet production, use of hMAT2 to produce AdoMet analogues bearing 18 non-native S-substitutions and the application of coupled hMAT2/RebM reactions to generate 4 rebeccamycin analogues bearing 4'-*O* non-native alkyl groups. Similar NP biosynthetic MT alkyl permissivity and corresponding coupled multi-enzyme platforms have since been reported for a range of NPs including: rapamycin (16-*O*-MT RapM: coupled hMAT/RapM system to produce 16-*O*-alkyl rapalogs[58]); coumarins (novobiocin 8-*C*-MT NovO: coupled SalL/NovO system to produce model coumarins including 8-*C*-isotopically-labeled derivatives[59,60]) and alkaloids/phenolics (coclaurine *N*-MT CNMT: coupled hMAT/CNMT system to produce 2-*N*-alkyl isoquinolones[61]; carboxy-S-adenosyl-L-methionine synthase in conjunction with CNMT or catechol-*O*-methyltransferase COMT to produce N- and O-carboxymethylated molecules[62]). Micklefield and colleagues also introduced an innovative coupled fungal tyrosinase - mammalian catechol-*O*-MT (COMT) system for selective peptide *O*-alkylation with non-native alkyl groups.[63] Brieke and collaborators reported the first proof of concept for MT-mediated chemoselective conjugation. This study employed two glycopeptide α-*N*-MTs (A40926 MtfAdbv and

pekiskomycin MtfApek) and led to the production of teicoplanin aglycon-**18** and **30** (**Figure 1.3**), the latter of which was successfully used in IEDDA conjugation reactions to tether an affinity ligand or fluorophore.[64] Enediyne MT-mediated chemoselective conjugation was also recently demonstrated using the permissive tiancimycin 7-*O*-MT TnmH[65]]. This study highlighted TnmH to turnover a range of anthraquinone acceptors and, in the presence of non-native AdoMet donors, catalyze production of tiancimycin 7-*O*-alkyl analogues. The corresponding tiancimycin-**20** (**Figure 1.3**) was subsequently used in CuAAC reactions to introduce tethers for antibody-conjugation.

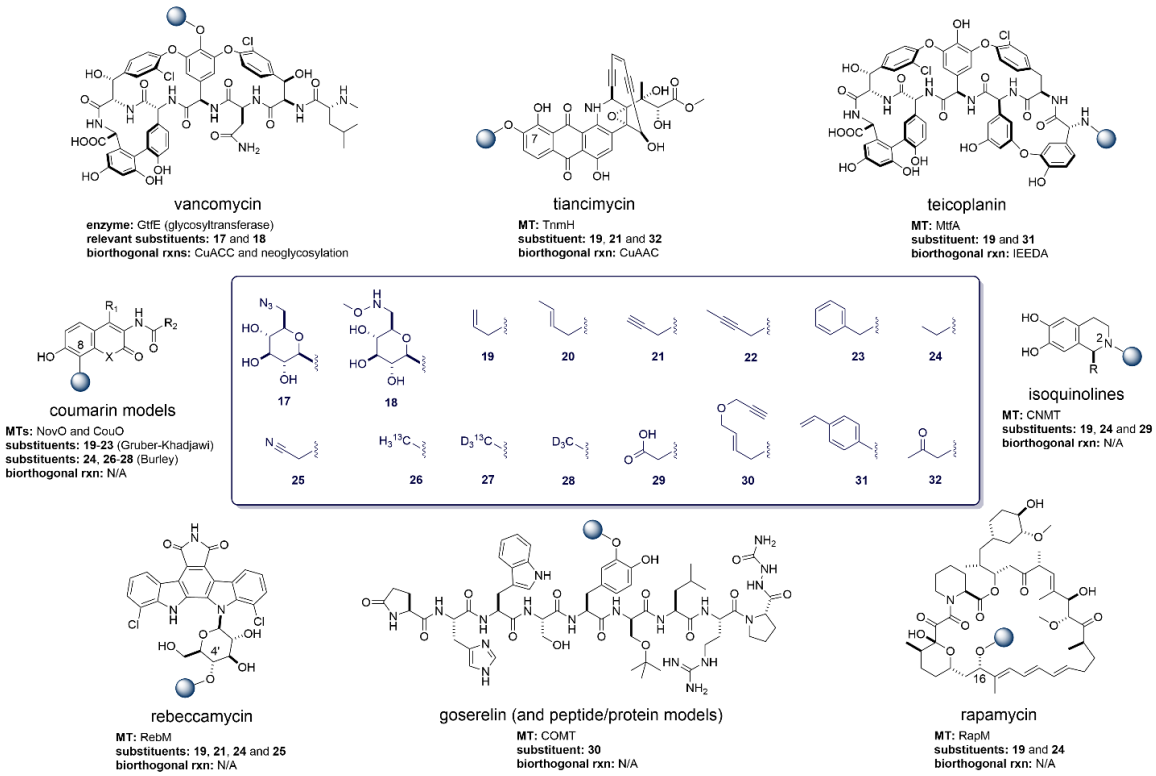

Figure 1.3. Natural products for which transferase-enable bioorthogonal chemoselective modification and/or MT-enable non-native alkylation has been reported. The regiochemistry of non-native modification is highlight by the blue ball with corresponding non-native substituents illustrated in the center box.

1.5 Conclusions

Notable advances in bioorthogonal chemoselective reaction and enzyme reagent (enzymes and non-native substrates) supports emerging transferase-mediated bioorthogonal platforms. While limited proof of concept examples for cell-based applications of MT-enabled bioorthogonal labeling/conjugation exist, three key barriers to broader use remain. First, unlike many of the commercially available kits/reagents for bioorthogonal chemoselective conjugation, the reagents (enzymes and non-native substrates) for MT-enabled platforms are highly specialized and largely inaccessible to the broader research community. Improved access to non-native AdoMet analogues via commercial sources and/or user-friendly production methods is expected to present new opportunities and unlock new discoveries. Second, the stability, PK, biodistribution and cellular uptake of non-native AdoMet analogues remain substantive barriers to cell-based and in vivo applications. Strategies to stabilize and/or 'deliver' AdoMet analogues as well as improved methods for in situ (cell and/or tissue-specific) production are anticipated to help circumvent these roadblocks. Finally, MT reaction rates and bioorthogonality (*i.e.*, selectivity for non-native substrates) fall far short of the corresponding rates or selectivities of the best bioorthogonal chemoselective reactions. The ongoing discovery and evolution/engineering of improved catalysts is expected to continue to narrow this gap.

References for Chapter One

(1) Nguyen, S.S; and Prescher, J.A. Developing bioorthogonal probes to span a spectrum of reactivities. *Nat. Rev. Chem.* **2020**, *4*, 476-489.

(2) Smeenk, M.L.; Agramunt, J.; Bonger, K.M. Recent developments in bioorthogonal chemistry and the orthogonality within. *Curr. Opin. Chem. Biol.* **2020**, *60*, 79-88.

(3) Porte, K.; Riberaud, M.; Châtre, R.; Audisio, D.; Papot, S.; Taran, F. Bioorthogonal reactions in animals. *Chem. Bio. Chem.* **2021**, *22*, 100-113.

(4) Tomkuvienė, M.; Mickutė, M.; Vilkaitis, G.; Klimašauskas, S. Repurposing enzymatic transferase reactions for targeted labeling and analysis of DNA and RNA. *Curr. Opin. Biotechnol.* **2019**, *55*, 114-123.

(5) Romero, E.; Jones, B.S.; Hogg, B.N.; Rué Casamajo, A.; Hayes, M.A.; Flitsch, S.L.; Turner, N.J.; Schnepel, C. Enzymatic late-stage modifications: Better late than never. *Angew Chem Int Ed Engl.* **2021**, *60*, 16824-16855.

(6) Sun, Q.; Huang, M.; Wei, Y. Diversity of the reaction mechanisms of SAM-dependent enzymes. *Acta Pharm Sin B.* **2020**, *11*, 632-650.

(7) Huber, T. D.; Johnson, B. R.; Zhang, J.; Thorson, J. S. AdoMet analog synthesis and utilization: Current state of the art. *Curr. Opin. Biotechnol.* **2016**, *42*, 189-197.

(8) Bennett, M. R.; Shepherd, S. A.; Cronin, V. A.; Micklefield, J. Recent advances in methyltransferase biocatalysis. *Curr. Opin. Chem. Biol.* **2017**, *37*, 97–106.

(9) Singh, S.; Zhang, J.; Huber, T.D.; Sunkara, M.; Hurley, K.; Goff, R.D.; Wang, G.; Zhang, W.; Liu, C.; Rohr, J.; Van Lanen, S.G.; Morris, A.J.; and Thorson, J.S. Facile chemoenzymatic strategies for the synthesis and utilization of *S*-adenosyl- L-methionine analogues. *Angew. Chemie Int. Ed.* **2014**, *53*, 3965–3969.

(10) Bothwell, I.R.; Luo, M. Large-scale, protection-free synthesis of *Se*-adenosyl- L-selenomethionine analogues and their application as cofactor surrogates of methyltransferases. *Org. Lett.* **2014**, *16*, 3056-3059.

(11) Huber, T.D.; Clinger, J.A.; Liu, Y.; Xu, W.; Miller, M.D.; Phillips Jr, G.N.; Thorson, J.S. Methionine adenosyltransferase engineering to enable bioorthogonal platforms for AdoMet-utilizing enzymes. *ACS Chem Biol*. **2020**, *15*, 695-705.

(12) Michailidou, F.; Klöcker, N.; Cornelissen, N.V.; Singh, R.K.; Peters, A.; Ovcharenko, A.; Kümmel, D.; Rentmeister, A. Engineered SAM synthetases for enzymatic generation of AdoMet analogs with photocaging groups and reversible DNA modification in cascade reactions. *Angew. Chem. Int. Ed. Engl.* **2021**, *60*,480-485.

(13) Davis, T.D.; Kunakom, S.; Burkart, M.D.; Eustaquio, A.S. Preparation, assay, and application of chlorinase SalL for the chemoenzymatic synthesis of *S*-adenosyl- L-methionine and analogs. *Methods Enzymol.* **2018**, *604*, 367-388.

(14) Tang, Q.; Grathwol, C.W.; Aslan-Üzel, A.S.; Wu, S.; Link, A.; Pavlidis, I.V.; Badenhorst, C.P; Bornscheuer, U.T. Directed evolution of a halide methyltransferase enables biocatalytic synthesis of diverse SAM analogs. *Angew Chem Int Ed Engl*. **2021**, *60*, 1524-1527.

(15) Huber, T.D.; Wang, F.; Singh, S.; Johnson, B.R.; Zhang, J.; Sunkara, M.; Van Lanen, S.G.; Morris, A.J.; Phillips Jr., G.N.; Thorson, J.S. Functional AdoMet isosteres resistant to classical AdoMet degradation pathways. *ACS Chem. Biol.* **2016**, *11*, 2484–2491.

(16) Breugst, M.; Reissig, H.U. Milestones of the 1,3-dipolar cycloaddition. *Angew*

Chem Int Ed Engl. **2020**, *59*, 12293-12307.

(17) Neumann, S.; Biewend, M.; Rana, S.; Binder, W.H. The CuAAC: principles, homogeneous and heterogeneous catalysts, and novel developments and applications. *Macromol Rapid Commun*. **2020**, *41*, e1900359.

(18) Dommerholt, J.; Rutjes, F.P.; Delft, F.L.V. Strain-promoted 1,3-dipolar cycloaddition of cycloalkynes and organic azides. *Top Curr Chem (Cham).* **2016**, 57-76.

(19) Svatunek, D.; Houszka, N.; Hamlin, T.A.; Bickelhaupt, F.M.; Mikula, H. Chemoselectivity of tertiary azides in strain-promoted alkyne-azide cycloadditions. *Chemistry*. **2019**, *25*, 754-758.

(20) Burke, E.G.; Gold, B.; Hoang, T.T.; Raines, R.T.; Schomaker, J.M. Fine-tuning strain and electronic activation of strain-promoted 1,3-dipolar cycloadditions with endocyclic sulfamates in SNO-OCTs. *J Am Chem Soc*. **2017**, *139*, 8029-8037.

(21) Kumar, G.S.; and Lin, Q. Light-triggered click chemistry. *Chem Rev*. **2020**, *121*, 6991-7031.

(22) Jiang, S.; Wu, X.; Liu, H.; Deng, J.; Zhang, X.; Yao, Z.; Zheng, Y.; Li, B.; Yu, Z. Ring-strain-promoted ultrafast diaryltetrazole–alkyne photoclick reactions triggered by visible light. *Chem Photo Chem*. **2020**, *4*, 327-331.

(23) Li, J.; Kong, H.; Zhu, C.; Zhang, Y. Photo-controllable bioorthogonal chemistry for spatiotemporal control of bio-targets in living systems. *Chem Sci.* **2020**, *11*, 3390-3396.

(24) Oliveira, B.L.; Guo, Z.; Bernardes, G.J.L. Inverse electron demand Diels-Alder reactions in chemical biology. *Chem Soc Rev*. **2017**, *46*, 4895-4950.

(25) Wu, H.; Devaraj, N.K. Advances in tetrazine bioorthogonal chemistry driven by the synthesis of novel tetrazines and dienophiles. *Acc Chem Res*. **2018**, *51*, 1249-1259.

(26) Reisacher, U.; Ploschik, D.;Rönicke, F.; Cserép, G.B.; Kele, P.; Wagenknecht, H.A. Copper-free dual labeling of DNA by triazines and cyclopropenes as minimal orthogonal and bioorthogonal functions. *Chem Sci.* **2019**, *10*, 4032-4037.

(27) Macias-Contreras, M.; He, H.; Little, K.N.; Lee, J.P.; Campbell, R.P.; Royzen, M.; Zhu, L. SNAP/CLIP-tags and strain-promoted azide-alkyne cycloaddition (SPAAC)/inverse electron demand Diels-Alder (IEDDA) for intracellular orthogonal/bioorthogonal labeling. *Bioconjug Chem.* **2020**, *31*, 1370-1381.

(28) Pljevaljcić, G.; Pignot, M.; Weinhold, E.; Pljevaljcic, G.; Pignot, M.; Weinhold, E. Design of a New Fluorescent Cofactor for DNA Methyltransferases and Sequence-Specific Labeling of DNA. *J. Am. Chem. Soc.* **2003**, *125*, 3486–3492.

(29) Zhang, C.; Weller, R.L.; Thorson, J.S.; Rajski, S.R. Natural product diversification using a non-natural cofactor analogue of *S*-adenosyl-L-methionine. *J. Am. Chem. Soc.* **2006**, *128*, 2760–2761.

(30) Dalhoff, C.; Lukinavičius, G.; Klimašauskas, S.; Weinhold, E. Direct transfer of extended groups from synthetic cofactors by DNA methyltransferases. *Nat. Chem. Biol.* **2006**, *2*, 31-32.

(31) Klöcker, N.; Weissenboeck, F.P; Rentmeister, A. Covalent labeling of nucleic acids. *Chem Soc Rev*. **2020**, *49*, 8749-8773.

(32) Vranken, C.; Deen, J.; Dirix, L.; Stakenborg, T.; Dehaen, W.; Leen, V.; Hofkens, J.; Neely, R.K. Super-resolution optical DNA mapping via DNA methyltransferase-directed click chemistry. *Nucleic Acids Res.* **2014**, *42*, e50.

(33) Lauer, M.H.; Vranken, C.; Deen, J.; Frederickx, W.; Vanderlinden, W.; Leen, V.; Gehlen, M.H.; Hofkens, J.; Neely, R.K. Methyltransferase-directed covalent coupling of fluorophores to DNA. *Chem Sci.* **2017**, *8*, 3804-3811.

(34) Heck, C.; Torchinsky, D.; Nifker, G.; Gularek, F.; Michaeli, Y.; Weinhold, E.; Ebenstein, Y. Label as you fold: Methyltransferase-assisted functionalization of DNA nanostructures. *Nanoscale*. **2020**, *12*, 20287-20291.

(35) Anhäuser, L.; Muttach, F.; Rentmeister, A. Reversible modification of DNA by methyltransferase-catalyzed transfer and light-triggered removal of photo-caging groups. *Chem Commun*. **2018**, *54*, 449-451.

(36) Heimes, M.; Kolmar, L.; Brieke, C. Efficient cosubstrate enzyme pairs for sequence-Specific methyltransferase-directed photolabile caging of DNA. *Chem. Commun.* **2018**, *54*, 12718-12721.

(37) Wilkinson, A.A.; Jagu, E.; Ubych, K.; Coulthard, S.; Rushton, A.E.; Kennefick, J.; Su, Q.; Neely, R.K.; Fernandez-Trillo. Site-selective and rewritable labeling of DNA through enzymatic, reversible, and click chemistries. *ACS Cent Sci.* **2020**, *6*, 525-534.

(38) Muthmann, N.; Hartstock, K.; Rentmeister, A. Chemo-enzymatic treatment of RNA to facilitate analyses. *Wiley Interdiscip Rev RNA*. **2020**, *11*, e1561.

(39) Holstein, J. M.; Stummer, D.; Rentmeister, A. Enzymatic modification of 5'-capped RNA and subsequent labeling by click chemistry. *Methods Mol. Biol.* **2016**, *1428*, 45-60.

(40) Holstein, J.M.; Schulz, D.; Rentmeister, A. Bioorthogonal site-specific labeling of the 5′-cap structure in eukaryotic mRNAs. *Chem Commun*. **2014**, *50*, 4478-4481.

(41) Muttach, F.; Rentmeister, A. A biocatalytic cascade for versatile one-Pot modification of mRNA starting from methionine analogues. *Angew. Chemie., Int. Ed*. **2016**, *55*, 1917-1920.

(42) Holstein, J.M.; Anhäuser, L.; Rentmeister, A. Modifying the 5′-cap for click reactions of Eukaryotic MRNA and to tune translation efficiency in living cells. *Angew. Chemie., Int. Ed.* **2016**, *55*, 10899-10903.

(43) Muttach, F.; Muthmann, N.; Reichert, D.; Anhäuser, L.; Rentmeister, A. A benzylic linker promotes methyltransferase catalyzed norbornene transfer for rapid bioorthogonal tetrazine ligation. *Chem Sci*. **2017**, *8*, 7947-7953.

(44) Holstein, J.M.; Muttach, F.; Schiefelbein, S. H.H.; Rentmeister, A. dual 5′ cap labeling based on regioselective RNA methyltransferases and bioorthogonal reactions. *Chem. - A Eur. J.* **2017**, *23*, 6165-6173.

(45) Hartstock, K.; Nilges, B.S.; Ovcharenko, A.; Cornelissen, N.V.; Püllen, N.; Lawrence-Dörner, A.M.; Leidel, S.A.; Rentmeister, A. Enzymatic or in vivo installation of propargyl groups in combination with click chemistry for the enrichment and detection of methyltransferase target sites in RNA. *Angew. Chem., Int. Ed.* **2018**, *57*, 6342-6346.

(46) Ovcharenko, A.; Weissenboeck, F.P.; Rentmeister, A. Tag-free internal RNA labeling and photocaging based on mRNA methyltransferases. *Angew. Chemie., Int. Ed*. **2020**, *6*0, 4098-4103.

(47) Osipenko, A.; Plotnikova, A.; Nainytė, M.; Masevičius, V.; Klimašauskas, S.; Vilkaitis, G. Oligonucleotide-addressed covalent 3'-terminal derivatization of small RNA strands for enrichment and visualization. *Angew. Chem., Int. Ed.* **2017**, *129*,

6507-6510.

(48) Braun, A.C.; Gutmann, M.; Lühmann, T.; Meinel, L. Bioorthogonal strategies for site-directed decoration of biomaterials with therapeutic proteins. *J Control Release.* **2018**, *273*, 68-85.

(49) Peters, W.; Willnow, S.; Duisken, M.; Kleine, H.; Macherey, T.; Duncan, K.E.; Litchfield, D.W.; Lüscher, B.; Weinhold, E. Enzymatic site-specific functionalization of protein methyltransferase substrates with alkynes for click labeling. *Angew. Chemie., Int. Ed.* **2010**, *49*, 5170-5173.

(50) Islam, K.; Bothwell, I.; Chen, Y.; Sengelaub, C.; Wang, R.; Deng, H.; Luo, M. Bioorthogonal profiling of protein methylation using azido derivative of *S*-adenosyl-L-methionine. *J. Am. Chem. Soc.* **2012**, *134*, 5909-5915.

(51) Guo, H.; Wang, R.; Zheng, W.; Chen, Y.; Blum, G.; Deng, H.; Luo, M. Profiling substrates of protein arginine *N*-methyltransferase 3 with *S*-adenosyl-L-methionine analogues. *ACS Chem. Biol.* **2014**, *9*, 476-484.

(52) Wang, R.; Islam, K.; Liu, Y.; Zheng, W.; Tang, H.; Lailler, N.; Blum, G.; Deng, H.; Luo, M. Profiling genome-wide chromatin methylation with engineered posttranslation apparatus within living cells. *J. Am. Chem. Soc.* **2013**, *135*, 1048-1056.

(53) Shimazu, T.; Barjau, J.; Sohtome, Y.; Sodeoka, M.; Shinkai, Y. Selenium-based *S*-adenosylmethionine analog reveals the mammalian seven-beta-strand methyltransferase METTL10 to be an EF1A1 lysine methyltransferase. *PLoS One*. **2014**, *9*, e105394.

(54) Doll, F.; Steimbach, R.R.; Zumbusch, A. Direct imaging of protein-specific

methylation in mammalian cells. *Chem Bio Chem.* **2019**, *20*, 1315-1325.

(55) Fu, X.; Albermann, C.; Jiang, J.; Liao, J.; Zhang, C.; Thorson, J.S. Antibiotic optimization via in vitro glycorandomization. *Nat Biotechnol*. **2003**, *21*, 1467-1469.

(56) Peltier-Pain, P.; Marchillo, K.; Zhou, M.; Andes, D.R.; Thorson, J.S. Natural product disaccharide engineering through tandem glycosyltransferase catalysis reversibility and neoglycosylation. *Org. Lett.* **2012**, *14*, 5086-5089.

(57) Stecher, H.; Tengg, M.; Ueberbacher, B.J.; Remler, P.; Schwab, H.; Griengl, H.; Gruber-Khadjawi, M. Biocatalytic Friedel-Crafts alkylation using non-natural cofactors. *Angew. Chemie.* **2009**, *121*, 9710-9712.

(58) Law, B.J.C.; Struck, A.W.; Bennett, M.R.; Wilkinson, B.; Micklefield, J. Site-specific bioalkylation of Rapamycin by the RapM 16-*O*-methyltransferase. *Chem. Sci.* **2015**, *6*, 2885-2892.

(59) Sadler, J.C.; Humphreys, L.D.; Snajdrova, R.; Burley, G.A. A tandem enzymatic sp2-C-methylation process: Coupling in situ *S*-adenosyl-L-methionine formation with methyl transfer. *Chem bio chem.* **2017**, *18*, 992-995.

(60) McKean, I.J.; Sadler, J.C.; Cuetos, A.; Frese, A.; Humphreys, L.D.; Grogan, G.; Hoskisson, P.A.; Burley, G.A. *S*-adenosyl methionine cofactor modifications enhance the biocatalytic repertoire of small molecule *C*-alkylation. *Angew. Chem., Int. Ed*. **2019**, *131*, 17583-17588.

(61) Bennett, M.R.; Thompson, M.L.; Shepherd, S.A.; Dunstan, M.S.; Herbert, A.J.; Smith, D.R.; Cronin, V.A.; Menon, B.R.; Levy, C.; Micklefield, J. Structure and biocatalytic scope of coclaurine *N*-methyltransferase. *Angew. Chem., Int. Ed*. **2018**, *130*, 10600-10604.

(62) Herbert, A.J.; Shepherd, S.A.; Cronin, V.A.; Bennett, M.R.; Sung, R.; Micklefield, J. Engineering orthogonal methyltransferases to create alternative bioalkylation pathways. *Angew. Chem., Int. Ed*. **2020**, *132*, 14950-14956.

(63) Struck, A.W.; Bennett, M.R.; Shepherd, S.A.; Law, B.J.C.; Zhuo, Y.; Wong, L.S.; Micklefield, J. An enzyme cascade for selective modification of tyrosine residues in structurally diverse peptides and proteins. *J. Am. Chem. Soc.* **2016**, *138*, 3038-3045.

(64) Brieke, C.; Yim, G.; Peschke, M.; Wright, G.D.; Cryle, M.J. Catalytic promiscuity of glycopeptide N-methyltransferases enables bio-orthogonal labeling of biosynthetic intermediates. *Chem Commun (Camb).* **2016**, *52*, 13679-13682.

(65) Adhikari, A.; Teijaro, C.N.; Yan, X.; Chang, C.Y.; Gui, C.; Liu, Y.C.; Crnovcic, I.; Yang, D.; Annaval, T.; Rader, C.; Shen, B. Characterization of TnmH as an *O*-methyltransferase revealing insights into tiancimycin biosynthesis and enabling a biocatalytic strategy to prepare antibody-tiancimycin conjugates. *J Med Chem*. **2020**, *63*, 8432-8441.

Chapter Two: Biochemical and structural studies of the carminomycin 4-*O*-methyltransferase DnrK

2.1 Introduction

Daunorubicin (DNR **1a**, also known as daunomycin) and the 14-hydroxy derivative doxorubicin (DXR, adriamycin) (**Figure 2.1A**) are anthracycline-based microbial natural products that have been used effectively to treat cancer for over four decades.[1] DNR and DXR are potent topoisomerase II inhibitors and both also induce free radical species that contribute to cumulative dose-limiting cardiotoxicity.[1-3] The producing strain for DNR (*Streptomyces peucetius*) was first isolated in the 1950s near a 13th-century castle in the Apulia region of southern Italy.[4] Subsequent *N*-nitroso-*N*-methylurea-based mutagenesis of this DNR-producer led to the first DXR-producing variant.[5,6] DNR and DXR and their producing strains subsequently served as early prototypical models that enabled many pioneering discoveries relating to aromatic polyketide and uniquely functionalized deoxysugar genetics and biosynthesis.[7,8] These studies revealed DNR biosynthesis to culminate with carminomycin (CAR, **1**) methyltransferase (MT)-catalyzed 4-*O*-methylation and subsequent DNR P450 hydroxylase-catalyzed C-14-hydroxylation to afford DXR.[9-11] Strohl and coworkers were the first to demonstrate the *S*-adenosylmethionine (AdoMet)-dependent 4-*O*-methylation reaction in vitro using crude extracts from several daunomycin-producing strains and also were the first to report preliminary biochemical studies of the native CAR 4-*O*-MT purified from *Streptomyces* sp. strain C5.[12] Subsequent genetic studies led to the discovery of the genes encoding the

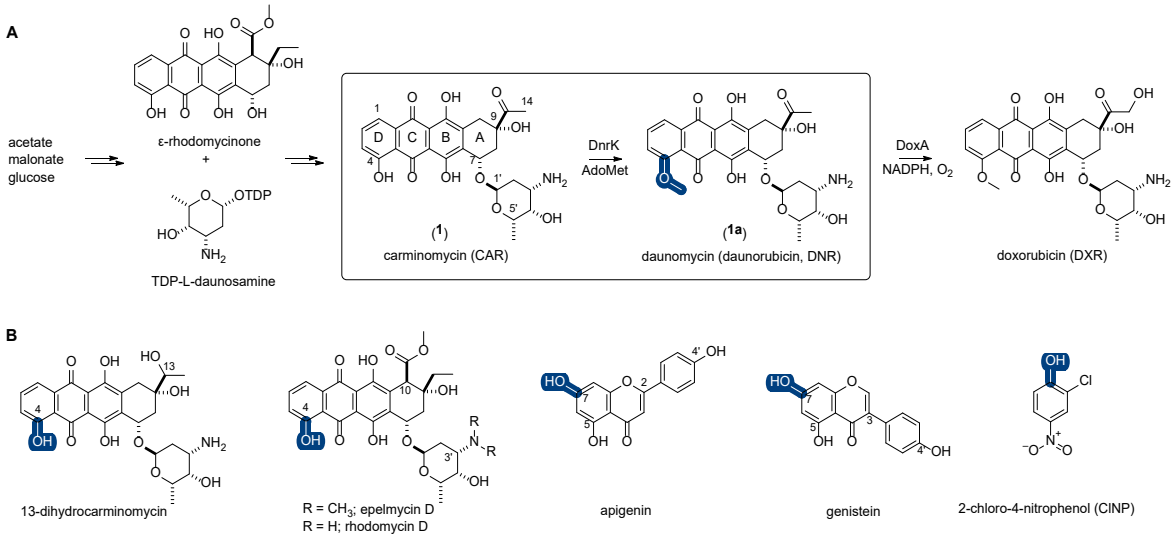

Figure 2.1. (A) Overview the final steps of DNR (1a) and DXR biosynthesis with emphasis on the DnrK-catalyzed methylation reaction (box) and DnrK regioselectivity (blue). **(B)** Previously reported DnrK or DauK substrates with MT regioselectivity highlighted (blue).

CAR 4-*O*-MT (*dnrK* from *S. peucetius* and *dauK* from *Streptomyces* sp. strain C5)[11,13] and opened the door to heterologous overproduction strains and bioconversion studies.[13-15] For example, the use of *dnrK* in heterologous strain engineering enabled production of non-native hybrid natural products as exemplified by the production of 4-*O*-methylepelmycin D by heterologous expression of *dnrK* in epelmycin-producing *S. violaceus* (**Figure 2.1B**).[16] Heterologous overproduction of DnrK in *E coli* by Hutchinson and coworkers set the stage for mechanistic, structural and biocatalysis applications.[14] Representative highlights include observed biocatalytic rate improvements with immobilized DnrK,[17,18] new MT mechanistic insights based on determined DnrK ligand-bound structures[18,19] and structure-based engineering such as the rational design of RdmB-like AdoMet-dependent monooxygenases from DnrK.[20]

The foundational DnrK structures also enabled computational docking studies as basis for the discovery of new DnrK methyl acceptors. These studies implicated prototypical flavones and isoflavones as putative substrates and confirmed facile DnrK turnover of apigenin and genistein (**Figure 2.1B**).[21] Inspired by the demonstrated ability of DnrK to methylate simpler non-anthracycline substrates, we recently reported a simple colorimetric assay for DnrK based on the substrate surrogate 2-chloro-4-nitrophenol (ClNP) (**Figure 2.1B**).[22] Ternary complex structure elucidation with DnrK, ClNP and a stabilized AdoMet isosteric substrate Ado^{t}Met also revealed the putative capacity of the DnrK active site to accommodate larger and/or more diverse methyl acceptors. To build on this observation and interrogate DnrK permissivity, herein we describe evaluation of 100 structurally and functionally diverse phenolic natural products of wide-ranging architectural complexity as potential DnrK substrates. Included in the demonstrated DnrK

substrates is 4-methylumbelliferone (4-MeUmb **75**, a fluorescent hydroxycoumarin drug frequently used as a real-time fluorescent indicator in enzyme assays)[23,24] and a range of complex natural products including anthracyclines, angucyclines, anthraquinone-fused enediynes, flavonoids, pyranonapthoquinones and polyketides. This study also provides previously undetermined DnrK kinetic parameters and a comparative evaluation of the impact anthracycline 4-*O*-methylation on cancer cell line cytotoxicity, 4E-BP1 phosphorylation and axolotl embryo tail regeneration).

2.2 Results and discussion

2.2.1 DnrK non-native acceptor scope

For substrate specificity studies, a representative set of structurally diverse, naturally-occurring hydroxy-aromatics were assessed as putative acceptors in the presence of DnrK and AdoMet. A total of 100 compounds were tested (**Table S2.1**). Assays were analyzed via LC-MS with new methylated products identified by a change in mass (mono-methylation D*m/z* = +14, di-methylation D*m/z* = +28 and tri-methylation D*m/z* = +42) and retention time compared to control in the absence of DnrK. The native substrate CAR (**1**) and the previously reported non-native substrate ClNP (k_{cat} = 0.019 ± 0.001 min^{-1}, K_m = 106 ± 10 μM under saturating [AdoMet])[22] were included as positive controls. Since the kinetic parameters for DnrK with native substrate **1** had not been previously reported, these values were determined as part of this study (CAR k_{cat} = 0.65 ± 0.03 min^{-1}, K_m = 50 ± 2 μM under saturating [AdoMet]). DnrK catalytic efficiency (k_{cat}/K_m) with **1** is nearly two orders of magnitude greater (77-fold) to that with ClNP (**Table 2.1**), primarily due to a

Table 2.1. Kinetic parameters of DnrK.

Substrate	k_{cat} (min^{-1})	K_m (μM)	k_{cat}/K_m (min^{-1} μM^{-1})	k_{cat}/K_m (relative)
CAR **1**	0.65 ± 0.03	50 ± 2	0.013	1
4-MeUmb **75**	0.036 ± 0.001	1160 ± 170	3.1×10^{-5}	0.002
ClNP	0.019 ± 0.001	106 ± 10	1.8×10^{-4}	0.013

notable difference in k_{cat}. The catalytic efficiencies for typical AdoMet-dependent MTs range from ~10 to 7200 M^{-1} s^{-1}.[25]

The first set of new non-native substrates identified were comprised of fused aromatic anthracene, tetracene or benz[a]nthracene scaffolds (**Figure 2.2**). With the exception of the tetracenomycins and tiancimycins, all members within this series contained the key *β*-hydroxy quinone signature of the native substrate CAR **1**. The simplest among these were the substituted anthraquinones alizarin (**2**, 13%), purpurin (**3**, 13%) and 9,10-seco-7-deoxy-nogalamycinone (**4**, 91%).[26] Anthraquinones represent a structurally and functionally diverse class of pharmacophores in which subtle structural changes can notably alter functional outcomes.[27-30] Comparative analysis of the anthraquinone set revealed CAR-like DnrK *β*-hydroxy regioselectivity in all **2**, **3** and **4** compounds. LC-MS could not delineate A ring versus C ring *β*-hydroxy alkylation in **4** nor *β*- or *γ*-hydroxy methylation for **2** or **3**. Intriguingly, no turnover was observed with representative anthraquinones containing only *β*-hydroxy substitutions such as quinizarin (**5**) or juglone (**6**).

The CAR-like tetracenes turned over by DnrK included aranciamycin (**7**, 97%),[31] 7-deoxy aranciamycin; SM 173B (**8**, 96%), steffimycin B (**9**, 15%),[32] nogalamycinone [nogalavinone (**10**) and auramycinone (**11**), 76% and 96%, respectively],[33] as well as 7-deoxy-nogalamycinone (**12**) and deoxyauramycinone (**13**), 62% and 20%, respectively.[26] Compared to **1**, the aranciamycin D ring has a C8 methoxy and differs slightly in the C7 glycosyl and C9 aliphatic substitutions. DnrK turnover of **7** and the C7-deoxy analogue of its aglycon (**8**, lacking both C7-OH and its appended 2-*O*-methyl-L-rhamnose) was quantitative and the corresponding DnrK aranciamycin product confirmed as

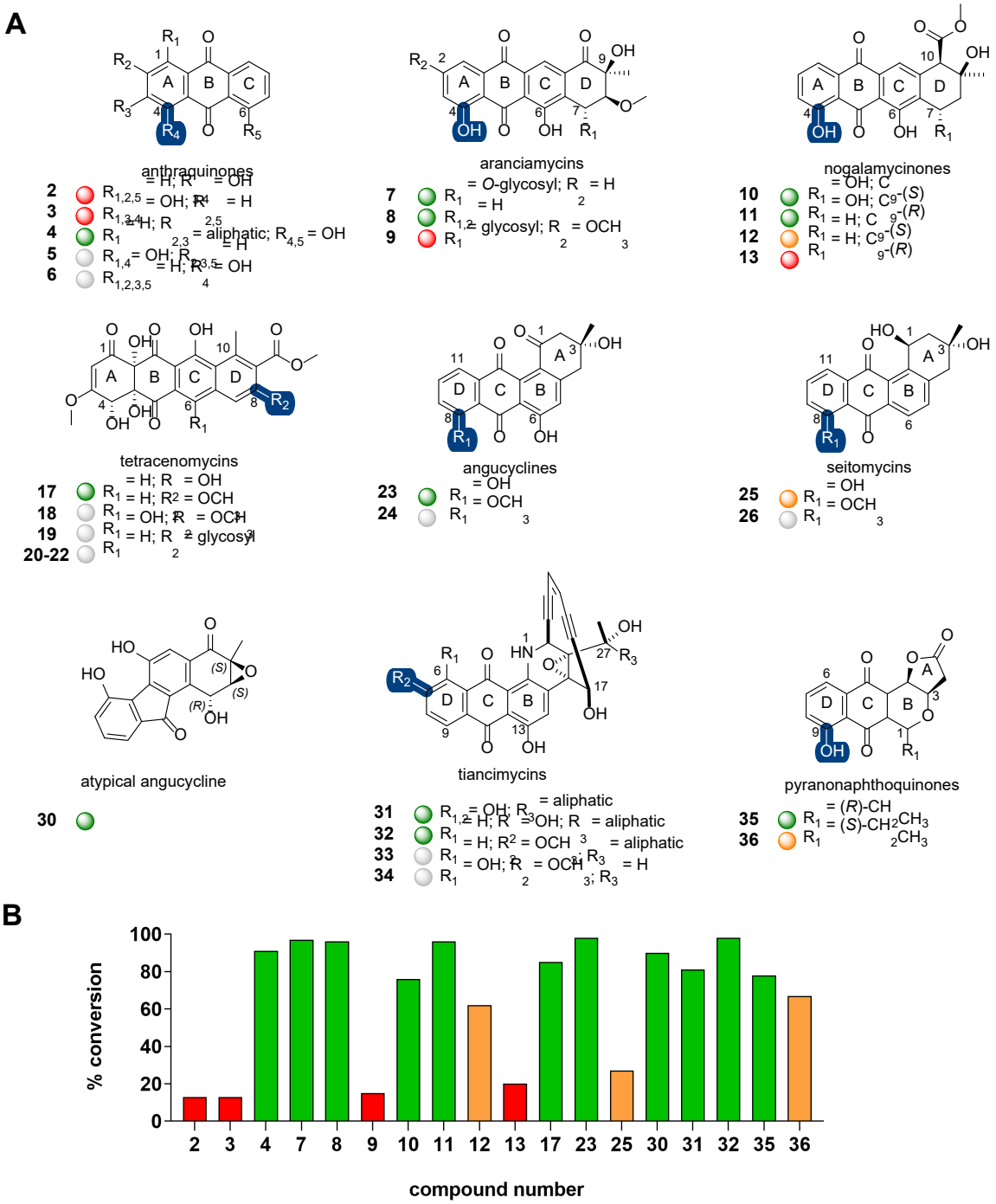

Figure 2.2. (A) Representative anthracene, tetracene, benz[a]anthracene and related DnrK substrates. Highlighted DnrK regioselectivity (blue), where determined, was based on isolation and structure elucidation (4-*O*-methoxy-arancinamycin **7a**), co-elution with product standards (**1a**, **18**, or assigned based on the presence of a single aromatic hydroxyl

(pyranonapthoquinones). **(B)** The percent conversion to product in an end point LC-MS assay (1 mM test agent, 3.2 mM AdoMet, 100 μM DnrK, 37 ºC, 16 h). Turnover is categorized in plot and under each structure as a colored ball as good (≥75%, green), moderate (>25% - <75%, orange), low (≤25%, red) and no turnover (grey).

4-*O*-methoxy-arancinamycin (**7a**) via product isolation and structure elucidation (**Figure 2.3 and Figure S2.1**). While DnrK appeared to tolerate a wide range of D ring structural modifications, the addition of a C2 methoxy substitution led to marked reduction in DnrK turnover. Compared to **8**, the structurally-related nogalamycinones (**10** and **11**) and 7-deoxynogalamycinones (**12** and **13**) lack the D ring C8 methoxy and contain a distinct C10 substitution. In case of nogalamycinones, the absence or presence of the C7 hydroxyl does comparatively impact DnrK turnover with DnrK favoring the C7-hydroxy analogues **10** and **11** over **12** and **13**. No DnrK-catalyzed conversion was observed in the presence of prototypical nogalamycins bearing a C1/C2 fused glycoside[34] (compound **14-16**); **Figure 2.4**.

Distinct from the CAR-like tetracenes, tetracenomycins lack the key *β*-hydroxy quinone signature of the native DnrK substrate. Tetracenomycins are natural products with antibiotic and anticancer activities that inhibit the polypeptide exit tunnel of the bacterial ribosome.[35] Facile DnrK-catalyzed turnover of 8-desmethyl tetracenomycin C (**17**, 85%) was observed, the reaction product of which had the same retention time and mass as tetracenomycin C (TCM C, **18**); **Figure S2.2**.[36] This surprising result implicated DnrK as a functional mimic of the TCM 8-*O*-MT TcmO.[9,37,38] In addition, While DnrK-catalyzed reactions with 6-hydroxy-TCM C (**19**) led to no product, C8-glycosides of 8-desmethyl TCM C (**20-22**) led to efficient TCM C (**18**) production in two (**20** and **22**) of the three cases. This result is consistent with glycoside hydrolysis and concomitant C8-methylation. Incubation of these three glycosides in the absence and presence of DnrK or AdoMet revealed that hydrolysis is non-enzymatic.

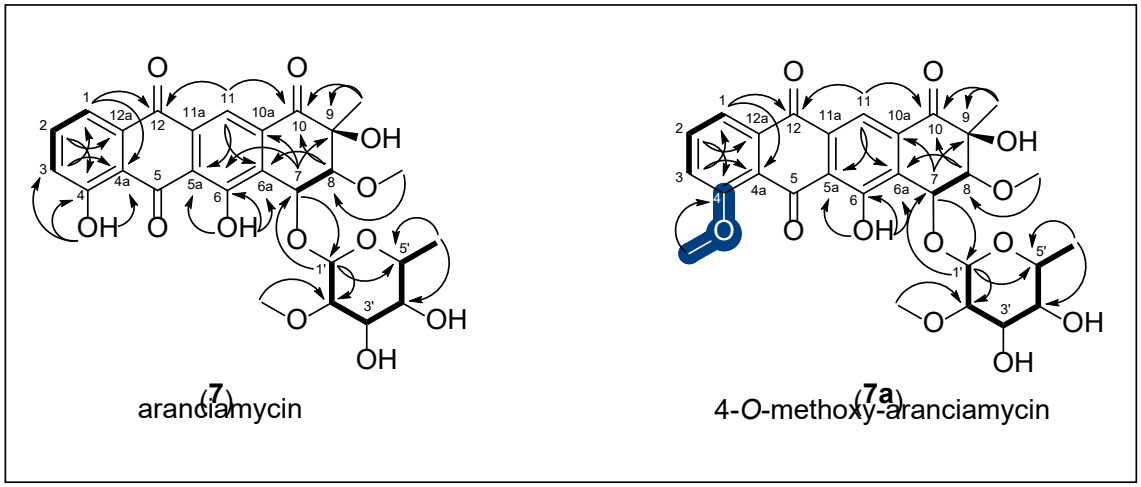

Figure 2.3. ^{1}H-^{1}H COSY (**—**) and key HMBC (→) correlations of aranciamycin **7** and DnrK methylated product 4-*O*-methoxyaranciamycin **7a**. The methyl group installed by DnrK is highlighted (blue).

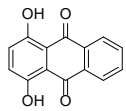

5
quinizarin

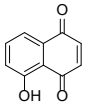

6
juglone

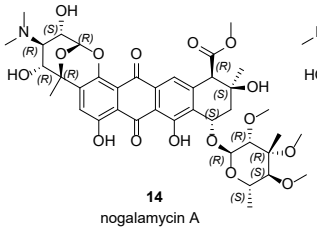

14
nogalamycin A

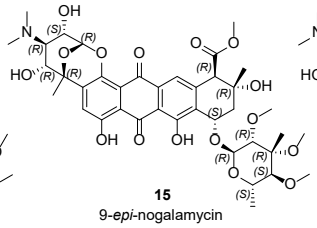

15
9-*epi*-nogalamycin

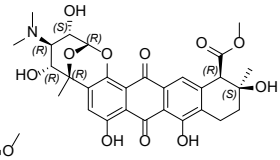

16
7-deoxynogalarol

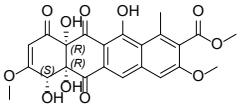

18
tetracenomycin C (TCM C)

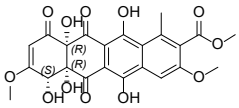

19
6-hydroxy-TCM C

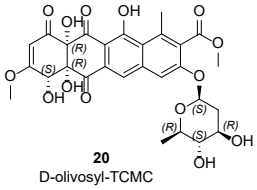

20
D-olivosyl-TCMC

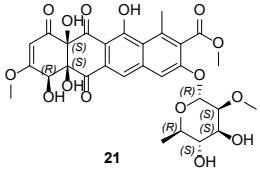

21
8-demethyl-8-α-L-rhamnosyl-TCMC

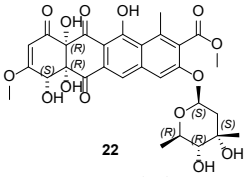

22
D-mycarosyl-TCMC

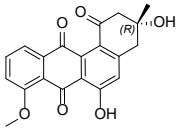

24
8-*O*-methylrabelomycin

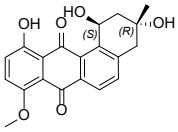

26
seitomycin

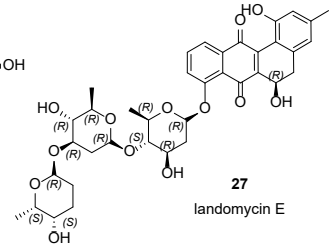

27
landomycin E

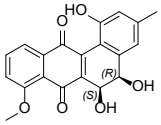

28
himalaquinone G

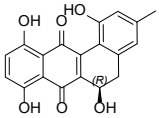

29
landomycinone

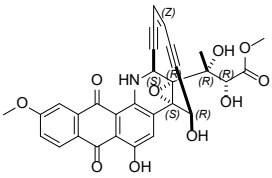

33
tiancimycin G (TNM G)

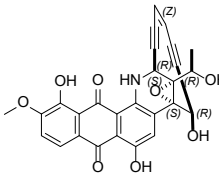

34
tiancimycin A (TNM A)

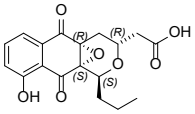

37
Frenolicin

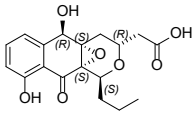

38
Frenolicin F

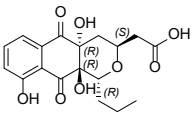

40
Frenolicin E

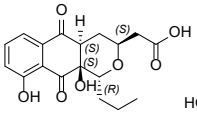

41
UCF13

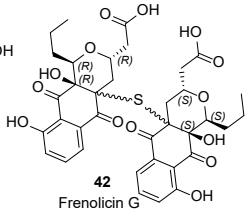

42
Frenolicin G

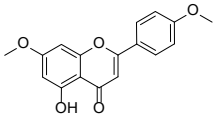

47
apigenin dimethyl ether

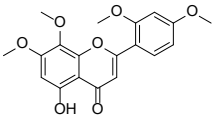

48
5-hydroxy-2',4',7,8-tetramethoxyflavone

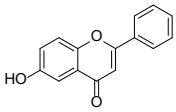

51
6-hydroxyflavone

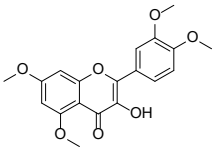

56
quercetin 5,7,3',4'-tetramethyl ether

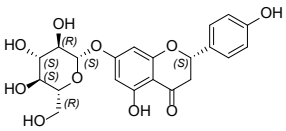

60
(-)-naringenin 7-β-D-glucoside

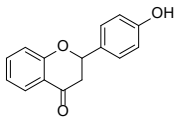

61
4'-hydroxyflavanone

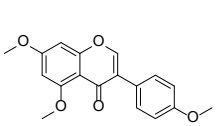

64
5,7,4'-trimethoxyisoflavone

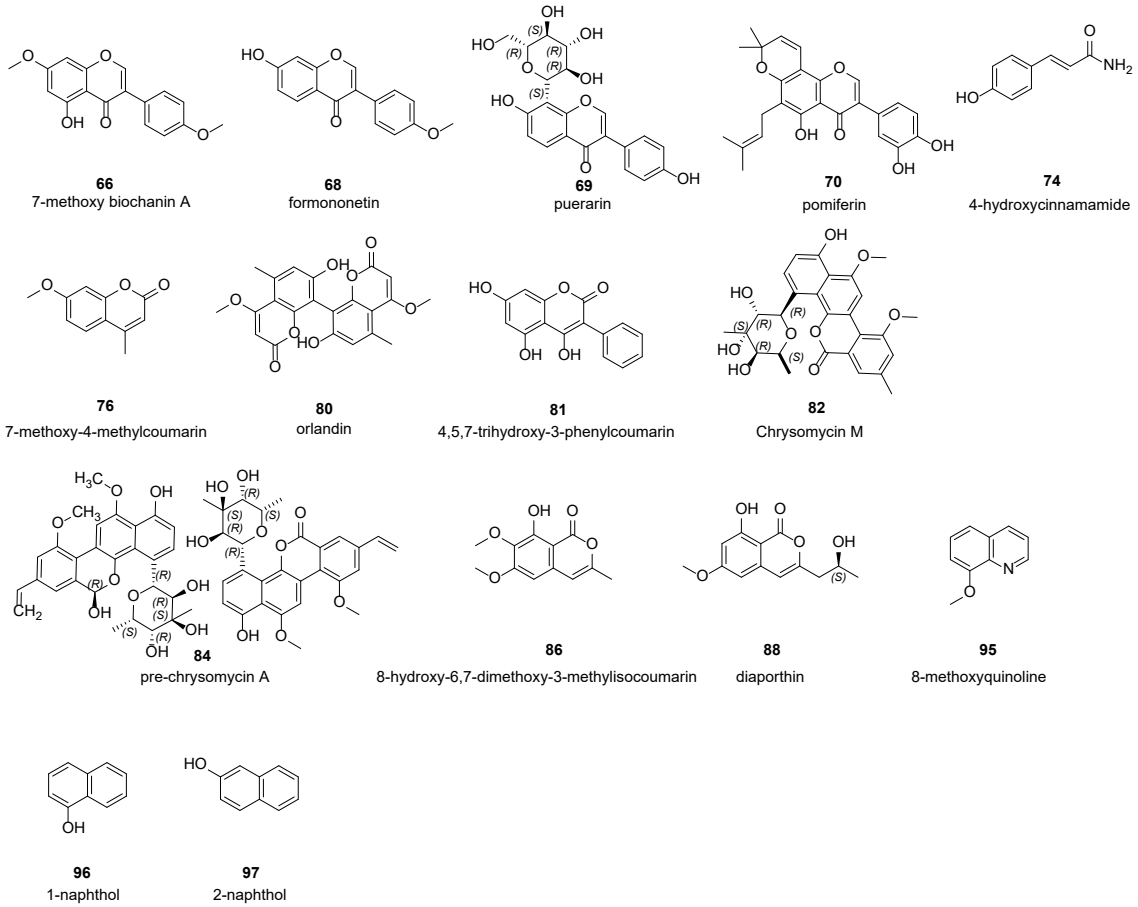

Figure 2.4. Structures of the molecules that were tested but did not turn over with DnrK.

Representative tetracyclic benz[a]anthracene DnrK substrates included naturally-occurring angucyclines, a structurally and functionally diverse class of natural product.[39] Specifically, rabelomycin (**23**, 98%)[40] and 8-*O*-desmethylseitomycin (**25**, 27%) in the presence of DnrK and AdoMet led to 8-*O*-methylrabelomycin (**24; Figure S2.3**) and seitomycin[41] (**26**; **Figure S2.4**), respectively. Consistent with DnrK angucycline C8 regioselectivity, C8-substituted analogues [*e.g.*, landomycin E[42] (**27**) and himalaquinone G[43] (**28**)] were not DnrK substrates (**Figure 2.4**). The inability of DnrK to alkylate landomycinone (**29**) may be due to the planar structure of landomycinone due to an aromatic A ring. DnrK was also able to catalyze methylation of fluostatin C (**30**), a benzofluorene-containing atypical angucycline that shares the same early biosynthetic pathway with the typical angucyclines.[44] While 90% putative mono-methylated product of **30** was detected, DnrK regioselectivity was not determined.

Similar to benz[a]anthracenes, enediyne-fused anthraquinones also contain a tetracyclic angular substructure.[45,46] As representatives of this natural product class, the tiancimycins (TNMs) are potent anticancer agents that function primarily as DNA-damaging agents.[47,48] Interestingly, while representative tiancimycins contain key C6 and/or C13 *β*-hydroxy quinone signatures, only C7-*O*-methylation was observed in the presence of DnrK and AdoMet. Specifically, DnrK enabled facile turnover in the presence of TNM C (**31**, 81%) and efficient conversion of TNM F (**32**, 98%) to TNM G (**33**; **Figure S2.5**). Consistent with this, an analogue lacking the requisite C7-OH (TNM A, **34**) led to no reaction. This surprising result implicated DnrK as a functional mimic of the TNM 7-*O*-MT TnmH.[49]

Many pyranonaphthoquinone (PNQ) natural products also contain an angular tetracyclic framework and a key C9 *β*-hydroxy quinone signature. Frenolicin B (FB, **35**),[50] the prototypical pyranonaphthoquinone, has potent anti-parasitic and anticancer activities and was recently found to selectively inhibit peroxiredoxins and glutaredoxins.[51] Evaluation of a representative set of naturally-occurring[52] revealed DnrK-catalyzed C9-*O*-methylation in a number of cases. This study led to two preliminary SAR observations. First, the relative A and B ring stereochemistry [*e.g.*, FB (**35**, 78%) versus *epi*-FB (**36**, 67%)] influences but does not prohibit catalysis. Second, the intact lactone (A ring) appears to be important as representative analogues with open lactones [*i.e.*, linear free acids; compound **37**-**42**; **Figure 2.4**] failed to turn over.

Flavonoids are polyphenolic plant secondary metabolites with anticancer, antidiabetic, anti-inflammatory, antiviral and cardio/neuro protective activities.[53,54] They are comprised of a fused chromone (1-benzopyran-4-one, benzo-γ-pyrones) core bearing a phenyl ring at either C2 (flavone) or C3 (isoflavones). Previous computational studies implicated a small set of substituted flavonoids (apigenin, genistein, kaempferol, luteolin, naringenin and quercetin) as putative DnrK substrates, computationally predicted C7-, C3'- and C4'-OH as the putative methylation sites and biochemically confirmed DnrK-catalyzed *in vitro* turnover of apigenin and genistein to their corresponding C7-*O*-methyl products (**Figure 2.1B**).[21] To extend this prior study, we evaluated a wide range of substituted benzo-γ-pyrones including representative flavones, flavonols, flavanones, isoflavones and related scaffolds (**Figure 2.5**). The prior docking study with representative flavones [apigenin (**43**) and luteolin (**44**)] predicted a preference of DnrK for C7 and C3'. Consistent with this prediction, representative flavones bearing a single free C7-OH [7-

hydroxyflavone (**45**) and 5,4′-dimethoxy-7-hydroxyflavone (**46**)] led to corresponding mono-methylated products (12% and 10%, respectively). The lack of turnover of flavones bearing a single C5-OH ([apigenin dimethyl ether (**47**) and 5-hydroxy-2',4',7,8-tetramethoxyflavone (**48**)] and the observed DnrK-catalyzed conversion of 5,7-dihydroxy-substituted chrysin (**49**, 26%) is also consistent with C7 regioselectivity. Likewise, the lack of turnover of flavones bearing a single C5-OH (**47** and **48**) and the observed DnrK-catalyzed conversion of 5,7,3',4-tetrahydroxy luteolin (**44**) to mono-, di- and tri-methyl products (20%, 72% and 8%, respectively) is consistent with the computational prediction of DnrK C3'-regioselectivity but, in contrast to the computational model, also implicates DnrK-catalyzed C4'-*O*-methylation. As further support for DnrK flavone C4'-regioselectivity, only mono-methylation was observed in the context of 7,4'-dihydroxyflavone (**50**, 30%) while the 5,7,4'-trihydroxy-substituted **43** led to both a mono-methylated product (26%)[21] and 7,4'-di-*O*-methoxy (**47**, 2%); **Figure S2.6**. Also distinct from the prior computational predictions, comparison of 6-hydroxy substituted (**51**, no turnover) to 6,2'-dihydroxy-substituted (**52**, 27%) suggests DnrK is capable of flavone C2'-*O*-methylation.

The prior docking study with representative flavonols (3-hydroxyflavone) kaempferol (**53**) and quercetin (**54**) predicted a preference of DnrK for C7.[21] Our in vitro studies with a representative flavonol (3-hydroxyflavone) series were consistent with the docking model. Specifically, mono-methylation in the context of kaempferol (**53**, 39%), quercetin (**54**, 12%) and galangin (**55**, 7%), was observed while a model flavonol bearing a single C3-OH [quercetin 5,7,3',4'-tetramethyl ether (**56**)] lacked turnover. Surprisingly,

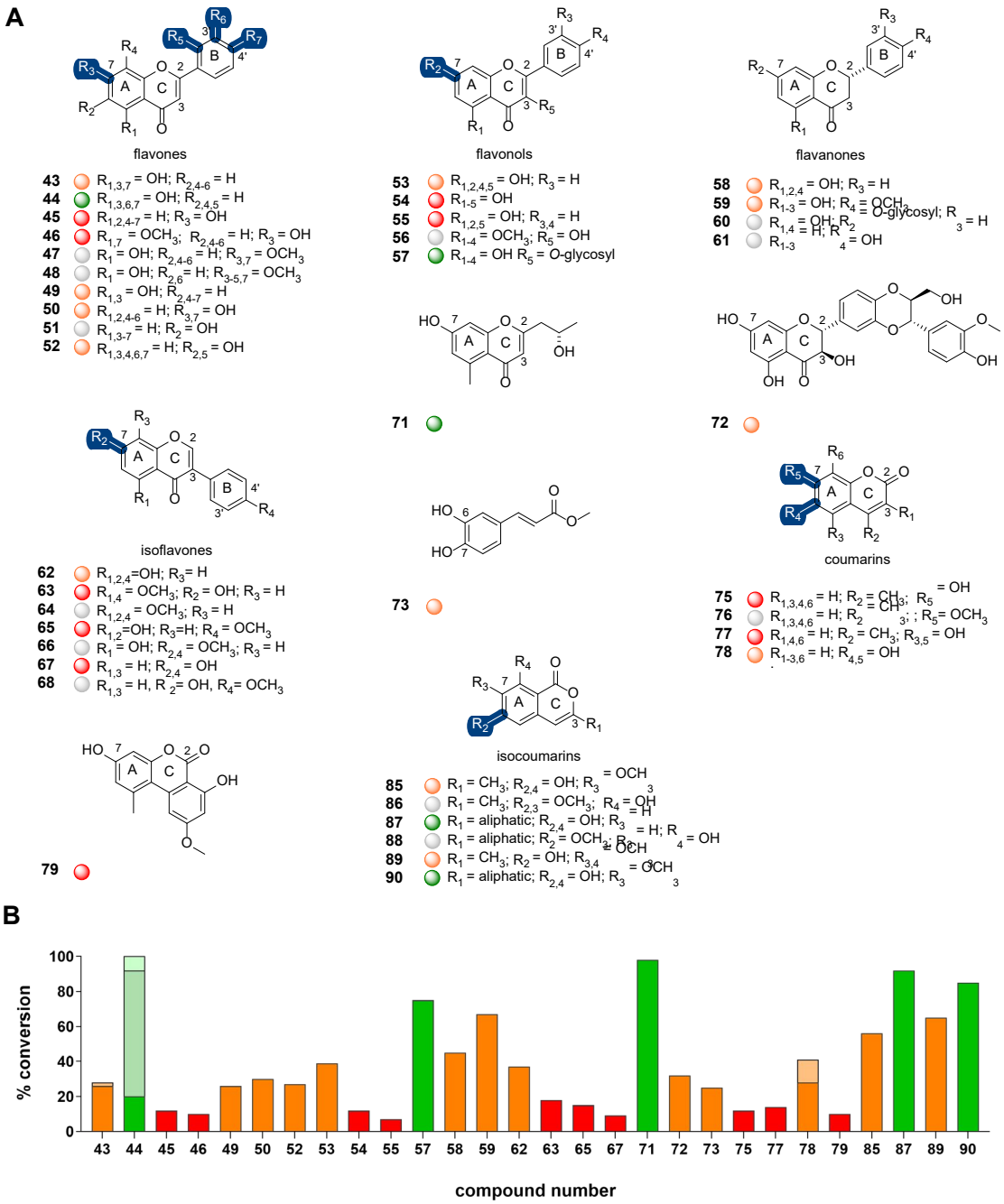

Figure 2.5. (A) Representative flavones, flavonols, flavanones, isoflavones, coumarins and related DnrK substrates. Highlighted DnrK regioselectivity (blue), where determined, was based on co-elution with product standards (**47**, **64**, **66**, **68**, **76**, **86** and **88**) or assigned based on the presence of a single aromatic hydroxyl (**45**, **46**, and **89**). **(B)** The percent conversion to product in an end point LC-MS assay (1 mM test agent, 3.2 mM AdoMet, 100 µM DnrK,

37 ºC, 16 h). Turnover is categorized in plot and under each structure as a colored ball as good (≥75%, green), moderate (>25% - <75%, orange), low (≤25%, red) and no turnover (grey). Percent di- and/or tri-methylation for compounds **43**, **44** and **78** are represented as lighter shades of each represented color.

DnrK was also able to accommodate additional steric bulk at C3 as exemplified by the turnover of the 3-α-L-rhamnoside-substituted quercitrin (**57**, 75%).

A C7 preference in the context of representative flavanones [2(*R*)- and 2-(*S*)-naringenin] was also implicated via docking.[21] Consistent with this, representative flavanones with a free C7-OH [2(*S*)-naringenin (**58**, 45%); 2(*S*)-hesperetin (**59**, 67%)] led to mono-methylated products while related flavanones lacking a free C7-OH [2(*S*)-naringenin 7-*β*-D-glucoside (**60**) or 4'-hydroxyflavanone (**61**)] failed to turnover in the presence of DnrK.

Docking studies with the representative isoflavone genistein **62** projected a preference of DnrK for C7 and C4'.[21] Consistent with C7-*O*-methylation, DnrK catalyzed the conversion of 5,4'-dimethoxy-7-hydroxyisoflavone (**63**) to 5,7,4'-trimethoxyisoflavone (**64**, 18%); **Figure S2.7**, the conversion of biochanin A **65** to the corresponding 7-methoxy biochanin A (**66**, 15%); **Figure S2.8**, and the production of 7-methoxy genistein from genistein (**62**, 37%).[21] Similarly, for models lacking a C5-OH, a shift from C7 regioselectivity to C4'-O-methylation was observed as exemplified by the DnrK-catalyzed conversion of daidzein (**67**) to formononetin [(**68**, 9%); **Figure S2.9**]. The addition of steric bulk at C8 (puerarin, **69**) or C6 and C8 (pomiferin, **70**) prohibited turnover (**Figure 2.4**).

DnrK also catalyzed methylation of three other flavonoid-related natural products; the bacterial metabolite 5-carbomethoxymethyl-2-heptyl-7-hydroxychrome (**71**),[55] the plant metabolite silybin B (**72**) with anticancer and antiviral activities,[56] and a phenylpropanoid-derived plant metabolite methyl caffeate (**73**).[57] While **71** and **72** each contain a free C7-OH and led to mono-methylated products (98% and 32%, respectively),

DnrK regioselectivity was not determined. Comparison of mono-methylation of 3,4-dihydroxy-substituded methyl caffeate (**73**, 25%) with 4-hydroxycinnamamide (**74**, no turnover); **Figure 2.4** implicates DnrK-catalyzed phenylpropanoid C-6-*O*-methylation similar to that observed with representative coumarins.

Coumarins are another major class of phenylpropanoid comprised of a fused chromone (1-benzopyran-2-one, benzo-α-pyrones) core (**Figure 2.5**). Like flavonoids, coumarins invoke diverse functions including anticoagulant, anticancer, antioxidant, antiviral, anti-diabetics, anti-inflammatory, antibacterial, antifungal and anti-neurodegenerative activities.[58,59] In addition, coumarins are also commonly used fluorophores.[60] DnrK catalyzed 7-*O*-methylation of the prototypical coumarin 4-methylumbelliferone [4-MeUmb, (**75**, 12%)], the product for which co-eluted with the 7-*O*-methoxy commercial standard [7-methoxy-4-methylcoumarin (**76**)] (**Figure S2.10**). The parent **75** is fluorescent under slightly basic conditions, the fluorescence of which can be abolished via C7-OH modification (*e.g.*, alkylation or glycosylation).[61] DnrK catalytic efficiency (k_{cat}/K_m) with **1** is nearly three orders of magnitude greater (500-fold) to that with **75** ($k_{cat} = 0.036 \pm 0.001$ min^{-1}, $K_m = 1160 \pm 170$ μM under saturating [AdoMet]; **Table 2.1**). DnrK-catalyzed turnover was also observed with 5,7-dihydroxy-4-methylcoumarin (**77**, 14%), 6,7-dihydroxycoumarin (**78**, 44%) and the benzo(*c*)coumarin 9-methoxy alternariol (**79**, 10%). Indicative of both C6 and C7 regioselectivity, the product distribution of **78** includes two chromatographically-distinct mono-methylated species (28% and 13%) and di-methylated product as a minor product (3%). Increasing coumarin steric bulk [orlandin (**80**), 4,5,7-trihydroxy-3-phenylcoumarin (**81**)] or representative chrysomycins (**82**-**84**); **Figure 2.4** prohibited alkylation.

The structurally similar polyketide-derived isocoumarins are biosynthetically distinct from phenylpropanoids but, like their coumarin counterparts, display diverse bioactivities.[62] DnrK isocoumarin C6-regioselectivity was established via the observed conversion of 6,8-dihydroxy-7-methoxy-3-methylisocoumarin (**85**) to the corresponding C6-methoxy product 8-hydroxy-6,7-dimethoxy-3-methylisocoumarin (**86**, 56%); **Figure S2.11** and orthosporin (**87**) to the corresponding C6-methoxy product diaporthin (**88**, 92%); **Figure S2.12**. Two additional isocoumarins bearing a free C6-OH [6-hydroxy-7,8-dimethoxy-3-methylisocoumarin (**89**, 65%); 6,8-dihydroxy-7-methoxy-3-hydroxymethylisocoumarin (**90**, 85%)] also led to DnrK-catalyzed mono-methylated products.

Structurally-related to coumarins, 2-quinolones are derived from anthranilic acid (**Figure 2.6**).[63] Both 4-hydroxy-quinolin-2(1H)-one (**91**, 51%) and its tautomer 2,4-dihydroxyquinoline (**92**, 37%) led to the same DnrK-catalyzed product, implicating a common tautomer as the substrate (**Figure S2.13**).[64] DnrK was also able to catalyze putative C8-OH methylation of the related 8-hydroxy-3,4-dihydro-2-quinolinone (**93**, 42%) and iodoquinol (**94**, 88%). By comparison, DnrK had no effect on 8-methoxyquinoline [(**95**); **Figure 2.4**] (consistent with C8-OH selectivity) or simple related scaffolds lacking the heterocyclic nitrogen such as naphthols (**96** and **97**); **Figure 2.4**. DnrK was also able to alkylate diverse fused benzoic acid containing natural products including the Hsp90 inhibitor radicicol (**98**, 44%),[65] the fatty acid synthase inhibitors platencin and platensimycin [(**99**, 26%) and (**100**, 28%), respectively][66-68] and related simpler pyramidamycins A and B [(**101**, 6%) and (**102**, 19%), respectively] (**Figure 2.4**).[69] Of particular note, DnrK was able to alkylate both the C9-OH and the C11 β-OH of radicicol

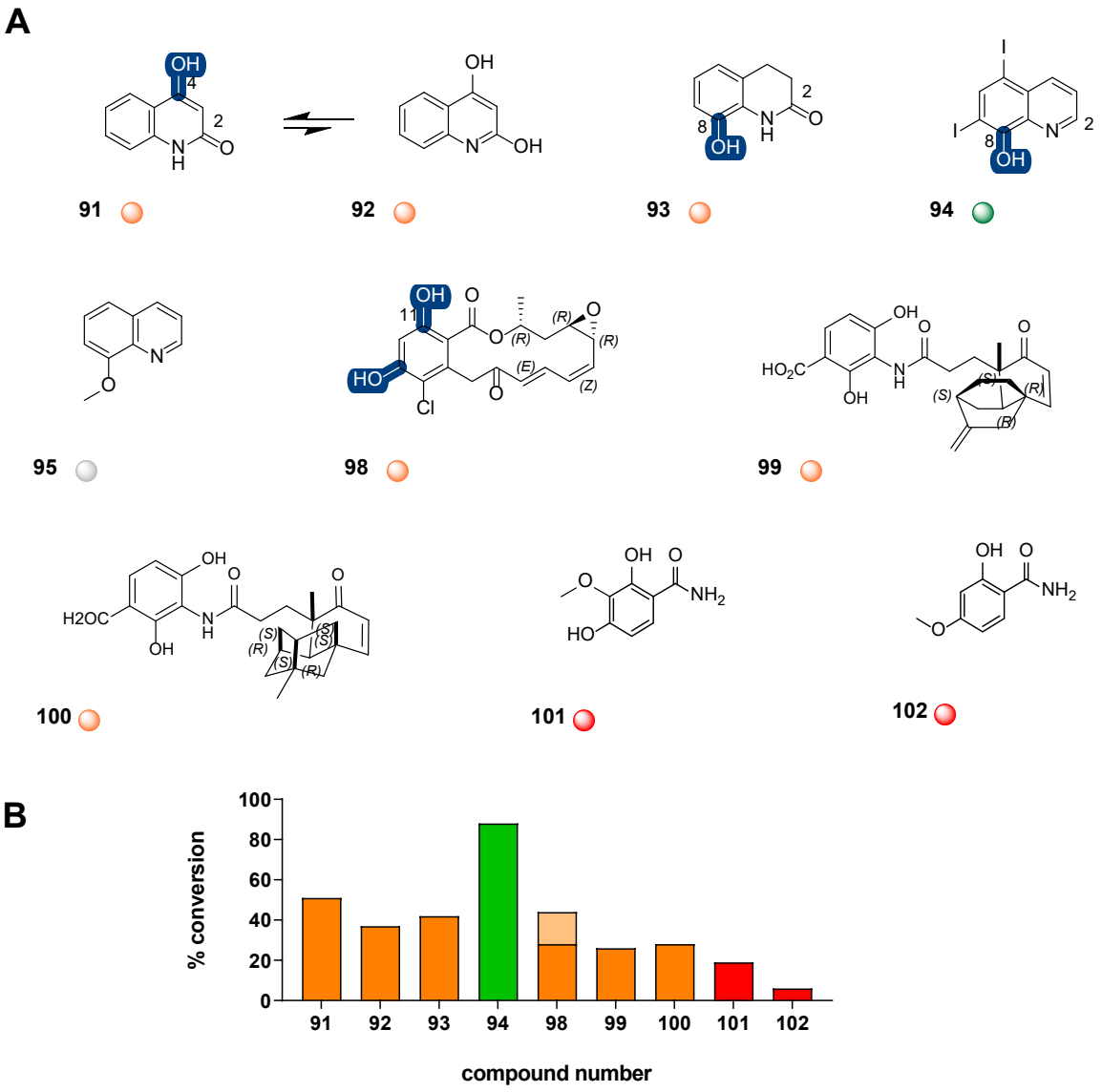

Figure 2.6. (A) Representative 2-quinolones, fused benzoic acid containing natural products and related DnrK substrates. Highlighted DnrK regioselectivity (blue), where determined, was based on the presence of a single aromatic hydroxyl [(**91**), (**93**) and (**94**)] and detection of mono-methylated product or two aromatic hydroxyls [(**98**)] and detection of mono and di-methylated products. **(B)** The percent conversion to product in an end point LC-MS assay (1 mM test agent, 3.2 mM AdoMet, 100 µM DnrK, 37 °C, 16 h). Turnover is categorized in plot and under each structure as a colored ball as good (≥75%, green),

moderate (>25% - <75%, orange), low (≤25%, red) and no turnover (grey). Percent di-methylation for compounds (**98**) is represented as lighter shades of orange color.

as evidenced by the production of two chromatographically-distinct mono-methyl species (23% and 5%) and a third di-methyl product (16%). While platencin (**99**), platensimycin (**100**) and the pyramidamycins (**101** and **102**) also share a common phenolic benzoic acid-type core and each led to a single mono-methyl product, regioselectivity in this series was not determined.

2.2.2 DnrK structure elucidation and relationships to other MTs with similar functions

To better understand acceptor binding, the crystal structure DnrK with the fluorescent hydroxycoumarin, **75** was determined to 1.84 Å in space group C2. The structure is quite similar to the other solved DnrK complexes, with pairwise Cα r.m.s.d between all protomers in 1TW2, 1TW3, 5EEG, 5EEH, and 5JR3 ranging between 0.2 and 1.3 Å. The electron density clearly shows the bound **75** acceptor and that the AdoMet added to the crystallization drop had broken down to AdoHcy (**Figure 2.7**). The hydroxyl of the acceptor is positioned to accept a methyl had AdoMet been bound with a water positioned between the AdoHcy sulfur and the hydroxyl of **75** (**Figure 2.8**). Because we found that DnrK can serve as a functional mimic of TnmH and TcmO, we compared these proteins. The structures share the methyltranferase fold and are quite similar with Cα r.m.s.d ranging from 1.8-2.5 Å for protomers of DnrK to TnmH (39% sequence identity) and 3.6-4.3 Å for

DnrK to the AlphaFold predicted structure of TcmO (24% sequence identity) (**Figure 2.9 and Figure 2.10**).

The binding tunnel of DnrK containing the AdoHcy and the **75** is open on 3 sides (near the nucleotide of AdoHcy, along the edge of the **75** and a smaller opening above it) (**Figure 2.11**). The large open area around the acceptor binding region allows the pocket to accommodate a number of different compounds as illustrated by the structures of DnrK in complex with AdoHcy and 4-methoxy-ϵ-rhodomycin T (M-ϵ-T) (PDBids 1TW2 and 1TW3), the complex with a tetrazole analog of AdoHcy (5EEG), and the complex with CINP (5EEH) all have a large open tunnel. In fact, in the structure with AdoHcy and CINP, we observed 5 CINP molecules in addition to the one position for methyl transfer bound within the tunnel.[22] Compared to the structure of TnmH and Predicted structure of TcmO, the binding tunnel in the acceptor binding region, is more open in DnrK. Looking at this difference in more detail, we see that the region between helices 11 and 12 of DnrK, residues 161-167 interrupt these two helicies and is flipped out of the binding pocket. Whereas the equivalent region of TnmH (and for Predicted TcmO structure) have the two helicies abutting with a kink at the end of helix 11 that changes the helix direction for helix 12. In TnmH, this puts R153 and in TcmO, N154 (the residues corresponding to D163 in DnrK) in proximity to the carboxylate of the AdoMet/AdoHcy, which closes off a section of the tunnel (**Figure 2.11B**).

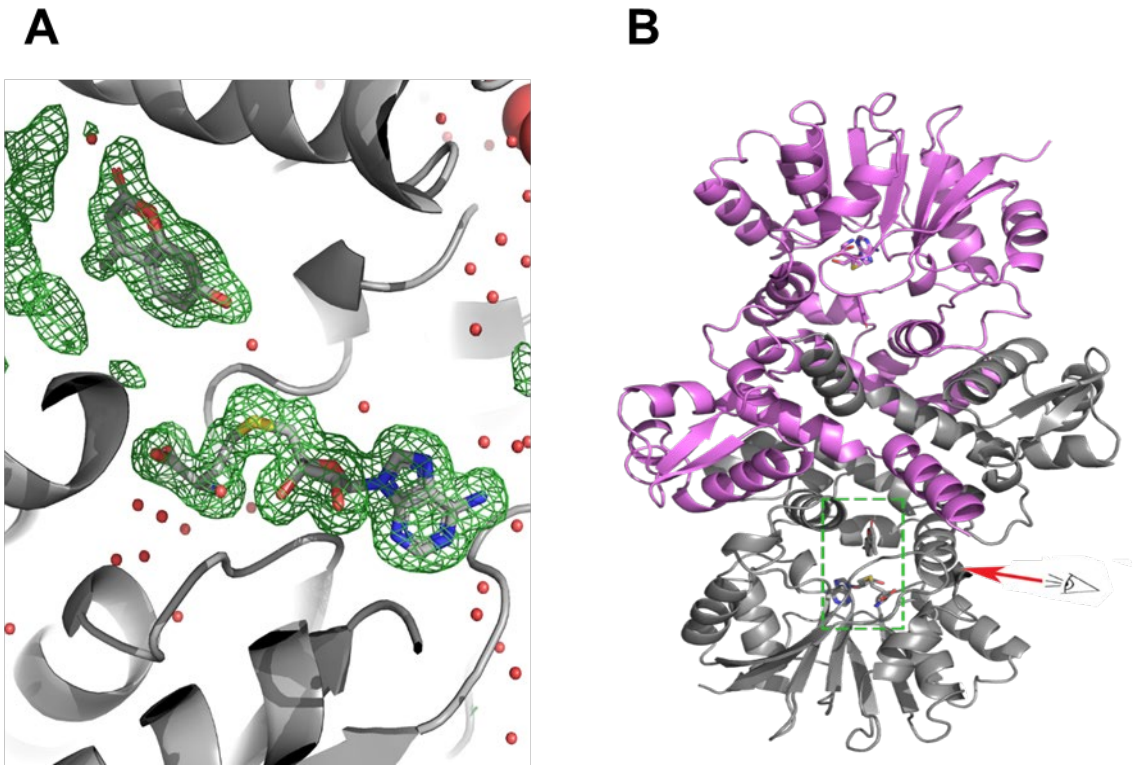

Figure 2.7. (A) Polder omit map (mFo-DFc) electron density contoured at 3.5 r.m.s.d. for the AdoHcy and 4-MeUmb (**75**) ligands in chain B of PDBid 5JR3. The density clearly shows that the AdoMet added to the crystallization drop has broken down to the AdoHcy product. The 4-MeUmb density shows that its hydroxyl is positioned for methyl transfer had AdoMet been bound. **(B)** view of the DnrK dimer rotated 90 degrees to show the viewing angle for (**A**). This figure was generated with PyMOL (version 2.5.2; Schrödinger).

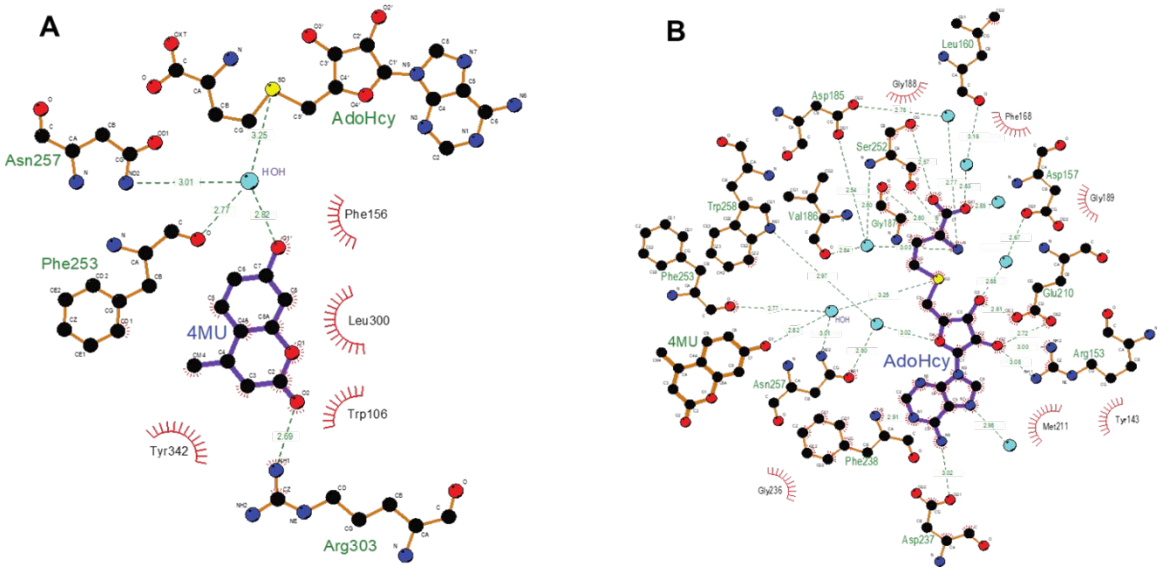

Figure 2.8. (A) Ligand binding environment of the 4-MeUmb (**75**). The water, that occupies the area near where the donor methyl from AdoMet would be expected, is coordinated by the hydroxyl of 4-MeUmb, the AdoHcy sulfur, the side chain amide of Asn 257 and the carbonyl of Phe 253. (B) Ligand binding environment of the AdoHcy showing the direct and water mediated interactions. This figure was made with LigPlot+ version 2.2.4.[88]

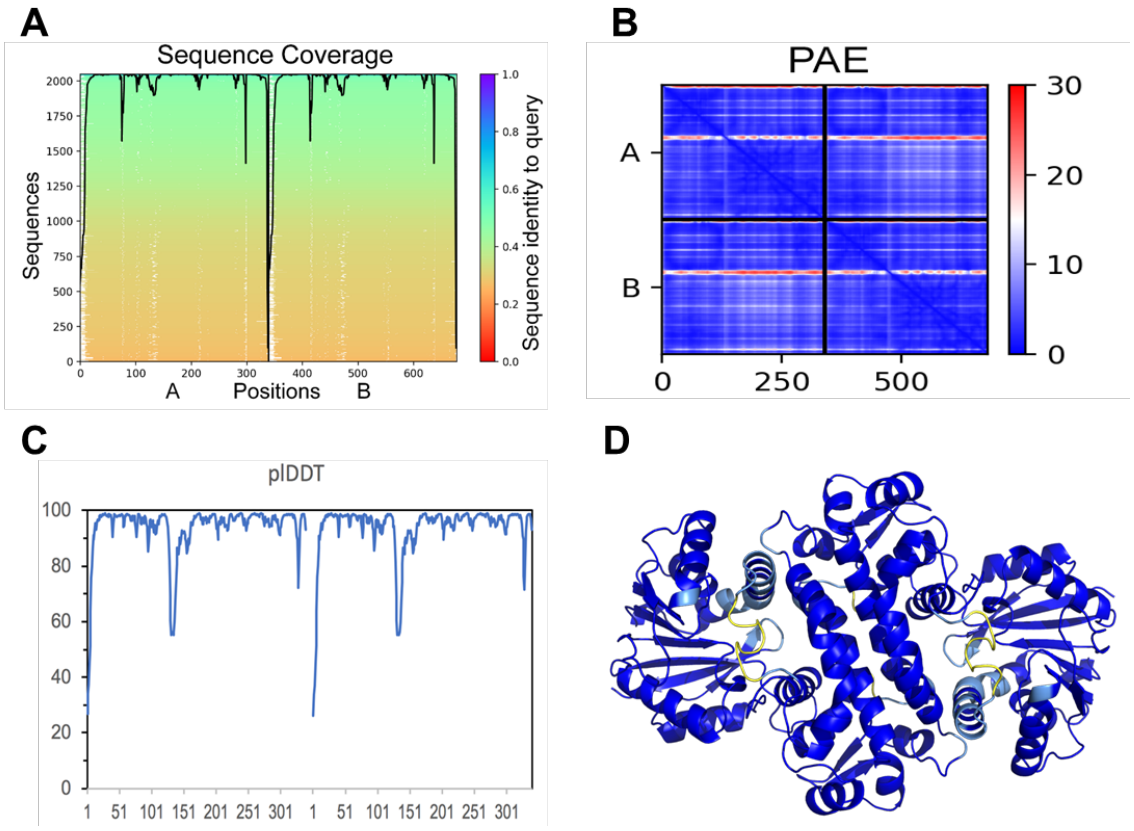

Figure 2.9. Prediction of the TcmO structure output from AlphaFold-multimer run from colabfold. **(A)** Analysis of the multiple sequence alignment from MMseqs2 used as input to AlphaFold showing the number of sequences in the MSA at each position as well as the similarity of those sequences to TcmO. **(B)** Predicted aligned error (PAE) produced by AlpahaFold2 for the homodimer prediction without templates which shows that there is high confidence in the arrangement both within the protomers and between them. **(C)** Predicted lDDT plot shows high confidence in the local structure for all but short regions at the N-terminus, C-terminus and the region from 129-138. **(D)** structure of Predicted dimer of TcmO colored by plDDT with dark blue > 90, light blue < 90 and > 70, yellow < 70 and > 50 and orange < 50.

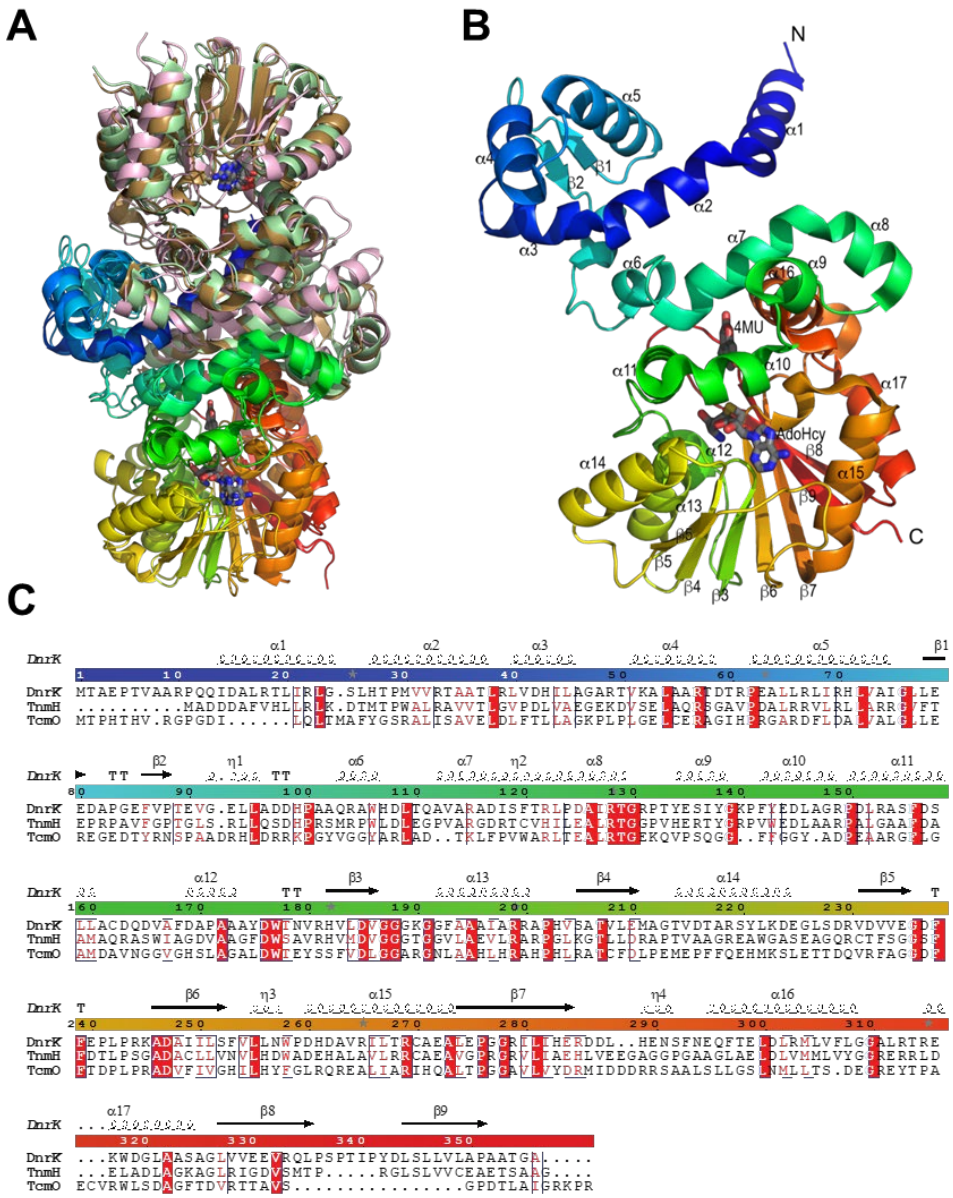

Figure 2.10. Superposition and alignment of DnrK (PDBid 5jr3, tan) with TnmH (PDBid 6clx, mint) and Predicted model for TcmO (pink). All three share the common methyltransferase fold **(A)** with an N-terminal dimerization domain, a C-terminal Rossmann fold domain that binds the AdoMet methyl donor and an acceptor binding in a cleft between these domains. **(B)** Shows the DnrK protomer with secondary structure elements labeled as in the alignment (**C**). The alignment was formatted with ESPript 3.0.[89]

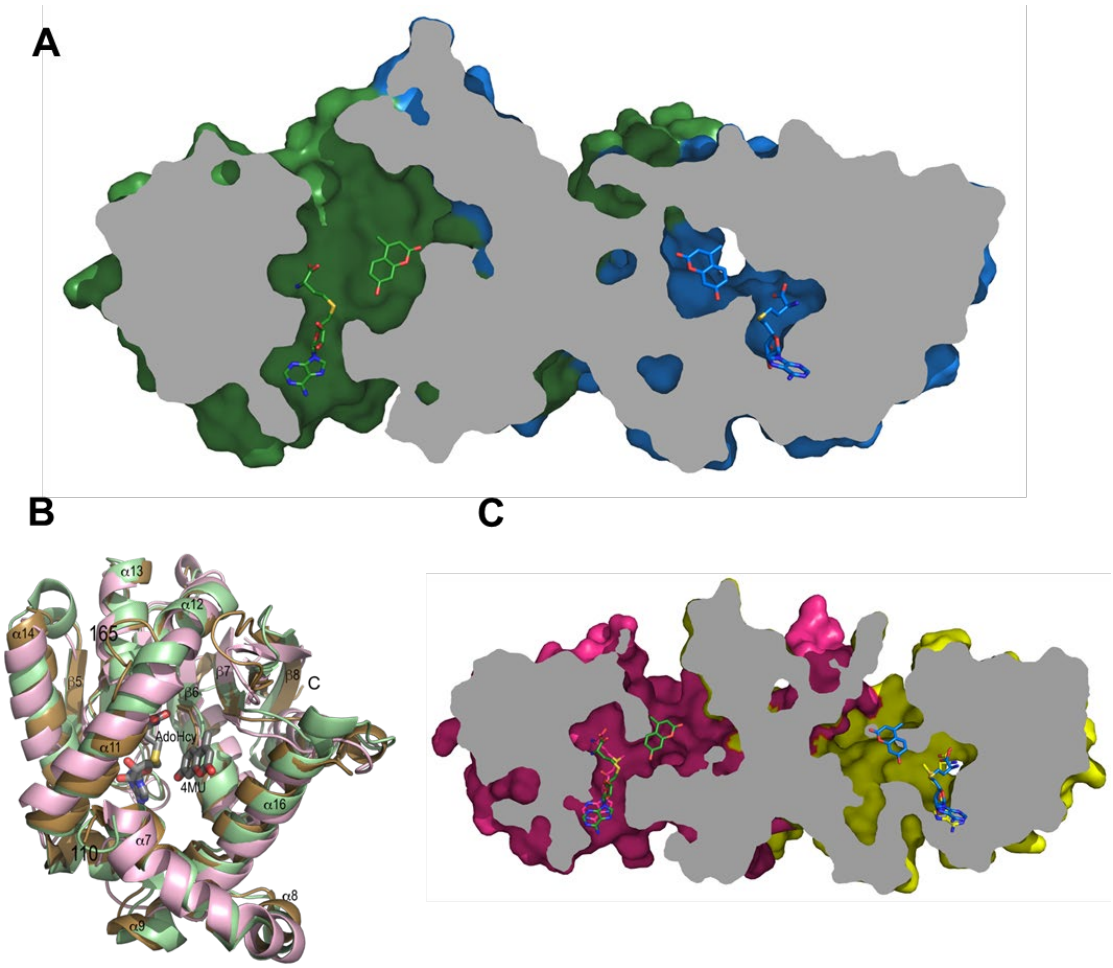

Figure 2.11. (A) Cut-view through the ligand binding tunnel of DnrK. The tunnel contains a large open area in the region of the 4-MeUmb (**75**) acceptor. **(B)** A superposition of DnrK (PDBid 5jr3, tan) with TnmH (PDBid 6clx, mint) and predicted model for TcmO (pink) with residues 1-109 removed to show how in DnrK the region between helicies 11 and 12 is flipped out, where in TnmH and TcmO helix 11 extends right up to helix 12. This results in R153 of TnmH (and N154 of the TcmO model) being positioned near the carboxylate of AdoHcy and reducing the size of the tunnel in this region. **(C)** Cut-view through the ligand binding tunnel of TnmH (PDBid 6clx) in the same orientation as **(A)**. The AdoHcy and 4-MeUmb ligands from DnrK are shown superimposed on the AdoMet from TmnH tfor reference. This figure was generated with PyMOL (version 2.5.2; Schrödinger).

2.2.3 Impact of methylation on the bioactivity of representative model compounds

A small exemplary set of compounds was selected to interrogate in three complementary assays (cancer cell line cytotoxicity, 4E-BP1 phosphorylation and axolotl tail regeneration) to enable a preliminary assessment of biocatalytic *O*-methylation on metabolite function. The parental scaffolds included in this set were CAR **1** and aranciamycin **7**, metabolites that structurally diverge from one another by their C7 glycosyl substituents as well as divergent substitution and stereochemistry at C9. Also included were the corresponding C4-*O*-methylated DnrK products of CAR and aranciamycin [(DNR/**1a**) and **7a**, respectively] and steffimycin B **9**[32] a naturally-occurring C2-*O*-methoxy analogue of **7**. While the *des*-methyl parent **1** was 30-200-fold more cytotoxic than **7** in the two representative cancer cell lines tested, C4-*O*-methylation of both **1** and **7** led to reductions in cytotoxicity of 7-15-fold for **1** and 4-7-fold for **7** (**Figure 2.12A and B**). The corresponding cytotoxicity of **9** reflects that of **7**/**7a**, consistent with other recent **9** cancer cell line cytotoxicity studies[70] and the reported notably reduced affinity of **9** for DNA compared to that of DNR or DXR.[71]

Among the multiple mechanisms put forth as drivers of anthracycline-induced cardiotoxicity, ROS generation and downstream ROS-mediated processes are a predominate contributing factor[1]. The phosphorylation status of the cap-dependent translational repressor 4E-BP1 is a correlative sensor for ROS-mediated cytotoxicity in cancer cell lines.[51] As highlight in **Figure 2.12C**, only **7** invokes a shift in 4E-BP1 phosphorylation indicative of ROS induction. Taken together with the cytotoxicity studies highlighted about, these data suggest minimal ROS contribution to cytotoxicity among the

structurally related high potency (**1** and **1a**) and most low potency (**7a** and **9**) analogues. In contrast, these data reveal the absence or presence of a C4-*O*-methoxy group in the low potency comparators (**7** and **7a**) to contribute to a putative mechanistic shift that ultimately alters cellular ROS status.

Prior studies in the regenerative salamander model (the Mexican axolotl, Ambystoma mexicanum) revealed tail regeneration to require a rapid escalation of ROS which occurs as a rapid response to axolotl tail amputation.[72] While all members of the test set were well-tolerated in a corresponding axolotl embryo tail regeneration assay,[43,73] only **9** inhibited tail regeneration (**Figure 2.12D**). This result highlights subtle anthracycline structural modifications to translate to dramatic shifts in regenerative outcomes where the divergence from the 4E-BP1p/ROS study described above may result, in part, from yet to be determined factors that contribute to differences in uptake and/or in vivo exposure.

2.3 Conclusions

In conclusion, methyltransferases are ubiquitous biocatalysts and, while it is well-established that many methyltransferases can use non-native AdoMet donors, stringent fidelity to the corresponding acceptor is typical among methyltransferases.[74] Within this context, the current study highlights DnrK as a unique among conventional methyltransferases by virtue of a demonstrated broad acceptor tolerance. The mechanistic and/or structural basis of DnrK's perceived atypical permissivity remains unclear. As described in the current study, DnrK's active-site features and general catalytic parameters are largely unremarkable in the context of aromatic *O*-methyltransferases. Yet, the current

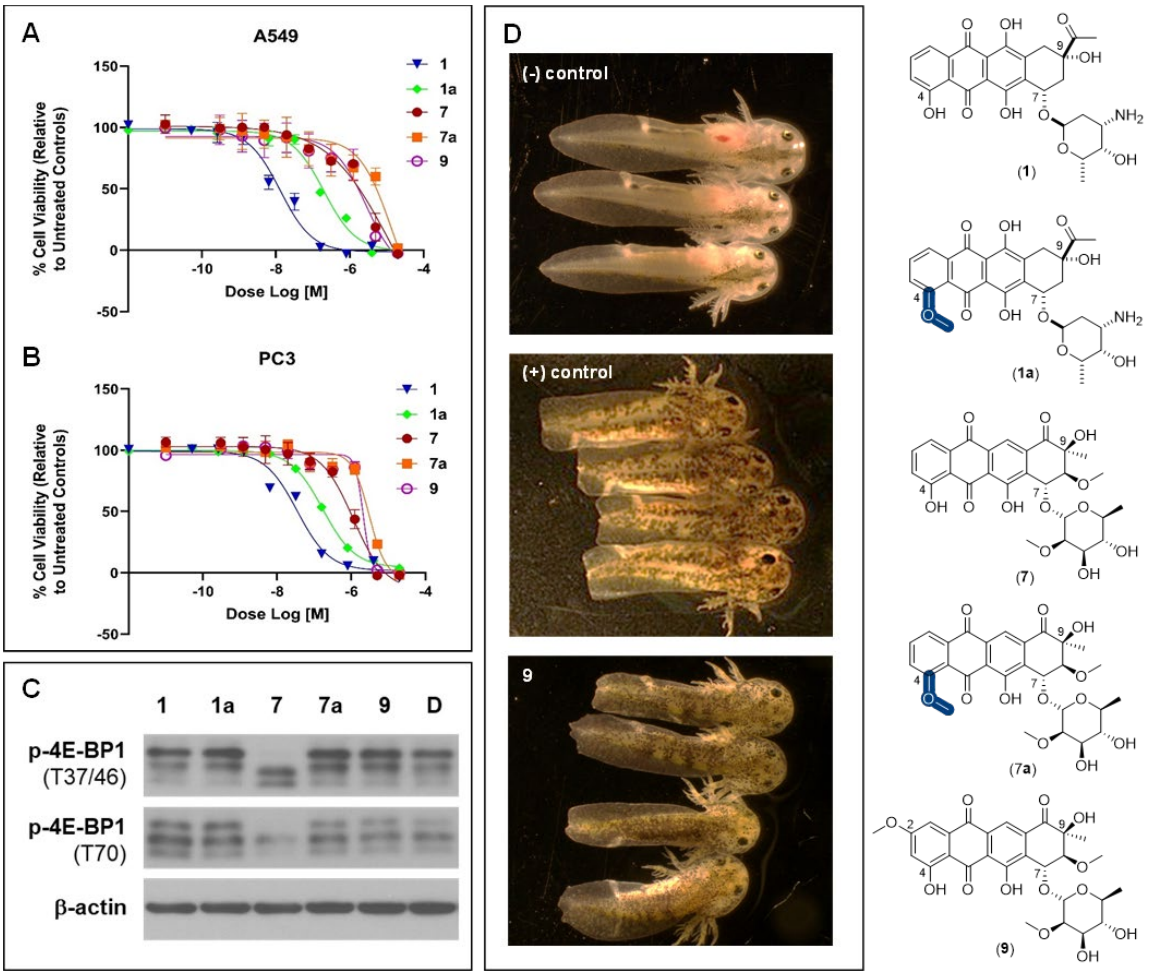

Figure 2.12. (A) Dose-response of compounds CAR **1**, DNR **1a,** aranciamycin **7**, 4-*O*-methoxyaranciamycin **7a** and steffimycin B **9** against A549 (non-small cell lung) human cancer cell line (72 h). **(B)** Dose-response of mentioned compounds against PC3 (prostate) human cancer cell line (72 h). A549: IC50 for the compounds (**1**, 13.09 nM), (**1a**, 199.0 nM), (**7**, 2.7 µM), (**7a**, 13.8 µM), (**9**, 2.8 µM). PC3: IC50 for the compounds (**1**, 34.98 nM), (**1a**, 170.1 nM), (**7**, 1.1 µM), (**7a**, 4.3 µM), (**9**, 3.1 µM). **(C)** HCT116 cells were treated with 2 µM of test compounds or DMSO (negative control) for 6 h followed by Western blot analysis for the indicated proteins. **(D)** the impact of 10 µM steffimycin B **9** on axolotl embryo tail regeneration at 7 dpa compared to vehicle (DMSO, negative control) and the Hsp90 inhibitor geldanamycin (positive control)

and previously reported DnrK ligand-bound structures do reinforce the evidence of DnrK's affinity for diverse ligands and ligand orientations.[18,22] Consistent with this, recent chimeric engineering studies also implicate the DnrK scaffold as a uniquely malleable biocatalytic template able to accommodate diverse chemistries.[20,75] While speculative, the potential of DnrK to productively orient diverse acceptors with the requisite activated alkyl donor (AdoMet) may suggest increased attention be given to key acceptor properties (*e.g.*, pK_a/nucleophilicity) in predicting putative non-native substrates. Within this context, the unique acceptor permissivity of DnrK may offer the unique potential for a more systematic study to probe the contribution of specific acceptor molecular features in catalysis. In addition, the uniquely permissive biocatalytic capabilities of DnrK revealed also opens the door for future synthetic biology and/or synthetic applications.

2.4 Materials and methods

2.4.1 General materials

Most compounds for substrate scope studies derived from the Spectrum Collection (Microsource Discovery Systems, Inc., Gaylordsville, CT) or the University of Kentucky Center for Pharmaceutical Research and Innovation Natural Products Repository (Lexington, KY). Tiancimycins, platensimycin and platencin were isolated as previously described.[47,67,68.76] Silybin B was provided by Professor Tom Prisinzano (University of Kentucky, Lexington, KY). Carminomycin (CAR, **1**) was purchased from Cayman Chemical Company (Ann Arbor, MI). *E. coli* BL21(DE3) competent cells and *S*-adenosyl-L-methionine (AdoMet, 32 mM solution in 10% EtOH/5 mM H_2SO_4) were purchased from

New England Biolabs (Ipswich, MA). Nickel-nitrilotriacetic acid resin was purchased from Thermo Fisher Scientific (Waltham, MA).

2.4.2 General methods

High resolution electrospray ionization (HRESI) mass spectra were recorded on AB SCIEX Triple TOF® 5600 system (AB Sciex, Framingham, MA, USA). HPLC-UV/MS analyses were accomplished with an Agilent *Infinity Lab LC/MSD* mass spectrometer (*MS* Model G6125B; Agilent Technologies, Santa Clara, CA, USA) equipped with an Agilent 1260 Infinity II Series Quaternary LC system and a Phenomenex NX-C18 column (250 × 4.6 mm, 5 μm) [Method **A**: solvent A: H_2O/0.1% formic acid, solvent B: CH_3CN; flow rate: 0.5 mL min^{-1}; 0-30 min, 5-100% B (linear gradient); 30-35 min, 100% B; 35-36 min, 100%-5% B; 36-40 min, 5% B]. Semi-preparative HPLC was accomplished using Phenomenex (Torrance, CA) C_{18} column (10 × 250 mm, 5 µm) on a Varian (Palo Alto, CA) ProStar Model 210 equipped with a photodiode diode array detector and a gradient elution profile [Method **B**: solvent A: H_2O/0.025% TFA; solvent B: CH_3CN; flow rate: 5.0 mL min^{-1}; 0-3 min, 10% B; 3-35 min, 10-100% B; 35-40 min, 100% B; 40-43 min, 100-10% B; 43-45 min, 10% B]. All NMR data was recorded at 400 MHz for ^1H and 100 MHz for ^{13}C with Varian Inova NMR spectrometers (Agilent, Santa Clara, CA, USA), where δ-values were referenced to respective solvent signals [$CDCl_3$, δ_H 7.24 ppm, δ_C 77.23 ppm]. A549 and PC3 cells were obtained from ATCC (Manassas, VA). All other biochemical and chemicals were reagent grade and purchased from Sigma-Aldrich (St. Louis, MO), unless otherwise noted.

2.4.3 Protein heterologous production and purification

N-His$_6$-DnrK and *N*-His$_6$-*S*-adenosyl-L-homocysteinease (SAHH) were produced and purified as previously described and used for all studies.[22,77]

2.4.4 DnrK in vitro assay

Assays followed the previously reported protocol[22] with minor changes. Specifically, for substrate specificity studies, DnrK reactions were conducted in a volume of 30 μL 50 mM Tris, pH 8.0, containing 3.2 mM AdoMet and 1 mM non-native acceptor and 100 and 40 μM affinity-purified DnrK and SAHH. Reactions were incubated at 37°C for 16 hr and subsequently quenched with an equal volume of MeOH followed by centrifugation (13,000*g*, 15 min) to remove the precipitated protein. Product formation was assessed by HPLC (Method A) and based on the integration of species at 254, 280, or 320 nm as previously reported.[22] Corresponding control reactions lacking DnrK or AdoMet led to no product. Inclusion of SAHH (an enzyme that degrades the co-product SAH/AdoHcy) in these reactions improved turnover by driving reaction equilibrium toward desired product formation.

2.4.5 DnrK kinetics

DnrK kinetic parameters were determined for both **1** and **75** acceptors (**Table 2.1**) using previously reported method.[22] Kinetic studies were conducted in triplicate using 10 μM of DnrK under saturating AdoMet (1.6 mM) and variable concentration of **1** [15 μM to 500 mM] or (**75**) [150 μM to 10 mM]] (**Figure 2.13**).

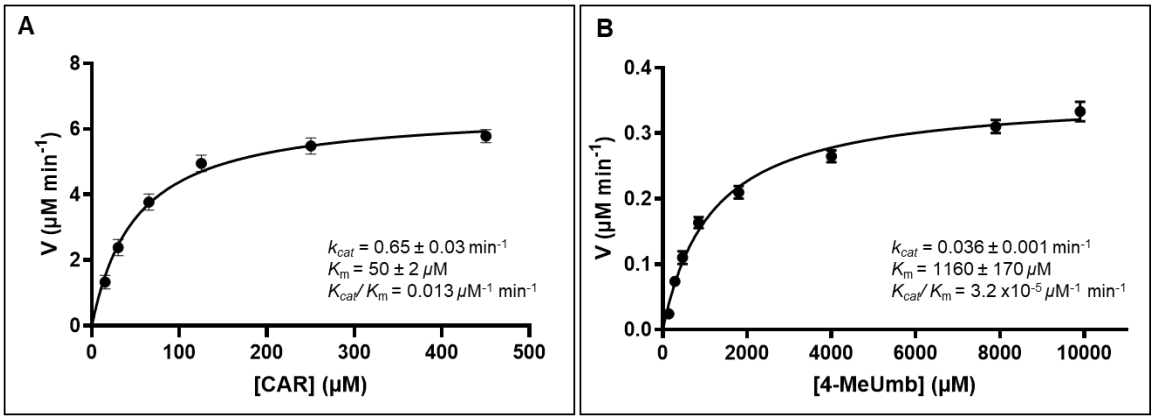

Figure 2.13. Determination of kinetic parameters for DnrK-catalyzed reactions using native (CAR, **1**) and non-native (4-MeUmb, **75**) substrates. [DnrK] = 10 μM in all experiments and assays were conducted via HPLC Method **B**. **(A)** [CAR] = varied, [AdoMet] = 1.6 mM. **(B)** [4-MeUmb] = varied, [AdoMet] = 1.6 mM.

2.4.6 DnrK crystallization and structure elucidation

The co-crystallization of DnrK with AdoHcy and 4-MeUmb **75** was achieved by mixing 0.2 μL of protein sample solution (20 mg/mL DnrK, 2.5 mM AdoMet, 7.5 mM **75** and 20 mM Tris, pH 8.0) with 0.2 μL of reservoir solution (1.26 M ammonium sulfate, 0.1 M Tris, pH 8.0 and 0.2 M lithium sulfate) at 20 °C using the hanging drop method. The crystals were then soaked and cryoprotected with 80% reservoir solution, 15% glycerol and 3 mM **75** and then flash cooled in liquid nitrogen for data collection.

X-ray diffraction data were collected at the Advanced Photon Source (Argonne National Laboratory) on Life Sciences Collaborative Access Team (LS-CAT) beamline 21-ID-F. Data sets were indexed, integrated and scaled using XDS.[78] The structure was phased using the isomorphous DnrK structure in complex with AdoHcy and 2-chloro-4-nitrophenol, PDB id 5EEH[22] as a starting model. The structural model was completed after several rounds of manual model building with COOT[79] and refinement with phenix.refine.[80] The structure was visualized and analyzed using a collaborative 3D graphics system.[81] The structural biology software applications used in this project were compiled and configured by SBGrid.[82] Data processing and refinement statistics are shown in **Table 2.2** and the structure was deposited in the worldwide Protein Data Bank with PDB id 5JR3.

Table 2.2. Crystal parameters, data collection, and refinement statistics.

	DnrK - AdoHcy/4MU
PDB	5JR3
Crystal parameters	
Space group	C 2
Unit-cell lengths (Å)	122.2, 111.1, 116.2
Unit cell angles (°)	90.0, 120.0, 90.0
Data collection statistics	
Beamline	APS 21-ID-F (LS-CAT)
Detector	Rayonix MX 225 CCD
Temperature	100 K
Wavelength (Å)	0.980
Resolution range (Å)	41.1-1.84
High resolution shell (Å)	(1.91-1.84)[a]
No. of reflections (measured / unique)	527978 (52330)
No. unique reflections	116127 (10926)
Completeness (%)	98.3 (94.5)
R_{merge}[b]	0.077 (0.450)
R_{meas}[c]	0.088 (0.511)
Redundancy	4.5 (4.5)
Mean I / sigma (I)	12.6 (3.3)
$CC_{1/2}$[d]	1.00 (0.90)
Refinement and model statistics	
R_{cryst} / R_{free}[e]	0.160 / 0.180
RMSD bonds (Å)	0.01
RMSD angles (°)	0.9
No. of protein chains / residues / non-H atoms	1030 / 8110
No. of waters	835
No. of Ligand molecules (SAH / 4MU / SO4)[f]	3 / 3 / 12
Average Ligand RSCC[g] (SAH / 4MU / SO4)	0.97 / 0.87 / 0.93
Average B factor - protein/ligand/solvent ($Å^2$)	32 / 40 / 42
No. TLS groups	3
Ramachandran plot (%)	
Favorable region	97.6
Additional allowed region	1.9
Disallowed region	0.5

[a]Values in parentheses are for the highest-resolution shell.

[b]$R_{merge} = \Sigma_h \Sigma_i |I_i(h) - \langle I(h)\rangle| / \Sigma_h \Sigma_i I_i(h)$, where $I_i(h)$ is the intensity of an individual measurement of the reflection and $\langle I(h)\rangle$ is the mean intensity of the reflection.

[c]$R_{meas} = \Sigma_h (n_h/(n_h-1)\, \Sigma_i |I_i(h) - \langle I(h)\rangle| / \Sigma_h \Sigma_i I_i(h)$, where n_h denotes the redundancy.

[d]$CC_{1/2} = \sum (x - \langle x\rangle)(y - \langle x\rangle)/[\sum(x - \langle x\rangle)^2 \Sigma(y - \langle y\rangle)^2]^{1/2}$

[e]$R_{cryst} = \Sigma_h ||F_{obs}| - |F_{calc}|| / \Sigma_h |F_{obs}|$, where F_{obs} and F_{calc} are the observed and calculated structure factor amplitudes, respectively. R_{free} was calculated as R_{cryst} using 2% of the randomly selected unique reflections that were omitted from structure refinement.

[f]wwPDB chemical component dictionary codes: SAH for AdoHcy; 4MU for 4-methylumbeliferonewere; SO4 for sulfate ion.

[g]ligand RSCC is the ligand real-space correlation coefficient, which provides an objective measure of the fit of atom coordinates to electron density.

2.4.7 Structure prediction of TcmO

The TcmO homodimer was predicted using AlphaFold-Multimer[83,84] with a multiple sequence alignment generated by MMSeqs2[85] in the ColabFold[86] notebook both with and without templates. The rank 1 model from the run without templates had the highest median pLDDT (0.97) and the lowest median PAE (3.8 Å) score and the AMBER relaxed[87] model from this run was selected for further analysis.

2.4.8 4-O-Methoxy aranciamycin production and structure elucidation

In a 15 mL sterile conical tube, a total volume of 5 mL DnrK reaction including 5.4 mg (10 mM DMSO stock) of previously isolated aranciamycin (**7**), 3.2 mM AdoMet and 100 and 40 μM affinity-purified DnrK and SAHH in 50 mM Tris, pH 8.0 under mentioned conditions were conducted and used for preparative DnrK-catalyzed methylation. Semi-preparative HPLC purification of the crude reaction (Method **B**, **Figure S2.1**) afforded compound (**7a**) in pure form as orange solid (3.0 mg, 55% yield). The molecular formula of (**7a**) was established as $C_{28}H_{30}O_{12}$ based on (+) and (-)-HRESIMS [*m/z* 559.1813 $[M + H]^+$ (calcd. 559.1910 for $C_{28}H_{31}O_{12}$); *m/z* 557.1649 $[M - H]^-$ (calcd. 557.1664 for $C_{28}H_{29}O_{12}$)], the corresponding D*m/z* =14 compared to that for **7** consistent with an additional methyl group. Consistent with this, the $^{13}C/^{1}H$/HSQC NMR of **7a** (**Table 2.3**) highlighted a missing 4-OH (δ_H 11.82, 1H, s) and an additional methoxy group (δ_H 4.09, 3H, s; δ_C 57.0). The connection of the OCH_3 at 4-position in compound **7a** was established based on the observed critical HMBC correlation from the singlet methoxy (δ_H 4.09; 4-OCH_3) to C-4 (δ_C 161.4). All other 2D-NMR ($^{1}H,^{1}H$-COSY and HMBC) correlations were

Table 2.3. ^{13}C (100 MHz) and ^{1}H (400 MHz) NMR spectroscopic data of **7** and **7a** in $CDCl_3$.[a]

No.	aranciamycin **7**		4-*O*-methylaranciamycin (**7a**)	
	δ_C, type	δ_H (mult, *J* in [Hz])	δ_C, type	δ_H (mult, *J* in [Hz])
1	120.9, CH	7.84 (d, 7.5)	120.8, CH	8.00 (dd, 7.6, 1.0)
2	138.4, CH	7.72 (d, 8.0)	137.0, CH	7.80 (dd, 8.4, 7.7)
3	125.2, CH	7.31 (d, 8.4)	118.6, CH	7.40 (d, 8.6, 1.1)
4	163.1, C		161.4, C	
4-OH		11.82 (s)		
4-OCH_3			57.0, CH_3	4.09 (s)
4a	115.9, C		120.5, C	
5	193.1, C		189.2, C	
5a	118.9, C		119.9, C	
6	162.5, C		162.6, C	
6-OH		12.81 (s)		13.75 (s)
6a	133.6, C		133.7, C	
7	72.1, CH	5.18 (d, 2.1)	72.4, CH	5.20 (d, 2.5)
8	85.8, CH	3.76 (brd, 2.2)	86.0, CH	3.76 (d, 2.5)
8-OCH_3	60.2, CH_3	3.54 (s)	60.2, CH_3	3.54 (s)
9	76.9, C		76.9, C	
9-CH_3	23.0, CH_3	1.51 (s)	23.1, CH_3	1.52 (s)
10	199.1, C		199.3, C	
10a	136.3, C		135.4, C	
11	117.9, CH	8.35 (s)	116.9, CH	8.35 (s)
11a	133.8, C		133.0, C	
12	180.6, C		181.6, C	
12a	133.6, C		135.8, C	
1′	100.8, CH	5.62 (brs)	100.7, CH	5.67 (brs)
2′	80.2, CH	3.52 (m)*	80.2, CH	3.50 (m)*
2′-OCH_3	59.0, CH_3	3.55 (s)	59.0, CH_3	3.54 (s)
3′	71.6, CH	3.54 (m)*	71.7, CH	3.54 (m)*
4′	73.5, CH	3.45 (m)*	73.7, CH	3.44 (m)*
5′	69.8, CH	3.81 (m)	69.6, CH	3.81 (m)
6′	17.8, CH_3	1.37 (d, 6.1)	17.8, CH_3	1.38 (d, 6.2)

[a] Assignments supported by gCOSY, gHSQC and gHMBC experiments. *Overlapped signals.

in full agreement with structure **7a** (**Figure 2.3**). Thus, compound **7a** was designated as 4-*O*-methoxy-arancinamycin.

2.4.9 Cancer cell line viability assay

Mammalian cell line cytotoxicity [A549 (non-small cell lung) and PC3 (prostate) human cancer cell lines] assays (**Figure 2.12A and B**) were accomplished in triplicate following our previously reported protocols.[42,52] Actinomycin D and H_2O_2 were used as positive controls.

2.4.10 Western blot analysis

Western blot analysis was performed as previously described.[43,51,72] Specifically, after treatment with test agent, HCT116 cells were lysed in NP-40 lysis buffer (50 mM Tris, pH 7.5, 150 mM NaCl, 1 mM EDTA, 1% NP-40, 10% glycerol, protease and phosphatase inhibitor cocktail). Protein concentrations were measured using the BCA protein assay reagent (Pierce, Waltham, MA). Equal amounts of lysate were subsequently resolved by SDS-PAGE, transferred to PVDF membranes, immunoblotted with specific primary and secondary antibodies, and detected using chemiluminescence (GE Healthcare, Chicago, IL) (**Figure 2.12C**). Antibodies for phospho-4E-BP1 (Thr37/46) (#2855), phospho-4E-BP1 (Thr70) (#13396) were purchased from Cell Signaling Technology (Danvers, MA). *β*-actin antibody (A5441; 1:10,000) was from Sigma-Aldrich.

2.4.11 Axolotl embryo tail regeneration assay

The axolotl embryo tail regeneration assay was conducted following our previously reported protocols.[43,72,73] Briefly, stage 42 embryos were manually hatched, administered benzocaine anesthesia (0.2 g in 10 ml EtOH/L water), and photographed (**Figure 2.12D**). Embryos were subsequently administered 2 mm tail amputations and then reared (in the absence or presence of test agent) at 18–19 ºC in 12-well microtiter plates containing 2.0 mL of artificial pond water (43.25 g NaCl, 0.625 g KCl, 1.25 g $MgSO_4$, 2.5 g $NaHCO_3$, and 1.25 g CaCl per 50 L charcoal filtered municipal water). The solutions were changed on days 3 and 5 post-amputation (DPA), and experiments were terminated on 7 DPA. Images of anesthetized embryos at 0, 3, 5 and 7 DPA were captured using an Olympus microscope with 0.5× objective lens and DP400 camera. All chemicals were dissolved in DMSO and diluted to 0.1% final DMSO concentration. Axolotls (RRID:AGSC_100E) were obtained from the Ambystoma Genetic Stock Center (RRID:SCR_006372). Vehicle (DMSO) was used as the negative control and the Hsp90 inhibitor geldanamycin was used as a positive control.

Supplementary table and figures for Chapter Two

Table S2.1. Non-native DnrK acceptors and corresponding methylated products. Predicted DnrK regioselectivity is highlighted in grey and determined DnrK regioselectivity is highlighted in blue.

ID	Compound	Structure	Mass (m/z)		Product	Mass (m/z)		%
			Theoretical	Experimental		Theoretical	Experimental	
2	alizarin	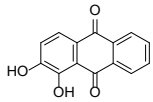	240.0	241.0[a]	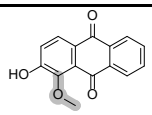	254.0	255.0[a]	13
3	purpurin	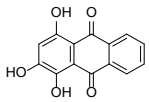	256.0	255.0[b]	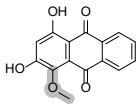	270.0	271.0[a]	13
4	9,10-seco-7-deoxy-nogalamycinone	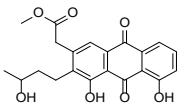	384.1	383.2[b]	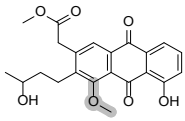	398.1	397.0[b]	91
7	aranciamycin	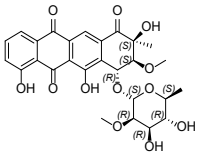	544.1	543.2[b]	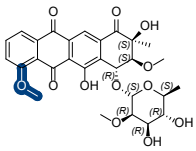	558.1	557.2[b]	97
8	SM 173B	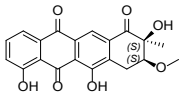	368.0	367.0[b]	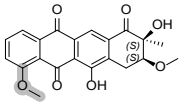	382.1	381.0[b]	96
9	steffimycin B	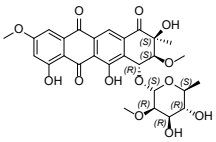	588.5	587.2[b]	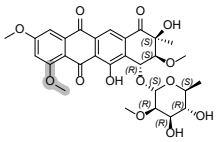	602.5	601.2[b]	15
10	nogalavinone	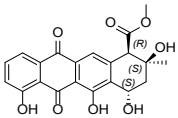	398.1	397.0[b]	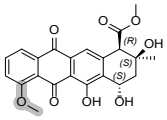	412.1	411.0[b]	76
11	auramycinone	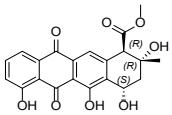	398.1	397.0[b]	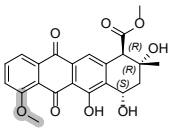	412.1	411.0[b]	96
12	7-deoxy-nogalamycinone	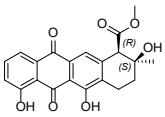	382.1	381.0[b]	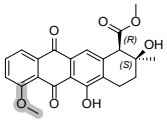	396.1	395.2[b]	62

ID	Compound	Structure	Mass (m/z)		Product	Mass (m/z)		%
			Theoretical	Experimental		Theoretical	Experimental	
13	deoxyaura mycinone		382.1	381.0[b]		396.1	395.0[b]	20
17	8-demethyltet racenomyci n C		458.0	457.9[b]		472.1	471.0[b]	85
23	rabelomyci n		338.0	337.0[b]		352.0	351.0[b]	98
25	8-*O*-desmethyls eitomycin		340.0	339.1[b]		354.1	355.1[a]	27
30	fluostatin C		324.0	323.0[b]		338.0	337.0[b]	90
31	tiancimycin C (TNM C)		559.1	558.0[b]		573.1	572.0[b]	81
32	tiancimycin F (TNM F)		543.1	542.0[b]		557.1	556.2[b]	98
35	frenolicin B		328.0	329.1[a]		342.1	343.1[a]	78
36	5-*epi*-frenolicin B		328.0	329.2[a]		342.1	343.2[a]	67
43	apigenin		270.0	269.0[b]		284.0	283.0[b]	26
						298.0	299.0[a]	2
44	luteolin		286.0	285.0[b]		300.0	299.0[b]	20

ID	Compound	Structure	Mass (m/z)		Product	Mass (m/z)		%
			Theoretical	Experimental		Theoretical	Experimental	
					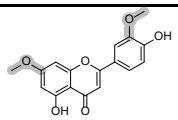	314.0	313.0[b]	72
					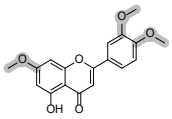	328.0	329.0[a]	8
45	7-hydroxyflavone	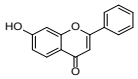	238.2	239.0[a]	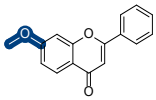	252.2	253.2[a]	12
46	5,4′-dimethoxy-7-hydroxyflavone	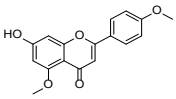	398.0	299.0[a]	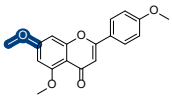	312.0	313.2[a]	10
49	chrysin	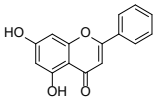	254.0	255.0[a]	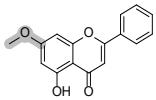	268.07	269.0[a]	26
50	7,4'-dihydroxyflavone	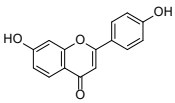	254.0	255.0[a]	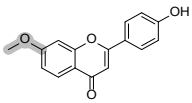	268.07	269.0[a]	30
52	6,2'-dihydroxyflavone	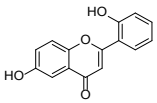	254.0	253.0[b]	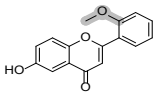	268.0	267.0[b]	27
53	kaempferol	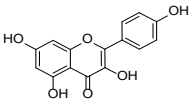	286.0	287.0[a]	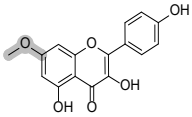	300.0	301.0[a]	39
54	quercetin	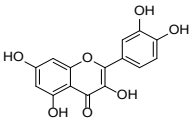	302.0	303.0[a]	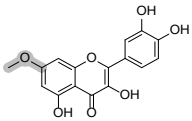	316.0	317.0[a]	12
55	galangin	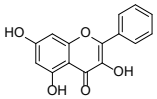	270.0	271.0[a]	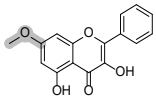	284.0	285.0[a]	7
57	quercitrin	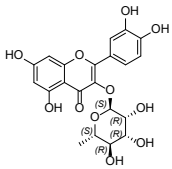	448.1	449.0[a]	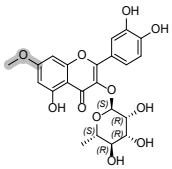	462.1	463.0[a]	75
58	2(*S*)-naringenin	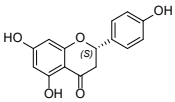	272.0	273.0[a]	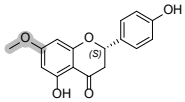	286.0	287.0[a]	45

ID	Compound	Structure	Mass (m/z)		Product	Mass (m/z)		%
			Theoretical	Experimental		Theoretical	Experimental	
59	2(*S*)-hesperetin	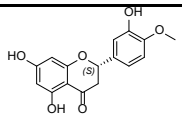	302.0	303.0[a]	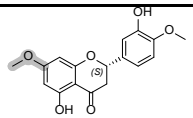	316.0	317.0[a]	67
62	genistein	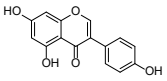	272.0	271.0[b]	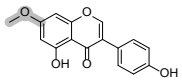	286.0	285.0[b]	37
63	5,4'-dimethoxy-7-hydroxyisoflavone	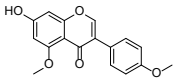	298.0	299.2[a]	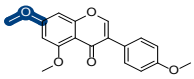	312.0	313.2[a]	18
65	biochanin A	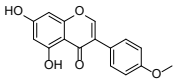	284.0	285.0[a]	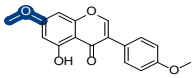	298.0	299.0[a]	15
67	daidzein	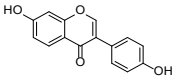	254.0	255.0[a]	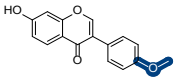	268.0	269.0[a]	9
71	5-carbomethoxymethyl-2-heptyl-7-hydroxychrome	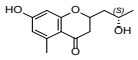	234.2	235.0[a]	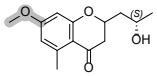	248.1	249.2[a]	98
72	silybin B	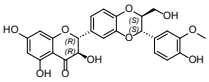	482.1	483.0[a]	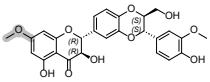	496.1	497.0[a]	32
73	methyl caffeate	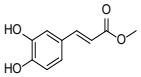	194.0	193.0[b]	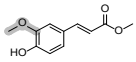	208.0	207.0[b]	25
75	4-methylumbelliferone (4-MeUmb)	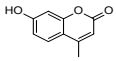	176.1	177.2[a]	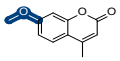	190.2	191.2[a]	12
77	5,7-dihydroxy-4-methylcoumarin	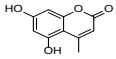	192.1	191.0[b]	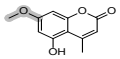	206.2	205.2[b]	14
78	6,7-dihydroxycoumarin	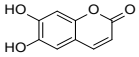	178.0	177.0[b]	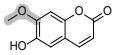 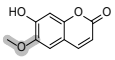 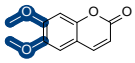	192.0 206.0	193.0[a] 207.0[a]	28 13 3
79	9-methoxy alternariol	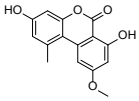	272.0	273.0[a]	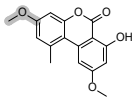	286.0	287.0[a]	10
85	6,8-dihydroxy-7-methoxy-3-methylisocoumarin	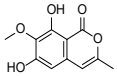	222.0	223.0[a]	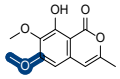	236.0	237.0[a]	56
87	orthosporin	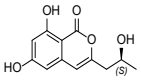	236.0	235.0[b]	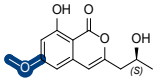	250.0	251.0[a]	92
89	6-hydroxy-7,8-dimethoxy-3-methylisocoumarin	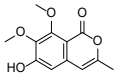	236.0	237.0[a]	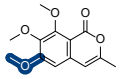	250.0	251.0[a]	65

ID	Compound	Structure	Mass (m/z)		Product	Mass (m/z)		%
			Theoretical	Experimental		Theoretical	Experimental	
90	6,8-dihydroxy-7-methoxy-3-hydroxymethylisocoumarin	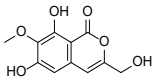	238.0	239.0[a]	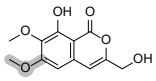	252.0	253.0[a]	85
91	4-hydroxy-quinolin-2(1H)-one		161.0	162.0[a]	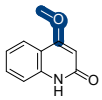	175.0	176.0[a]	51
92	2,4-dihydroxyquinoline	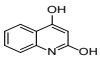	161.0	162.0[a]	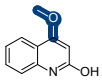	175.0	176.0[a]	37
93	8-hydroxy-3,4-dihydro-2-quinolinone		163.2	164.2[a]	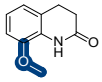	177.2	178.2[a]	42
94	iodoquinol	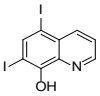	396.8	397.8[a]	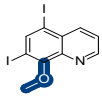	410.8	411.8[a]	88
98	radicicol	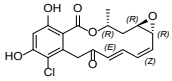	364.0	365.0[a]	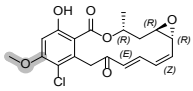	378.0	379.0[a]	23
					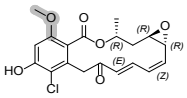			5
					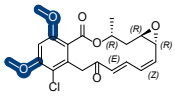	392.0	393.0[a]	16
99	platencin	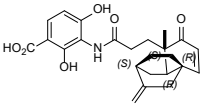	425.2	426.2[a]	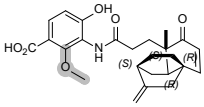	439.2	440.2[a]	26
100	platensimycin	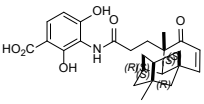	441.2	442.2[a]	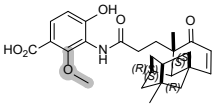	455.2	456.2[a]	28
101	pyramidamycins A	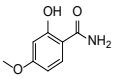	167.0	168.0[a]	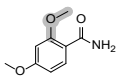	181.2	182.2[a]	19
102	pyramidamycins B	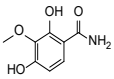	183.2	184.2[a]	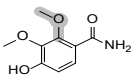	197.2	198.2[a]	6

[a] (+)-ESIMS, $[M+H]^+$; [b] (-)-ESIMS, $[M-H]^-$

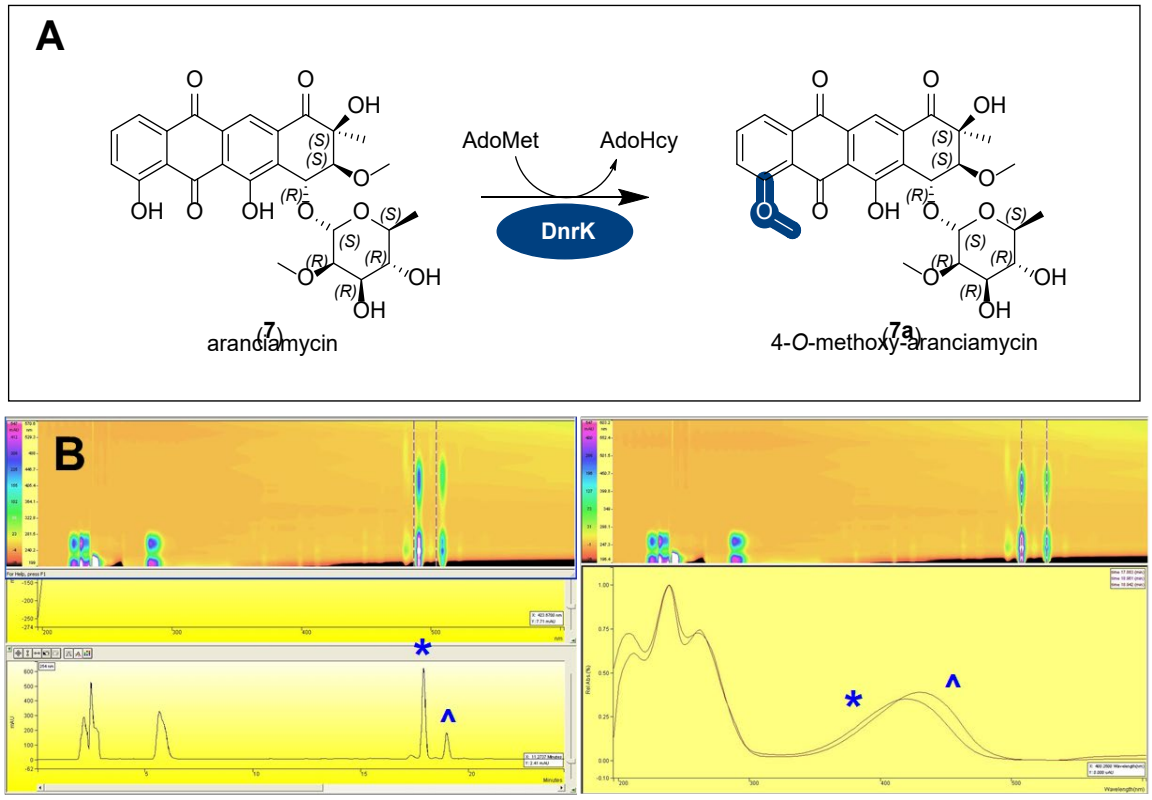

Figure S2.1. (A) General DnrK reaction with aranciamycin **7**^ as substrate and DnrK reaction/methylated product 4-*O*-methoxyaranciamycin **7a***. **(B)** Semi-preparative HPLC profile of DnrK 4-*O*-methylated **7a** using HPLC (Method **B**).

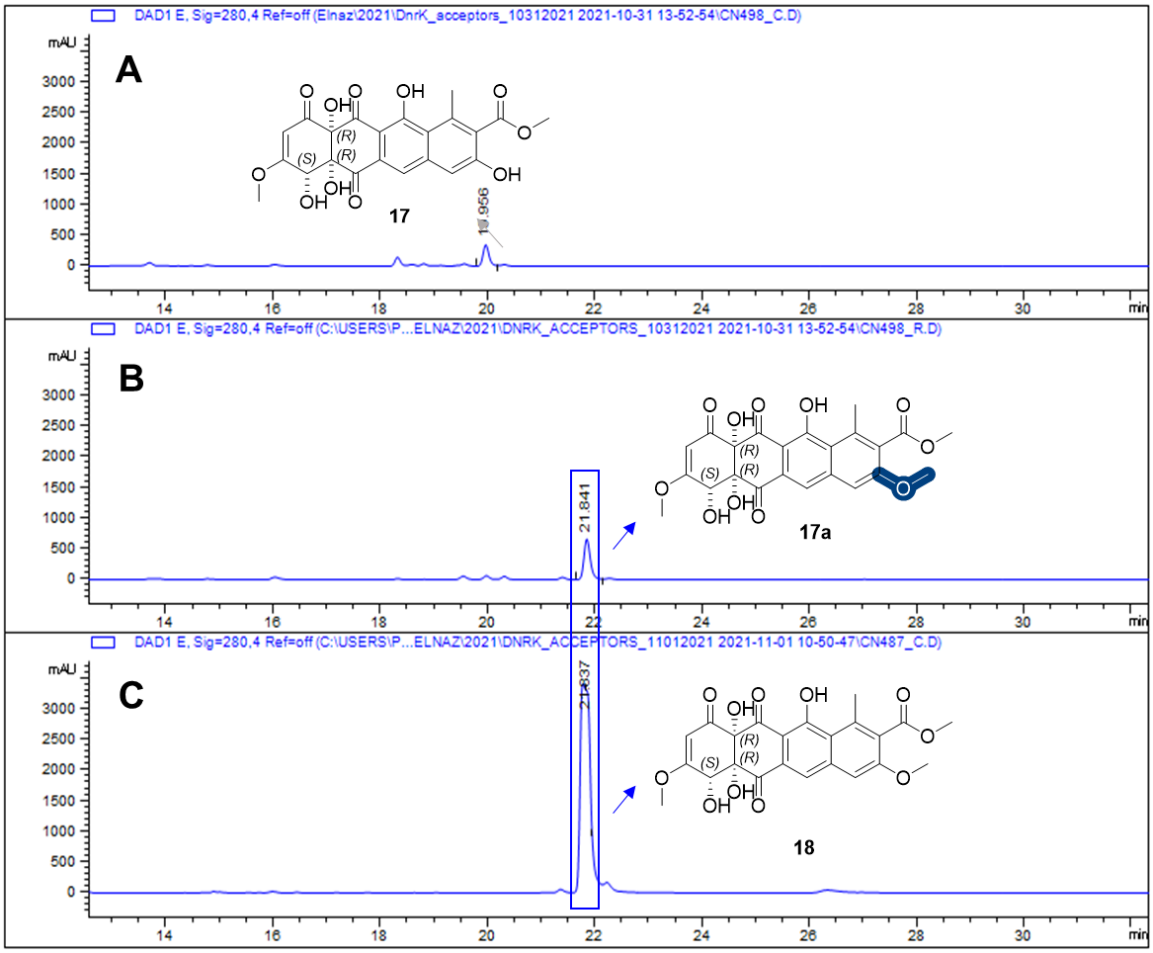

Figure S2.2 Test agent 8-desmethyltetracenomycin C **17** in the **(A)** absence and **(B)** presence of DnrK. **(C)** Elution profile of tetracenomycin C **18** standard.

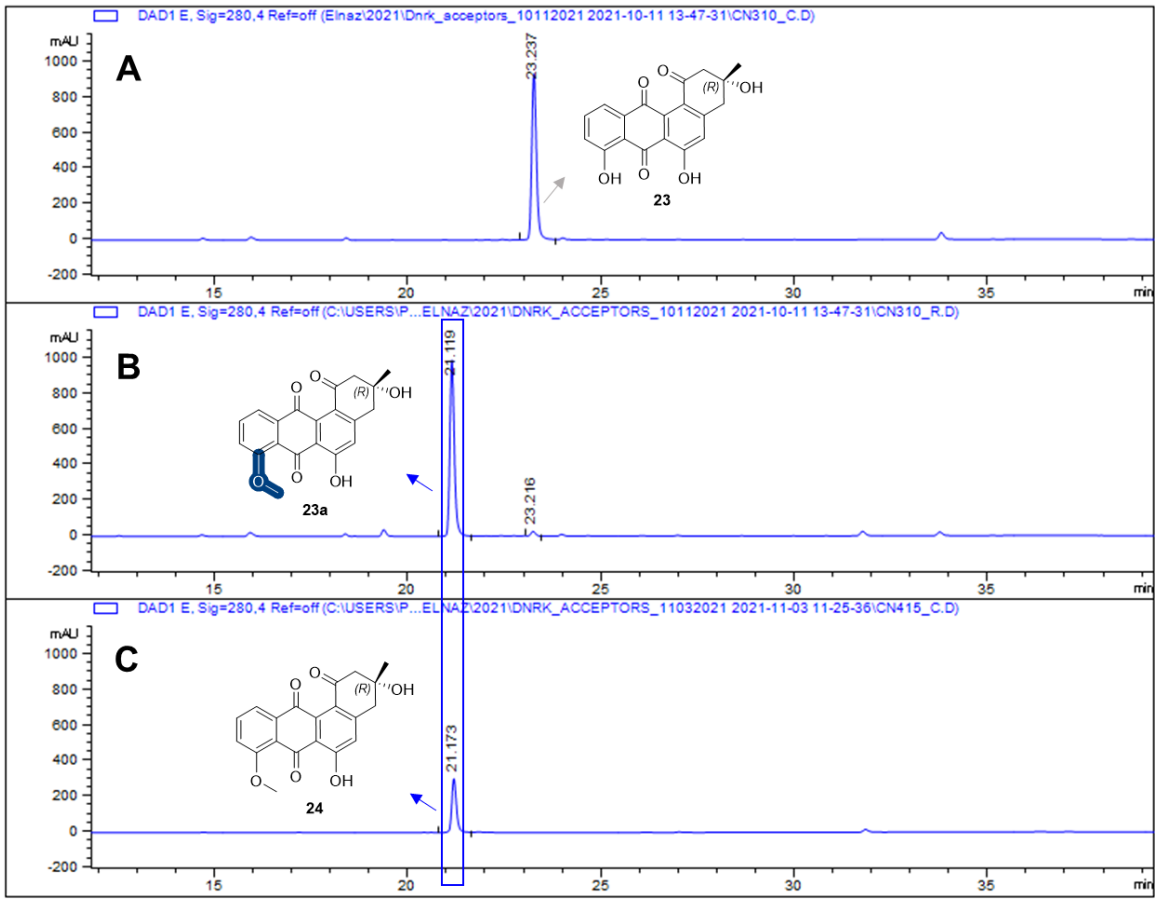

Figure S2.3 Test agent rabelomycin (**23**) in the **(A)** absence and **(B)** presence of DnrK. **(C)** Elution profile of 8-*O*-methylrabelomycin (**24**) standard.

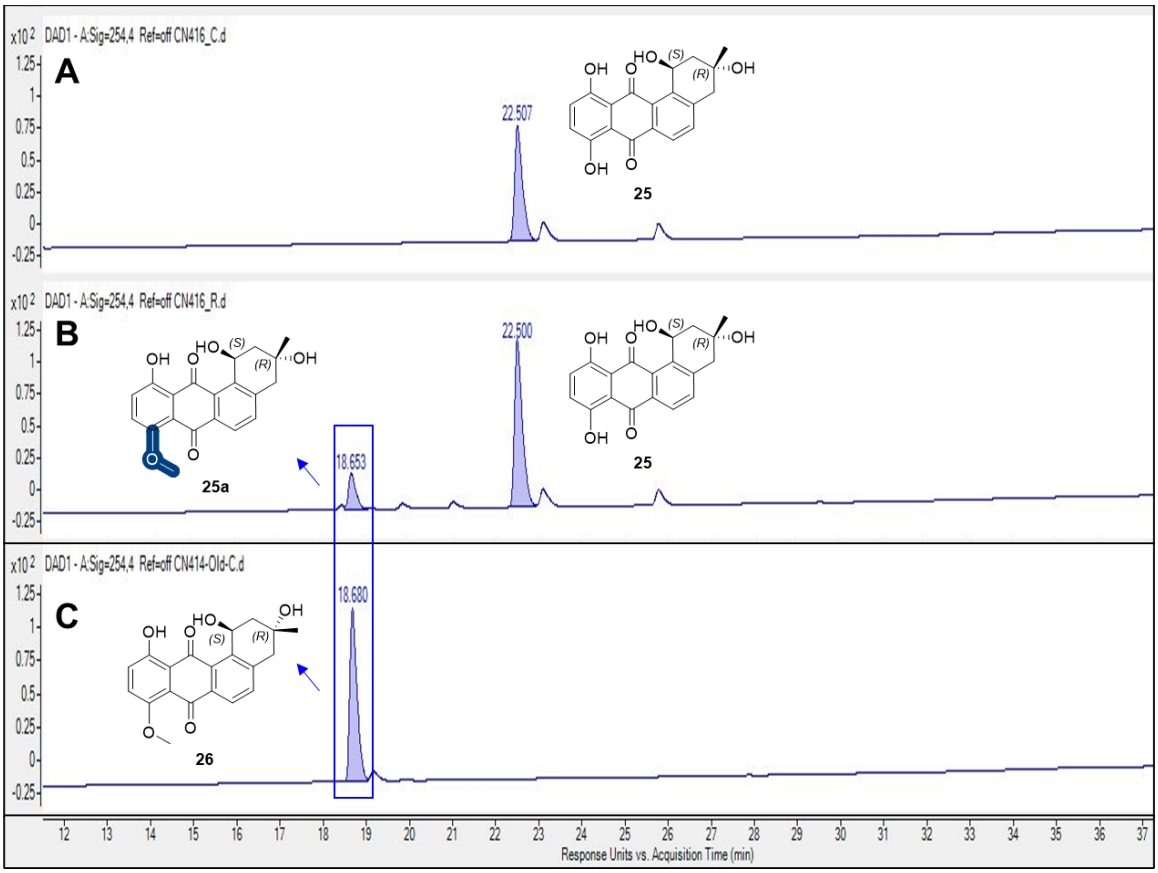

Figure S2.4 Test agent 8-*O*-desmethylseitomycin (**25**) in the **(A)** absence and **(B)** presence of DnrK. **(C)** Elution profile of seitomycin (**26**) standard.

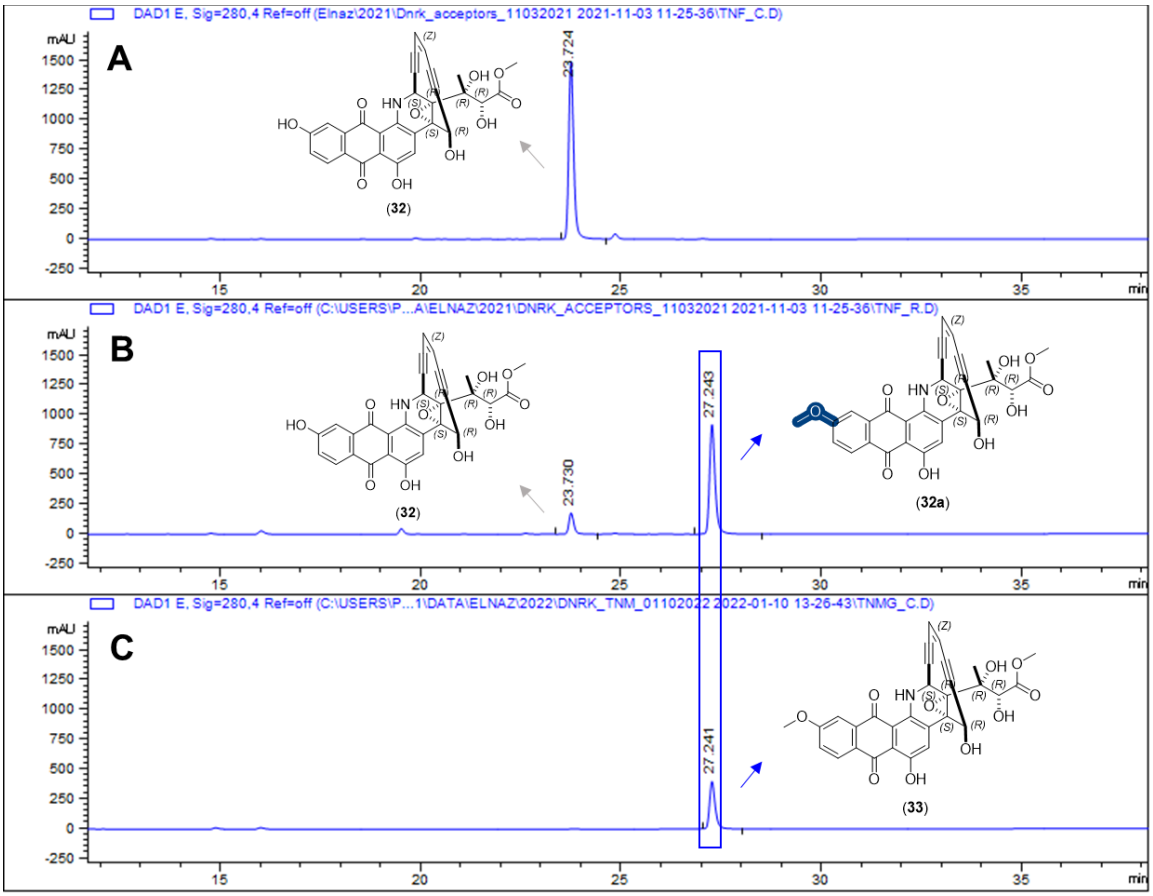

Figure S2.5 Test agent tiancimycin F (**32**) in the **(A)** absence and **(B)** presence of DnrK. **(C)** Elution profile of tiancimycin G (**33**) standard.

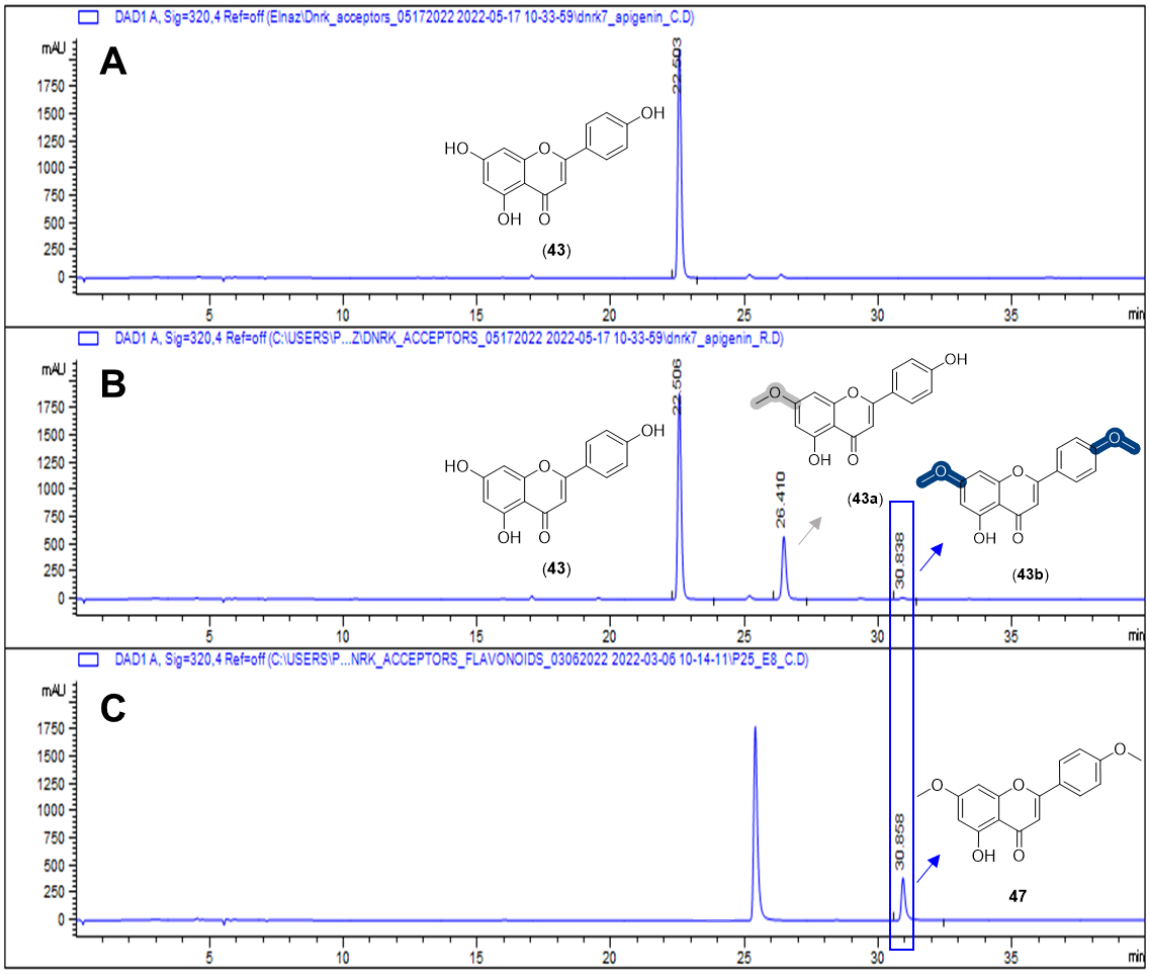

Figure S2.6 Test agent apigenin (**43**) in the **(A)** absence and **(B)** presence of DnrK. **(C)** Elution profile of apigenin dimethyl ether (**47**) standard.

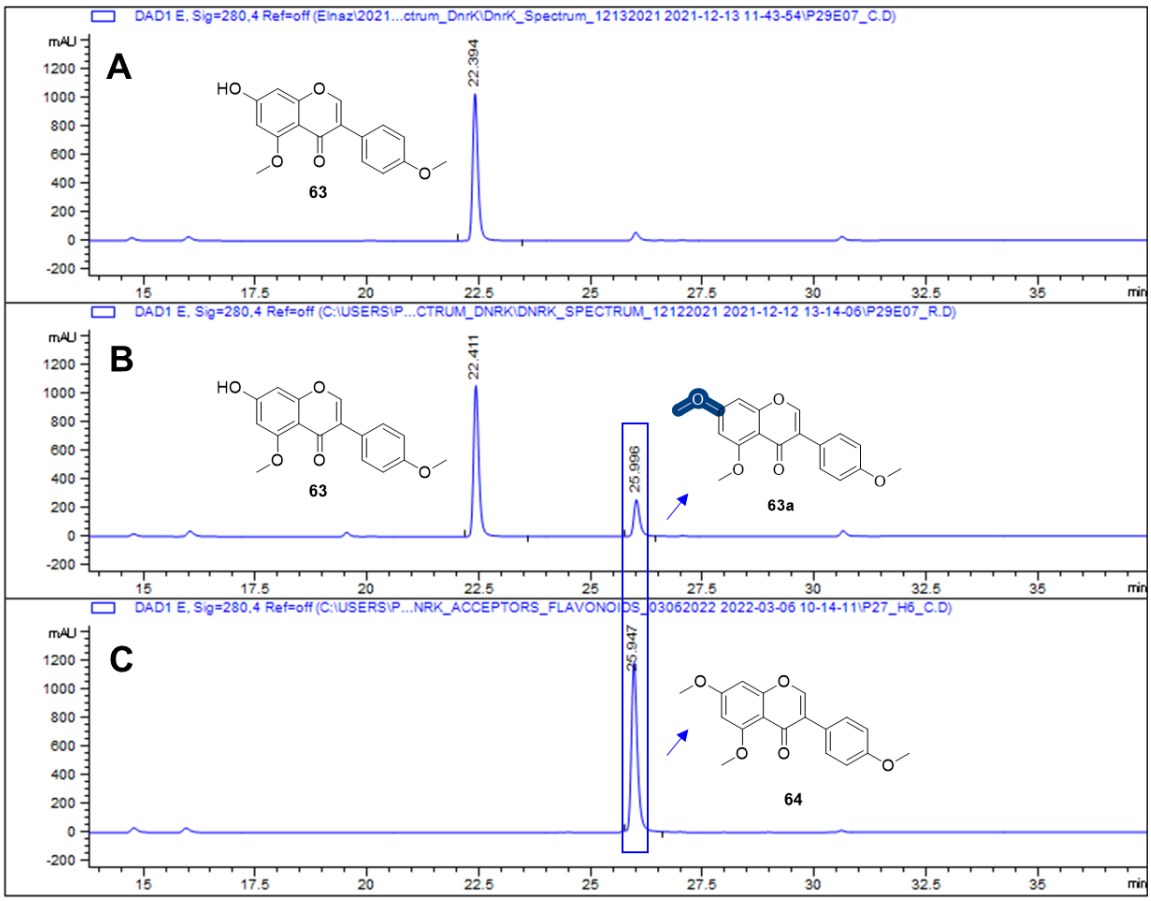

Figure S2.7 Test agent 5,4'-dimethoxy-7-hydroxyisoflavone (**63**) in the **(A)** absence and **(B)** presence of DnrK. **(C)** Elution profile of 5,7,4'-trimethoxyisoflavone (**64**) standard.

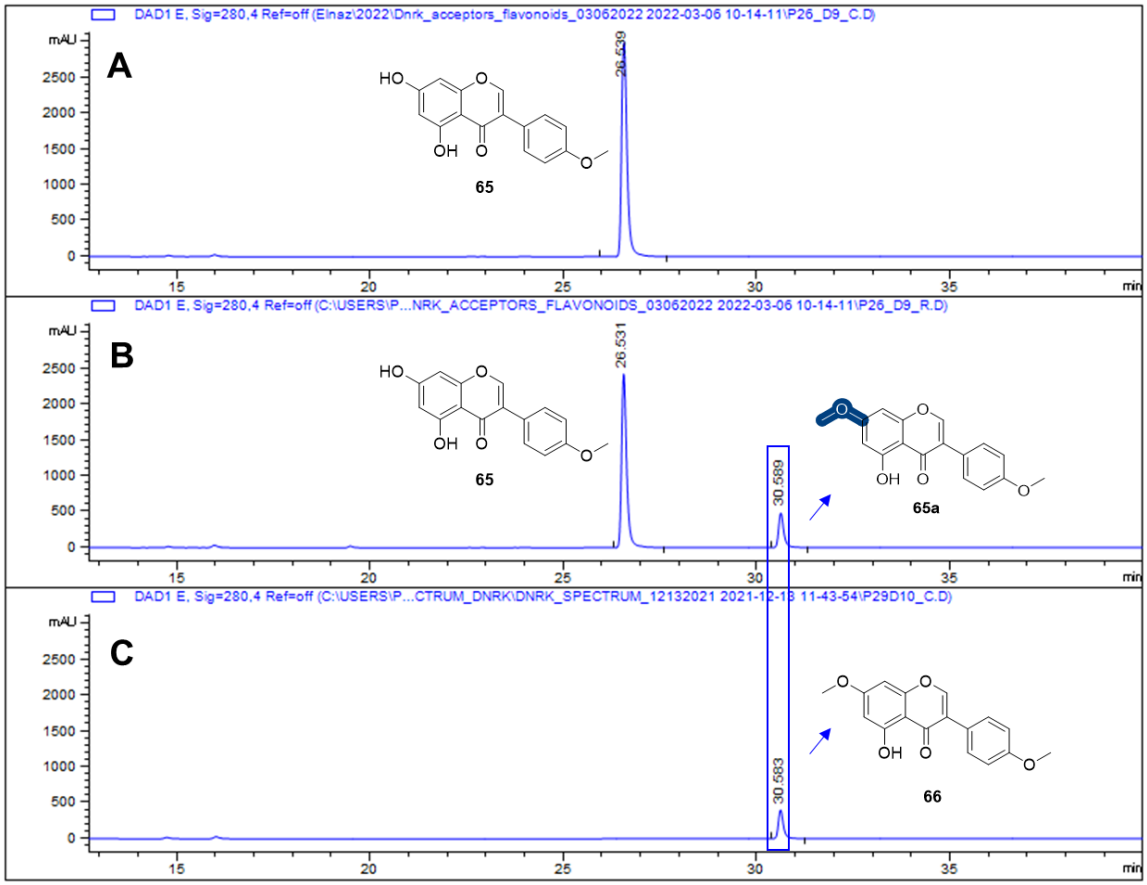

Figure S2.8 Test agent biochanin A (**65**) in the **(A)** absence and **(B)** presence of DnrK. **(C)** Elution profile of 7-methoxy-biochanin A (**66**) standard.

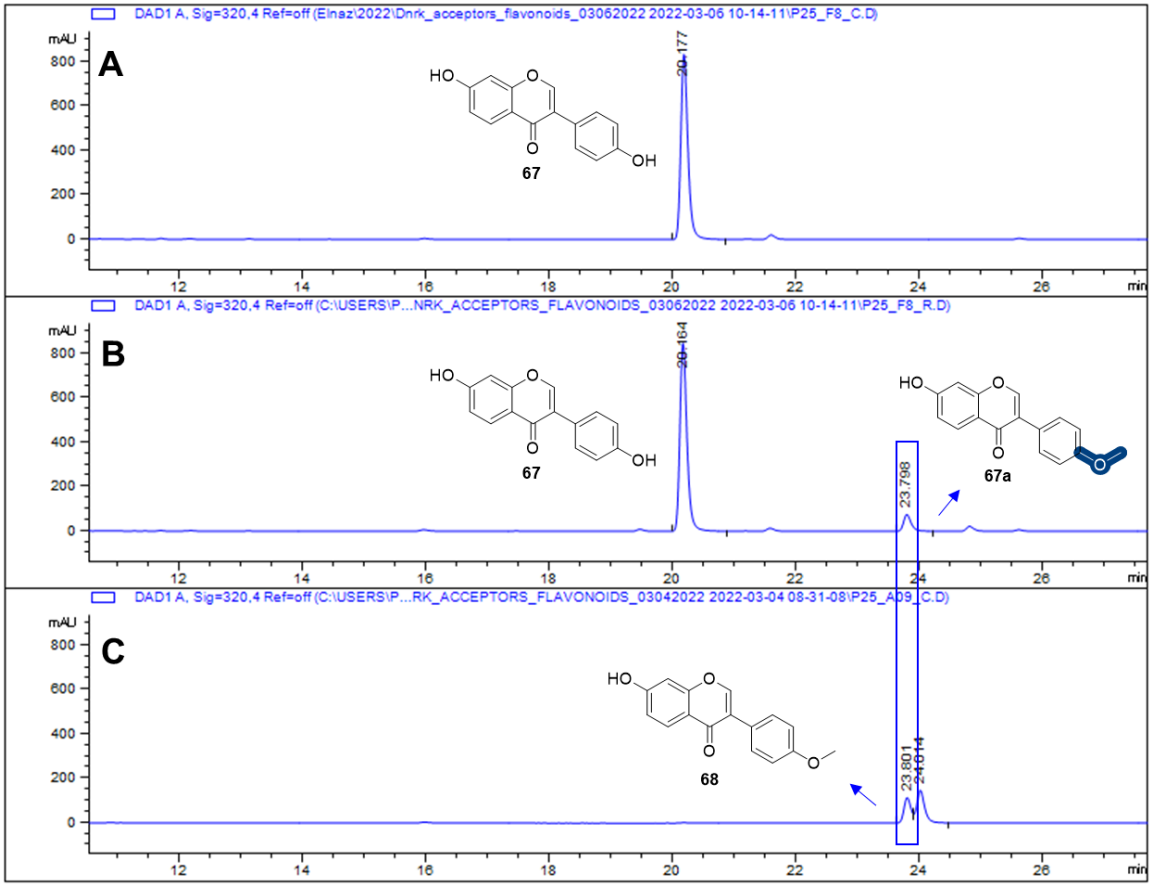

Figure S2.9 Test agent daidzein (**67**) in the **(A)** absence and **(B)** presence of DnrK. **(C)** Elution profile of formononetin (**68**) standard.

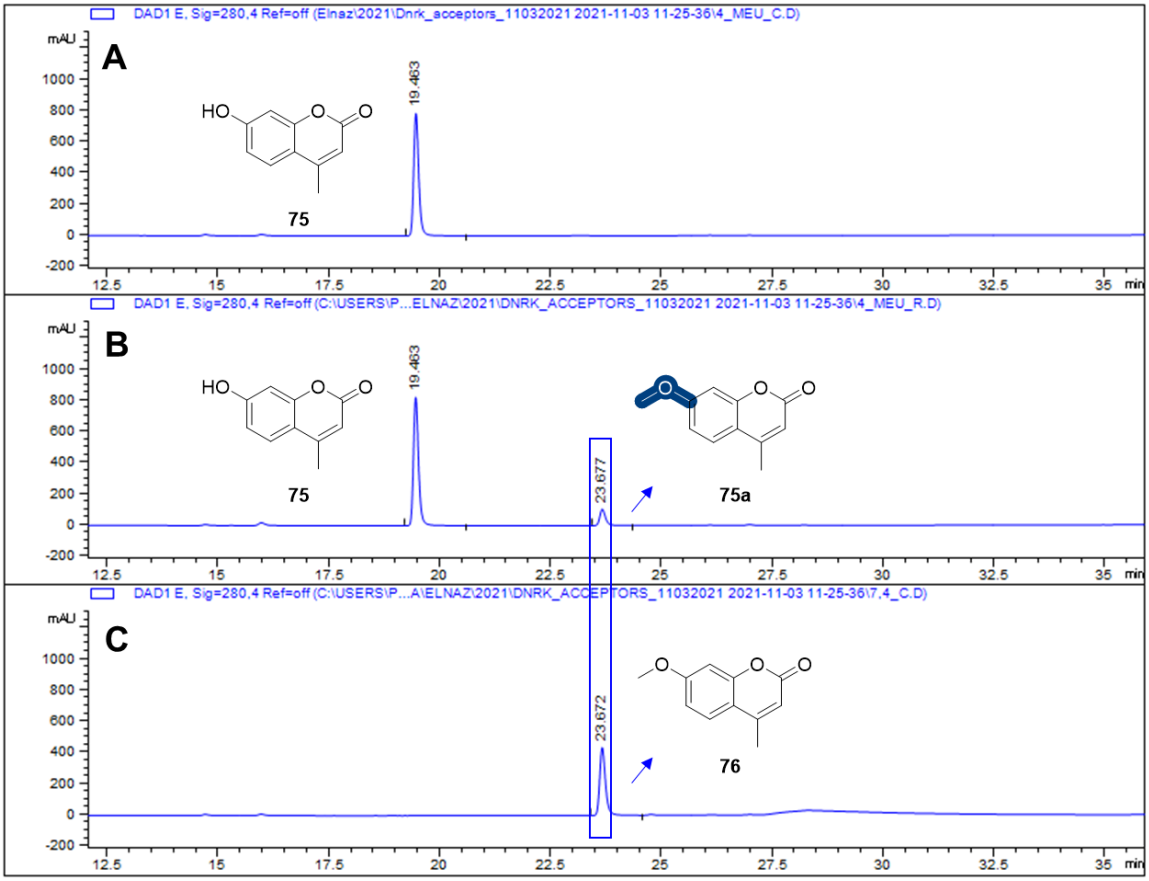

Figure S2.10 Test agent 4-MeUmb (**75**) in the **(A)** absence and **(B)** presence of DnrK. **(C)** Elution profile of 7-methoxy-4-methylcoumarin (**76**) standard.

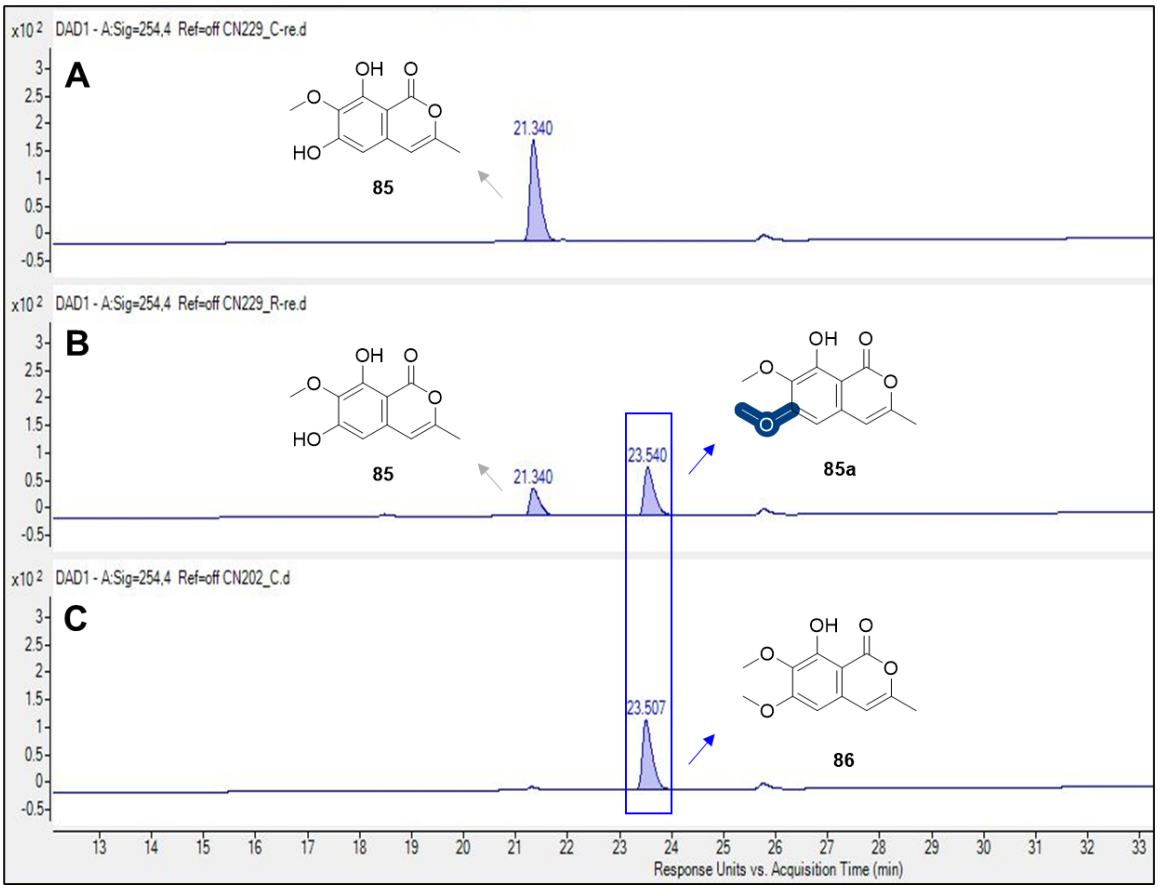

Figure S2.11 Test agent 6,8-dihydroxy-7-methoxy-3-methylisocoumarin (**85**) in the **(A)** absence and **(B)** presence of DnrK. **(C)** Elution profile of 8-hydroxy-6,7-dimethoxy-3-methylisocoumarin (**86**) standard.

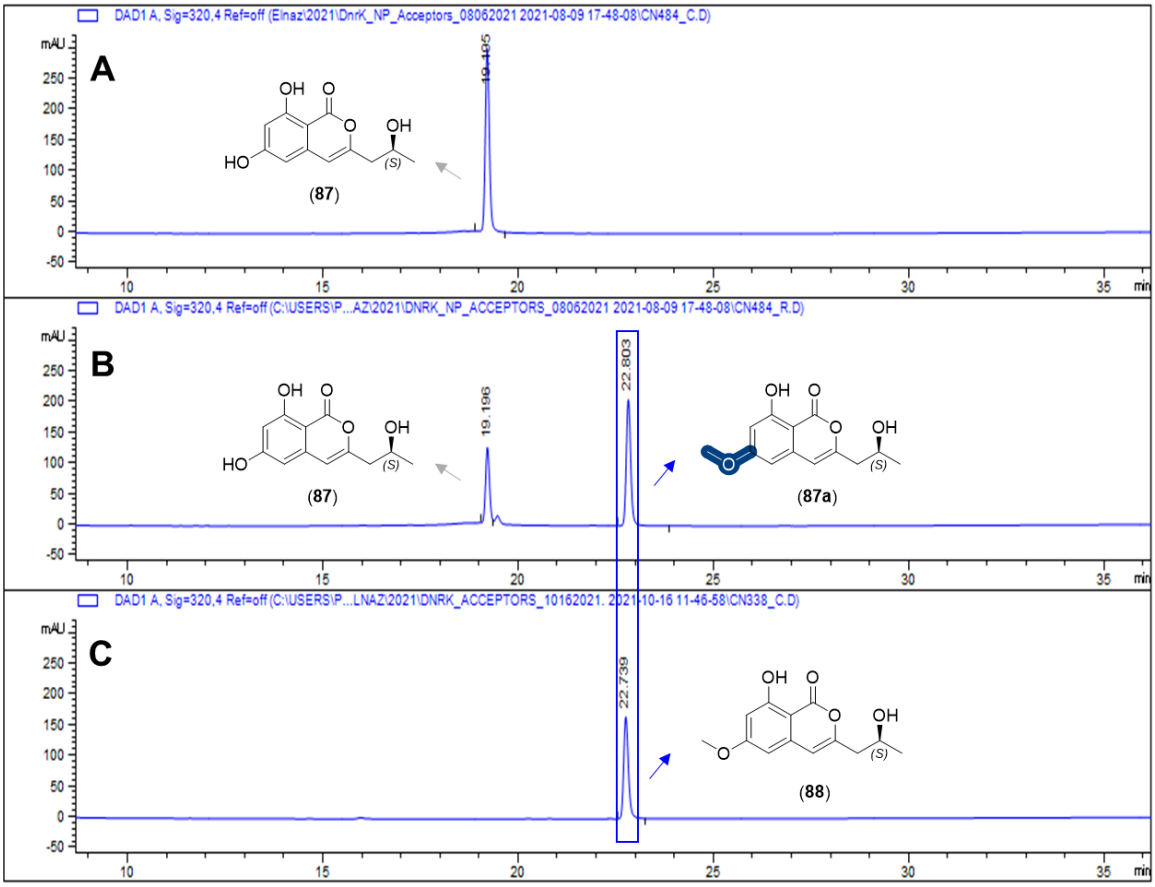

Figure S2.12 Test agent orthosporin (**87**) in the **(A)** absence and **(B)** presence of DnrK. **(C)** Elution profile of diaporthin (**88**) standard.

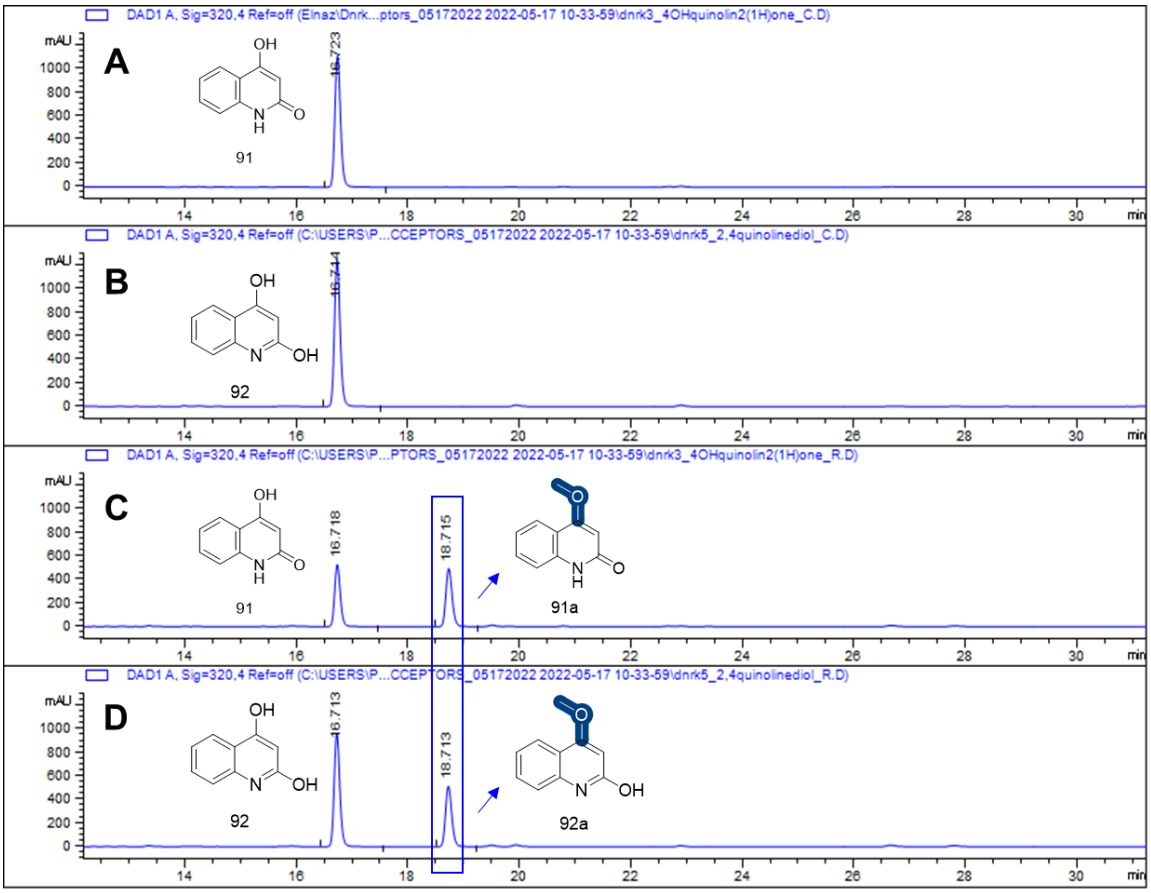

Figure S2.13 Test agents 4-hydroxy-quinolin-2(1*H*)-one (**91**) and 2,4-dihydroxyquinoline (**92**) in the **(A and B)** absence and **(C and D)** presence of DnrK.

References for Chapter Two

(1) Van der Zanden, S., Qiao, X., and Neefjes, J. New insights into the activities and toxicities of the old anticancer drug doxorubicin. *FEBS J.* **2021**, *288*, 6095-6111.

(2) Bristow, M.R., Thompson, P.D., Martin, R.P., Mason, J.W., Billingham, M.E., and Harrison, D.C. Early anthracycline cardiotoxicity. *Am. J. Med.* **1978**, *65*, 823-832.

(3) McGowan, J.V., Chung, R., Maulik, A., Piotrowska, I., Walker, J.M., and Yellon, D.M. Anthracycline chemotherapy and cardiotoxicity. *Cardiovasc. Drugs Ther.* **2017**, *31*, 63-75.

(4) Camerino, B., and Palamidessi, G. Derivati della parazina II. Sulfonamdopir. *Gazz. Chim. Ital.* **1960**, *90*, 1802-1815.

(5) Di Marco, A., Cassinelli, G., and Arcamone, F. The discovery of daunorubicin. *Cancer Treat Rep*. **1981**, *65*, 3-8.

(6) Arcamone, F., Cassinelli, G., Fantini, G., Grein, A., Orezzi, P., Pol, C., and Spalla, C. Adriamycin, 14-Hydroxydaunomycin, a new antitumor antibiotic from S. peucetius var. caesius. *Biotechnol. Bioeng*. **1969**, *11*, 1101-1110.

(7) Hulst, M.B., Grocholski, T., Neefjes, J.J., van Wezel, G.P., and Metsä-Ketelä, M. Anthracyclines: biosynthesis, engineering and clinical applications. *Nat. Prod. Rep*. **2022**, *39*, 814-841.

(8) Binaschi, M., Bigioni, M., Cipollone, A., Rossi, C., Goso, C., Maggi, C.A., Capranico., G., and Animati., F. Anthracyclines: selected new developments. *Curr. Med. Chem. Anticancer Agents.* **2001***, 1*, 113-130.

(9) Hutchinson, C.R. Biosynthetic studies of daunorubicin and tetracenomycin C. *Chem. Rev*. **1997**, *97*, 2525-2536.

(10) Hutchinson, C.R., and Colombo, A.L. Genetic engineering of doxorubicin production in Streptomyces peucetius: a review. *J. Ind. Microbiol. Biotechnol*. **1999**, *23*, 647-652.

(11) Dickens, M.L., Priestley, N.D., and Strohl, W.R. In vivo and in vitro bioconversion of epsilon-rhodomycinone glycoside to doxorubicin: functions of DauP, DauK, and DoxA. *J. Bacteriol*. **1997**, *179*, 2641-2650.

(12) Connors, N.C., and Strohl, W.R. Partial purification and properties of carminomycin 4-*O*-methyltransferase from *Streptomyces sp. strain C5*. *J. Gen. Microbiol*. *1993*, **139**, 1353-1362.

(13) Dickens, M.L., Ye, J., and Strohl, W.R. Analysis of clustered genes encoding both early and late steps in daunomycin biosynthesis by *Streptomyces sp.* strain C5. *J. Bacteriol*. **1995**, *177*, 536-543.

(14) Madduri, K., Torti, F., Colombo, A.L., and Hutchinson, C.R. Cloning and sequencing of a gene encoding carminomycin 4-*O*-methyltransferase from *Streptomyces peucetius* and its expression in *Escherichia coli*. *J. Bacteriol*. **1993**, *175*, 3900-3904.

(15) Madduri, K., and Hutchinson, C.R. Functional characterization and transcriptional analysis of a gene cluster governing early and late steps in daunorubicin biosynthesis in *Streptomyces peucetius*. *J. Bacteriol*. **1995**, *177*, 3879-3884.

(16) Miyamoto, Y., Ohta, S., Johdo, O., Nagamatsu, Y., and Yoshimoto, A. Production of a new hybrid anthracycline 4-*O*-methylepelmycin by heterologous expression of dnrK in epelmycin-producing *Streptomyces violaceus*. *J. Antibiot. Tokyo*. **2000**, *53*, 828-836.

(17) Scotti, C., and Hutchinson, C.R. Immobilization and properties of carminomycin 4-*O*-methyltranferase, the enzyme which catalyzes the final step in the biosynthesis of daunorubicin in *Streptomyces peucetius*. *Biotechnol. Bioeng*. **1995**, *48*, 133-140.

(18) Jansson, A., Koskiniemi, H., Mäntsälä, P., Niemi, J., and Schneider, G. Crystal structure of a ternary complex of DnrK, a methyltransferase in daunorubicin biosynthesis, with bound products. *J. Biol. Chem*. **2004**, *279*, 41149-41156.

(19) Fewer, D.P., and Metsä-Ketelä, M. A pharmaceutical model for the molecular evolution of microbial natural products. *FEBS J.* **2020**, *287*, 1429-1449.

(20) Grocholski, T., Dinis, P., Niiranen, L., Niemi, J., and Metsä-Ketelä, M. Divergent evolution of an atypical *S*-adenosyl-L-methionine–dependent monooxygenase involved in anthracycline biosynthesis. *Proc. Natl. Acad. Sci. U.S.A*. **2015**, *112*, 9866-9871.

(21) Kim, N.Y., Kim, J.H., Lee, Y.H., Lee, E.J., Kim, J., Lim, Y., Chong, Y.H. and Ahn, J.H. *O*-Methylation of flavonoids using DnrK based on molecular docking. *J. Microbiol. Biotechnol.* **2007**, *17*, 1991-1995.

(22) Huber, T.D., Wang, F., Singh, S., Johnson, B.R., Zhang, J., Sunkara, M., Van Lanen, S.G., Morris, A.J., Phillips Jr, G.N. and Thorson, J.S. Functional AdoMet isosteres resistant to classical AdoMet degradation pathways. *ACS. Chem. Biol*. **2016**, *11*, 2484-2491.

(23) Zheng, J., Wei, W., Lan, X., Zhang, Y., and Wang, Z. Fluorescent microplate assay method for high-throughput detection of lipase transesterification activity. *Anal. Biochem*. **2018**, *549*, 26-28.

(24) Williams, G.J., and Thorson, J.S. A high-throughput fluorescence-based

glycosyltransferase screen and its application in directed evolution. *Nat. Protoc*. **2008**, *3*, 357-362.

(25) Jalali, E. and Thorson, J.S. Enzyme-mediated bioorthogonal technologies: catalysts, chemoselective reactions and recent methyltransferase applications. *Curr. Opin. Biotechnol*. **2021**, *69*, 290-298.

(26) Wang, R., Nguyen, J., Hecht, J., Schwartz, N., Brown, K.V., Ponomareva, L.V., Niemczura, M., van Dissel, D., van Wezel, G.P., Thorson, J.S., Metsä-Ketelä, M., Shaaban, K.A., and Nybo, S.E. A BioBricks metabolic engineering platform for the biosynthesis of anthracyclinones in *Streptomyces coelicolor*. *ACS Synth. Biol*. **2022**, *11*, 4193-4209.

(27) Malik, E.M., and Müller, C.E. Anthraquinones as pharmacological tools and drugs. *Med. Res. Rev.* **2016**, *36*, 705-748.

(28) Siddamurthi, S., Gutti, G., Jana, S., Kumar, A., and Singh, S.K. Anthraquinone: a promising scaffold for the discovery and development of therapeutic agents in cancer therapy. *Future Med. Chem*. **2020**, *12*, 1037-1069.

(29) Campora, M., Francesconi, V., Schenone, S., Tasso, B., and Tonelli, M. Journey on naphthoquinone and anthraquinone derivatives: New Insights in Alzheimer's disease. *Pharmaceuticals*. **2021**, *14*, 33.

(30) Singh, J., Hussain, Y., Luqman, S., and Meena, A. Purpurin: A natural anthraquinone with multifaceted pharmacological activities. *Phytother. Res*. **2020**, *35*, 2418-2428.

(31) Cheema, M.T., Ponomareva, L.V., Liu, T., Voss, S.R., Thorson, J.S., Shaaban, K.A., and Sajid, I. Taxonomic and metabolomics profiling of actinobacteria atrains from

Himalayan collection sites in Pakistan. *Curr. Microbiol*. **2021**, *78*, 3044-3057.

(32) Brodasky, T.F., and Reusser, F. Steffimycin B, a new member of the steffimycin family: isolation and characterization. *J. Antibiot. Tokyo*. **1974**, *27*, 809-813.

(33) Torkkell, S., Kunnari, T., Palmu, K., Hakala, J., Mäntsälä, P., and Ylihonko, K. Identification of a cyclase gene dictating the C-9 stereochemistry of anthracyclines from *Streptomyces nogalater*. Antimicrob. *Agents Chemother*. **2000**, *44*, 396-399.

(34) Siitonen, V., Nji Wandi, B., Törmänen, A.P., and Metsä-Ketelä, M. Enzymatic synthesis of the *C*-glycosidic moiety of nogalamycin R. *ACS. Chem. Biol*. **2018**, *13*, 2433-2437.

(35) Osterman, I.A., Wieland, M., Maviza, T.P., Lashkevich, K.A., Lukianov, D.A., Komarova, E.S., Zakalyukina, Y.V., Buschauer, R., Shiriaev, D.I., Leyn, S.A. and Zlamal, J.E. Tetracenomycin X inhibits translation by binding within the ribosomal exit tunnel. *Nat. Chem. Biol.* **2020**, *16*, 1071-1077.

(36) Egert, E., Noltemeyer, M., Siebers, J., Rohr, J., and Zeeck, A. The structure of tetracenomycin C. *J. Antibiot Tokyo*. **1992**, *45*, 1190-1192.

(37) Decker, H., Summers, R.G., and Hutchnson, C.R. Overproduction of the acyl carrier protein component of a type II polyketide synthase stimulates production of tetracenomycin biosynthetic intermediates in *Streptomyces glaucescens*. *J. Antibiot Tokyo*. **1994**, *47*, 54-63.

(38) Nguyen, J.T., Riebschleger, K.K., Brown, K.V., Gorgijevska, N.M., and Nybo, S.E. A BioBricks toolbox for metabolic engineering of the tetracenomycin pathway. *Biotechnol. J.* **2022**, *17*, e2100371.

(39) Kharel, M.K., Pahari, P., Shepherd, M.D., Tibrewal, N., Nybo, S.E., Shaaban, K.A.,

and Rohr, J. Angucyclines: Biosynthesis, mode-of-action, new natural products, and synthesis. *Nat. Prod. Rep.* **2012***, 29*, 264-325.

(40) Liu, W.C., Parker, L., Slusarchyk, S., Greenwood, G.L., Graham, S.F., and Meyers, E. Isolation, characterization, and structure of rabelomycin, a new antibiotic. *J. Antibiot Tokyo*. **1970**, *23*, 437-441.

(41) Abdelfattah, M., Maskey, R.P., Asolkar, R.N., Gruen-Wollny, I., and Laatsch, H. Seitomycin: isolation, structure elucidation and biological activity of a new angucycline antibiotic from a terrestrial *Streptomycete*. *J. Antibiot Tokyo*. **2003**, *56*, 539-542.

(42) Shaaban, K.A., Srinivasan, S., Kumar, R., Damodaran, C., and Rohr, J. Landomycins P−W, cytotoxic angucyclines from *Streptomyces cyanogenus* S-136. *J. Nat. Prod*. **2011**, *74*, 2-11.

(43) Zhang, Y., Cheema, M.T., Ponomareva, L.V., Ye, Q., Liu, T., Sajid, I., Rohr, J., She, Q.B., Voss, S.R., Thorson, J.S. and Shaaban, K.A. Himalaquinones A–G, angucyclinone-derived metabolites produced by the Himalayan isolate *Streptomyces sp.* PU-MM59. *J. Nat. Prod*. **2021**, *84*, 1930-1940.

(44) Yang, C., Huang, C., Zhang, W., Zhu, Y. and Zhang, C. Heterologous expression of fluostatin gene cluster leads to a bioactive heterodimer. *Org. Lett.* **2015**, *17*, 5324-5327.

(45) Yan, X. Anthraquinone-fused enediynes: discovery, biosynthesis and development. *Nat. Prod. Rep*. **2022**, *39*, 703-728.

(46) Galm, U., Hager, M.H., Van Lanen, S.G., Ju, J., Thorson, J.S., and Shen, B. Antitumor antibiotics: bleomycin, enediynes, and mitomycin. *Chem. Rev.* **2005**,

105, 739-758.

(47) Yan, X., Chen, J.J., Adhikari, A., Teijaro, C.N., Ge, H., Crnovcic, I., Chang, C.Y., Annaval, T., Yang, D., Rader, C. and Shen, B. Comparative studies of the biosynthetic gene clusters for anthraquinone-fused enediynes shedding light into the tailoring steps of tiancimycin biosynthesis. *Org. Lett*. **2018**, *20*, 5918-5921.

(48) Zhuang, Z., Jiang, C., Zhang, F., Huang, R., Yi, L., Huang, Y., Yan, X., Duan, Y. and Zhu, X. Streptomycin-induced ribosome engineering complemented with fermentation optimization for enhanced production of 10-membered enediynes tiancimycin-A and tiancimycin-D. *Biotechnol. Bioeng*. **2019**, *116*, 1304-1314.

(49) Adhikari, A., Teijaro, C.N., Yan, X., Chang, C.Y., Gui, C., Liu, Y.C., Crnovcic, I., Yang, D., Annaval, T., Rader, C. and Shen, B. Characterization of TnmH as an *O*-methyltransferase revealing insights into tiancimycin biosynthesis and enabling a biocatalytic strategy to prepare antibody–tiancimycin conjugates. *J. Med. Chem.* **2020**, *63*, 8432-8441.

(50) Iwai, Y., Kora, A., Takahashi, Y., Hayashi, T., Awaya, J., Masuma, R., Oiwa, R. and Omura, S. Production of deoxyfrenolicin and a new antibiotic, frenolicin B by Streptomyces roseofulvus strain AM-3867. *J. Antibiot Tokyo*. **1978**, *31*, 959-965.

(51) Ye, Q., Zhang, Y., Cao, Y., Wang, X., Guo, Y., Chen, J., Horn, J., Ponomareva, L.V., Chaiswing, L., Shaaban, K.A., Wei, Q., Anderson, B.D., St Clair, D.K., Zhu, H., Leggas, M., Thorson, J.S., and She, Q.B. Frenolicin B targets peroxiredoxin 1 and glutaredoxin 3 to trigger ROS/4E-BP1-mediated antitumor effects. *Cell. Chem. Biol.* **2019**, *26*, 366-377.

(52) Wang, X., Shaaban, K.A., Elshahawi, S.I., Ponomareva, L.V., Sunkara, M., Zhang,

Y., Copley, G.C., Hower, J.C., Morris, A.J., Kharel, M.K. and Thorson, J.S. Frenolicins C–G, pyranonaphthoquinones from *Streptomyces sp*. RM-4-15. *J. Nat. Prod*. **2013**, *76*, 1441-1447.

(53) Mutha, R.E., Tatiya, A.U., and Surana, S.J. Flavonoids as natural phenolic compounds and their role in therapeutics: An overview. *J. Pharm. Sci.* **2021**, *7*, 1-13.

(54) Alzaabi, M.M., Hamdy, R., Ashmawy, N.S., Hamoda, A.M., Alkhayat, F., Khademi, N.N., Al Joud, S.M. A., El-Keblawy, A.A., and Soliman, S.S. M. Flavonoids are promising safe therapy against COVID-19. *Phytochem. Rev.* **2021**, *21*, 291-312.

(55) Xu, J., Kjer, J., Sendker, J., Wray, V., Guan, H., Edrada, R., Lin, W., Wu, J. and Proksch, P. Chromones from the endophytic fungus Pestalotiopsis sp. isolated from the Chinese mangrove plant Rhizophora mucronata. *J. Nat. Prod*. **2009**, *72*, 662-665.

(56) Srivastava, R., Tripathi, S., Unni, S., Hussain, A., Haque, S., Dasgupta, N., Singh, V. and Mishra, B.N. Silybin B and cianidanol inhibit Mpro and spike protein of SARS-CoV-2: Evidence from in silico molecular docking studies. *Curr. Pharm. Des*. **2021**, *27*, 3476-3489.

(57) Xiang, M., Su, H., Hu, J. and Yan, Y. Isolation, identification and determination of methyl caffeate, ethyl caffeate and other phenolic compounds from *Polygonum amplexicaule var. sinense*. *J. Med. Plants Res*. **2011***, 5*, 1685-1691.

(58) Stefanachi, A., Leonetti, F., Pisani, L., Catto, M. and Carotti, A. Coumarin: A natural, privileged and versatile scaffold for bioactive compounds. *Molecules.* **2018**, *23*, 250.

(59) Carneiro, A., Matos, M.J., Uriarte, E., and Santana, L. Trending topics on coumarin and its derivatives in 2020. *Molecules*. **2021**, *26*, 501.

(60) Sun, X.Y., Liu, T., Sun, J., and Wang, X.J. Synthesis and application of coumarin fluorescence probes. *RSC Adv.* **2020**, *10*, 10826-10847.

(61) Williams, G.J., Zhang, C., and Thorson, J.S. Expanding the promiscuity of a natural-product glycosyltransferase by directed evolution. *Nat. Chem. Biol*. **2007**, *3*, 657-662.

(62) Noor, A.O., Almasri, D.M., Bagalagel, A.A., Abdallah, H.M., Mohamed, S.G.A., Mohamed, G.A., and Ibrahim, S.R.M. Naturally occurring isocoumarins derivatives from endophytic fungi: Sources, isolation, structural characterization, biosynthesis, and biological activities. *Molecules.* **2020**, *25*, 395.

(63) Kishimoto, S., Hara, K., Hashimoto, H., Hirayama, Y., Champagne, P.A., Houk, K.N., Tang, Y. and Watanabe, K. Enzymatic one-step ring contraction for quinolone biosynthesis. *Nat. Commun*. **2018**, *9*, 2826.

(64) Aly, A.A., El-Sheref, E.M., Mourad, A.E., Bakheet, M.E. M., and Bräse, S. 4-Hydroxy-2-quinolones: syntheses, reactions and fused heterocycles. *Mol. Divers.* **2020**, *24*, 477-524.

(65) Khandelwal, A., Crowley, V.M. and Blagg, B.S.J. Natural product inspired N-terminal Hsp90 inhibitors: from bench to bedside? *Med. Res. Rev*. **2016**, *36*, 92-118.

(66) Wang, J., Soisson, S.M., Young, K., Shoop, W., Kodali, S., Galgoci, A., Painter, R., Parthasarathy, G., Tang, Y.S., Cummings, R., Ha, S., Dorso, K., Motyl, M., Jayasuriya, H., Ondeyka, J., Herath, K., Zhang, C., Hernandez, L., Allocco, J., Basilio, A., Tormo, J.R., Genilloud, O., Vicente, F., Pelaez, F., Colwell, L., Lee,

S.H., Michael, B., Felcetto, T., Gill, C., Silver, L.L., Hermes, J.D., Bartizal, K., Barrett, J., Schmatz, D., Becker, J.W., Cully, D, Singh, S.B. Platensimycin is a selective FabF inhibitor with potent antibiotic properties. *Nature*. **2006**, *441*, 358-361.

(67) Smanski, M.J., Peterson, R.M., Rajski, S.R. and Shen, B. Engineered Streptomyces platensis strains that overproduce antibiotics platensimycin and platencin. *Antimicrob. Agents Chemother*. **2009**, *53*, 1299-1304.

(68) Rudolf, J.D., Dong, L.B. and Shen, B. Platensimycin and platencin: Inspirations for chemistry, biology, enzymology, and medicine. *Biochem. Pharmacol*. **2017**, *133*, 139-151.

(69) Shaaban, K.A., Shepherd, M.D., Ahmed, T.A., Nybo, S.E., Leggas, M. and Rohr, J. Pyramidamycins AD and 3-hydroxyquinoline-2-carboxamide; cytotoxic benzamides from *Streptomyces sp.* DGC1. *J. Antibiot. Tokyo*. **2012**, *65*, 615-622.

(70) Huseman, E.D., Byl, J.A.W., Chapp, S.M., Schley, N.D., Osheroff, N. and Townsend, S.D. Synthesis and cytotoxic evaluation of arimetamycin A and its daunorubicin and doxorubicin hybrids. *ACS Cent. Sci*. **2021**, *7*, 1327-1337.

(71) Dall'Acqua, F., Vedaldi, D. and Gennaro, A. Studies on the interaction between steffimycins and DNA. *Chem. Biol. Interact.* **1979**, *25*, 59-70.

(72) Al Haj Baddar, N.W., Chithrala, A. and Voss, S.R. Amputation-induced reactive oxygen species signaling is required for axolotl tail regeneration. *Dev. Dyn*. **2019**, *248*, 189-196.

(73) Ponomareva, L.V., Athippozhy, A., Thorson, J.S. and Voss, S.R. Using Ambystoma mexicanum (Mexican axolotl) embryos, chemical genetics, and microarray analysis

to identify signaling pathways associated with tissue regeneration. *Comparative Biochemistry and Physiology Part C: Toxicol. Pharmacol.* **2015**, *178*, 128-135.

(74) Dinis, P., Tirkkonen, H., Wandi, B.N., Siitonen, V., Niemi, J., Grocholski, T. and Metsä-Ketelä, M. Evolution-inspired engineering of anthracycline methyltransferases. *PNAS Nexus*. **2023**, *2*, pgad009.

(75) Grocholski, T., Yamada, K., Sinkkonen, J., Tirkkonen, H., Niemi, J. and Metsä-Ketelä, M. Evolutionary trajectories for the functional diversification of anthracycline methyltransferases. *ACS Chem. Biol*. **2019**, *14*, 850-856.

(76) Yan, X., Ge, H., Huang, T., Hindra, Yang, D., Teng, Q., Crnovčić, I., Li, X., Rudolf, J.D., Lohman, J.R. Zhu, X., Huang, Y., Zhao, L.X., Jiang, Y., Van Nieuwerburgh, F., Rader, C., Duan, Y., Shen, B. Strain prioritization and genome mining for enediyne natural products. *mBio*. **2016***, 7*, e02104-021016.

(77) Singh, S., Zhang, J., Huber, T.D., Sunkara, M., Hurley, K., Goff, R.D., Wang, G., Zhang, W., Liu, C., Rohr, J. Van Lanen, S.G. Morris, A.J., and Thorson, J.S. Facile chemoenzymatic strategies for the synthesis and utilization of *S*-adenosyl-(L)-methionine analogues. *Angew. Chem., Int. Ed.* **2014**, *53*, 3965-3969.

(78) Kabsch, W. XDS. *Acta Crystallogr. D Biol. Crystallogr*. **2010**, *66*, 125-132.

(79) Emsley, P., Lohkamp, B., Scott, W.G. and Cowtan, K. Features and development of Coot. *Acta Crystallogr. D Biol. Crystallogr.* **2010**, *66*, 486-501.

(80) Liebschner, D., Afonine, P.V., Baker, M.L., Bunkóczi, G., Chen, V.B., Croll, T.I., Hintze, B., Hung, L. W., Jain, S., McCoy, A.J. Moriarty, N.W., Oeffner, R.D., Poon, B.K., Prisant, M.G., Read, R.J., Richardson, J.S., Richardson, D.C., Sammito, M.D., Sobolev, O.V., Stockwell, D.H., Terwilliger, T.C., Urzhumtsev, A.G., Videau, L.L.,

Williams, C.J., Adams, P.D. Macromolecular structure determination using X-rays, neutrons and electrons: recent developments in Phenix. *Acta Crystallogr. D Biol. Crystallogr*. **2019**, *75*, 861-877.

(81) Yennamalli, R., Arangarasan, R., Bryden, A., Gleicher, M. and Phillips Jr, G.N. Using a commodity high-definition television for collaborative structural biology. *J. Appl. Crystallogr.* **2014***, 47*, 1153-1157.

(82) Morin, A., Eisenbraun, B., Key, J., Sanschagrin, P.C., Timony, M.A., Ottaviano, M. and Sliz, P. Collaboration gets the most out of software. *Elife*. **2013***, 2*, e01456.

(83) Evans, R., O'Neill, M., Pritzel, A., Antropova, N., Senior, A., Green, T., Žídek, A., Bates, R., Blackwell, S., Yim, J., Ronneberger, O., Bodenstein, S., Zielinski, M., Bridgland, A., Potapenko, A., Cowie, A., Tunyasuvunakool, K., Jain, R., Clancy, E., Kohli, P., Jumper, J., and Hassabis, D. Protein complex prediction with AlphaFold-Multimer. *BioRxiv.* **2021**, 2021-2110.

(84) Jumper, J., Evans, R., Pritzel, A., Green, T., Figurnov, M., Ronneberger, O., Tunyasuvunakool, K., Bates, R., Žídek, A., Potapenko, A. Bridgland, A., Meyer, C., Kohl, S.A.A., Ballard, A.J., Cowie, A., Romera-Paredes, B., Nikolov, S., Jain, R., Adler, J., Back, T., Petersen, S., Reiman, D., Clancy, E., Zielinski, M., Steinegger, M., Pacholska, M., Berghammer, T., Bodenstein, S., Silver, D., Vinyals, O., Senior, A.W., Kavukcuoglu, K., Kohli, P., and Hassabis, D. Highly accurate protein structure prediction with AlphaFold. *Nature*. **2021**, *596*, 583-589.

(85) Mirdita, M., Steinegger, M., and Söding, J. MMseqs2 desktop and local web server app for fast, interactive sequence searches. *Bioinformatics*. **2019**, *35*, 2856-2858.

(86) Mirdita, M., Schütze, K., Moriwaki, Y., Heo, L., Ovchinnikov, S., and Steinegger,

M. ColabFold: making protein folding accessible to all. *Nat. Methods*. **2022**, *19*, 679-682.

(87) Eastman, P., Swails, J., Chodera, J.D., McGibbon, R.T., Zhao, Y., Beauchamp, K.A., Wang, L.P., Simmonett, A.C., Harrigan, M.P., Stern, C.D., Wiewiora, R.P., Brooks, B.R., and Pande, V.S. OpenMM 7: Rapid development of high-performance algorithms for molecular dynamics. *PLoS Comput. Biol*. **2017**, *13*, e1005659.

(88) Laskowski, R.A. and Swindells, M.B. LigPlot+: multiple ligand-protein interaction diagrams for drug discovery. *J Chem Inf Model*. **2011**, *51*, 2778-2786.

(89) Robert, X. and Gouet, P. Deciphering Key Features in Protein Structures with the New ENDscript Server. *Nucleic Acids Res*. **2014**, *42*, W320-W324.

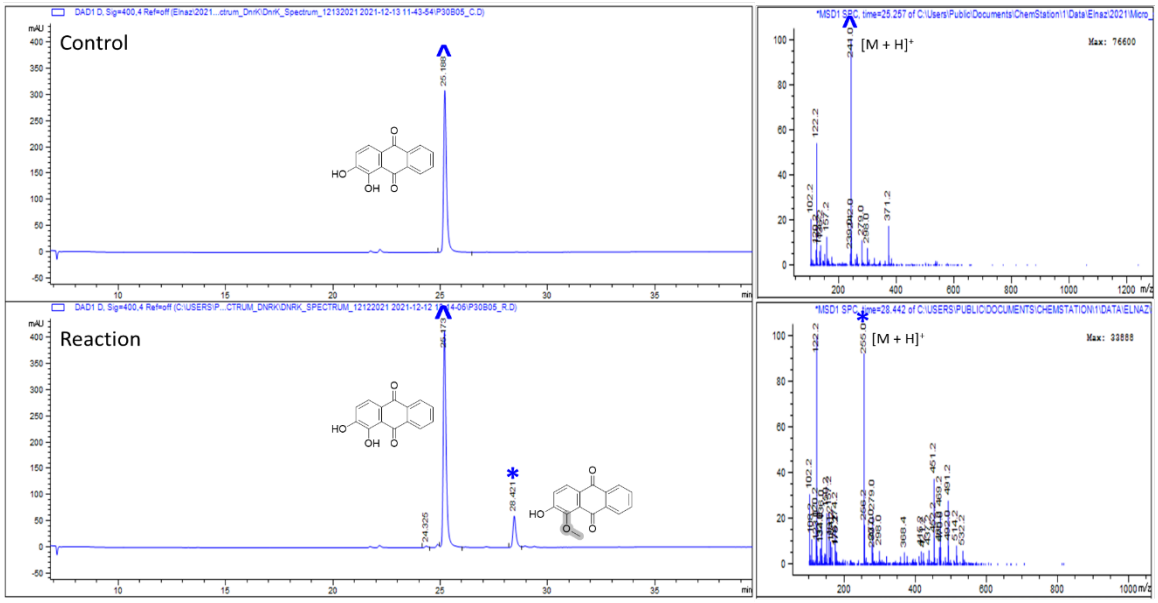

Figure S2.14. LC-MS analysis of alizarin (**2**)^ and the corresponding DnrK-catalyzed reaction product*. Predicted DnrK regioselectivity is highlighted in grey.

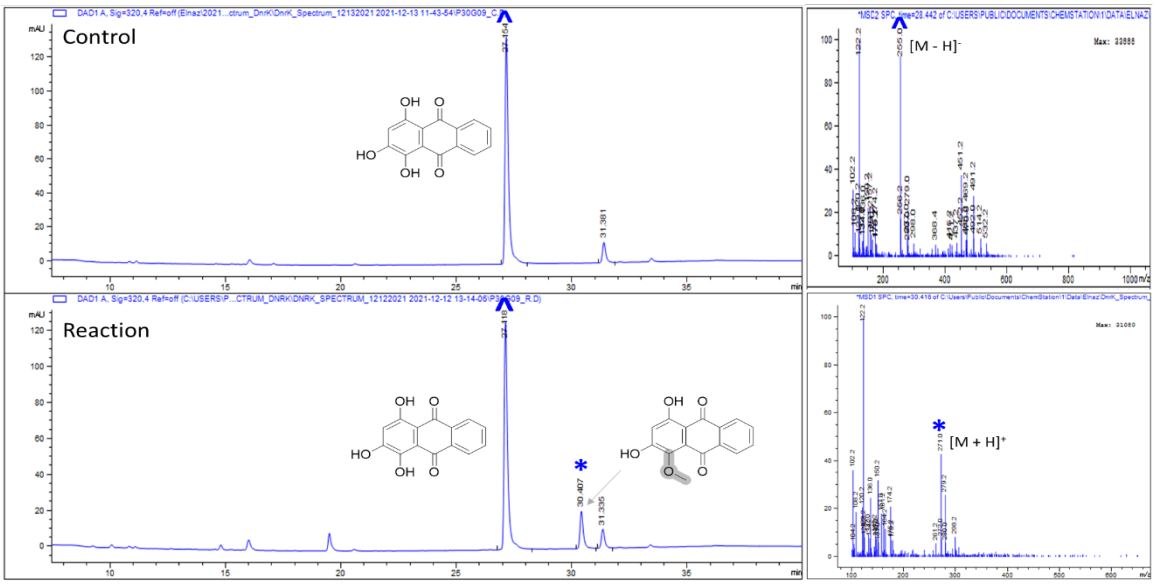

Figure S2.15. LC-MS analysis of purpurin (**3**)^ and the corresponding DnrK-catalyzed reaction product*. Predicted DnrK regioselectivity is highlighted in grey.

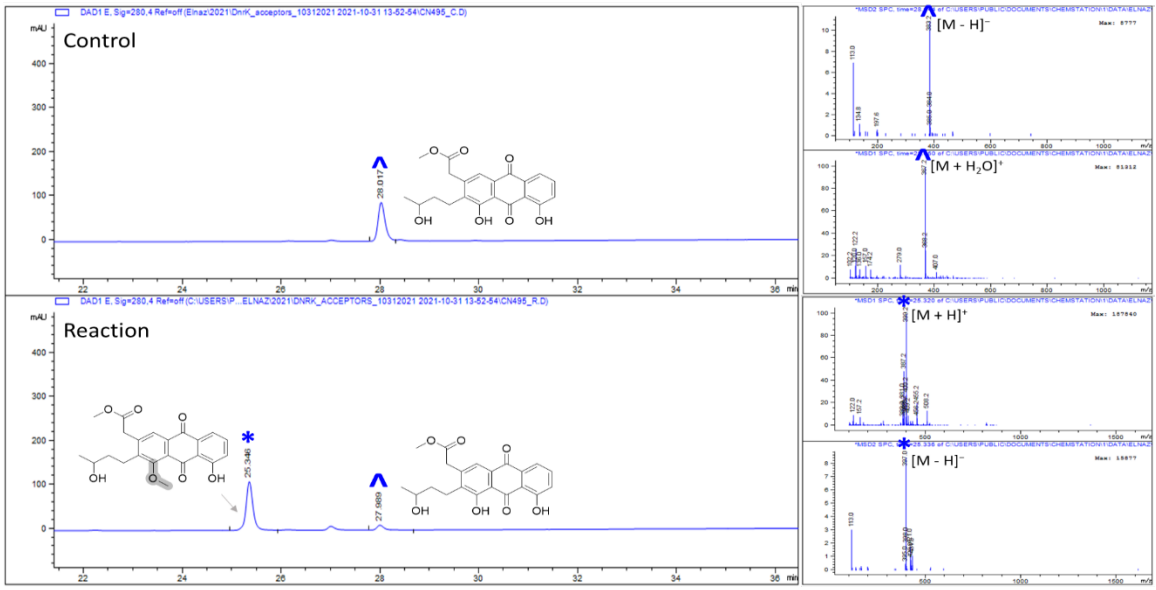

Figure S2.16. LC-MS analysis of 9,10-seco-7-deoxy-nogalamycinone (**4**)^ and the corresponding DnrK-catalyzed reaction product*. Predicted DnrK regioselectivity is highlighted in grey.

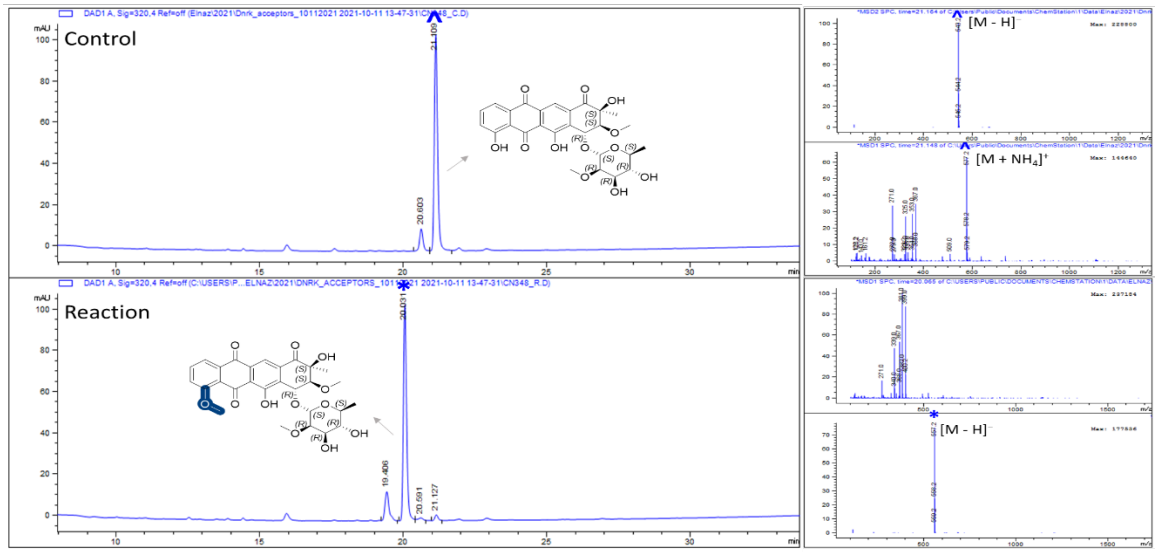

Figure S2.17. LC-MS analysis of aranciamycin (**7**)^ and the corresponding DnrK-catalyzed reaction product 4-*O*-methoxyaranciamycin (**7a**)*. Determined DnrK regioselectivity is highlighted in blue.

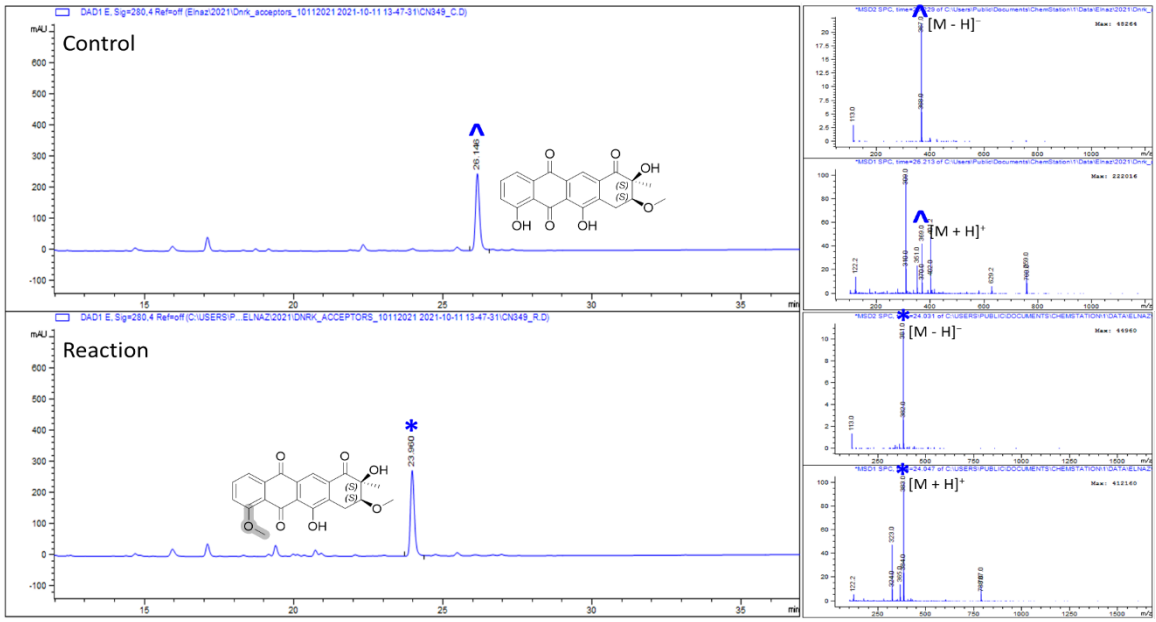

Figure S2.18. LC-MS analysis of SM 173B (**8**)^ and the corresponding DnrK-catalyzed reaction product*. Predicted DnrK regioselectivity is highlighted in grey.

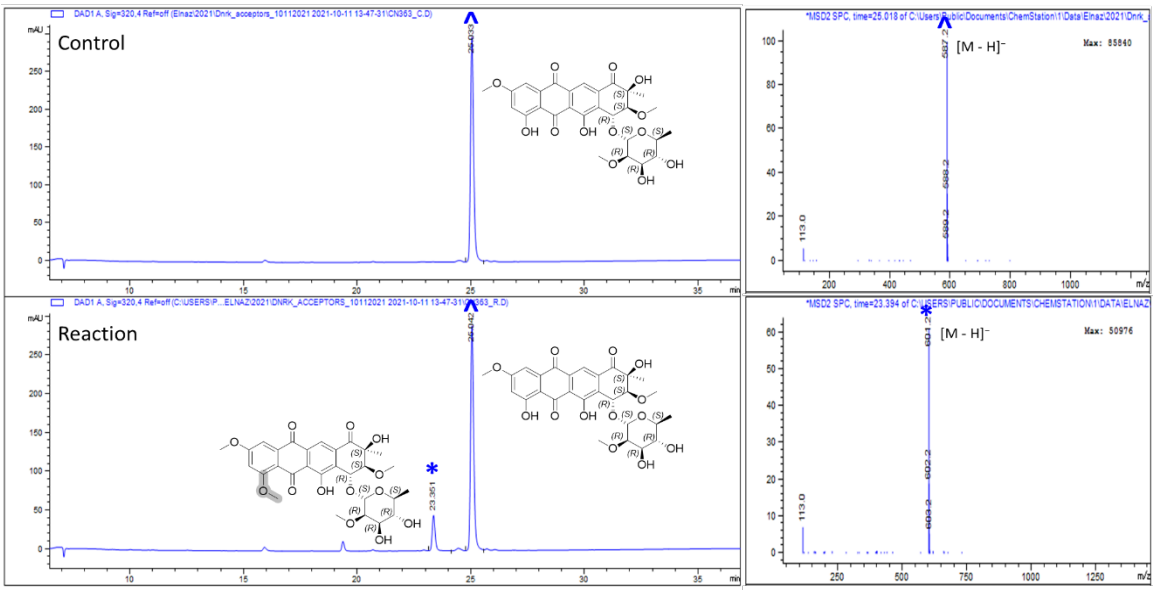

Figure S2.19. LC-MS analysis of steffimycin B (**9**)^ and the corresponding DnrK-catalyzed reaction product*. Predicted DnrK regioselectivity is highlighted in grey.

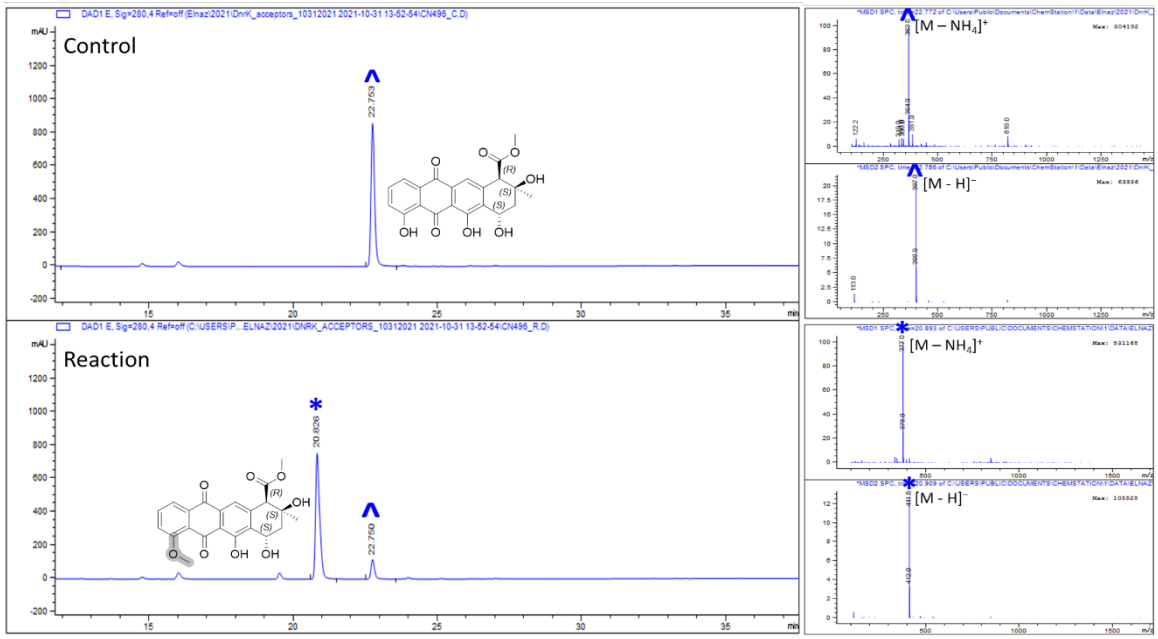

Figure S2.20. LC-MS analysis of nogalavinone (**10**)^ and the corresponding DnrK-catalyzed reaction product*. Predicted DnrK regioselectivity is highlighted in grey.

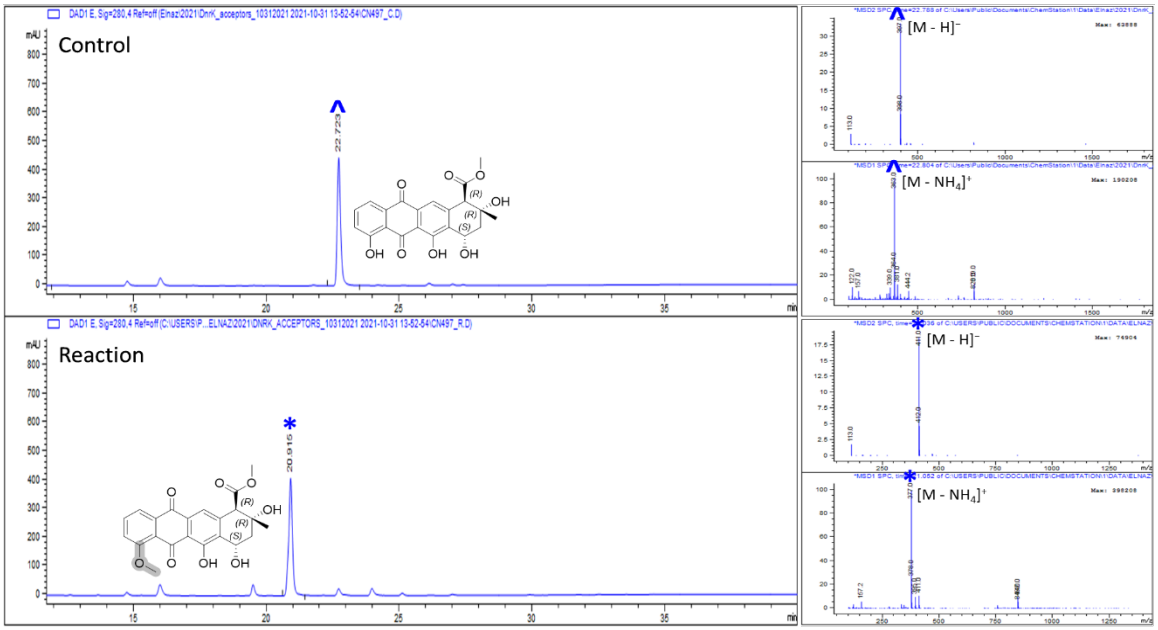

Figure S2.21. LC-MS analysis of auramycinone (**11**)^ and the corresponding DnrK-catalyzed reaction product*. Predicted DnrK regioselectivity is highlighted in grey.

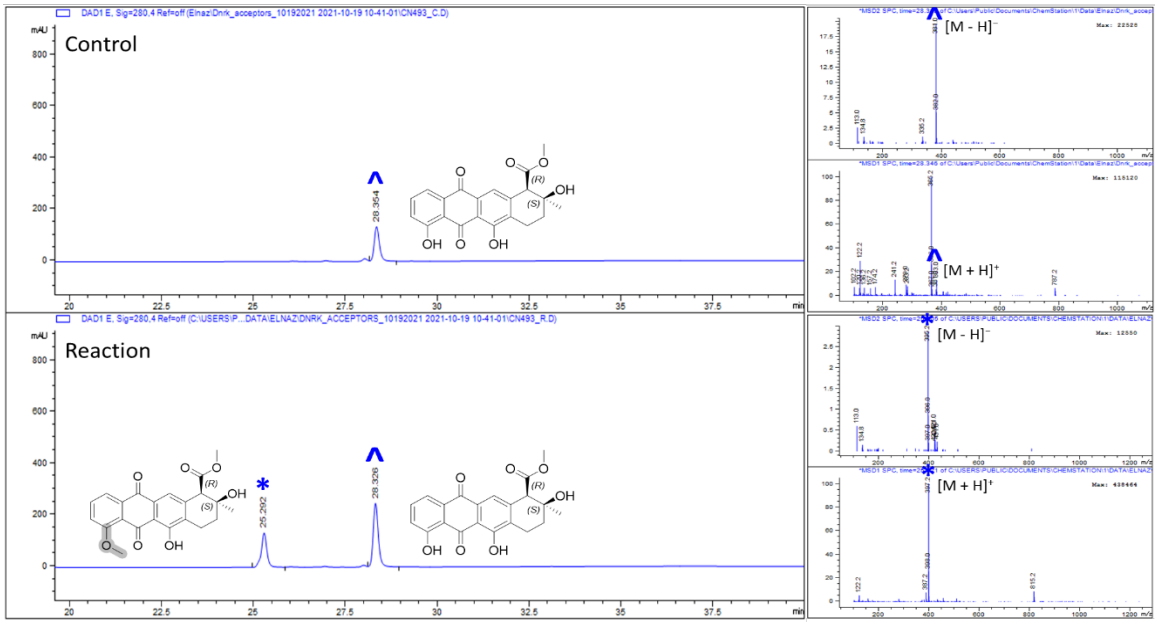

Figure S2.22. LC-MS analysis of 7-deoxy-nogalamycinone (**12**)^ and the corresponding DnrK-catalyzed reaction product*. Predicted DnrK regioselectivity is highlighted in grey.

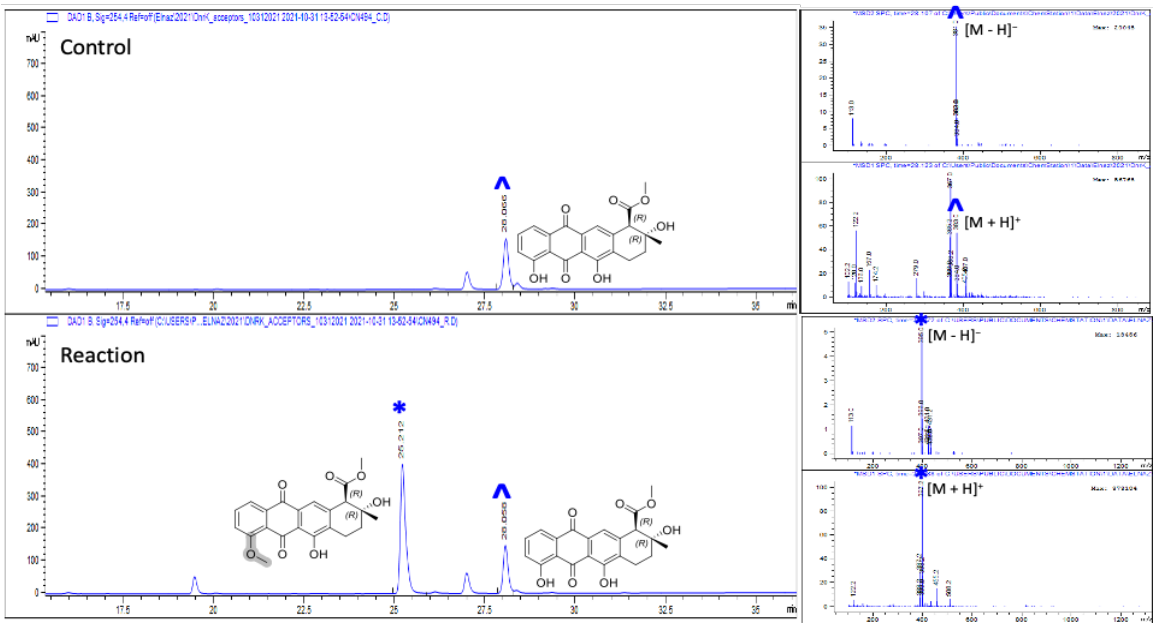

Figure S2.23. LC-MS analysis of deoxyauramycinone (**13**)^ and the corresponding DnrK-catalyzed reaction product*. Predicted DnrK regioselectivity is highlighted in grey.

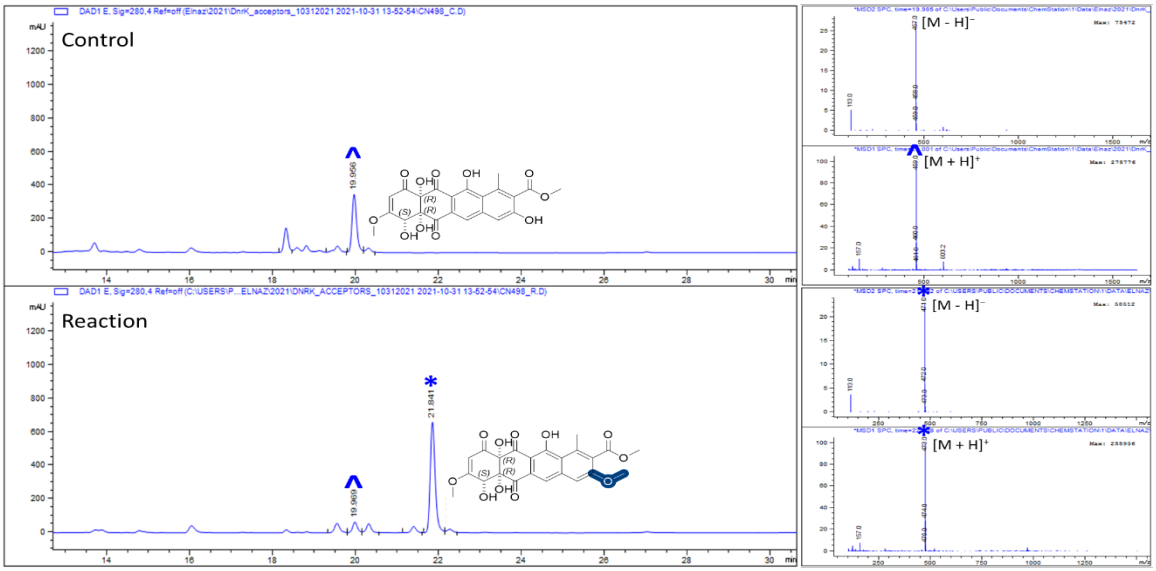

Figure S2.24. LC-MS analysis of 8-demethyltetracenomycin C (**17**)^ and the corresponding DnrK-catalyzed reaction product*. Determined DnrK regioselectivity is highlighted in blue.

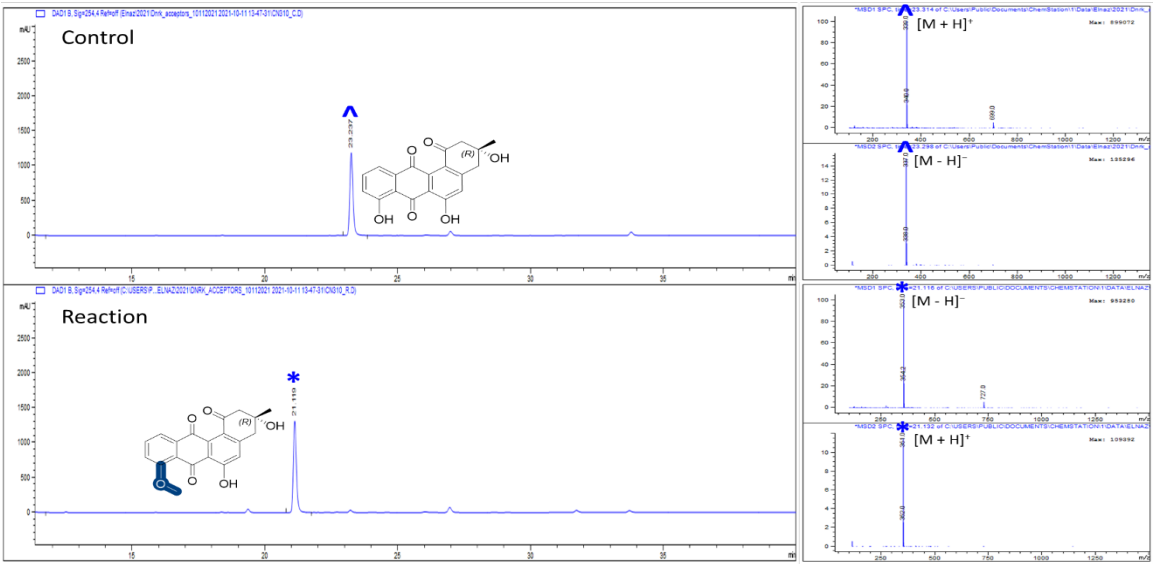

Figure S2.25. LC-MS analysis of rabelomycin (**23**)^ and the corresponding DnrK-catalyzed reaction product*. Determined DnrK regioselectivity is highlighted in blue.

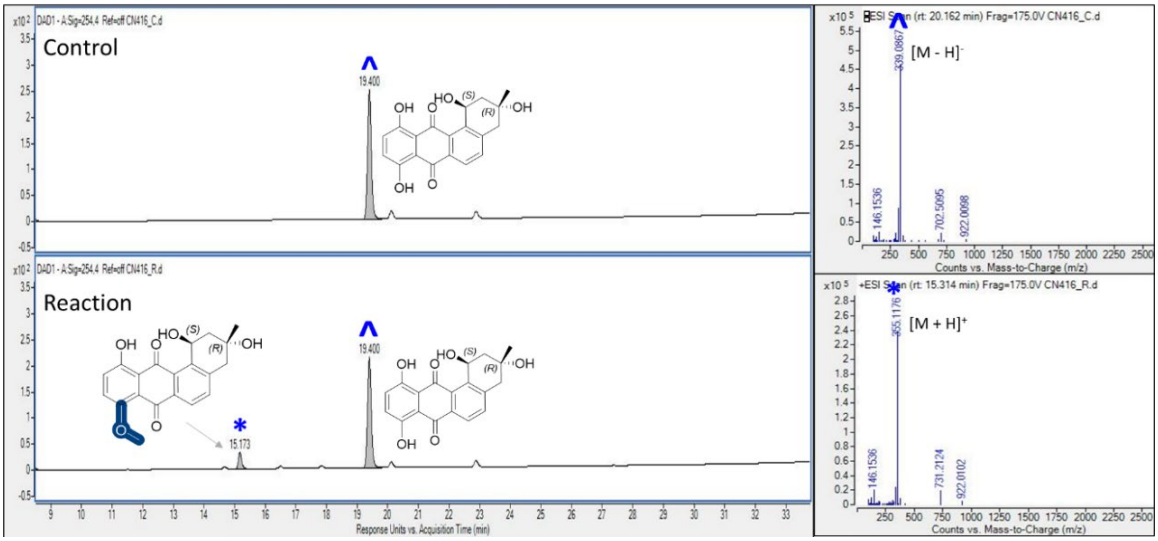

Figure S2.26. LC-MS analysis of 8-O-desmethylseitomycin (**25**)^ and the corresponding DnrK-catalyzed reaction product*. Determined DnrK regioselectivity is highlighted in blue.

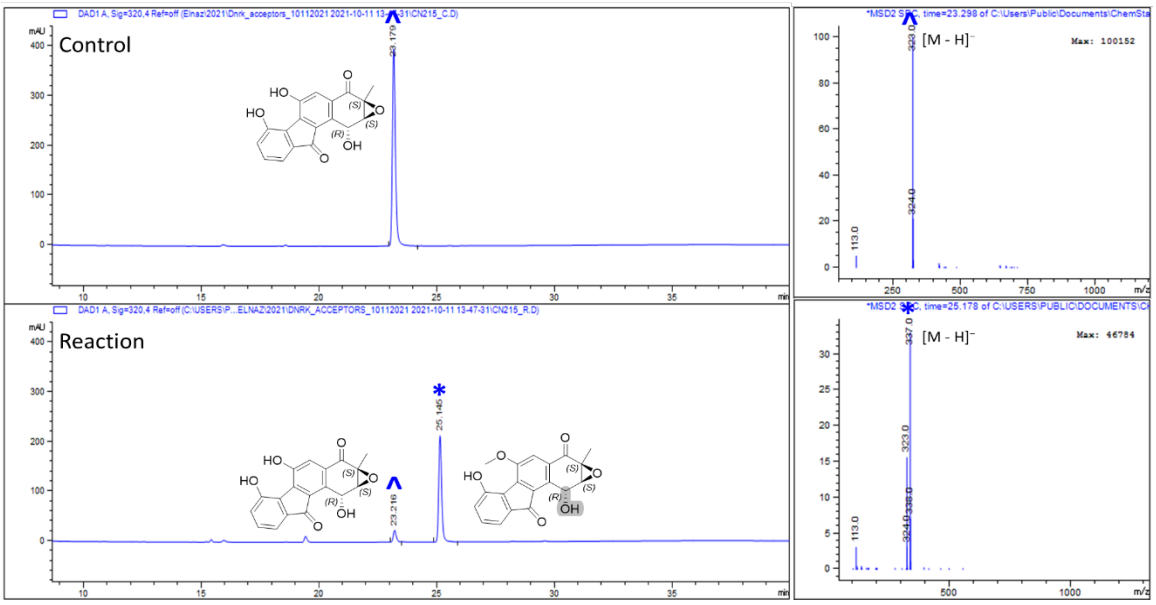

Figure S2.27. LC-MS analysis of fluostatin C (**30**)^ and the corresponding DnrK-catalyzed reaction product*. Predicted DnrK regioselectivity is highlighted in grey.

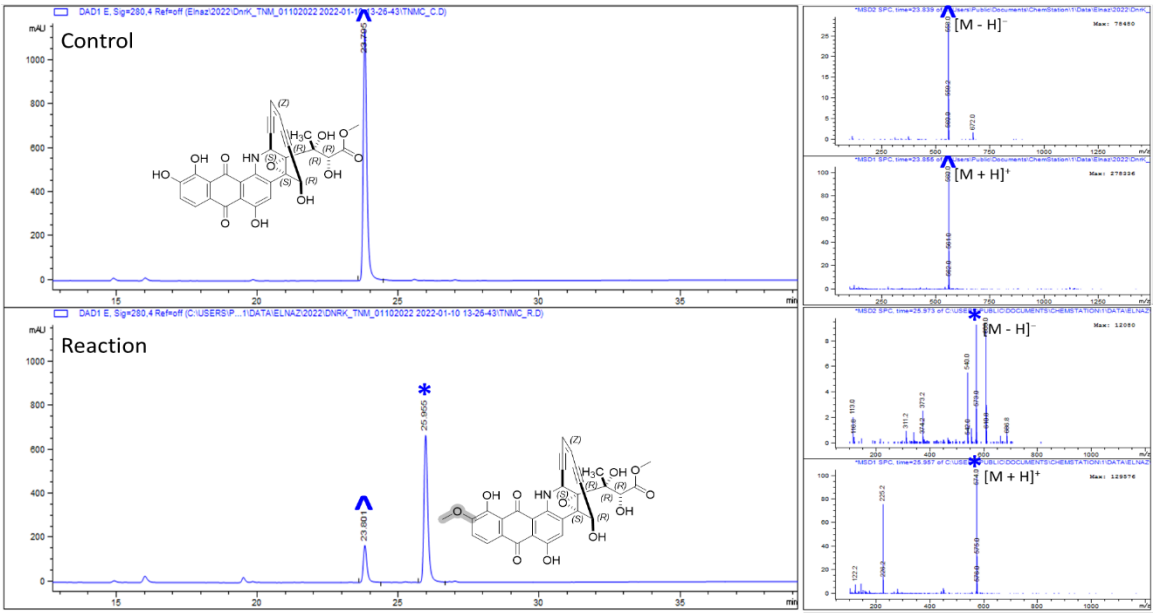

Figure S2.28. LC-MS analysis of tiancimycin C (**31**)^ and the corresponding DnrK-catalyzed reaction product*. Predicted DnrK regioselectivity is highlighted in grey.

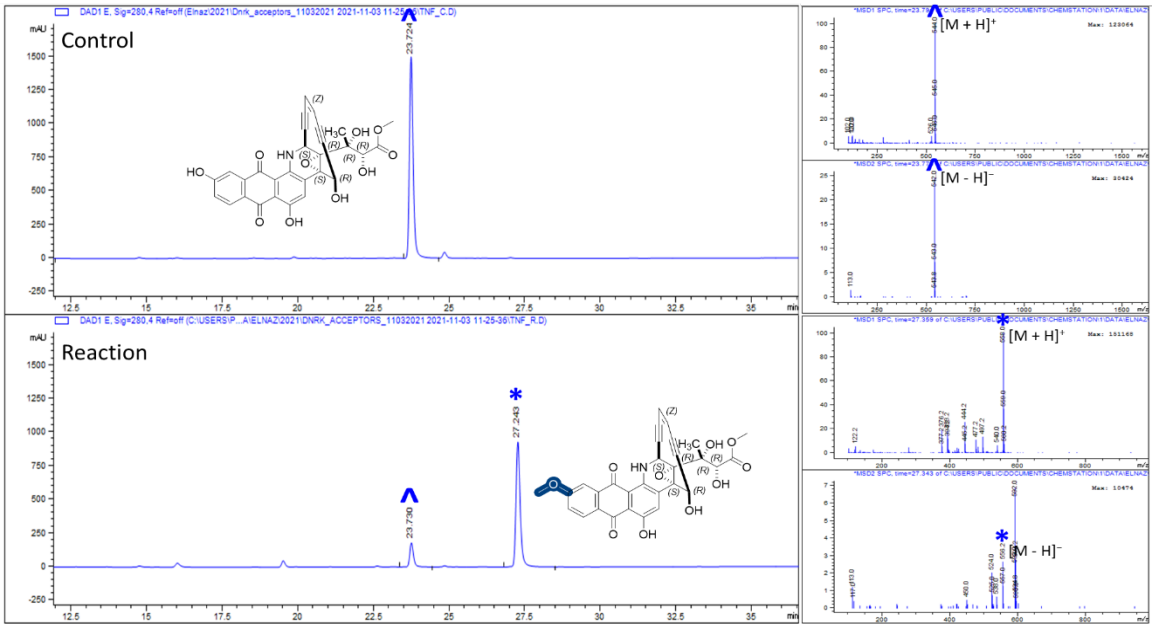

Figure S2.29. LC-MS analysis of tiancimycin F (**32**)^ and the corresponding DnrK-catalyzed reaction product*. Determined DnrK regioselectivity is highlighted in blue.

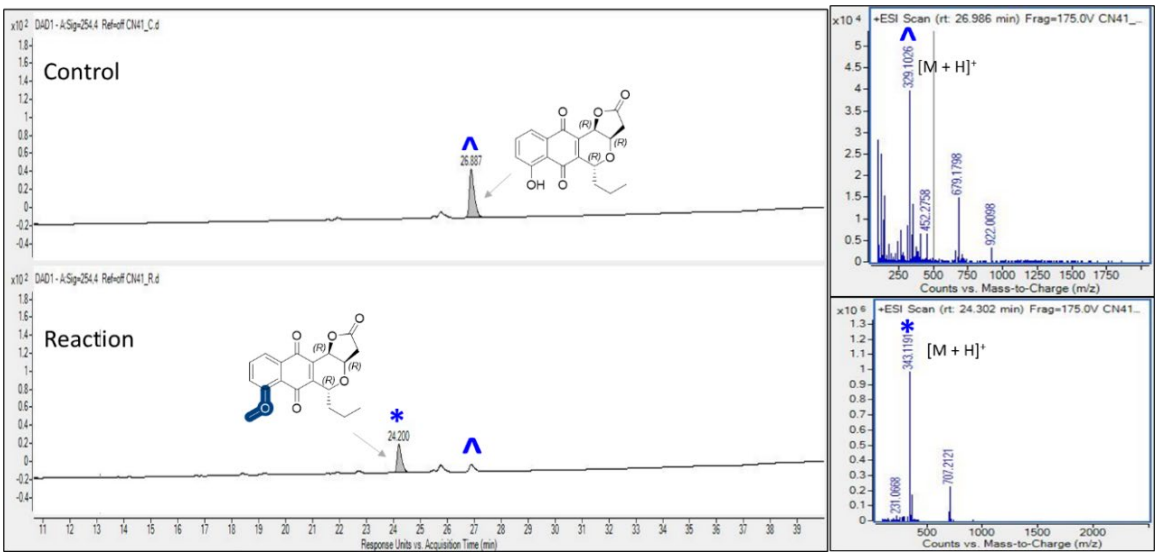

Figure S2.30. LC-MS analysis of frenolicin B (**35**)^ and the corresponding DnrK-catalyzed reaction product*. Determined DnrK regioselectivity is highlighted in blue.

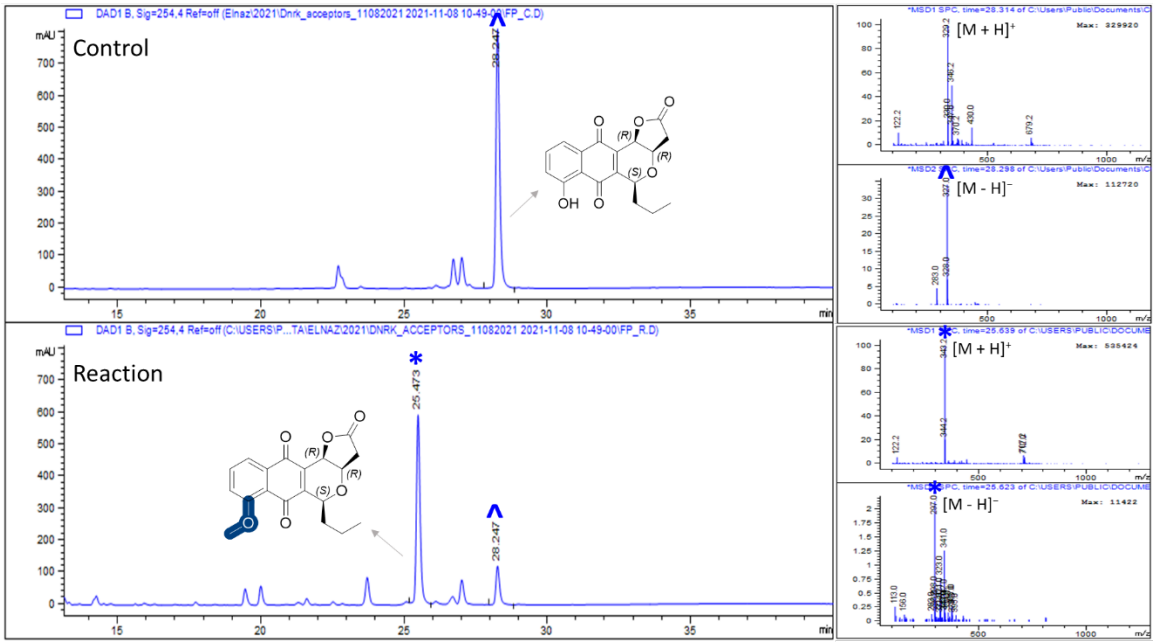

Figure S2.31. LC-MS analysis of 5-epi-frenolicin B (**36**)^ and the corresponding DnrK-catalyzed reaction product*. Determined DnrK regioselectivity is highlighted in blue.

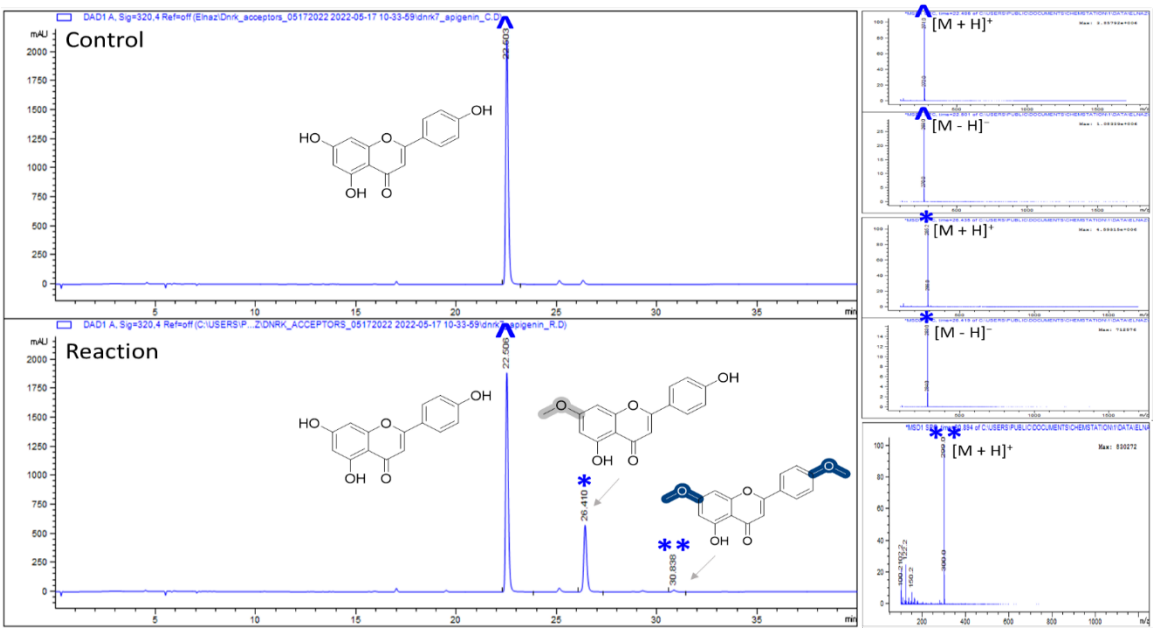

Figure S2.32. LC-MS analysis of apigenin (**43**)^ and the corresponding DnrK-catalyzed mono* and di** reaction products. Determined DnrK regioselectivity is highlighted in blue and predicted DnrK regioselectivity is highlighted in grey.

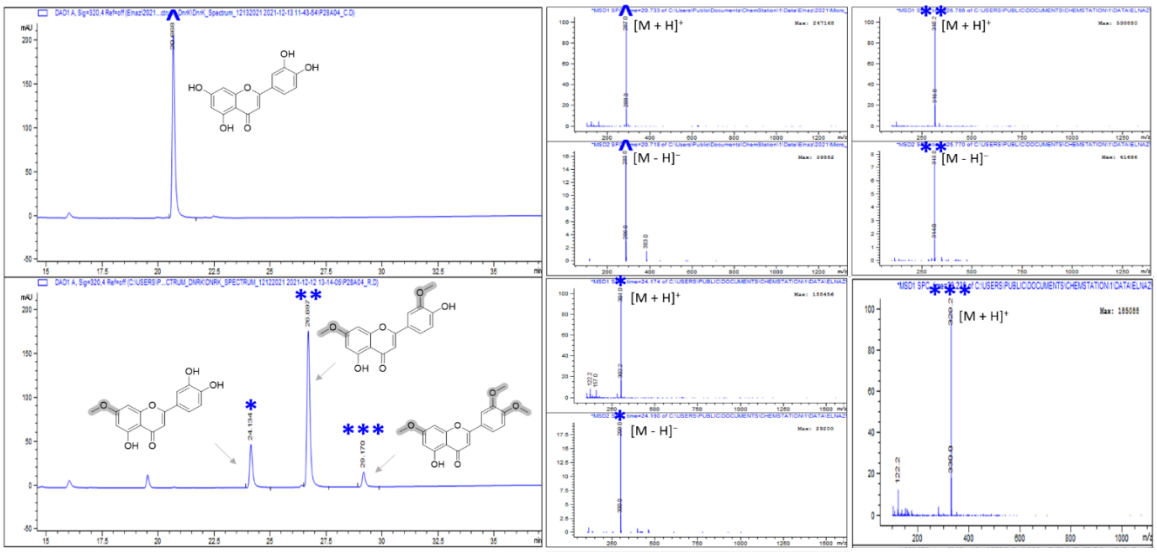

Figure S2.33. LC-MS analysis of luteolin (**44**)^ and the corresponding DnrK-catalyzed mono*, di** and tri*** products. Predicted DnrK regioselectivity is highlighted in grey.

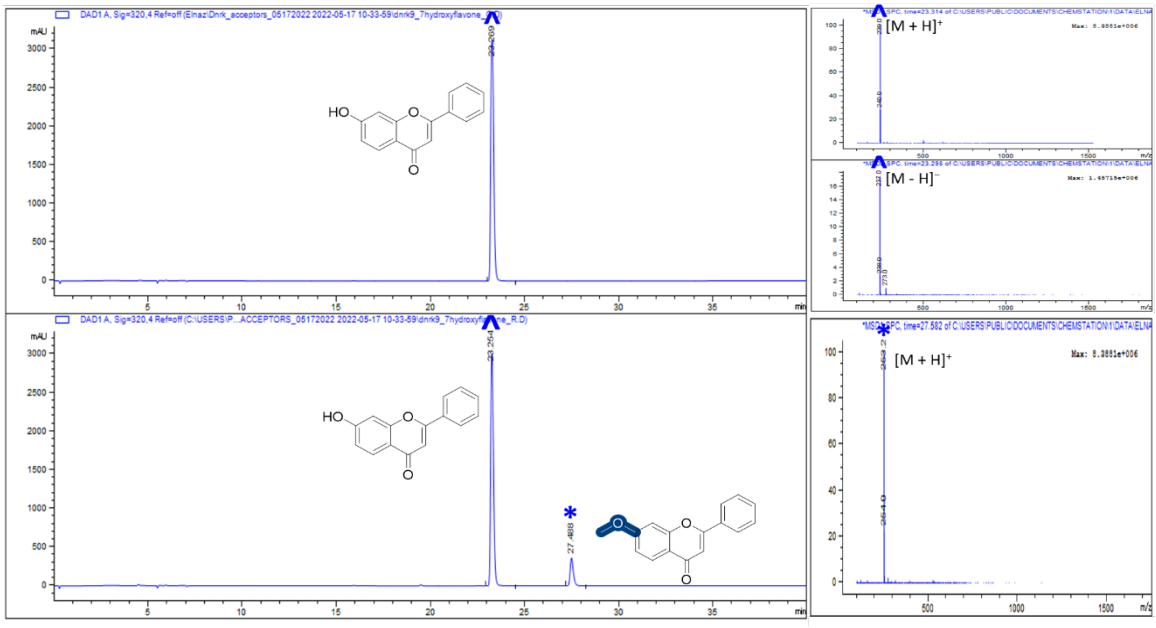

Figure S2.34. LC-MS analysis of 7-hydroxyflavone (**45**)^ and the corresponding DnrK-catalyzed reaction product*. Determined DnrK regioselectivity is highlighted in blue.

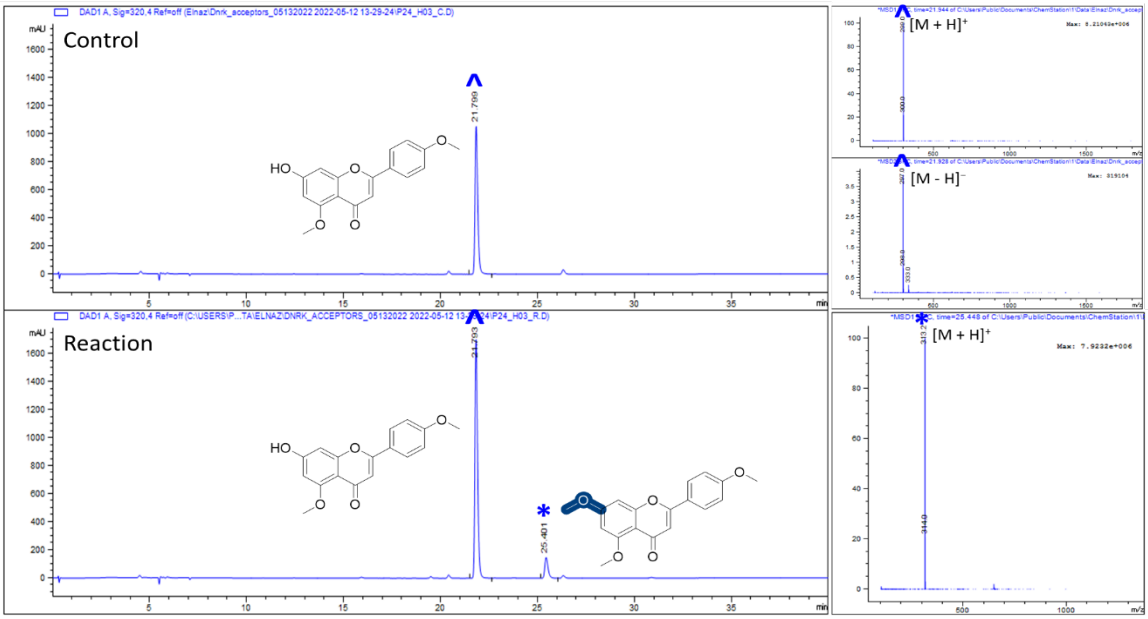

Figure S2.35. LC-MS analysis of 5,4′-dimethoxy7-hydroxyflavone (**46**)^ and the corresponding DnrK-catalyzed reaction product*. Determined DnrK regioselectivity is highlighted in blue

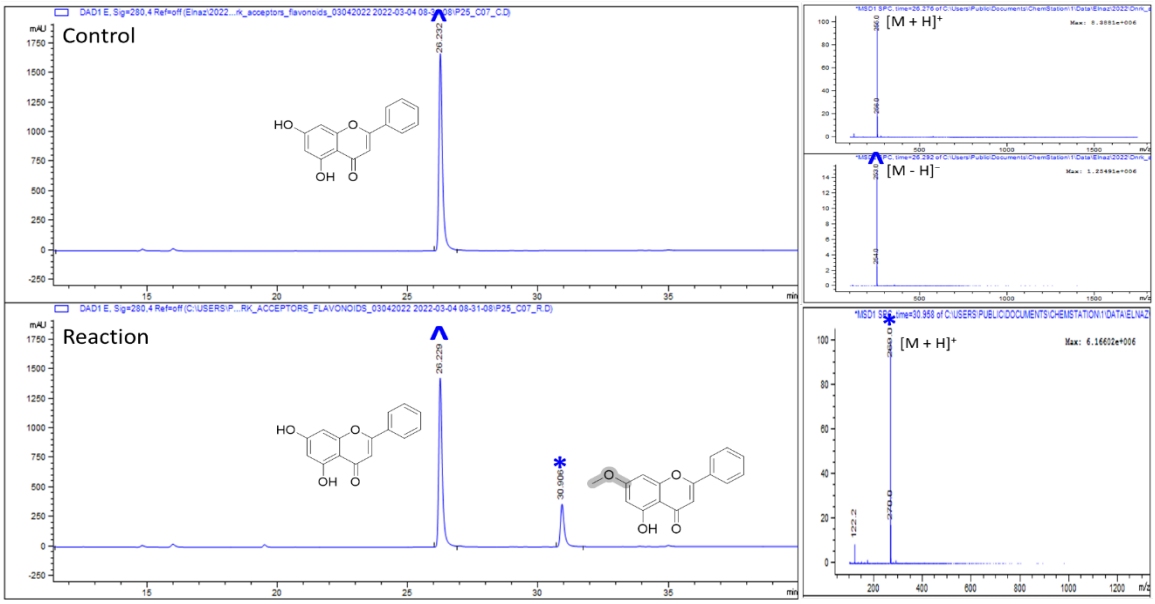

Figure S2.36. LC-MS analysis of chrysin (**49**)^ and the corresponding DnrK-catalyzed reaction product*. Predicted DnrK regioselectivity is highlighted in grey.

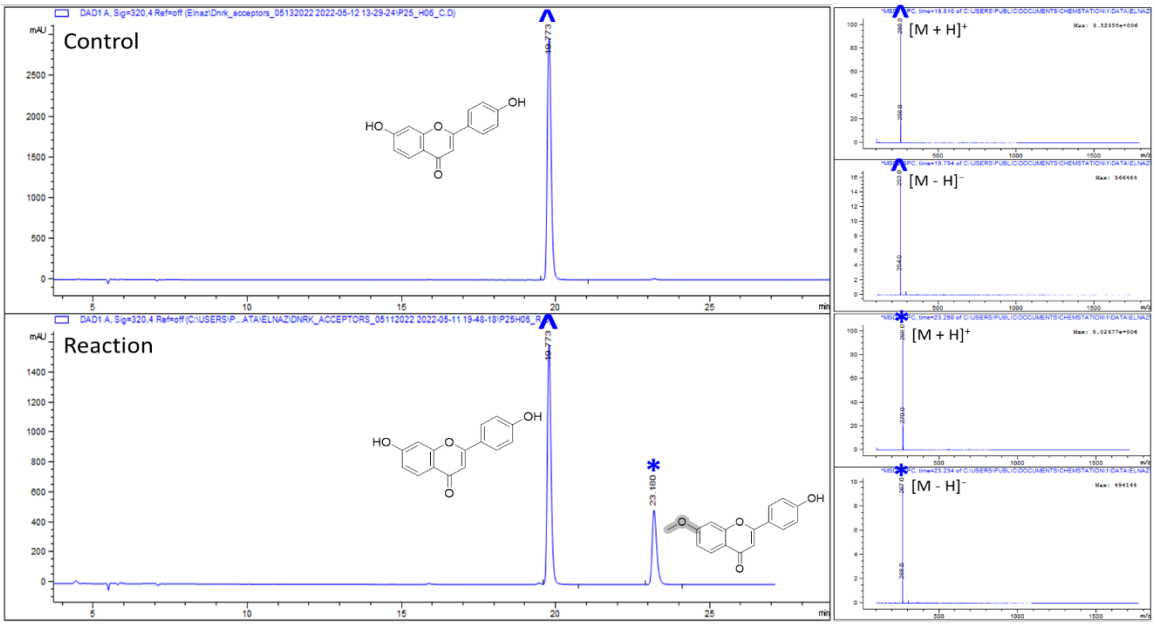

Figure S2.37. LC-MS analysis of 7,4'-dihydroxyflavone (**50**)^ and the corresponding DnrK-catalyzed reaction product*. Predicted DnrK regioselectivity is highlighted in grey.

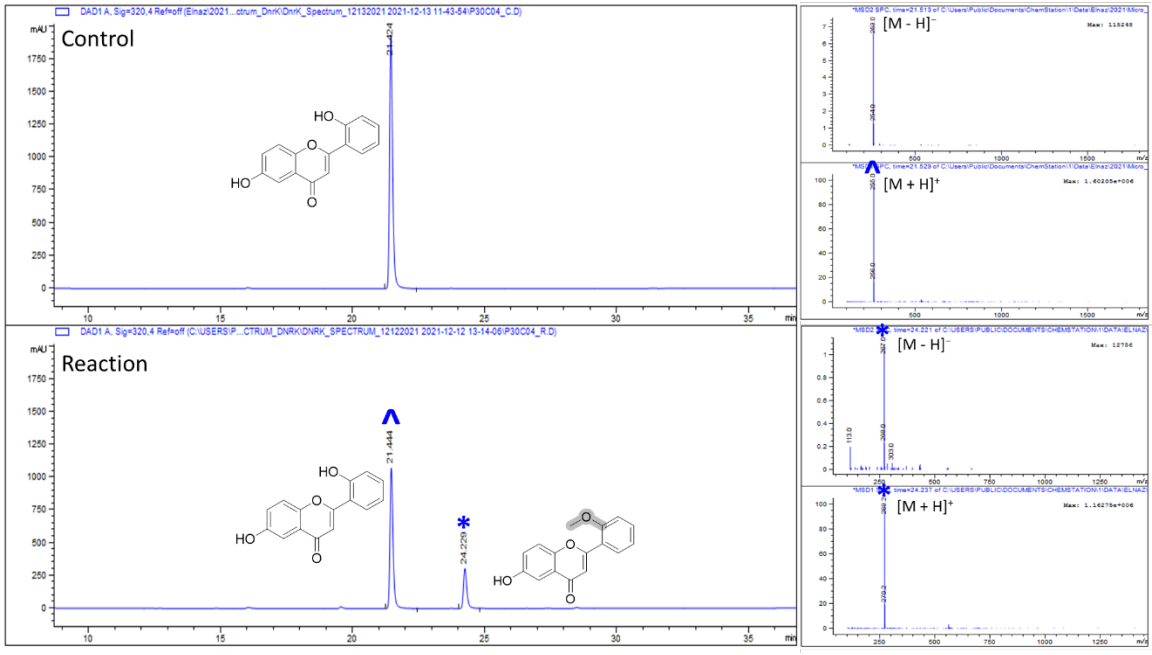

Figure S2.38. LC-MS analysis of 6,2'-dihydroxyflavone (**52**)^ and the corresponding DnrK-catalyzed reaction product*. Predicted DnrK regioselectivity is highlighted in grey.

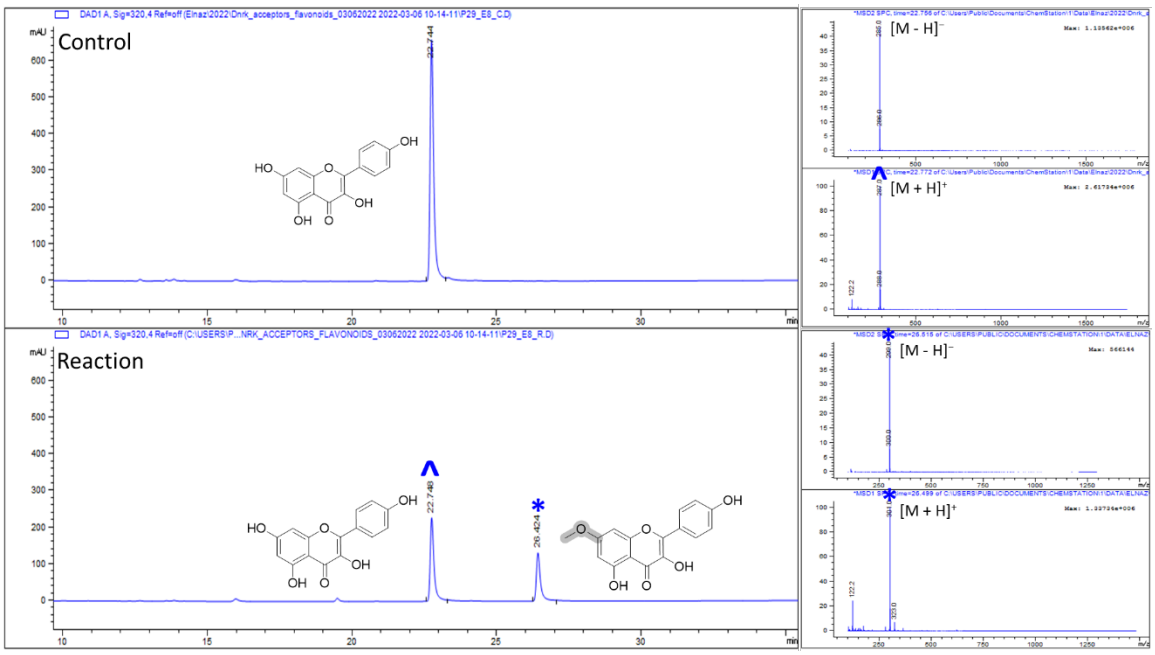

Figure S2.39. LC-MS analysis of kaempferol (**53**)^ and the corresponding DnrK-catalyzed reaction product*. Predicted DnrK regioselectivity is highlighted in grey.

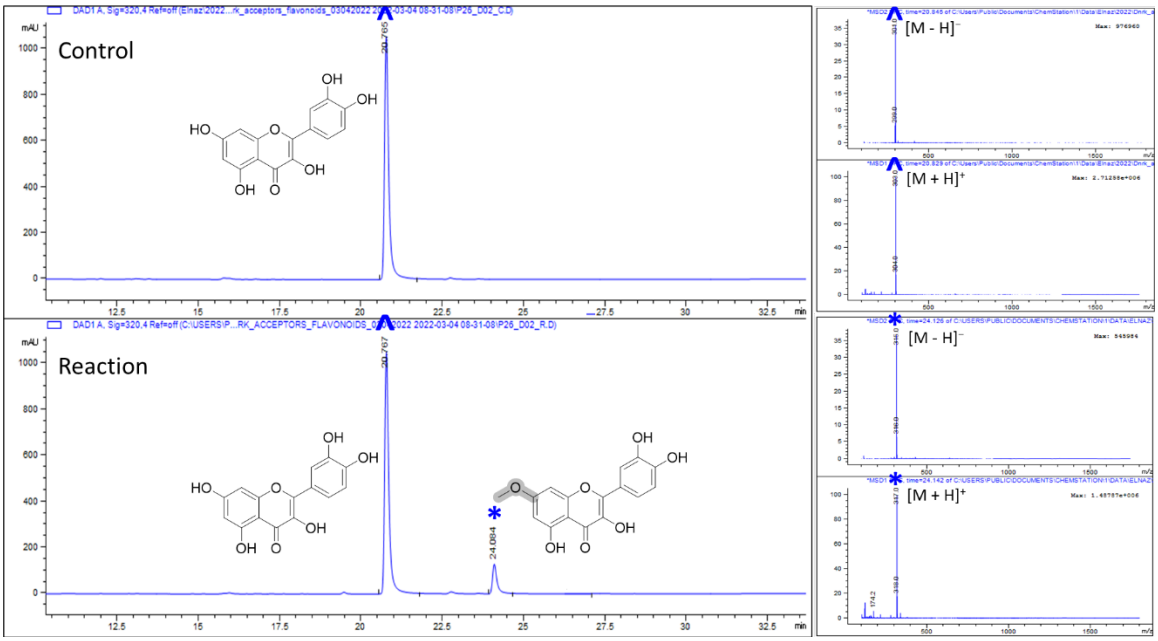

Figure S2.40. LC-MS analysis of quercetin (**54**)^ and the corresponding DnrK-catalyzed reaction product*. Predicted DnrK regioselectivity is highlighted in grey.

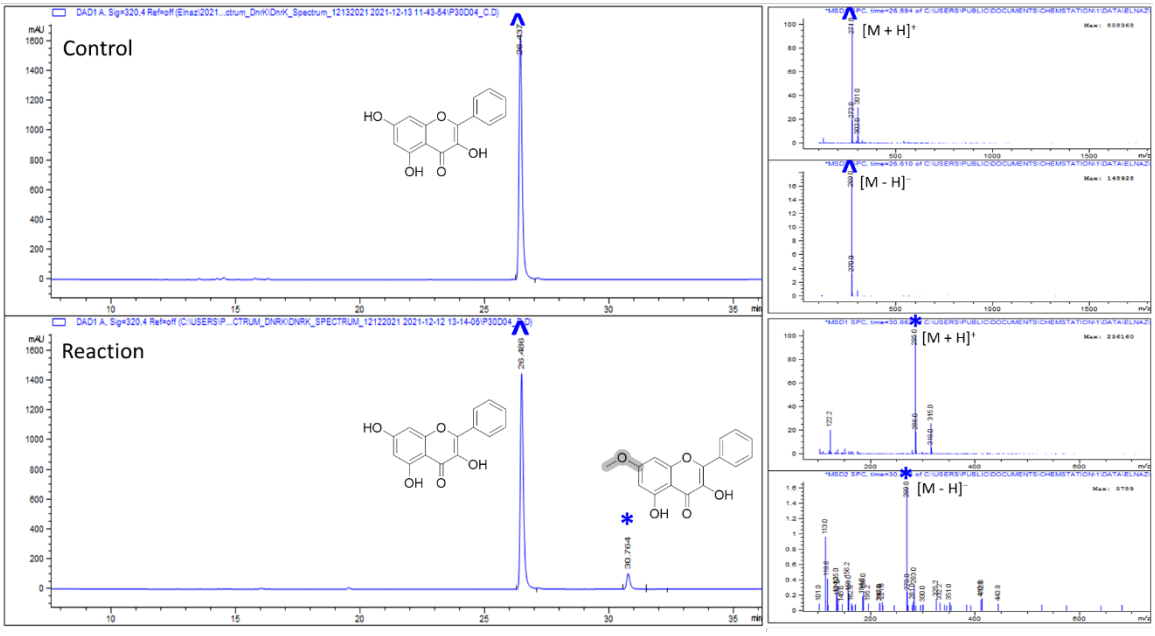

Figure S2.41. LC-MS analysis of galangin (**55**)^ and the corresponding DnrK-catalyzed reaction product*. Predicted DnrK regioselectivity is highlighted in grey.

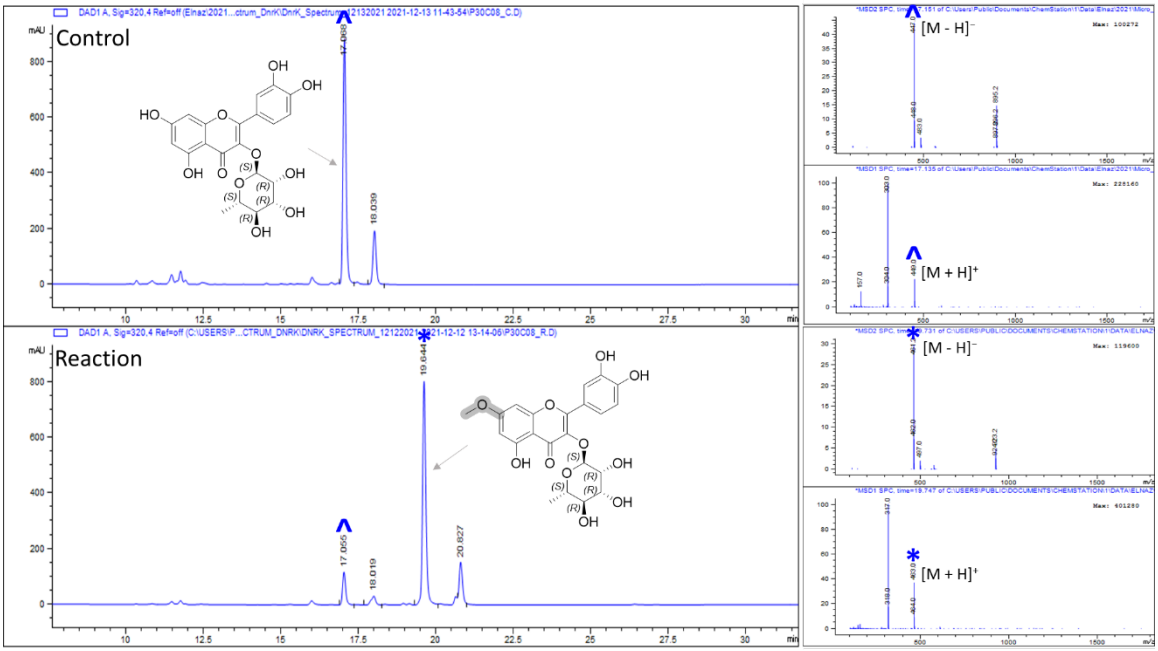

Figure S2.42. LC-MS analysis of quercitrin (**56**)^ and the corresponding DnrK-catalyzed reaction product*. Predicted DnrK regioselectivity is highlighted in grey.

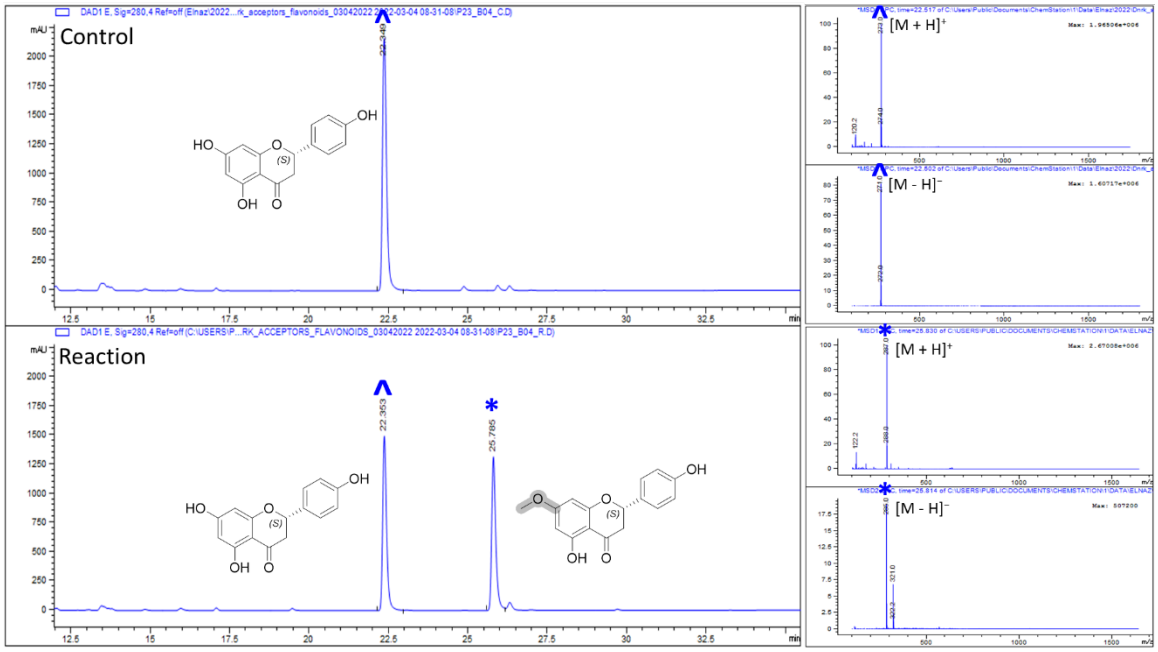

Figure S2.43. LC-MS analysis of 2(S)-naringenin (**58**)^ and the corresponding DnrK-catalyzed reaction product*. Predicted DnrK regioselectivity is highlighted in grey.

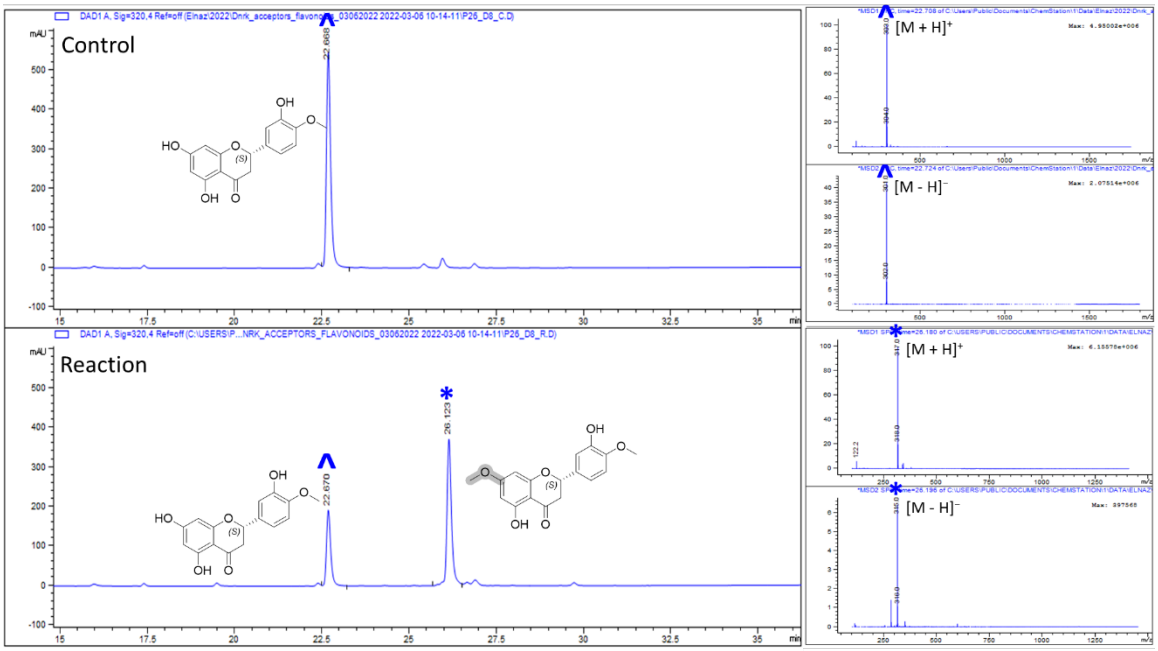

Figure S2.44. LC-MS analysis of 2(S)-hesperetin (**59**)^ and the corresponding DnrK-catalyzed reaction product*. Predicted DnrK regioselectivity is highlighted in grey.

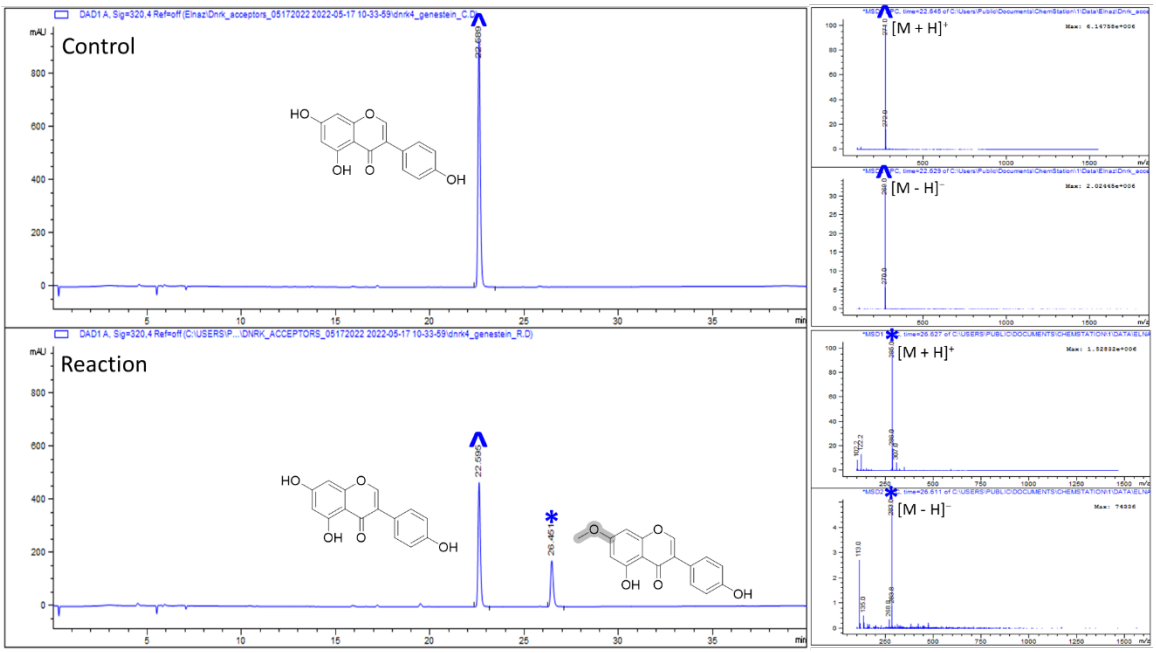

Figure S2.45. LC-MS analysis of genistein (**62**)^ and the corresponding DnrK-catalyzed reaction product*. Predicted DnrK regioselectivity is highlighted in grey.

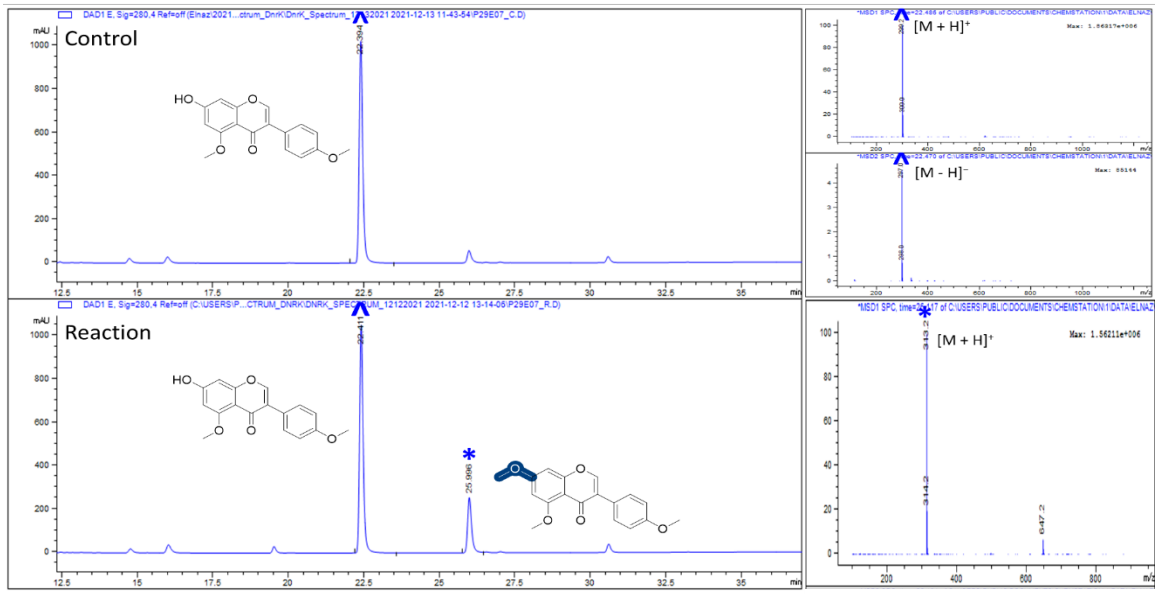

Figure S2.46. LC-MS analysis of 5,4'-dimethoxy-7-hydroxyisoflavone (**63**)^ and the corresponding DnrK-catalyzed reaction product*. Determined DnrK regioselectivity is highlighted in blue.

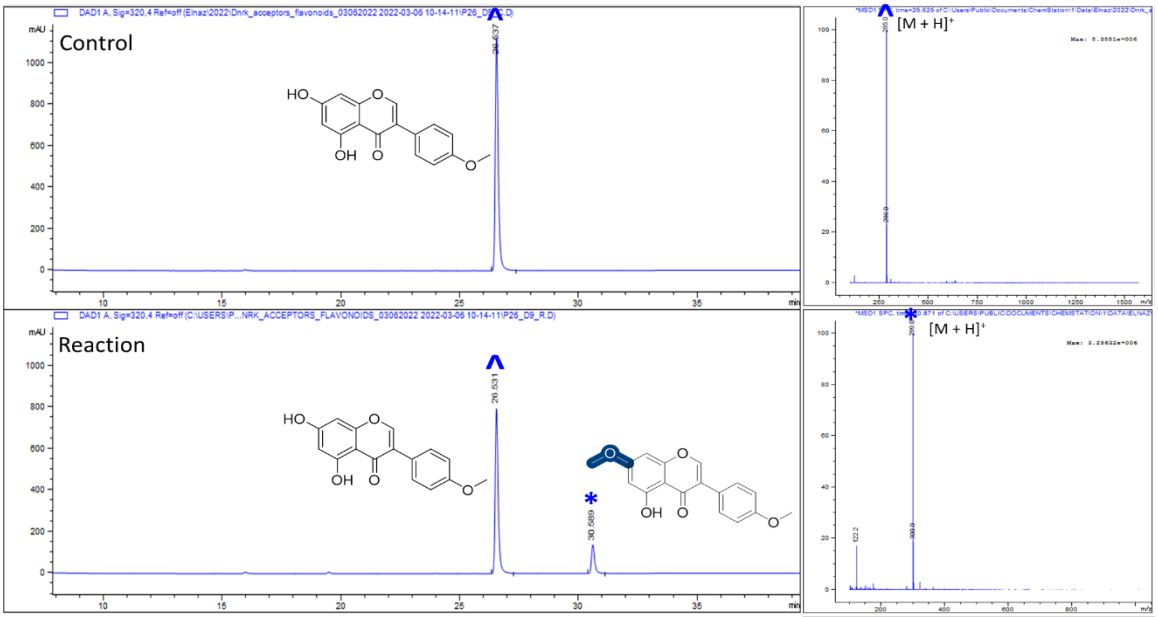

Figure S2.47. LC-MS analysis of biochanin A (**65**)^ and the corresponding DnrK-catalyzed reaction product*. Determined DnrK regioselectivity is highlighted in blue.

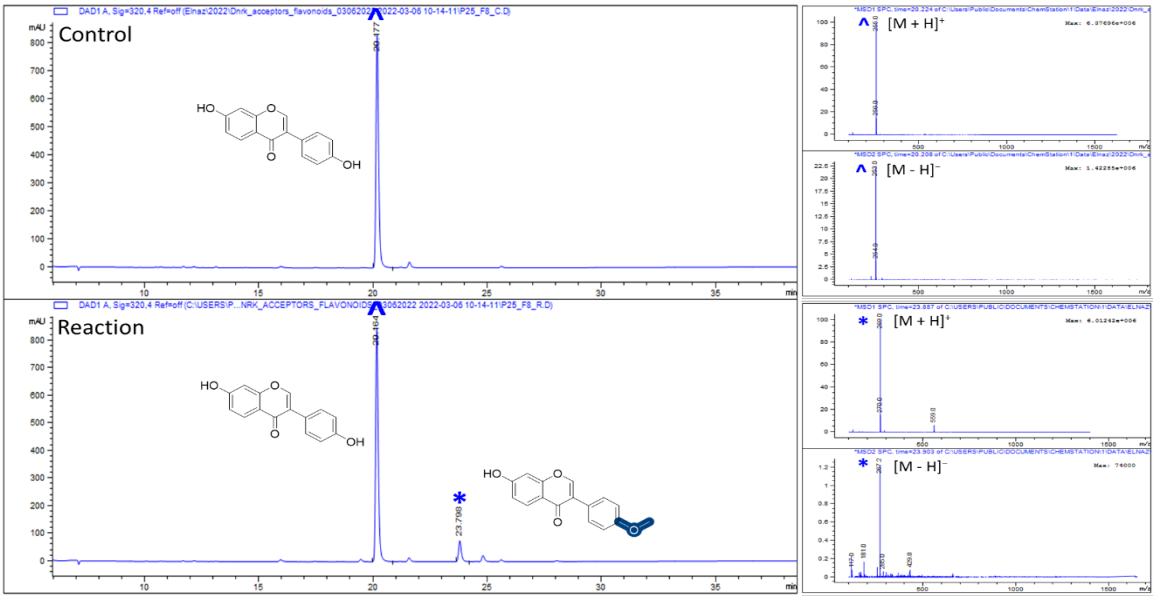

Figure S2.48. LC-MS analysis of daidzein (**67**)^ and the corresponding DnrK-catalyzed reaction product*. Determined DnrK regioselectivity is highlighted in blue.

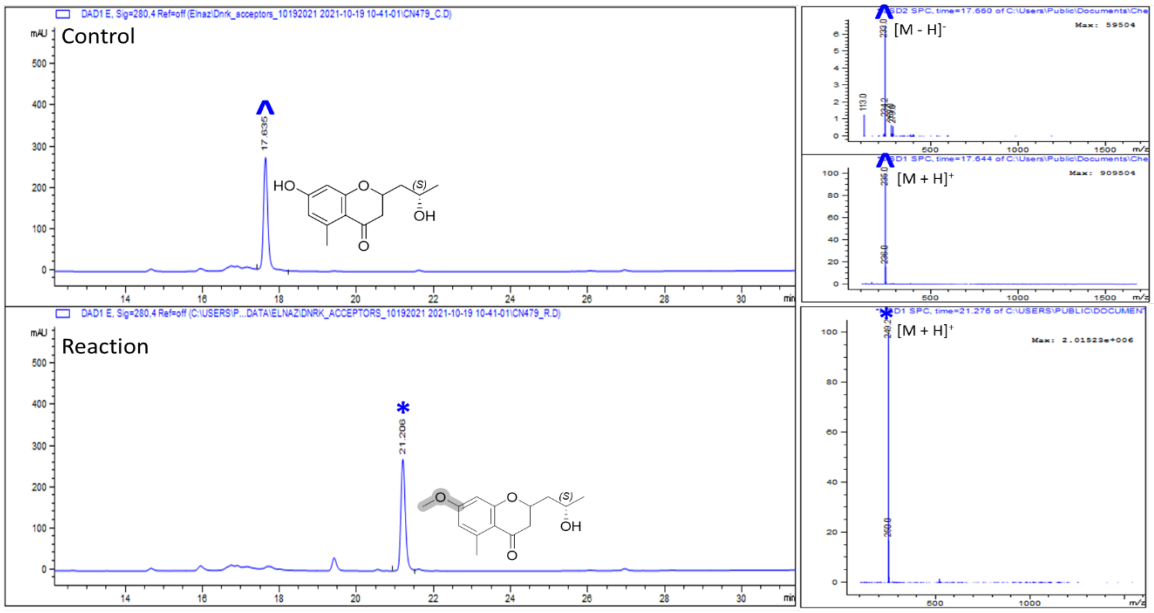

Figure S2.49. LC-MS analysis of 5-carbomethoxymethyl-2-heptyl-7-hydroxychrome (**71**)^ and the corresponding DnrK-catalyzed reaction product*. Predicted DnrK regioselectivity is highlighted in grey.

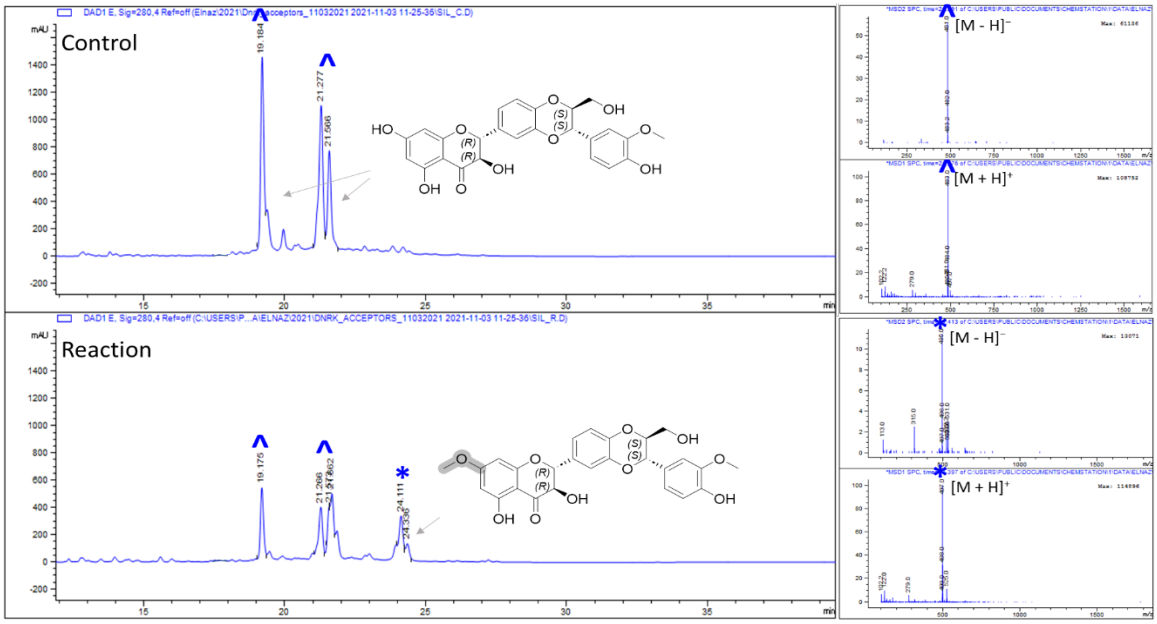

Figure S2.50. LC-MS analysis of silybin B (**72**)^ and the corresponding DnrK-catalyzed reaction product*. Predicted DnrK regioselectivity is highlighted in grey.

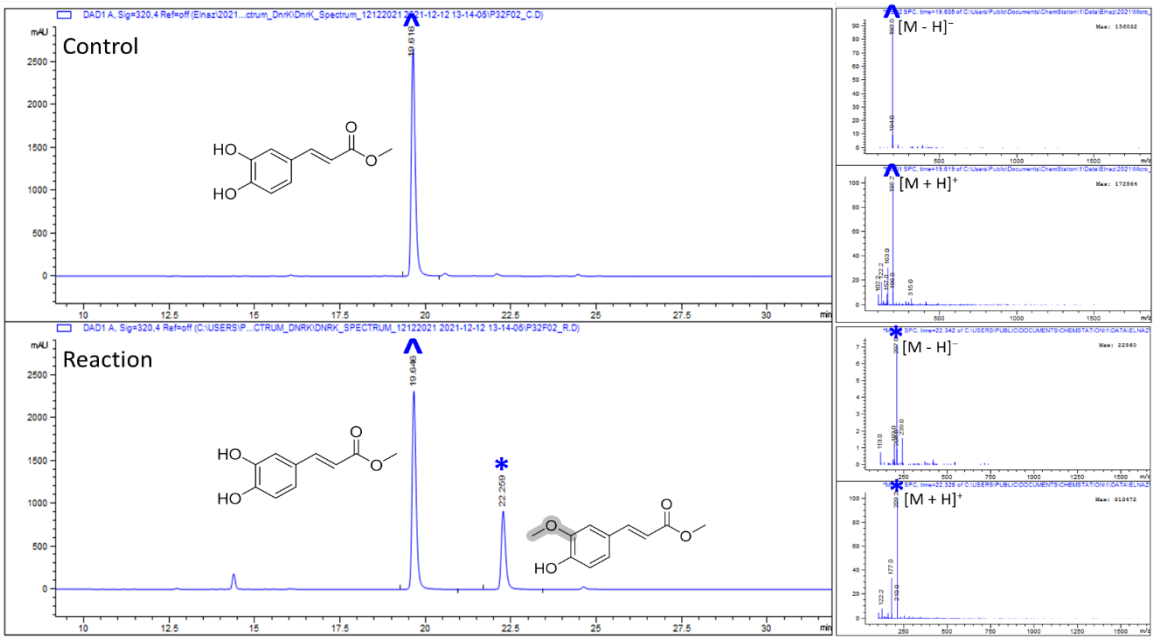

Figure S2.51. LC-MS analysis of methyl caffeate (**73**)^ and the corresponding DnrK-catalyzed reaction product*. Predicted DnrK regioselectivity is highlighted in grey.

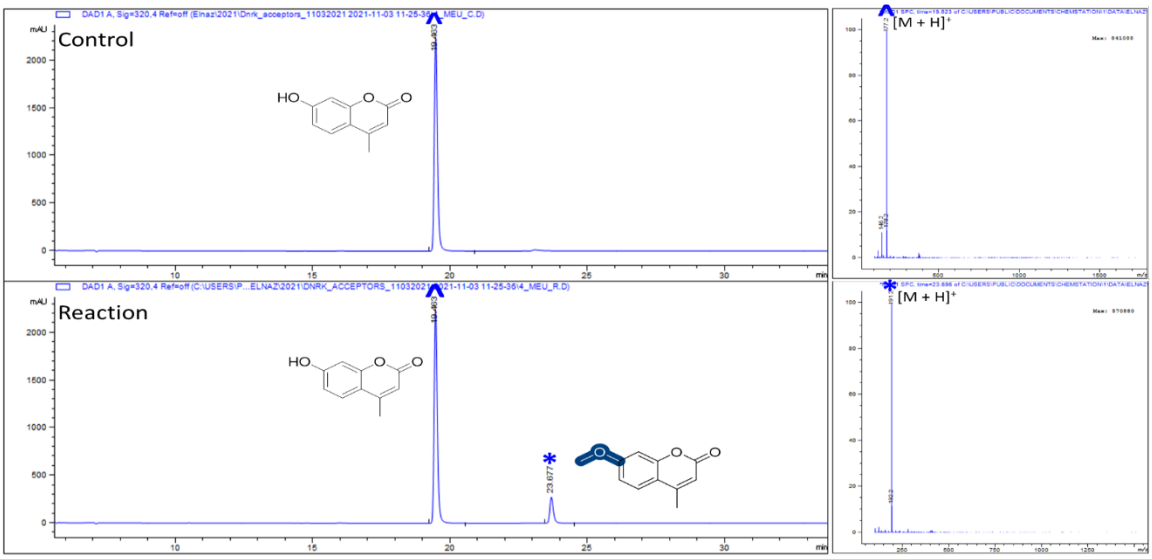

Figure S2.52. LC-MS analysis of 4-methylumbelliferone (**75**)^ and the corresponding DnrK-catalyzed reaction product*. Determined DnrK regioselectivity is highlighted in blue.

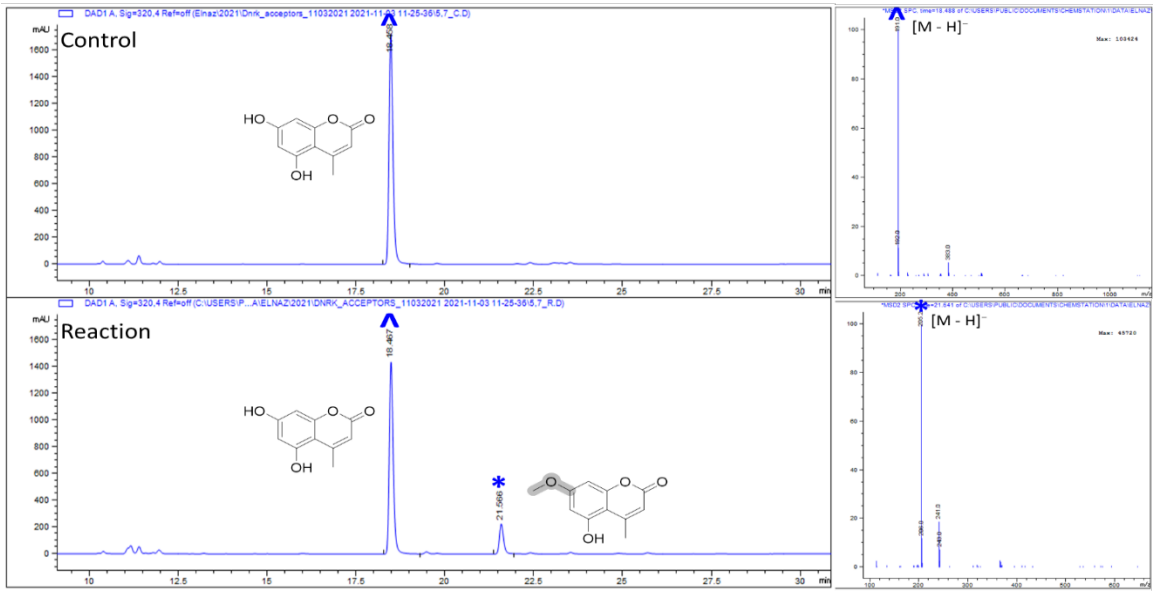

Figure S2.53. LC-MS analysis of 5,7-dihydroxy-4-methylcoumarin (**77**)^ and the corresponding DnrK-catalyzed reaction product*. Predicted DnrK regioselectivity is highlighted in grey.

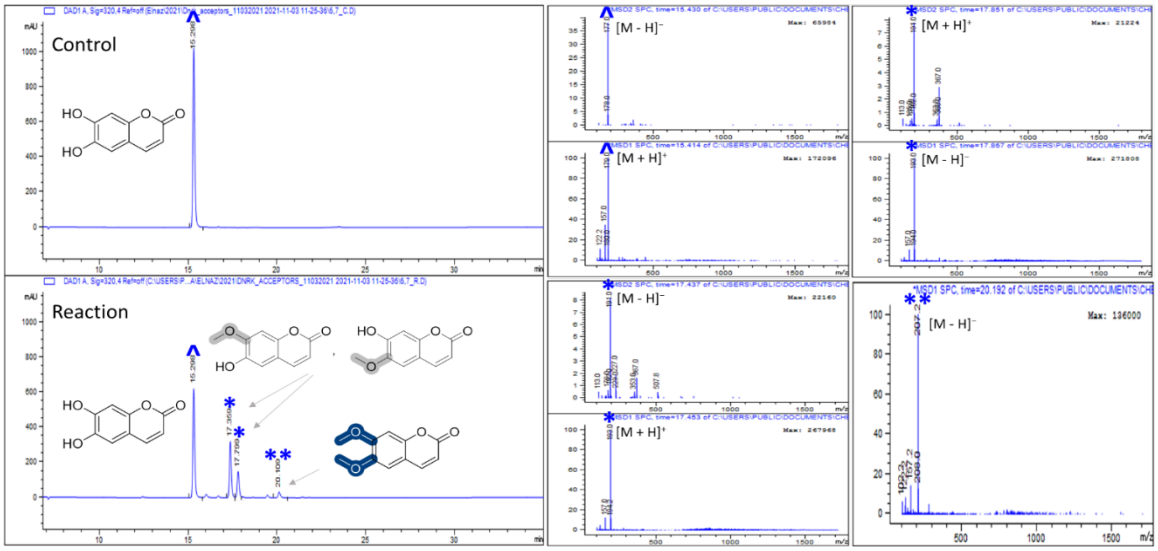

Figure S2.54. LC-MS analysis of 6,7-dihydroxycoumarin (**78**)^ and the corresponding DnrK-catalyzed two mono* and one di** reaction products. Determined DnrK regioselectivity is highlighted in blue and Predicted DnrK regioselectivity is highlighted in grey.

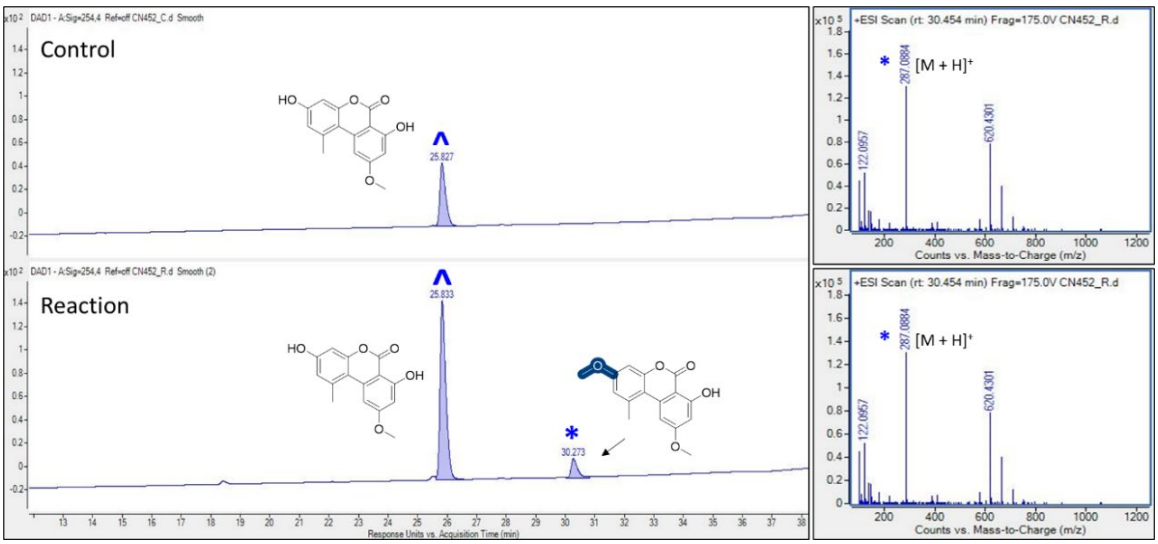

Figure S2.55. LC-MS analysis of 9-methoxy alternariol (**79**)^ and the corresponding DnrK-catalyzed reaction product*. Determined DnrK regioselectivity is highlighted in blue.

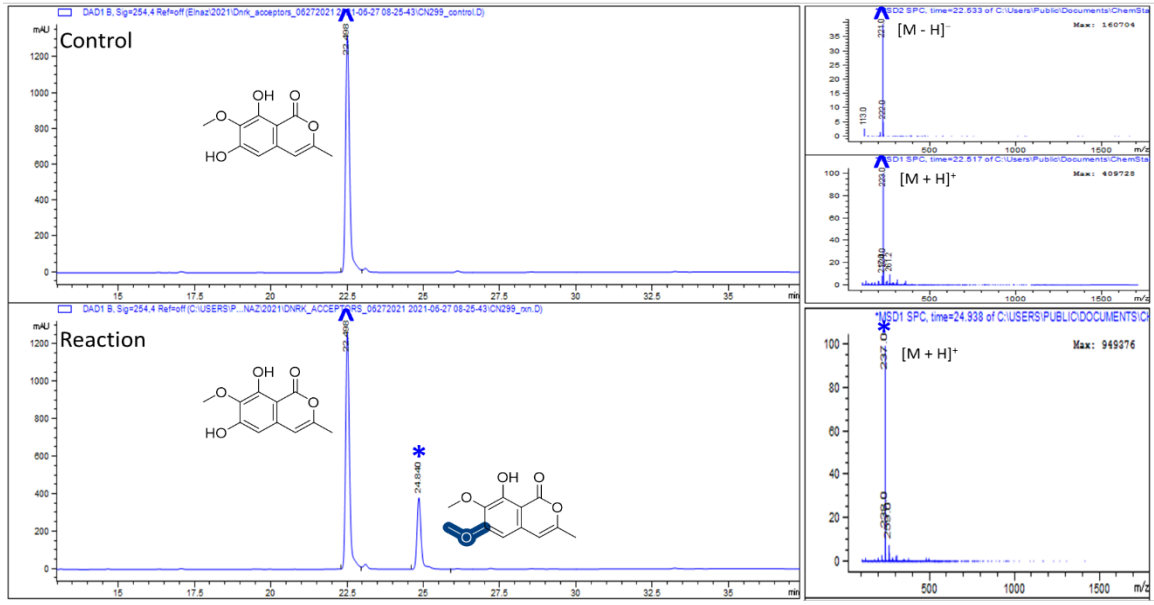

Figure S2.56. LC-MS analysis of 6,8-dihydroxy-7-methoxy-3-methylisocoumarin (**85**)^ and the corresponding DnrK-catalyzed reaction product*. Determined DnrK regioselectivity is highlighted in blue.

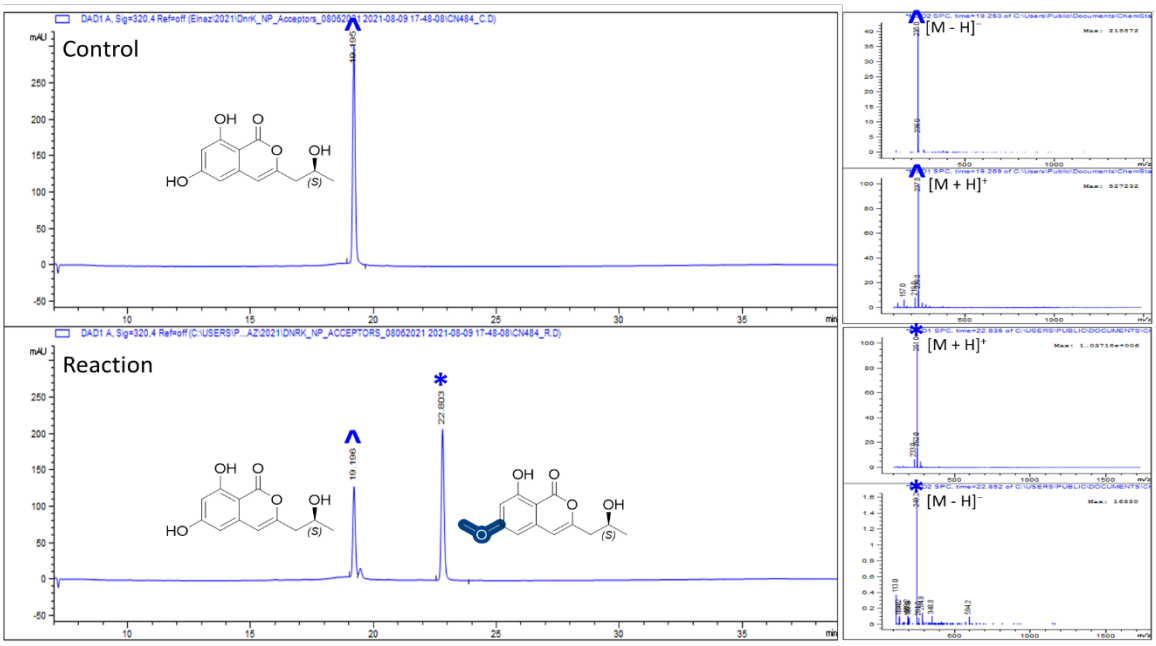

Figure S2.57. LC-MS analysis of orthosporin (**87**)^ and the corresponding DnrK-catalyzed reaction product*. Determined DnrK regioselectivity is highlighted in blue.

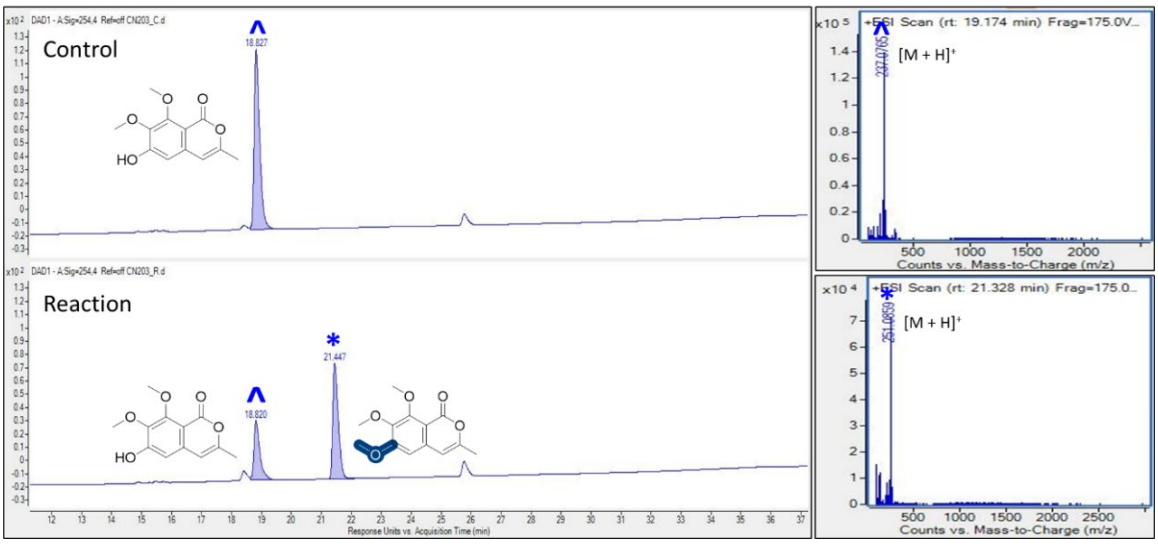

Figure S2.58. LC-MS analysis of 6-hydroxy-7,8-dimethoxy-3-methylisocoumarin (**89**)^ and the corresponding DnrK-catalyzed reaction product*. Determined DnrK regioselectivity is highlighted in blue.

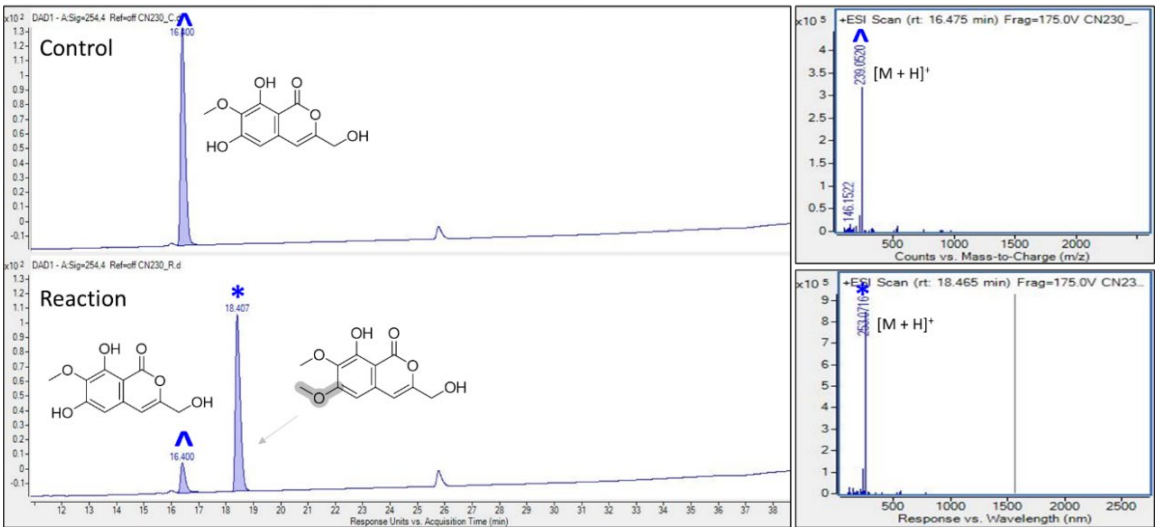

Figure S2.59. LC-MS analysis of 6,8-dihydroxy-7-methoxy-3-hydroxymethylisocoumarin (**90**)^ and the corresponding DnrK-catalyzed reaction product*. Predicted DnrK regioselectivity is highlighted in grey.

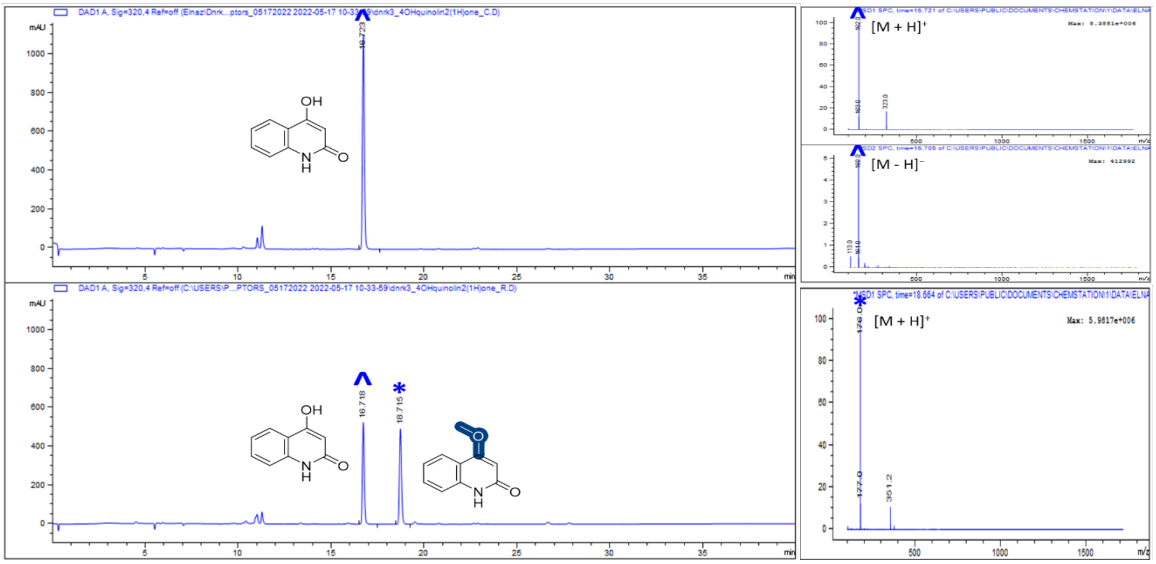

Figure S2.60. LC-MS analysis of 4-hydroxy-quinolin-2(1H)-one (**91**)^ and the corresponding DnrK-catalyzed reaction product*. Determined DnrK regioselectivity is highlighted in blue.

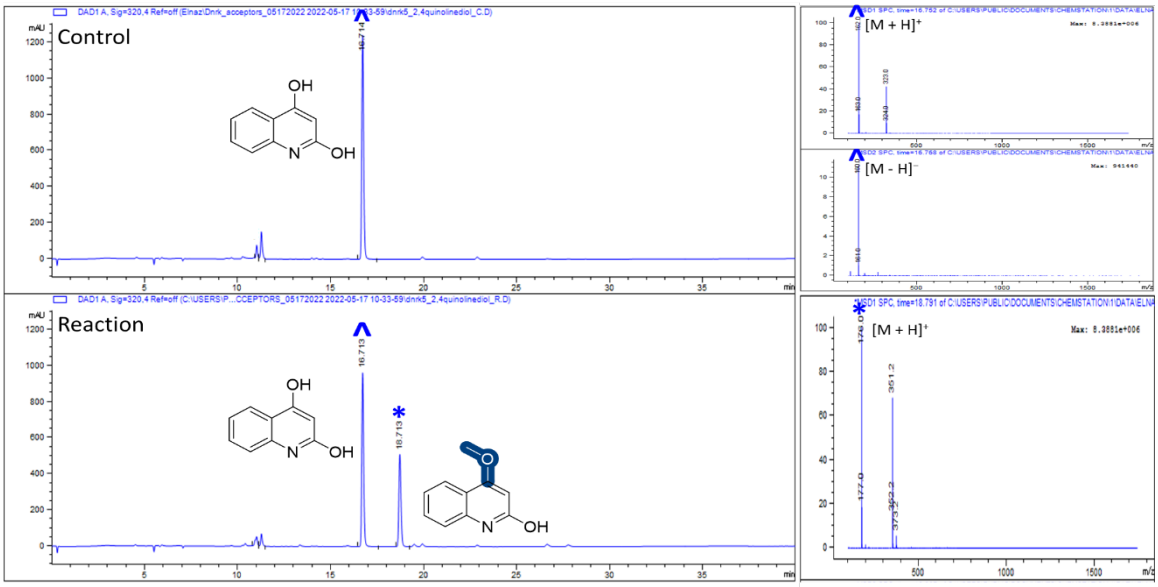

Figure S2.61. LC-MS analysis of 2,4-dihydroxyquinoline (**92**)^ and the corresponding DnrK-catalyzed reaction product*. Determined DnrK regioselectivity is highlighted in blue.

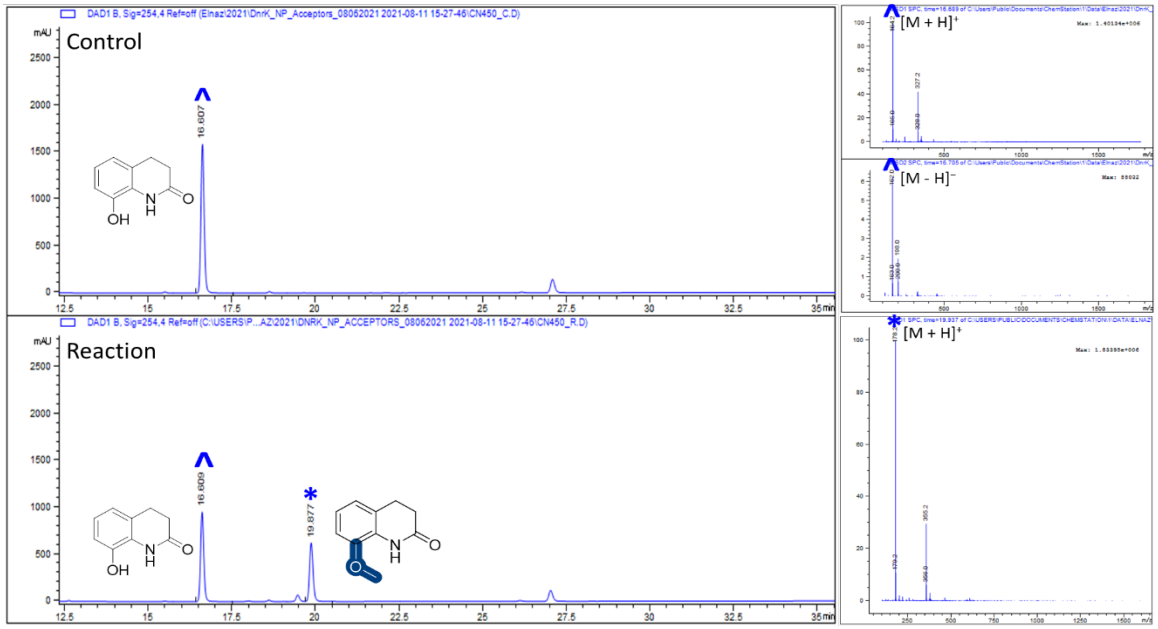

Figure S2.62. LC-MS analysis of 8-Hydroxy-3,4-dihydro-2-quinolinone (**93**)^ and the corresponding DnrK-catalyzed reaction product*. Determined DnrK regioselectivity is highlighted in blue.

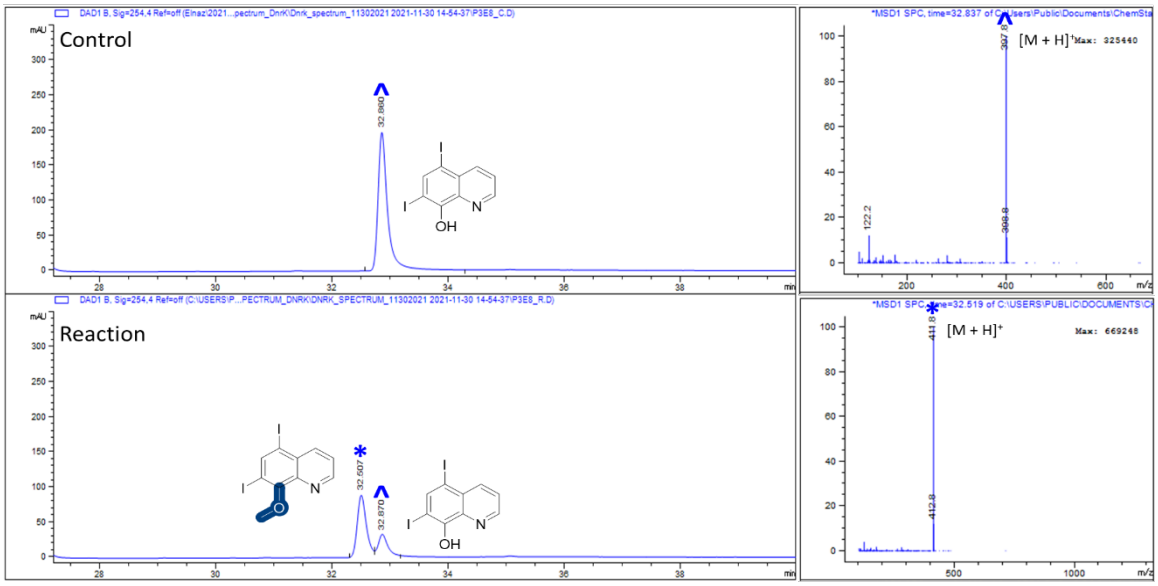

Figure S2.63. LC-MS analysis of iodoquinol (**94**)^ and the corresponding DnrK-catalyzed reaction product*. Determined DnrK regioselectivity is highlighted in blue.

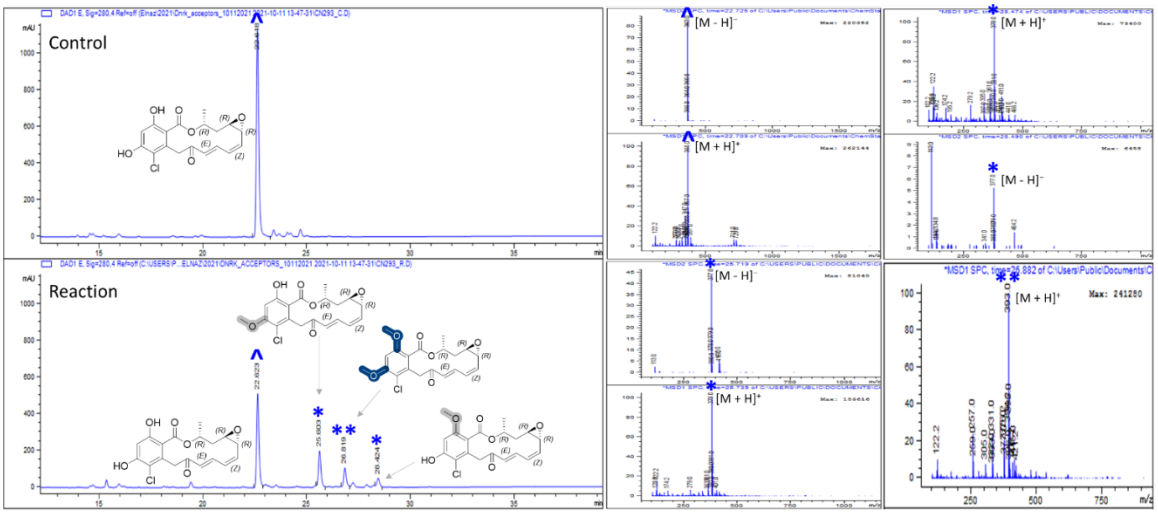

Figure S2.64. LC-MS analysis of radicicol (**98**)^ and the corresponding DnrK-catalyzed two mono* and one di** reaction products. Determined DnrK regioselectivity is highlighted in blue and Predicted DnrK regioselectivity is highlighted in grey.

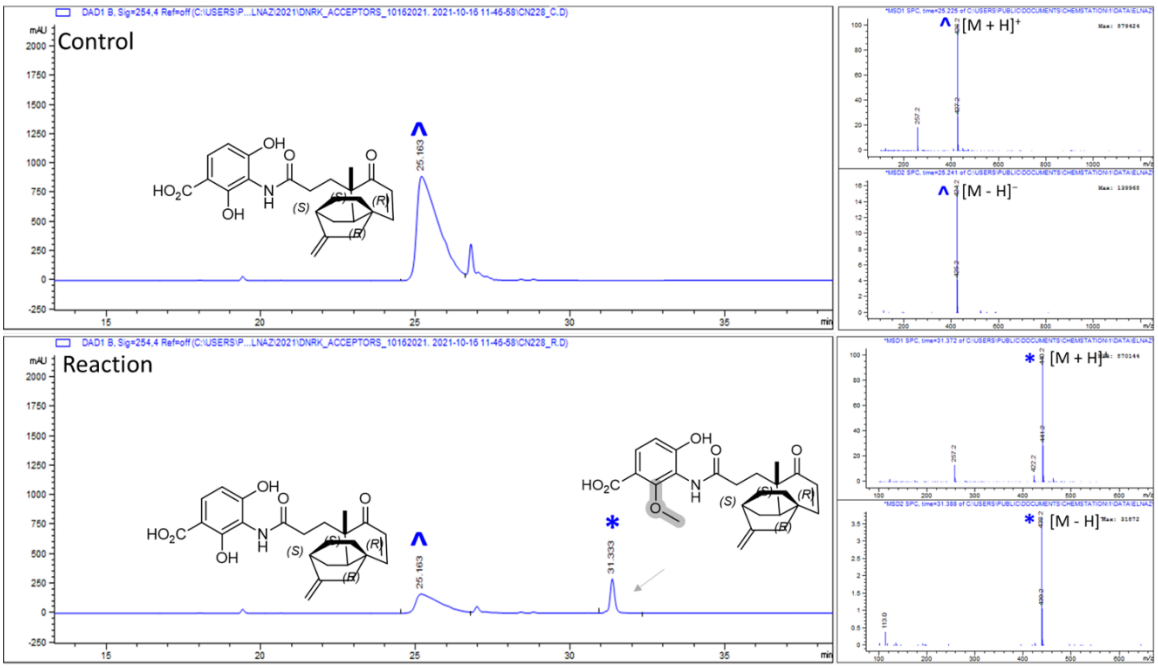

Figure S2.65. LC-MS analysis of platencin (**99**)^ and the corresponding DnrK-catalyzed reaction product*. Predicted DnrK regioselectivity is highlighted in grey.

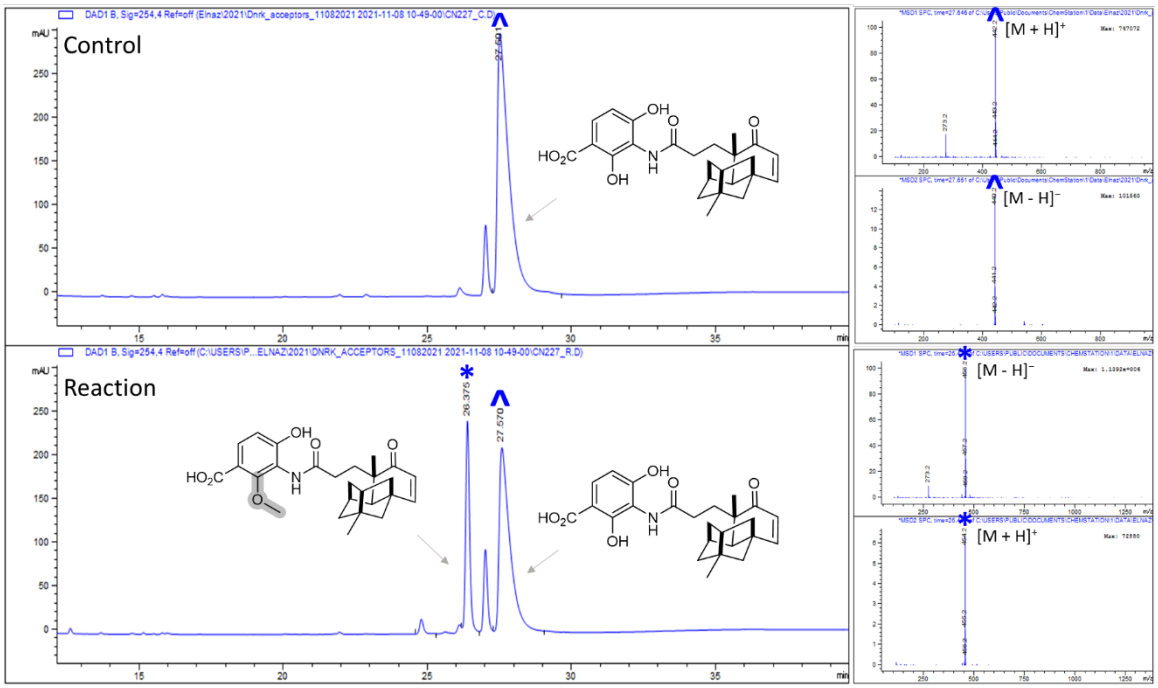

Figure S2.66. LC-MS analysis of platensimycin (**100**)^ and the corresponding DnrK-catalyzed reaction product*. Predicted DnrK regioselectivity is highlighted in grey.

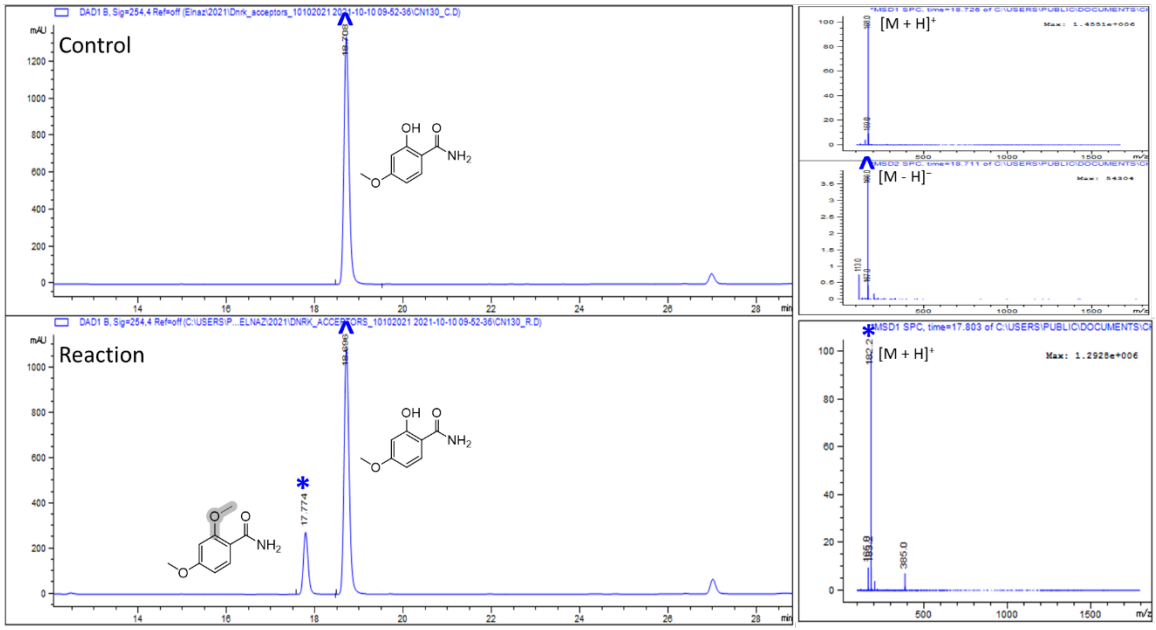

Figure S2.67. LC-MS analysis of pyramidamycin A (**101**)^ and the corresponding DnrK-catalyzed reaction product*. Predicted DnrK regioselectivity is highlighted in grey.

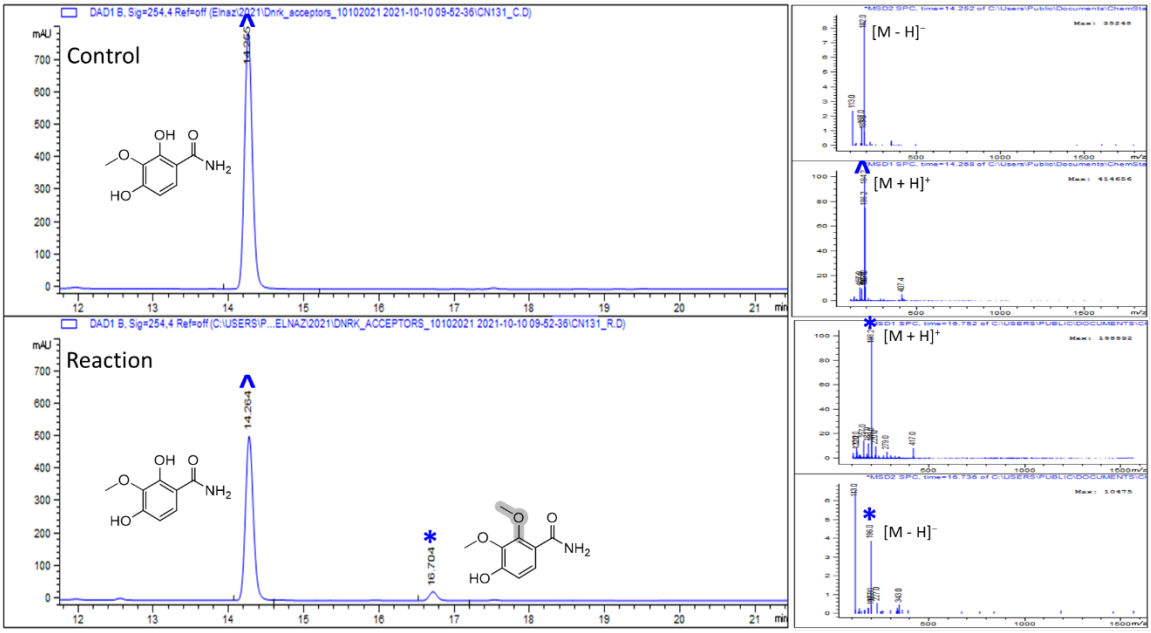

Figure S2.68. LC-MS analysis of pyramidamycin B (**102**)^ and the corresponding DnrK-catalyzed reaction product*. Predicted DnrK regioselectivity is highlighted in grey.

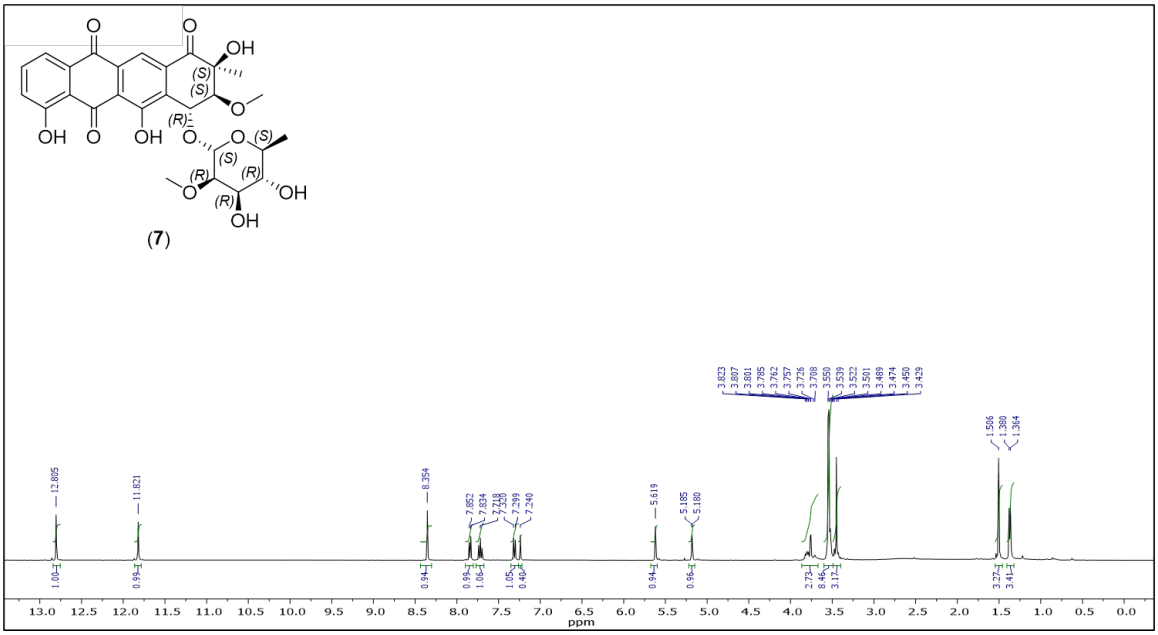

Figure S2.69. ^{1}H NMR spectrum ($CDCl_3$, 400 MHz) of aranciamycin (**7**).

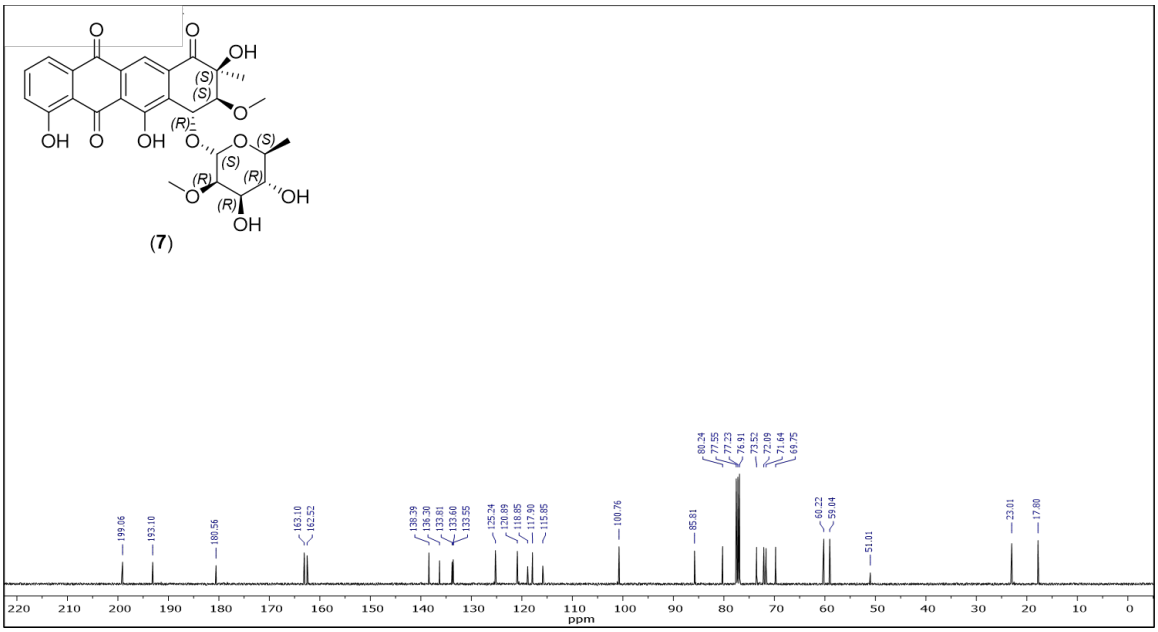

Figure S2.70. ^{13}C NMR spectrum ($CDCl_3$, 100 MHz) of aranciamycin (**7**)

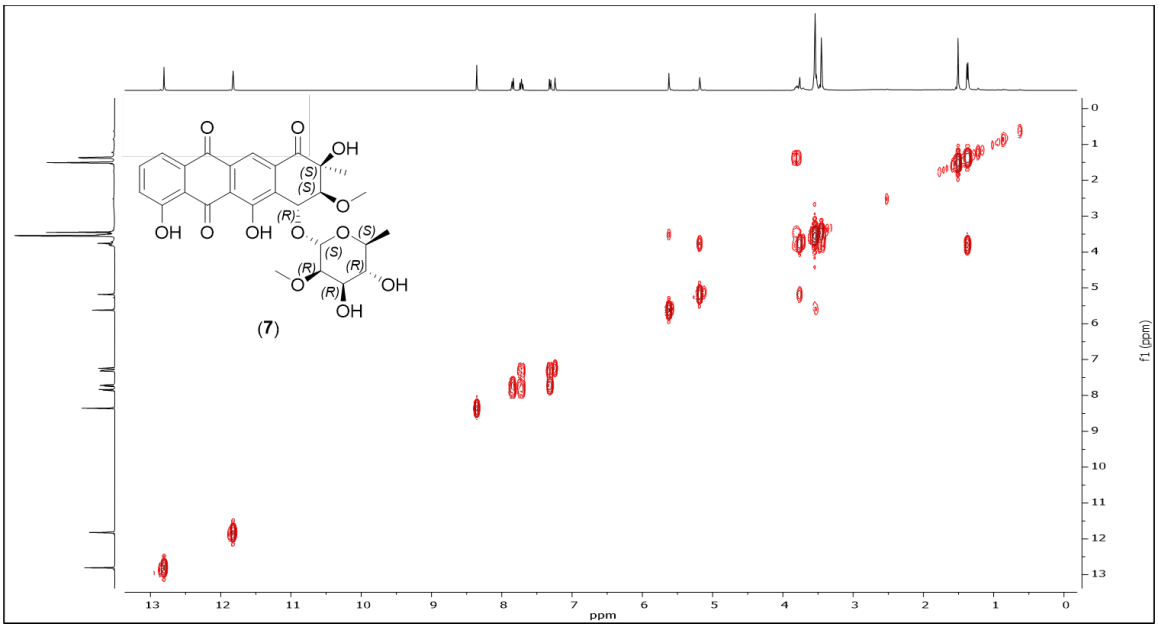

Figure S2.71. $^{1}H,^{1}H$-COSY spectrum ($CDCl_3$, 400 MHz) of aranciamycin (**7**).

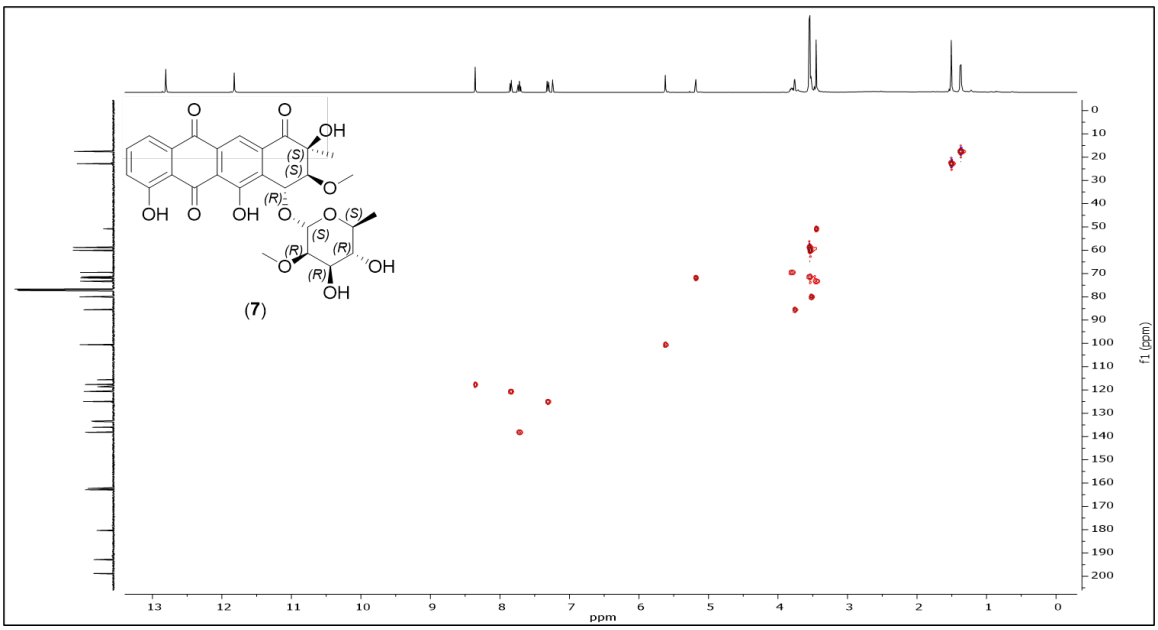

Figure S2.72. HSQC spectrum ($CDCl_3$, 400 MHz) of aranciamycin (**7**).

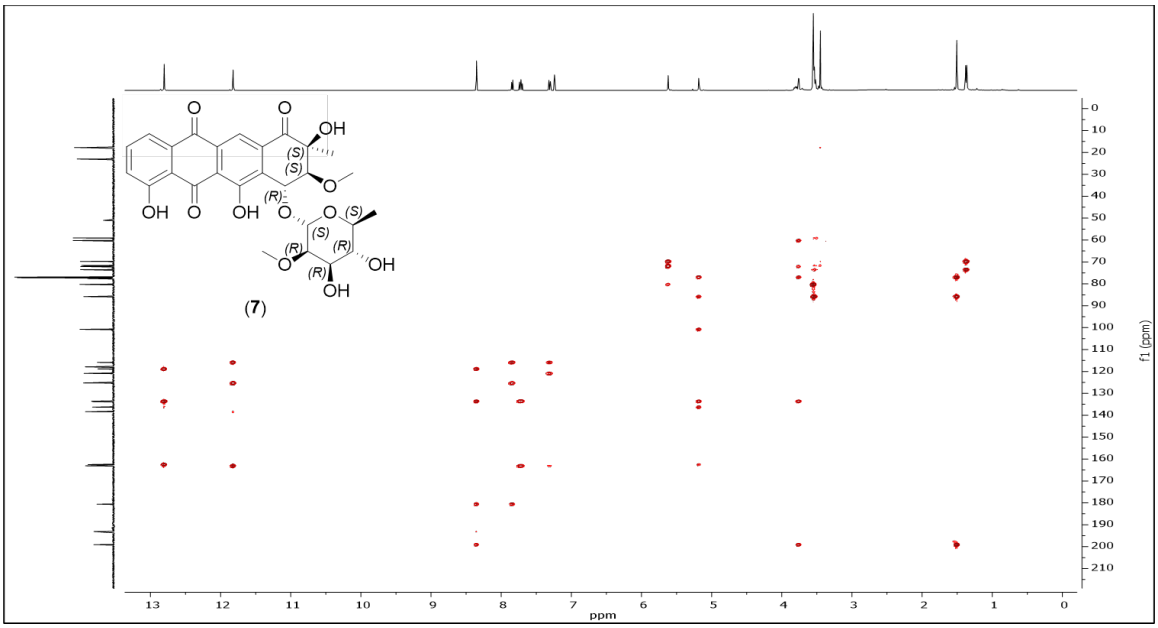

Figure S2.73. HMBC spectrum ($CDCl_3$, 400 MHz) of aranciamycin (**7**).

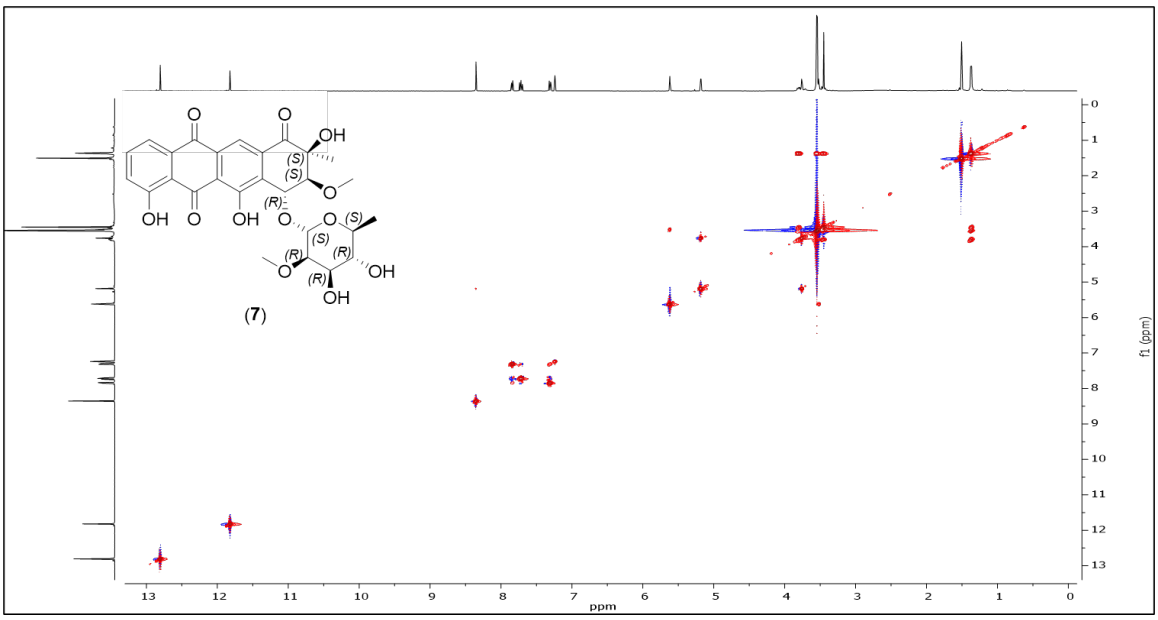

Figure S2.74. TOCSY spectrum ($CDCl_3$, 400 MHz) of aranciamycin (**7**).

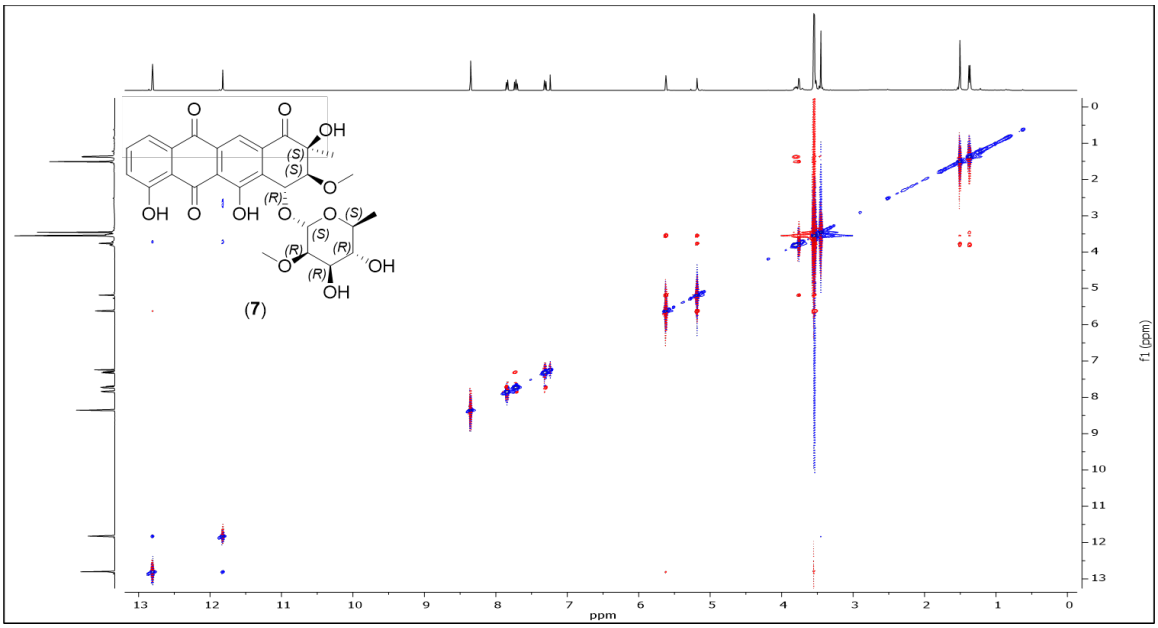

Figure SS2.75. NOESY spectrum ($CDCl_3$, 400 MHz) of aranciamycin (**7**).

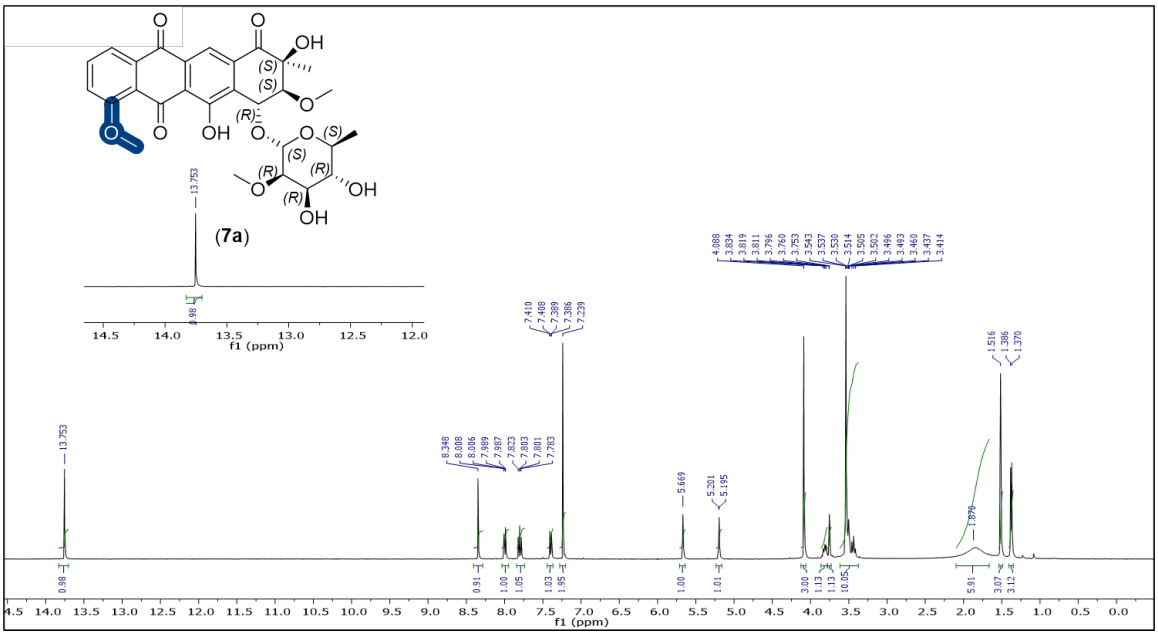

Figure S2.76. ^{1}H NMR spectrum ($CDCl_3$, 400 MHz) of 4-*O*-methoxyaranciamycin (**7a**).

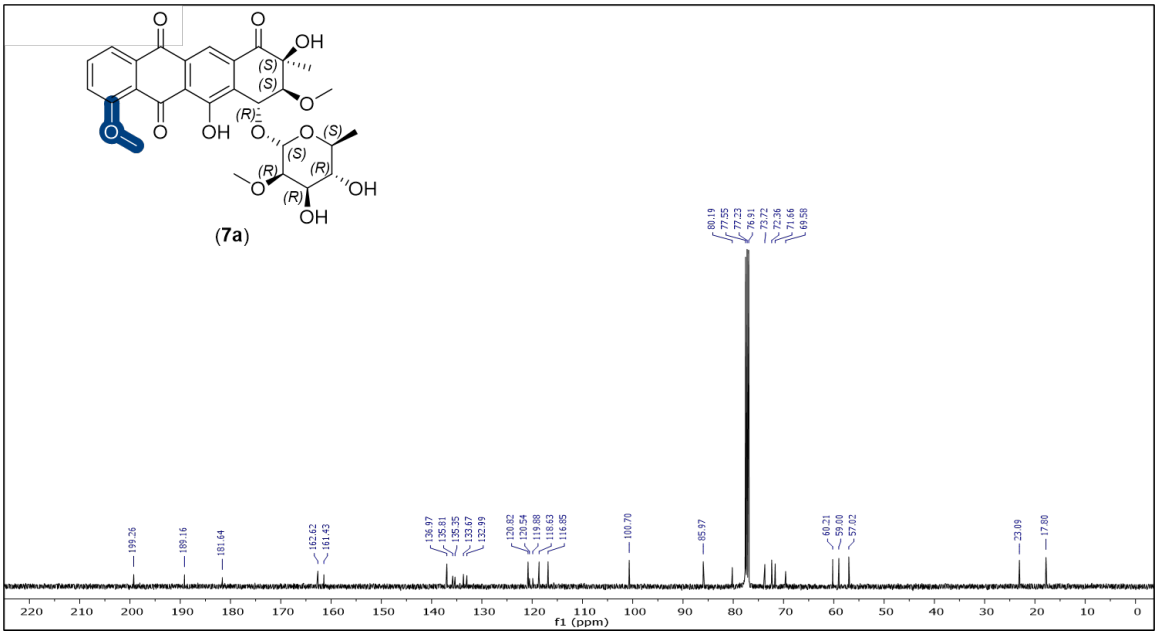

Figure S2.77. ^{13}C NMR spectrum ($CDCl_3$, 100 MHz) of 4-*O*-methoxyaranciamycin (**7a**).

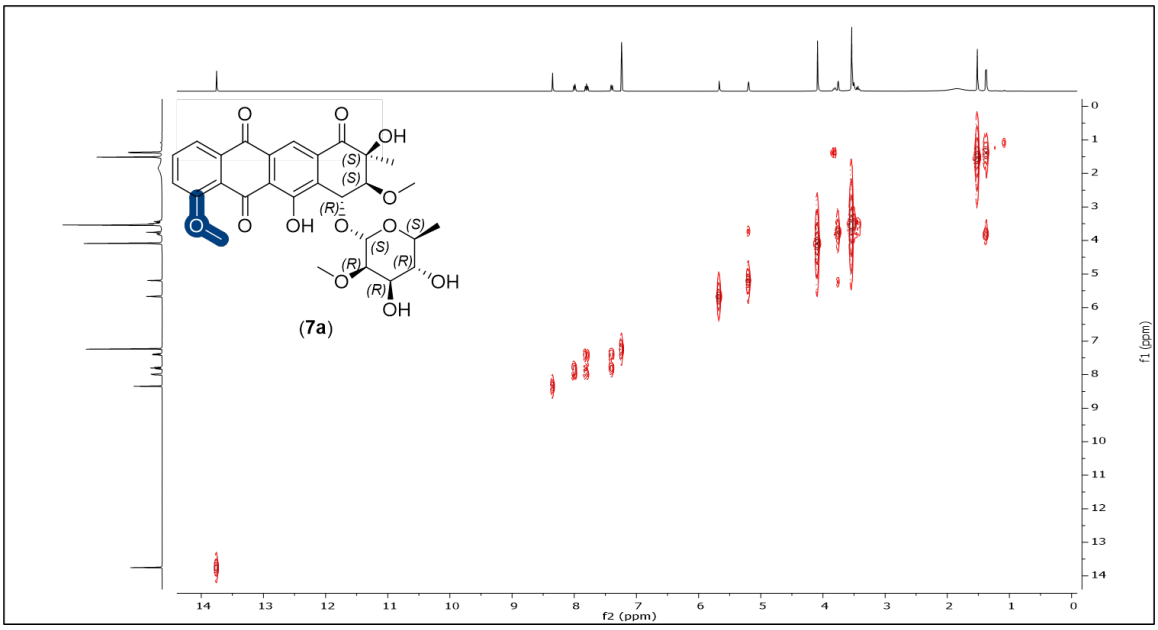

Figure S2.78. ^{1}H,^{1}H-COSY spectrum ($CDCl_3$, 400 MHz) of 4-*O*-methoxyaranciamycin (**7a**).

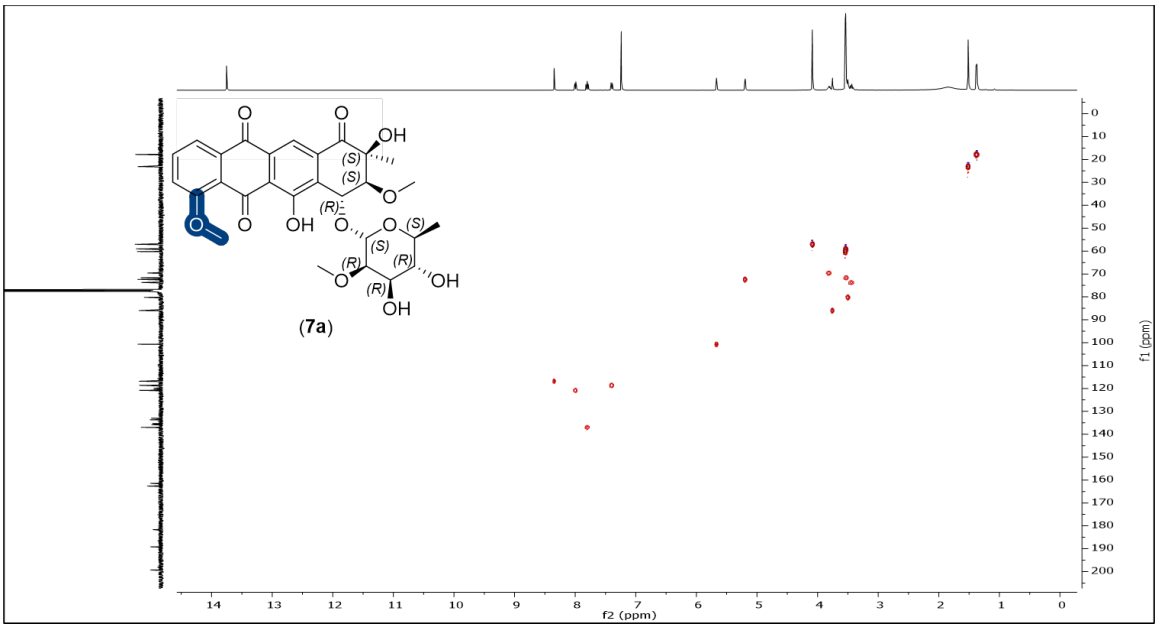

Figure S2.79. HSQC spectrum ($CDCl_3$, 400 MHz) of 4-*O*-methoxyaranciamycin (**7a**).

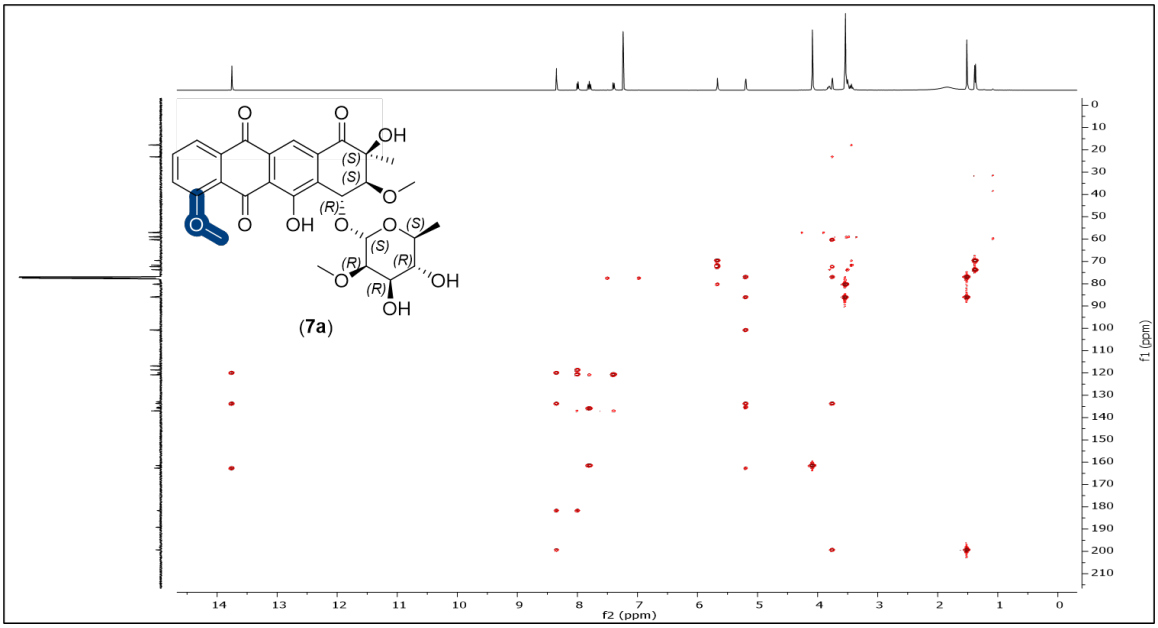

Figure S2.80. HMBC spectrum ($CDCl_3$, 400 MHz) of 4-*O*-methoxyaranciamycin (**7a**).

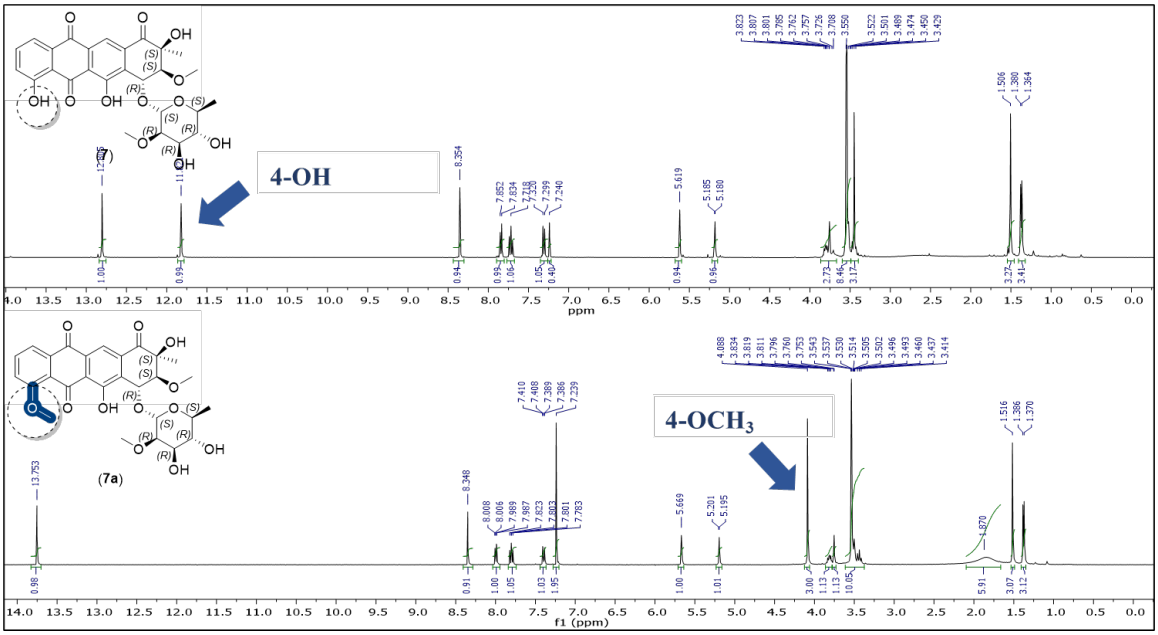

Figure S2.81. Comparison of the ^{1}H NMR spectrum ($CDCl_3$, 400 MHz) of **7** and **7a**.

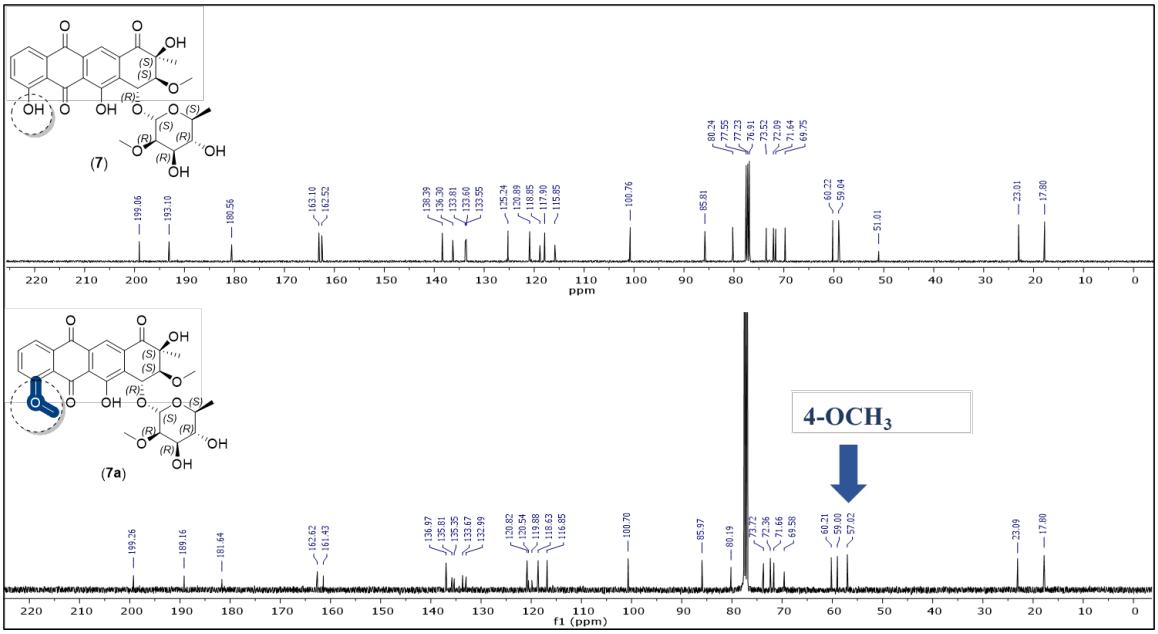

Figure S2.82. Comparison of the ^{13}C NMR spectrum ($CDCl_3$, 100 MHz) of **7** and **7a**.

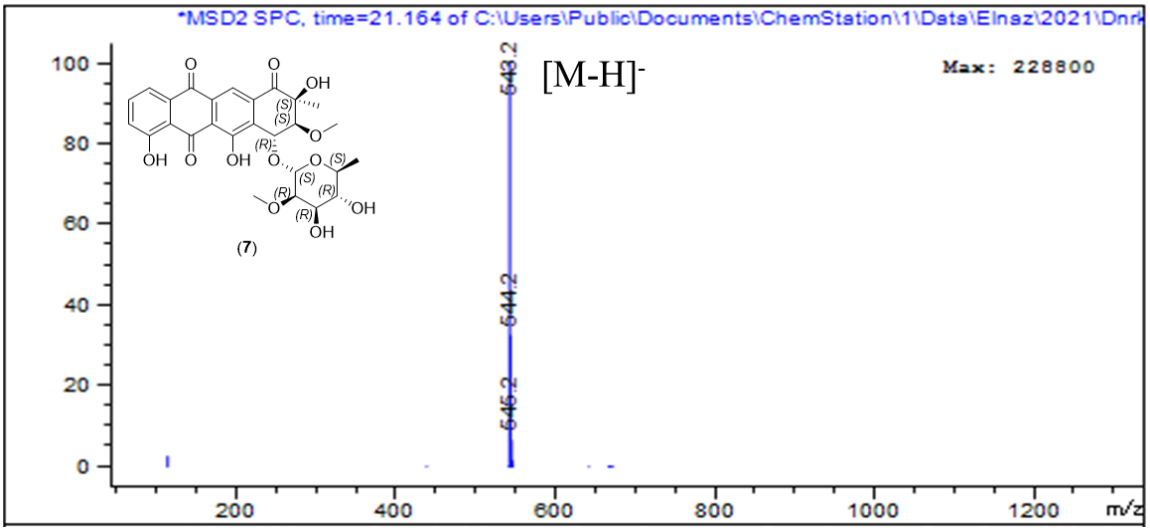

Figure S2.83. (-)-ESI-MS of aranciamycin (**7**; MW: 544.2).

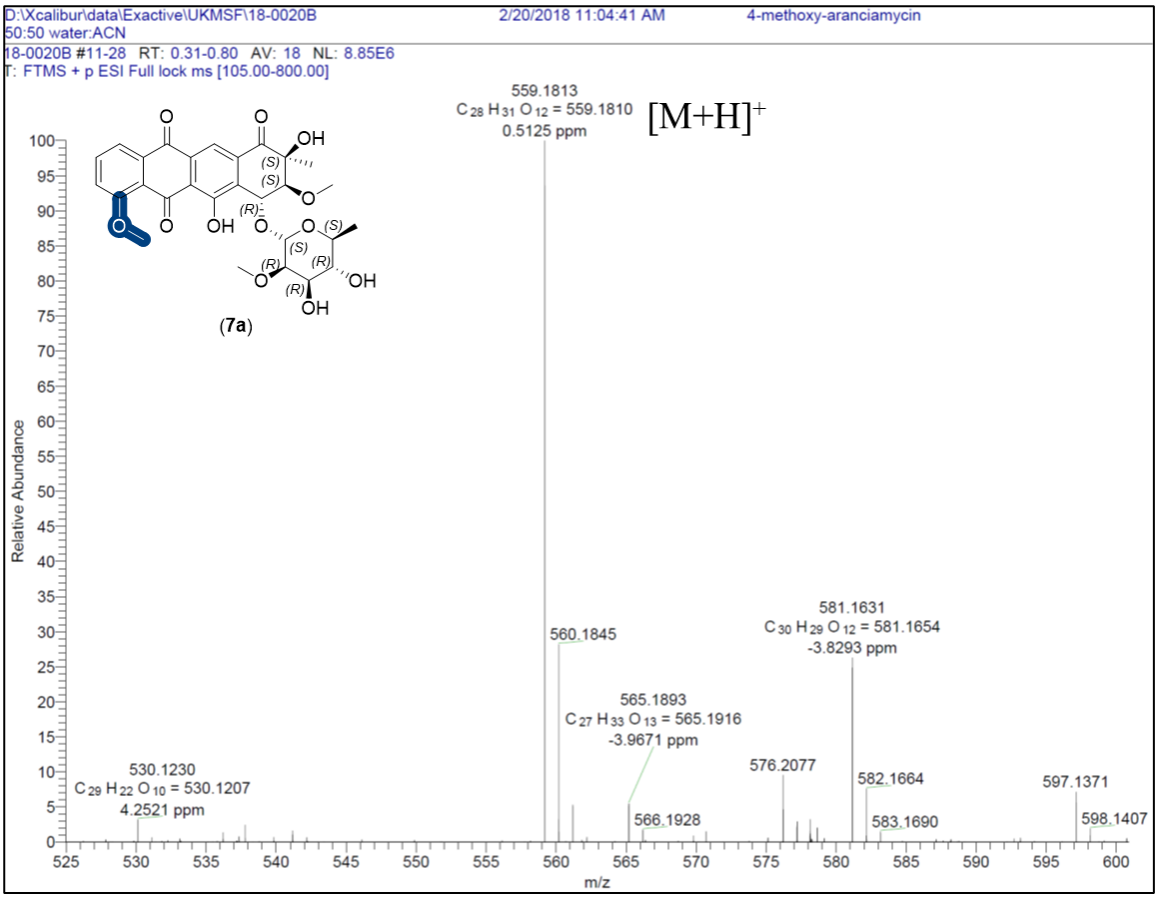

Figure S2.85. (+)-HRESI-MS of 4-*O*-methoxyaranciamycin (**7a**).

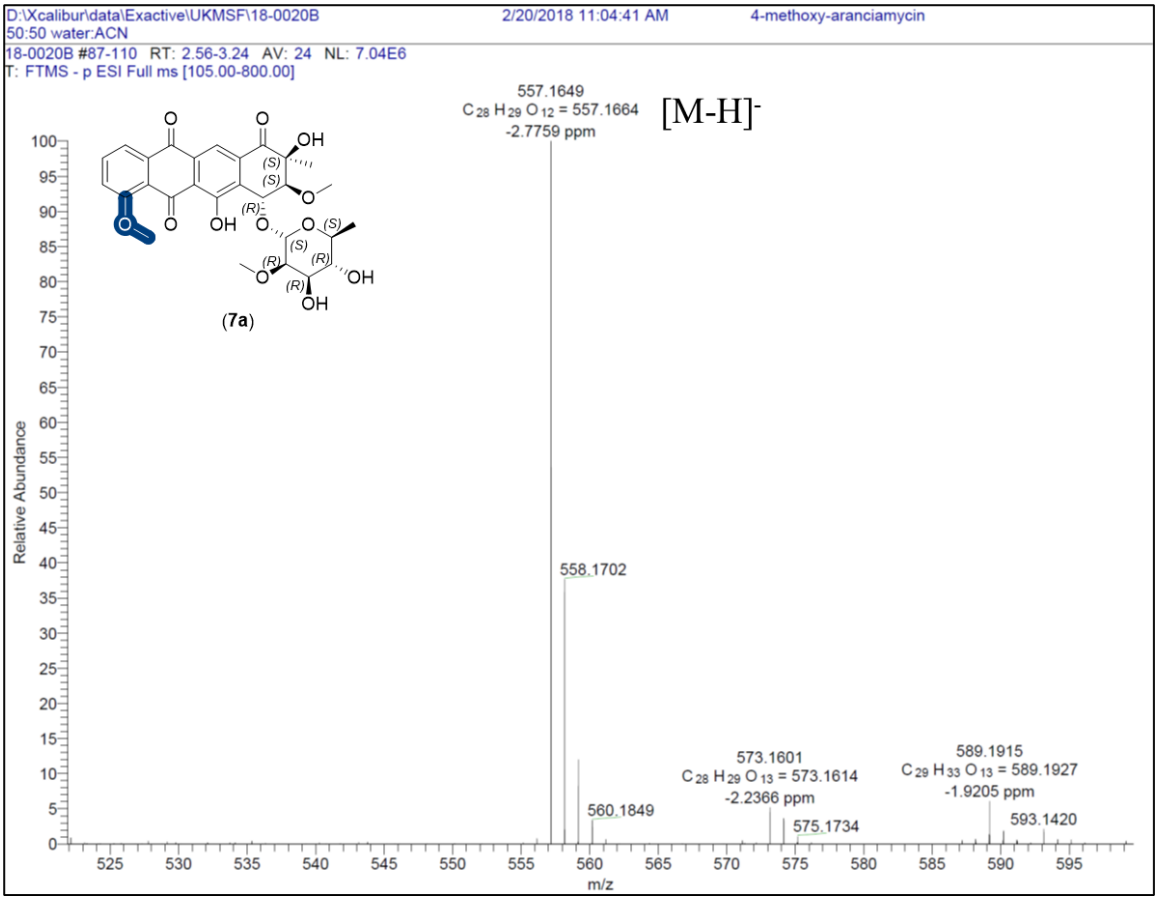

Figure S2.85. (-)-HRESI-MS of 4-*O*-methoxyaranciamycin (**7a**).

Chapter Three: Broadening the scope of DnrK unnatural acceptors and donors

3.1 Introduction

Methyltransferases (MTs) are ubiquitous biocatalysts that modulate the chemical and functional properties of a vast array of natural biomolecules through the simple addition of a methyl group.[1-6] While MTs are generally perceived to display native substrate methyl acceptor fidelity, a unique feature of MTs is their ability to use non-native *S*-adenosyl-L-methionine (AdoMet or SAM) analogues as co-substrates to enable facile non-native alkylation of DNA, RNA, proteins and small molecule metabolites. This unique MT biocatalytic capability has been leveraged *in vitro* and in cells for MT-catalyzed regio- and stereoselective biomolecule modification to introduce new structural features, bioorthogonal chemoselective functional groups and/or molecular probes.[1-6] Among the many biochemically annotated biosynthetic MTs, the carminomycin (CAR) 4-*O*-MT DnrK catalyzes the late-stage conversion of CAR to daunorubicin (DNR; **Figure 3.1A**).[7-10] Recent DnrK acceptor profiling studies revealed unusual permissivity, with demonstrated DnrK-catalyzed turnover of an array of structurally-diverse non-native natural products including anthracyclines, angucyclines, enediynes, flavonoids, pyranonapthoquinones and polyketides.[11] To further explore DnrK's biocatalytic potential, here we describe a new observed activity of DnrK to catalyze *S*- and *N*-alkylation of thionucleobases, thionucleosides and benzoxazoles in the context of both AdoMet (methyl) or non-native AdoMet (alkyl) donors. To facilitate this study, we also highlight an improved scalable, chromatography-free platform for non-native AdoMet synthesis and introduce *S*-(cyclopropylmethyl)-L-homocysteine as an alkyl donor for the first time in

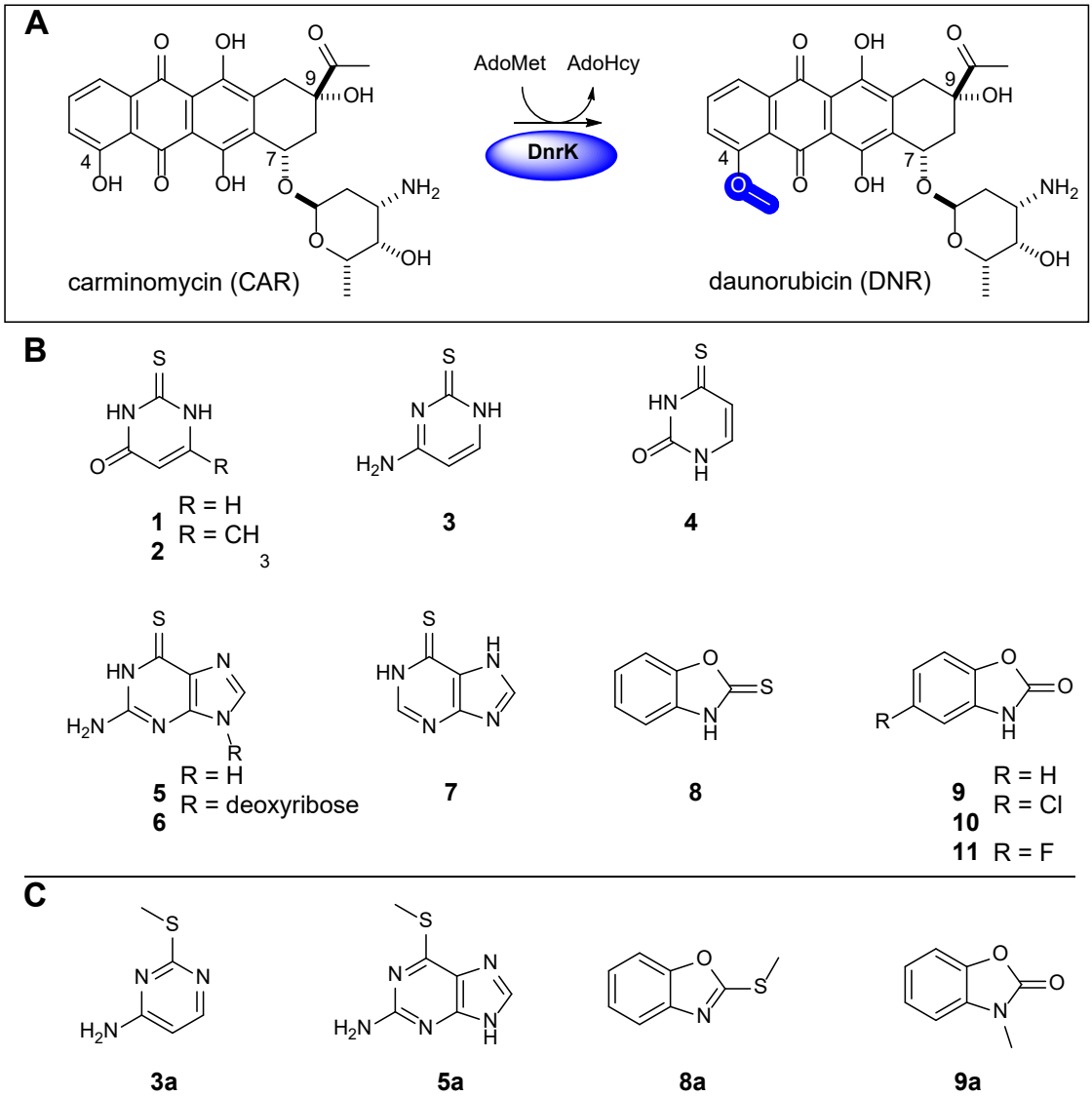

Figure 3.1. General DnrK reaction with **(A)** native substrate carminomycin (CAR) **(B)** Non-native DnrK acceptors (**1-11**) **(C)** commercial standards. The DnrK regioselectivity is highlighted in blue.

MT-catalyzed reactions. To illustrate the general utility of the AdoMet synthetic platform, non-native donors were evaluated with DnrK (in both *O*- and *S*-alkylation reactions) and the coumermycin A1 biosynthetic *C*-MT CouO[12] (in representative *C*-alkylation reactions).

3.2 Results and discussion

A recent DnrK pilot screen with structurally diverse small molecules revealed putative DnrK-catalyzed turnover of heteroatom-containing non-native acceptors.[11] To extend this preliminary discovery and further probe DnrK's biocatalytic capabilities, DnrK was tested with a representative set of thiopyrimidines, thiopurines and benzoxazoles (**Figure 3.1B**). DnrK reactions (50 mM Tris-HCl, pH 8.0; 3.2 mM AdoMet; 1 mM acceptor **1-11**; 30 and 100 μM of purified *S*-adenosyl homocysteine hydrolase (SAHH) and DnrK, respectively; 37 °C, 16 h) were analyzed via LC-MS (see the Supporting Information) and new methylated products were identified by a shift in both mass (D*m/z* = +14) and retention time compared to controls in the absence of DnrK. Out of 15 putative acceptors tested, 11 led to new product (**Figure 3.1B**) with yields ranging from 6% to quantitative conversion (**Table 3.1**). SAHH (an enzyme that degrades the co-product SAH/AdoHcy) was included in reactions to favor desired product formation via a shift in the reaction equilibrium. No turnover was observed in the presence of representative commercially available product standards (**Figure 3.1C**).

Among the thiopyrimidines, quantitative conversion was observed with thiouracil (**1**) while the corresponding 6-methyl-substituted comparator (**2**, 36%), thiocytosine (**3**, 57%) and 4-thiouracil (**4**, 84%) also led to methylated products. To determine DnrK

Table 3.1. Non-native DnrK acceptors and their putative methylated products. Predicted DnrK regioselectivity is highlighted in grey and determined DnrK regioselectivity is highlighted in blue.

ID	Compound	Structure	Mass (m/z)		Product	Mass (m/z)		%
			Theoretical	Experimental		Theoretical	Experimental	
1	thiouracil		128.0	127.0[b]	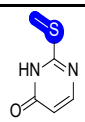	142.0	143.0[a]	quant.
2	6-methyl-2-thiouracil	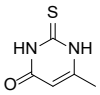	142.0	141.0[b]	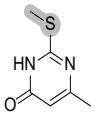	156.0	155.0[b]	36
3	thiocytosine	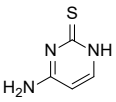	127.2	128.2[a]	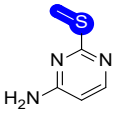	141.2	142.2[a]	57
4	4-thiouracil	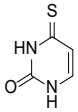	128.0	127.0[b]	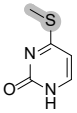	142.0	143.0[a]	84
5	thioguanine	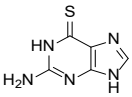	167.0	166.0[b] 168.0[a]	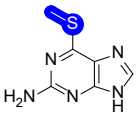	181.0	180.0[b] 182.0[a]	quant.
6	thioguanosine	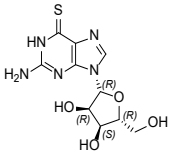	299.0	298.0[b]	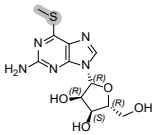 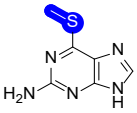	313.0 181.0	314.0[a] 180.0[b]	28 65
7	6-mercaptopurine	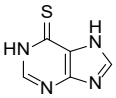	152.0	151.0[b] 153.0[a]	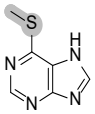	166.0	165.0[b] 167.0[a]	quant.
8	2-mercaptobenzoxazole	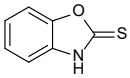	151.2	150.0[b]	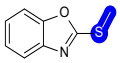	165.2	166.2[a]	quant.

ID	Compound	Structure	Mass (m/z)		Product	Mass (m/z)		%
			Theoretical	Experimental		Theoretical	Experimental	
9	2-benzoxazolinone	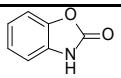	135.0	134.0[b]	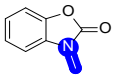	149.0	150.0[a]	20
10	chlorzoxazone	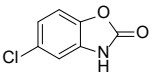	169.0	170.0[a]	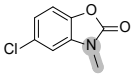	183.0	184.0[a]	6
11	5-fluoro-2(3H)-benzoxazolone	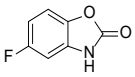	153.0	152.0[b]	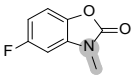	167.0	168.0[a]	12

[a] (+)-ESIMS, $[M + H]^+$; [b] (-)-ESIMS, $[M - H]^-$

regioselectivity for **1**, the reaction was scaled and subsequent product purification and structure elucidation revealed 2-(methylthio)pyrimidin-4(3*H*)-one (**1a**) as the final product (**Figure S3.1**). The nature of the DnrK-catalyzed **3** product was determined by co-elution with the commercial standards 2-(methylthio)pyrimidin-4-amine (**3a**, **Figure S3.2**). For thiopurines, quantitative conversion was observed with thioguanine (**5**) and 6-mercaptopurine (**7**). Turnover was also observed with the nucleoside of **5** (thioguanosine, **6**, 28%) where the predominate observed product (**5a**, 65%) derived from non-enzymatic hydrolysis of the glycosidic bond under reaction conditions. The nature of the DnrK-catalyzed **5** product (from either the thioguanine or thioguanosine reactions) was determined by co-elution with the commercial standard 6-methylthioguanine (**5a**, **Figure S3.3**). For representative structurally similar benzoxazoles, quantitative conversion was also observed with 2-mercaptobenzoxazole (**8**) while reduced turnover was observed among comparators lacking the C2 thiol (2-benzoxazolinones **9-11**, <20%). Intriguingly, a shift from *S*-methylation (**8**) to *N*-methylation (**9-11**) was observed in this latter series based on the co-elution of reaction products with commercial standards 2-(methylthio)benzoxazole and 3-methyl-2-benzoxazolinone (**8a** and **9a**, respectively; **Figure S3.4 and S3.5**). Corresponding DnrK kinetic parameters for a representative thiopyrimidine (**1**), thiopurine (**5**) and benzoxazole (**8**) also tracked with the end point assays (**Figure 3.2** and **Table 3.2**). While the observed k_{cat} in the presence **8** approached that of native substrate CAR, the three non-native substrates displayed 17-40-fold increases in K_m.

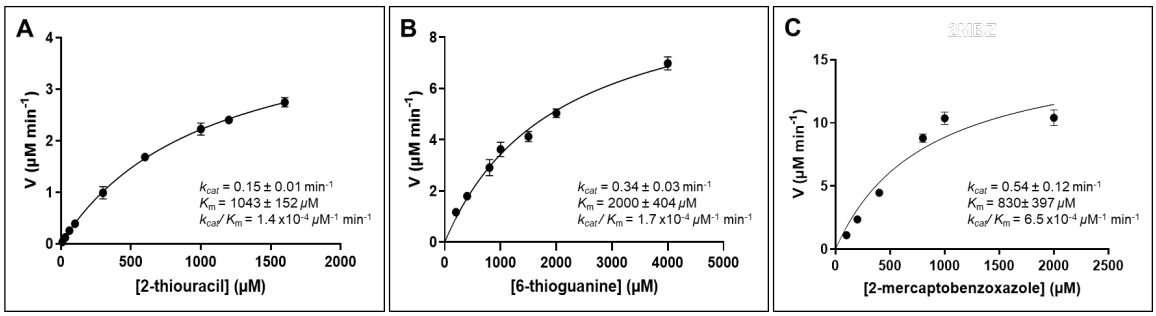

Figure 3.2. Determination of kinetic parameters for DnrK-catalyzed reactions using non-native substrates. [DnrK] = 30 μM in all experiments and assays were conducted via HPLC Method **A**. **(A)** [thiouracil (**1**)] = varied, [AdoMet] = 3.2 mM. **(B)** [thioguanine (**5**)] = varied, [AdoMet] = 3.2 mM. **(C)** [2-mercaptobenzoxazole (**8**)] = varied, [AdoMet] = 3.2 mM.

Table 3.2. Kinetic parameters of DnrK with native and non-native substrates.

Substrate	k_{cat} (min^{-1})	K_m (μM)	k_{cat}/K_m (min^{-1} μM^{-1})	k_{cat}/K_m (relative)
CAR	0.65 ± 0.03	50 ± 2	0.013	1
thiouracil (**1**)	0.15 ± 0.01	1043 ± 152	1.4×10^{-4}	0.011
thioguanine (**5**)	0.34 ± 0.03	2000 ± 404	1.7×10^{-4}	0.013
2-mercaptobenzoxazole (**8**)	0.54 ± 0.12	830 ± 397	6.5×10^{-4}	0.05

A small diverse set of non-native AdoMet alkyl donors were subsequently selected to next assess the ability of DnrK to accommodate non-native alkyl donors within the context of non-native thiopyrimidines, thiopurines and benzoxazoles. Such AdoMet donors are synthesized via chemical synthesis[15-17] or chemoenzymatic methods. The latter typically employ either a methionine adenosyltransferase (MAT) with ATP and a non-native L-methionine (Met)[18-20] or a halogenase (e.g., SalL or FDAS) with 5′-chloro or 5′-fluoro-5′-deoxyadenosine.[21,22] For the MAT-based strategies, various *S*-alkylation strategies have enabled the synthesis of requisite non-native Met analogues,[23-26] all of which require multiple steps with often tedious product purification at each stage. To streamline this approach, we developed a modified scalable 4 step synthetic strategy that avoids chromatography in most cases simply by virtue of Boc protection (**Figure 3.3**). Step 1 was acid-catalyzed synthesis of L,L-homocystine (**12**) from inexpensive 65 g of Met following a previously reported method.[27] The corresponding disulfide **12** was recovered as a precipitate to afford 23 g of optically pure **12** in 39% yield. Facile Boc-protection of **12** (Step 2) was key to subsequent chromatography-free manipulations. Boc was selected as a hydrophobic protecting group resistant to the Step 3 dissolving sodium metal reduction. Nearly 36 g of the corresponding product **13** was recovered via extraction in 89% yield with an estimated purity of > 99% based on NMR. Step 3 followed our previous protocol[18] for single vessel Na/NH3 reduction and *S*-alkylation in the presence alkyl halide. Eight diverse alkyl halides were assessed in this reaction, the crude products from six of which could be recovered as precipitates in yields ranging from 84% to quantitative recovery. Products deriving from crotyl bromide (purchased as 85% mixture of cis and trans isomers) and 1-azido-2-bromoethane were purified via chromatography to afford the

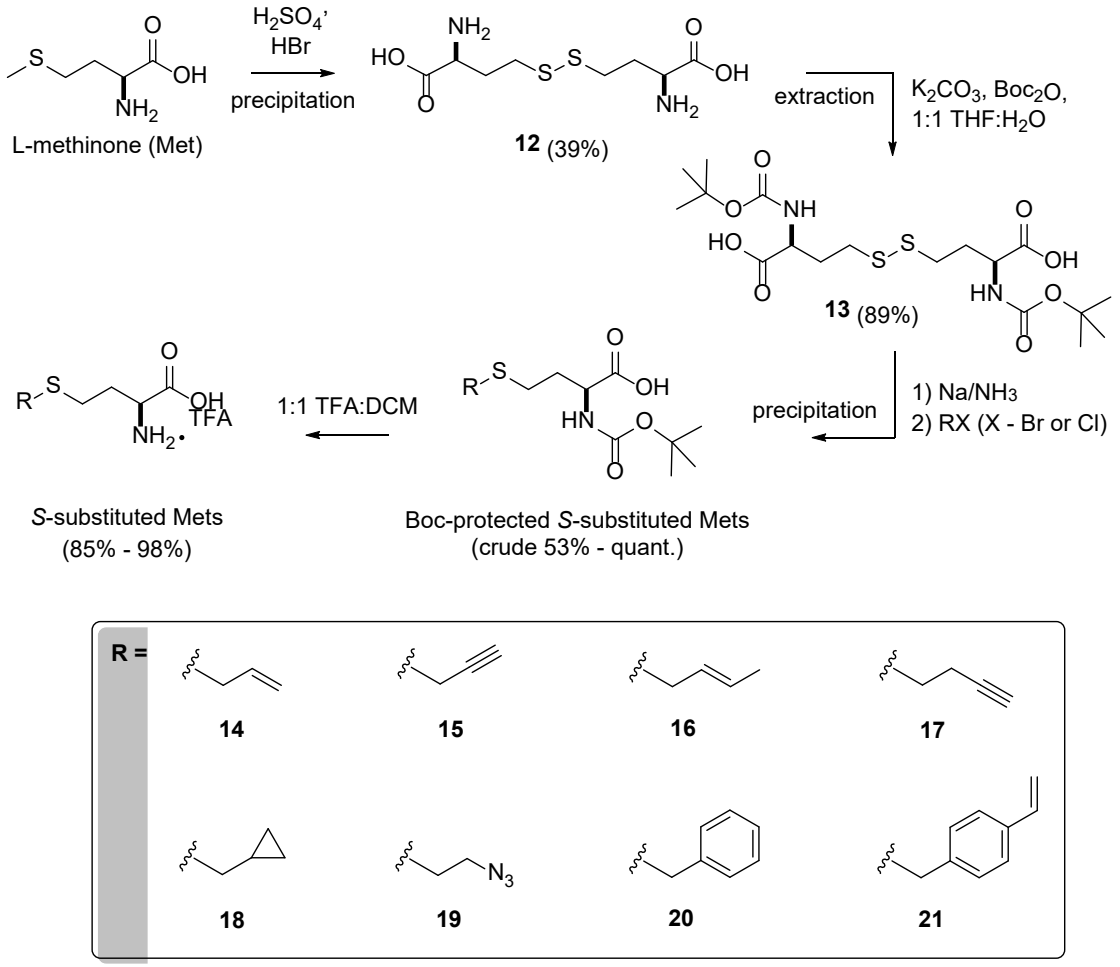

Figure 3.3. Synthesis steps of S-substituted Met analogues (**14-21**).

desired **16** (**Figure S3.6**) and **19** in 65% and 53% yields, respectively. In Step 4, Boc-protected non-native Met analogues were deprotected using TFA/DCM (1:1) in ≤10 min at room temperature and the final TFA salts of Met analogues (**14-21**), recovered via evaporation (yields ranging from 85%-98% and estimated purities ranging from 95%->99% based NMR) and used directly in all MAT-catalyzed and MAT/MT-coupled reactions.

Compatibility of the new Met analogue preparative synthetic strategy with downstream MAT and MAT/MT coupled reactions was subsequently evaluated (**Figure 3.4**). Previous studies revealed the catalytic subunit of human AdoMet synthase (hMAT2A) as a uniquely permissive catalyst to enable the synthesis of non-native AdoMet analogues.[18] The non-native *S*-substituted Met series from **Figure 3.3** were evaluated as hMAT2A substrates following a similar strategy (**Figure 3.4A**). Specifically, reactions [1 mM ATP, 1 mM *S*-substituted Met (*i.e.*, **14-21**), 50 μM of hMAT2A in 25 mM Tris-HCl pH 8.0, 10 mM $MgCl_2$, 50 mM KCl at 37 °C for 16 h] were analyzed via LC-MS where turnover was based on the combined desired product and AdoMet analogue-derived degradation product 5'-methyl-thio(seleno)-5'-deoxyadenosine (MTA) present.[28,29] As controls, no turnover was observed in the absence of hMAT2A, *S*- substituted Met or ATP. Importantly, this study revealed TFA salts derived from the new Met analogue preparative synthetic strategy to be well-tolerated by hMAT2A. In particular, the production of 7 out 9 analogues (**Figure 3.4A**) exceeded that deriving from the best previously reported chemoenzymatic preparations (**Ado14**-**Ado17** and **Ado19**; 50%, 5%, 3%, 17% and 19% respectively).[18] In some cases [*e.g.*, Ado-vinylbenzyl **21** (15%) and the new analogue Ado-cyclopropylmethyl **18** (23%)], poor solubility under standard assay conditions likely

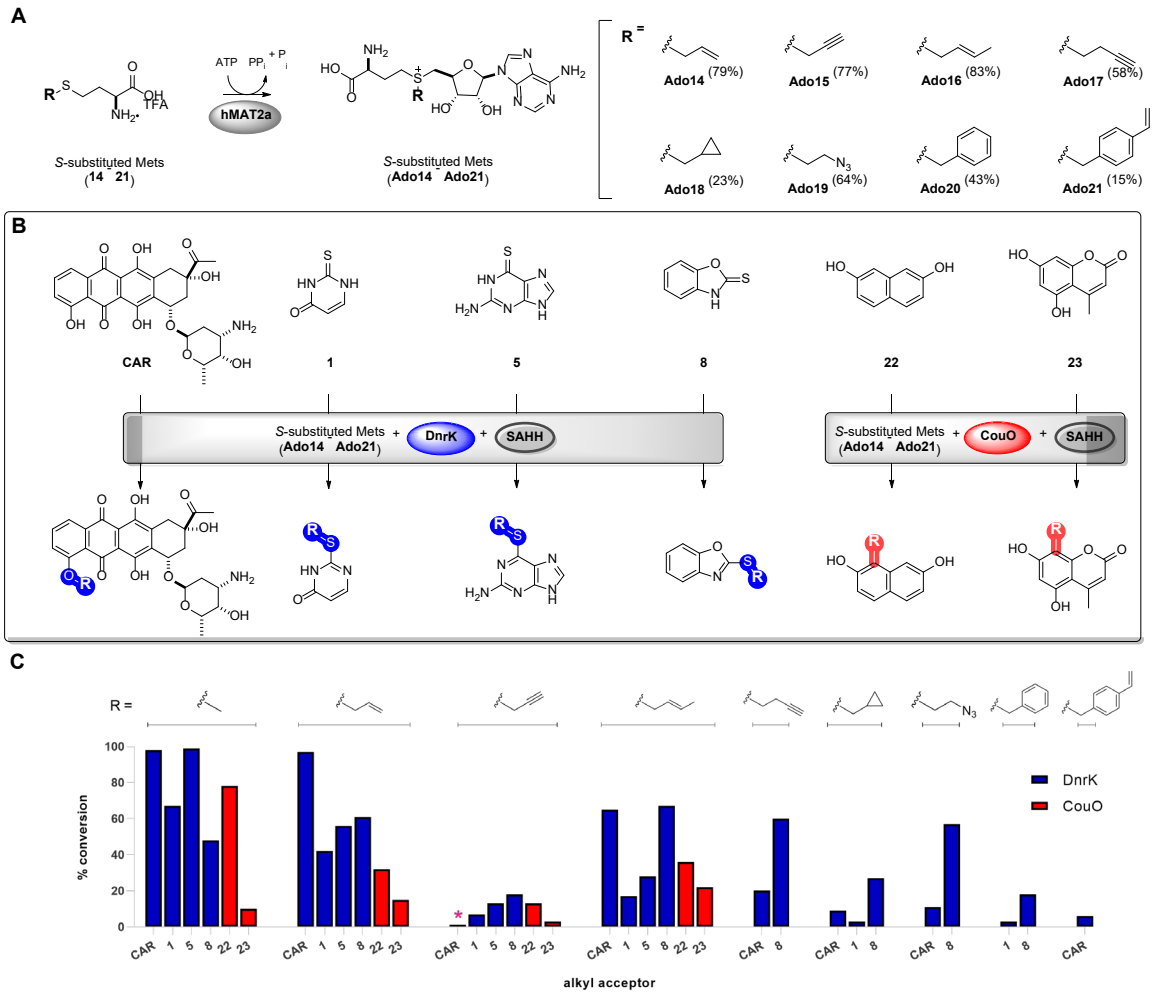

Figure 3.4. (A) Schematic overview and turnover percentage of synthetic *S*-substituted Met analogues (**14-21**) to the corresponding AdoMet donors (**Ado14-Ado21**) catalyzed by hMAT2A. (**B**) These AdoMet analogues are accepted by represented DnrK and CouO MTs to enzymatically alkylate native (CAR) and selected non-native DnrK acceptors (**1**, **5** and **8**) and that of non-native CouO acceptors (**22** and **23**). (**C**) Reaction conversions of alkyl acceptors determined by LC-MS. Conversion rate of degraded propargyl-CAR analogue to propanone-CAR is designated by a pink star.

contributed to reduced proficiencies. Importantly, this assessment confirmed that synthetic reagents deriving from the revised synthetic preparative Met analogue method were directly compatible with MAT-catalyzed reactions. The combined chemoenzymatic study enabled efficient access to 6 previously reported analogues (**Ado14**-**Ado17** and **Ado19**-**Ado20**) and modest entry to one previously unreported comparator (**Ado18**). Six members (**Ado14**-**Ado17**, **Ado19** and **Ado21**) of this diverse set contain chemoselective functional groups.

DnrK and the coumermycin A_1 *C*-MT CouO[15-17] were selected as MT models to next evaluate the compatibility of newly synthesized non-native Met analogues with single vessel MAT/MT coupled reactions (Figure 1B). Specifically, the non-native *S*-substituted Met series from Scheme 2 were evaluated as hMAT2A/DnrK or hMAT2A/CouO substrates following standard reaction protocols.[16,18] Specifically, reactions [1 mM ATP, 2 mM *S*-substituted Met donor (*i.e.*, **14**-**21**), 1 mM acceptor (*i.e.*, CAR, **1**, **5**, **8**, **22** or **23**), 50 μM of hMAT2A, 100 μM MT (DnrK or CouO), 30 μM SAHH in 25 mM Tris-HCl pH 8.0, 10 mM $MgCl_2$, 50 mM KCl at 37 °C for 16 h] were analyzed for product formation via LC-MS. No reaction was observed in controls lacking Met analogue, hMAT2A and MT (DnrK or CouO).

For DnrK-catalyzed reactions, acceptor proficiency in the presence of non-native donors generally paralleled previously described kinetic competence (k_{cat}/K_m) and end point assays under saturating AdoMet (*i.e.*, **8** > **1** ≈ **5** for non-native *S*-alkylation/benzylation). Consistent with the isolation and structure elucidation of the DnrK-catalyzed product in the presence of CAR and **Ado14** (4-*O*-allyl CAR; **Figure S3.7** and **Table 3.3**), regioselectivity of all DnrK-catalyzed reactions in the presence of non-

Table 3.3. ^{13}C (150 MHz) and ^{1}H (600 MHz) NMR spectroscopic data of 4-*O*-allyloxycarminomycin in CD_3OD.[a]

No.	4-*O*-allyloxycarminomycin				
	δ_C, type	δ_H (mult, *J* in [Hz])	No.	δ_C, type	δ_H (mult, *J* in [Hz])
1	120.9, CH	8.03 (dd, 7.7, 1.0)	11a	112.6, C	
2	137.2, CH	7.84 (dd, 8.5, 7.7)	12	188.5, C	
3	121.9, CH	7.58 (dd, 8.6, 1.1)	12a	136.9, C	
4	161.7, C		13	213.5, C	
4a	122.3, C		14	24.5, CH_3	2.35 (s)
5	188.6, C		1′	101.3, CH	5.49 (brd, 3.8)
5a	112.8, C		2′	29.7, CH_2	2.05 (td, 12.8, 3.9)
					1.90 (dd, 12.7, 4.7)
6	157.7, C		3′	48.7, CH	3.60 (ddd, 12.8, 4.7,
6a	136.2, C		4′	68.2, CH	3.65 (brm)
7	72.2, CH	5.16 (dd, 5.4, 2.8)	5′	68.0, CH	4.31 (m)
8	37.3, CH_2	2.34 (dd, 14.7, 2.7)	6′	17.1, CH_3	1.29 (d, 6.6)
		2.21 (dd, 14.6, 5.4)			
9	77.4, C		1″	71.2, CH_2	4.82 (brm)
10	33.3, CH_2	3.09 (s)	2″	133.9, CH	6.16 (ddt, 17.2,
10a	135.8, C		3″	118.0,	5.72 (dq, 17.3, 1.8)
11	156.5, C			CH_2	5.36 (dq, 10.7, 1.6)

[a]Assignments supported by COSY, HSQC and HMBC experiments.

native donors were anticipated to mirror previously described studies. Similar to prior precedent,[15] smaller *β*-unsaturated donors (*e.g.*, **Ado14**-**Ado16**) generally functioned best in DnrK-catalyzed reactions. However, DnrK-catalyzed reactions of **8** in combination with larger donors (*e.g.*, **Ado16**-**Ado19** and **Ado20**) displayed curious synergistic improvements, consistent with the DnrK biocatalytic flexibility noted in Chapter 2. While degradative conversion of **Ado15** to the corresponding *S*-propanone species was previously observed in chemoenzymatic MT-catalyzed reactions,[30,31] such degradation in the current study was only observed in DnrK-catalyzed CAR-*O*-alkylation reactions. Corresponding CouO model reactions evaluated C1-alkylation of previously characterized non-native acceptors 2,7-naphthalenediol (**22**) and C8-alkylation of 7-dihydroxy-4-methylcoumarin (**23**).[12-14] In contrast to DnrK, CouO-catalyzed reactions displayed less overall donor permissivity in the context of non-native acceptors **22** and **23** but, like DnrK, also displayed some preference to smaller *β*-unsaturated donors (*e.g.*, **Ado14-Ado16**). Cumulatively, the combined reactions in **Figure 3.4B** enabled the synthesis of 12 known compounds[32] and 22 previously unreported compounds. In the context of CAR, this also allowed for a simple proof of concept assessment of the impact of CAR 4-*O*-alkylation on cancer cell line cytotoxicity (**Figure 3.5**). Specifically, increasing the size of the alkyl substituent led to notable reductions in potency against the human non-small cell carcinoma cell line A549 [IC_{50}: CAR, 26 nM 4-*O*-methyl CAR (*i.e.*, DNR), 314 nM; 4-*O*-allyloxy CAR, 1 μM].

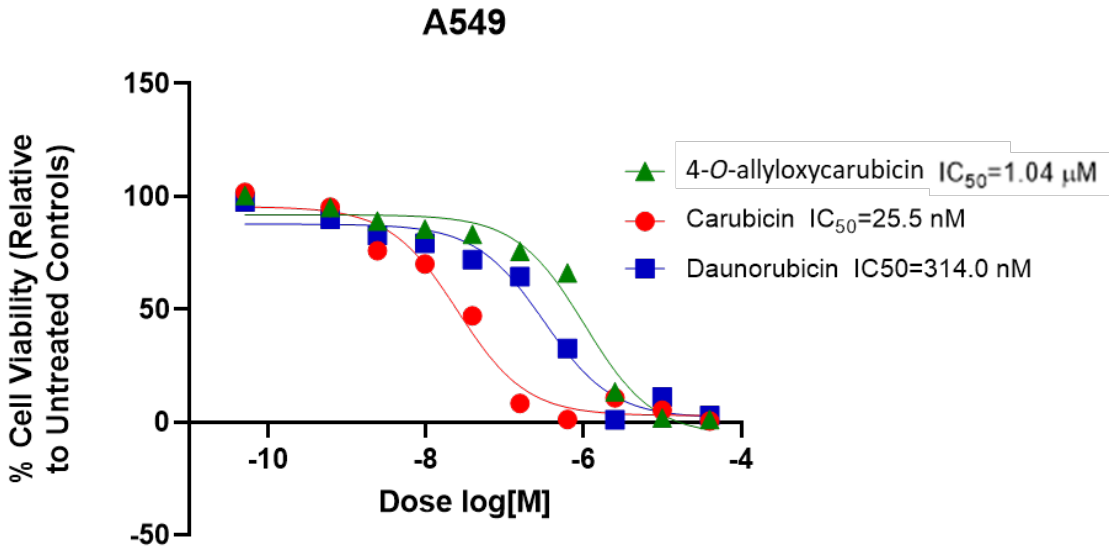

Figure 3.5. Dose-response of compounds carubicin (CAR), daunorubicin (DNR) and 4-*O*-allyloxycarminomycin against A549 (non-small cell lung) human cancer cell line (72 h). A549: IC50 for the compounds CAR (25.5 nM), DNR (314 nM) and 4-*O*-allyloxycarminomycin (1.04 µM).

R3.3 Conclusions

In conclusion, this work advances a refined preparative strategy for the synthesis of non-native AdoMet donors, exposes new DnrK biocatalytic *O*-, *S*- and *N*-alkylating capabilities and highlights the chemoenzymatic synthesis of previously unreported carminomycins and model thiopyrimidines, thiopurines and benzoxazoles. While most of the *O*-, *S*- or *N*-alkyl/benzyl products of the DnrK-catalyzed model reactions described are readily accessible via conventional synthesis, this work presents the potential for new synthetic biology applications using MAT-engineered product strains fed with non-native Met analogues. This work also exposes new opportunities for MT catalytic bioorthogonality. Specifically, while MT regio- and stereoselectivity is governed by ligand active-site affinity and orientation, this study also sets the stage to explore the potential for altering MT selectivity via putative fine-tuning of acceptor nucleophile reactivity (*e.g.*, via site-selective incorporation of thiopyrimidines/thiopurines in nucleic acid substrates).

3.4 Experimental procedures

3.4.1 General materials and methods

4-Methyl-2-thiouracil, thioguanosine and 6-mercaptopurine were obtained from the Spectrum Collection (Microsource Discovery Systems, Inc., Gaylordsville, CT). Carminomycin was purchased from Cayman Chemical Company (Ann Arbor, MI). *E. coli* BL21(DE3) competent cells and *S*-adenosyl-L-methionine (AdoMet, 32 mM solution in 10% EtOH/5 mM H_2SO_4) were purchased from New England Biolabs (Ipswich, MA). Nickel-nitrilotriacetic acid resin was purchased from Thermo Fisher Scientific (Waltham,

MA). The A549 cell line were obtained from ATCC (Manassas, VA). The gene sequence encoding*Streptomyces rishiriensis C*-methyltransferase (CouO) can be found at GenBank as accession numberQ9F8T9.1.[39] All general chemicals and reagents were purchased from Sigma-Aldrich (St. Louis, MO, USA), unless otherwise stated.

High resolution electrospray ionization (HRESI) mass spectra were recorded on an AB SCIEX Triple TOF® 5600 system (AB Sciex, Framingham, MA, USA) coupled with an Eksigent Ekspert micro LC 200 system with source temperature of 150 °C, ion spray voltage floating (ISVF) of 5000 V in positive mode. HPLC-UV/MS analyses were accomplished with an Agilent Infinity Lab LC/MSD mass spectrometer (MS Model G6125B; Agilent Technologies, Santa Clara, CA, USA) equipped with an Agilent 1260 Infinity II Series Quaternary LC system and a Phenomenex NX-C18 column (250 × 4.6 mm, 5 µm) [Method **A**: solvent A: H_2O/0.1% formic acid, solvent B: CH_3CN; flow rate: 0.5 mL min-1; 0-30 min, 5-100% B (linear gradient); 30-35 min, 100% B; 35-36 min, 100%-5% B; 36-40 min, 5% B]. Semi-preparative HPLC was accomplished using Agilent 1260 Infinity II (Prep HPLC) system equipped with a Diode Array Detector (DAD) and a Gemini 5 µm C18 110 Å, LC column 250 × 10 mm (Phenomenex, Torrance, CA) [Method **B**: solvent A: H_2O/0.025% TFA; solvent B: CH_3CN; flow rate: 5.0 mL min^{-1}; 0-2 min, 20% B; 2-20 min, 20-75% B; 20-21 min, 75-100% B; 21-23 min, 100% B; 23-24 min, 100-10% B; 24-25 min, 10% B; Method **C**: solvent A: H_2O/0.025% TFA; solvent B: CH_3CN; flow rate: 5.0 mL min^{-1}; 0-2 min, 90% B; 2-28 min, 90-25% B; 28-31 min, 25-0% B; 31-33 min, 0% B; 33-34 min, 0-90% B; 34-36 min, 90% B; Method **D**: solvent A: H_2O/0.025% TFA; solvent B: CH_3CN; flow rate: 5.0 mL min^{-1}; 0-2 min, 95% B; 2-14 min, 95-75% B; 14-16 min, 75-25% B; 16-18 min, 25% B; 18-19 min, 25-95% B; 19-20 min, 95% B].

All NMR spectra were recorded at 500 or 400 MHz for ^{1}H and 125 or 100 MHz for ^{13}C with Varian Inova NMR spectrometers (Agilent, Santa Clara, CA, USA) unless otherwise noted. NMR spectra for 2-(methylthio)pyrimidin-4(3*H*)-one (**1a**) and 4-*O*-allyoxycarminomycin were recorded at 600 MHz (14.1 T) using a Bruker Avance Neo console equipped with a TCI 5 mm cryoprobe (Bruker BioSpin Corporation, Billerica, MA). Corresponding δ-values reference respective solvent signals [CD_3OD, δH 3.31 ppm, δC 49.15 ppm; D_2O, δH 4.65 ppm; TFA, δC 116.5 and 164.4 ppm; DMSO-d6, δH 2.50 ppm, δC 39.51 ppm] and multiplicities are indicated as s (singlet), d (doublet), dd (doublet of doublet), t (triplet), q (quartet) and m (multiplet).

3.4.2 Heterologous enzyme production and enzyme purification

N-His_6-DnrK,[40] *N*-His_6-*S*-adenosyl-L-homocysteinease (SAHH) and *N*-His_6-hMAT2A[18] were produced and purified as previously described and utilized for all studies. For CouO, a plasmid construct pET28a-His_6-CouO bearing the codon-optimized *couO* gene was purchased from GenScript (Cat. No. SC1010; Piscataway, NJ). This construct was confirmed via sequencing, transformed into *E. coli* BL21(DE3) and subsequent heterologous protein production and affinity purification of *N*-His_6-CouO followed standard DnrK protocol.[40] Approximately 6 mg of purified *N*-His_6-CouO was obtained from 1 L fermentation based on A_{280} and ε_{280}= 31065. The final purified protein was drop frozen and stored at -80°C until used.

3.4.3 In vitro enzymatic assays

All chemoenzymatic reactions were conducted following previously reported protocols.[18,40] Product formation for each reaction was assessed using HPLC method **A** and based on the integration of species at 254, 280, or 320 nm as well as HRMS and ESI mass spectra with positive (+) mode. The assays were repeated twice under identical conditions and the reported percentage conversions represent an average value of two assays.

3.4.4 Kinetic measurements of DnrK reactions

DnrK kinetic parameters were determined for thiouracil (**1**), thioguanine (**5**) and 2-mercaptobenzoxazole (**8**) (**Table 3.2**) following our previously reported method.[40] Kinetic studies employed 30 μM of DnrK under saturating AdoMet (3.2 mM) and variable concentration of **1** [10 μM to 1600 mM], **5** [200 μM to 4000 mM] or **8** [100 μM to 2000 mM] and kinetic parameters were derived from Michaelis-Menten reciprocal plots (**Figure 3.2**).

*3.4.5 General procedure for the large-scale production of L,L-homocystine (**12**)*

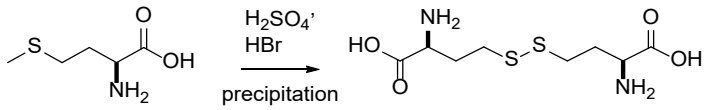

L-methinone (Met) **12** (39%)

Commercially available L-methionine (64.8 g, 434 mmol), 48% HBr aqueous solution (45 mL, 568 mmol) and concentrated H_2SO_4 (48.7 mL, 869 mmol) were treated in a manner identical to the previously published study[27] with selected reaction conditions. The reaction was heated for 9 h at 100°C while stirring in a stream of N_2. The precipitated crystal crude was then dissolved in 300 mmol of 2 N solution of NaOH, followed by 3 h

stirring at room temperature and neutralization by 37% HCl to obtain 23 g of white solid **12** (39% yield). ^{1}H NMR (D_2O/TFA = 20/1, 400 MHz): δ 3.84 (t, *J* = 6.5 Hz, 1H), 2.50 (t, *J* = 6.5 Hz, 2H), 1.90-2.08 (m, 2H); ^{13}C NMR (D2O/TFA = 20/1, 100 MHz) δ 173.2, 53.2, 34.1, 30.9 ppm.

*3.4.6 General procedure for the large-scale production of N-Boc-L,L-homocystine (**13**)*

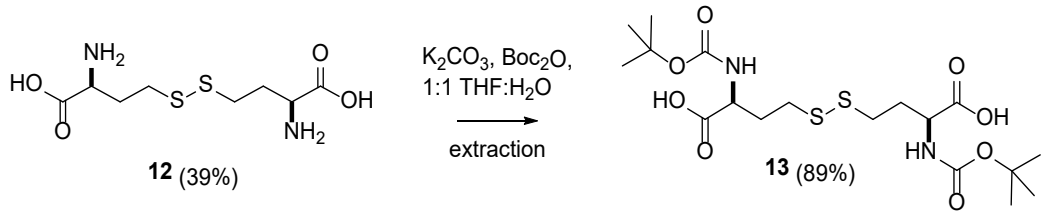

The **12** prep (23 g, 85.70 mmol) was dissolved in 300 mL THF/ddH2O (1:1) and to this was added K_2CO_3 (35.5 g, 256.8 mmol) at 0°C under stirring until a white color solution created. Subsequently, Boc anhydride (56 g, 256.6 mmol) was introduced to the reaction mixture and the temperature were increased to 50°C with stirring for 3 h. Upon reaction completion based upon TLC (9:1 $CHCl_3$/MeOH), the reaction was stopped and cooled to 0 °C, THF was removed and the mixture acidified to pH 2.5 with 1 N HCl. The mixture was extracted using 4L separatory funnel with EtOAc (3 x 1L) and the recovered organics combined, washed with ddH2O (3 x 1L) and 1L brine. Then, the crude was washed using vacuum filtration and 2.5 L hexane and concentrated under vacuum to afford the desired product **13** as a white powder (35.65 g, 89% yield). ^{1}H NMR (DMSO, 400 MHz): δ 7.14 (d, *J* = 8.1 Hz, 1H), 3.98 (td, *J* = 9.1 Hz, 1H), 2.71 (t, *J* = 7.3 Hz, 2H), 1.83 - 2.11 (m, 2H), 1.37 (s, 9H);^{13}C NMR (DMSO, 100 MHz) δ 174.1, 156.0, 78.5, 52.6, 34.5, 30.7, 28.6 ppm.

*3.4.7 General procedure for disulfide bond reduction, S-alkylation and deprotection of Met analogues (**14-21**)*

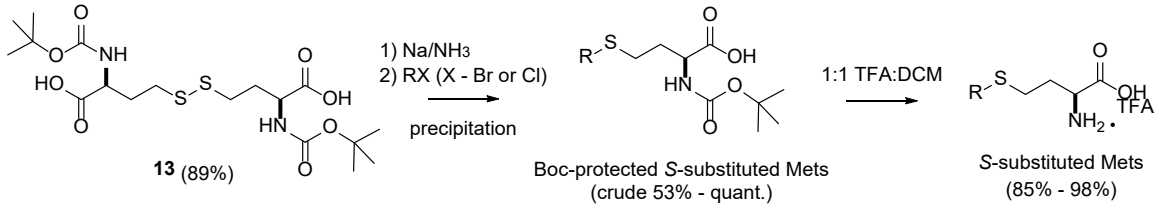

The general strategy for the synthesis of the non-native Met analogues employed reductive alkylation of the corresponding **13** and Boc-deprotection following previously reported methods with slight modifications.[18,41] Specifically, the resulting residues from alkylation step were dissolved in EtOAc under ice bath, and the pH was subsequently adjusted to pH 2.5 by the addition of 10% citric acid. The organics were extracted with EtOAc/ddH_2O and the solvent was removed under reduced pressure to ultimately afford the desired Boc-protected crudes in 53%-quant.% yields. The removal of the Boc protecting was carried out with TFA/DCM (1:1) within 5-10 min at room temperature. The solvent was evaporated under reduced pressure and the crude was dissolved in $CHCl_3$ and evaporated under reduced pressure again for 3 to 4 times. To remove traces of TFA as much as possible, the preps were dissolved in 1 mL of ddH_2O and lyophilized over night to ultimately afford the desired **14-21** Met preps in yields ranging from 85%-98% and purities ranging from 95%->99% based on LC-MS and NMR.

***S*-allyl-*L*-homocysteine TFA salt (14)**. With allyl bromide (1.14 mL, 13.44 mmol) and **13** (3 g, 6.40 mmol) yielded 3.12 g (89% yield) of crude reaction. Deprotection of 0.5 g (1.81 mmol) crude afforded **14** (0.29 g, 94 % yield) as a sticky white solid. ^{1}H NMR (D_2O, 400 MHz) δ 5.63 - 5.73 (m, 1 H), 5.03 (m, 2 H), 4.03 (t, J = 6.3 Hz, 1 H), 3.07 (d, J = 7.3, 2 H),

2.54 (t, J = 7.6, 2 H), 1.99 - 2.16 (m, 2 H); ^{13}C NMR (D_2O, 100 MHz) δ 171.7, 133.6, 117.7, 51.8, 33.2, 29.2, 24.8; HRESI Calcd for $C_7H_{14}NO_2S$ ($[M+H]^+$) m/z 176.0739; measured m/z 176.0735.

***S*-(prop-2-yn-1-yl)-*L*-homocysteine TFA salt (15).** With propargyl bromide (1.4 mL, 13.44 mmol) and **13** (3 g, 6.40 mmol) yielded 3.28 g (90% yield) of crude reaction. Deprotection of 1.3 g (5.10 mmol) crude afforded **15** (860 mg, 96 % yield) as a white oil.^{1}H NMR (D_2O/TFA = 20/1, 400 MHz) δ 4.08 (t, J = 6.4 Hz, 1 H), 3.22 (d, J = 2.6 Hz, 2 H), 2.73 (t, J = 7.5 Hz, 2 H), 2.51 (t, J = 2.6 Hz, 1 H), 2.23 – 2.03 (m, 2 H); ^{13}C NMR (D_2O/TFA = 20/1, 100 MHz) δ 171.5, 80.1, 72.1, 51.5, 28.9, 26.0, 17.8; HRESI Calcd for $C_7H_{12}NO_2S$ ($[M+H]^+$) m/z 174.0583; measured m/z 174.0581.

(*E*)-*S*-(but-2-en-1-yl)-*L*-homocysteine TFA salt (16). Crotyl bromide was purchased and used as 85% mixture of cis and trans. With crotyl bromide (0.45 mL, 4.36 mM) and **13** (1 g, 2.18 mmol) yielded 1.16 g (92% yield) of crude reaction containing mixture of isomers (70:30). Small portion of crude (50 mg, 0.17 mmol) were subsequently purified using semi-preparative HPLC (Method **D**, **Fig. S7**) affording 21 mg of Boc protected **16** (65% yield) and deprotection yielded **16** (12.8 mg, 94% yield) as a white solid. ^{1}H NMR (D_2O, 500 MHz) δ 5.41 (m, 1 H), 5.21 (m, 1 H), 3.96 (t, J = 5.2 Hz, 1 H), 2.91 (d, J = 6 Hz, 2 H), 2.41 (t, J = 6 Hz, 2 H), 1.92 – 2.00 (m, 2 H), 1.43 (d, J = 5.2 Hz, 3 H); ^{13}C NMR (D_2O, 125 MHz) δ 173.1, 131.5, 127.6, 53.3, 34.1, 30.9, 26.5, 18.5. HRESI Calcd for $C_8H_{16}NO_2S$ ($[M+H]^+$) m/z 190.0896; measured m/z 190.0892.

***S*-(but-3-yn-1-yl)-*L*-homocysteine TFA salt (17).** With 4-bromo-1-butyne (1.26 mL, 13.44 mmol) and **13** (3 g, 6.40 mmol) yielded 4.04 g (quant.% yield) of crude reaction. Deprotection of 0.5 g (1.74 mmol) crude afforded **17** (0.32 g, 98 % yield) as a brown oil.^{1}H

NMR (D_2O, 400 MHz) δ 4.04 (t, *J* = 6.4 Hz, 1 H), 2.61 (q, *J* = 7.2 Hz, 4 H), 2.38 (td, *J* = 6.8 Hz, 2.6 Hz, 1 H), 2.25 (t, *J* = 2.6 Hz, 1 H), 2.00 - 2.07 (m, 2 H); ^{13}C NMR (D_2O, 100 MHz) δ 171.6, 83.6, 70.3, 51.7, 29.4, 26.9, 26.3, 18.6; HRESI Calcd for $C_8H_{14}NO_2S$ ($[M+H]^+$) m/z 188.0739; measured m/z 188.0739.

***S*-(cyclopropylmethyl)-*L*-homocysteine TFA salt (18).** With bromomethylcyclopropane (0.12 mL, 1.28 mM) and **13** (0.3 g, 0.64 mmol) yielded 0.37 g (quant.% yield) of crude reaction. Deprotection of crude afforded **18** (0.22 g, 98% yield) as a white solid. ^1H NMR (D_2O, 500 MHz) δ 3.95 (t, *J* = 6Hz, 1 H), 2.64 (t, *J* = 7.5 Hz, 2 H), 2.40 (d, *J* = 7.5 Hz, 2 H), 2.03 – 2.06 (m, 2 H), 0.85 – 0.88 (m, 1 H), 0.44 (d, *J* = 8 Hz, 2 H), 0.09 (d, *J* = 4.5 Hz, 2 H);^{13}C NMR (D_2O, 100 MHz) δ 171.8, 52.5, 36.2, 29.9, 26.2; 10.3, 4.6 (2 carbons); HRESI Calcd for $C_8H_{16}NO_2S$ ($[M+H]^+$) m/z 190.0896; measured m/z 190.0896.

***S*-(2-azidoethyl)-*L*-homocysteine TFA salt (19).** 1-azido-2-bromoethane was purchased from Enamine (Kyiv, Ukraine). With this mixture (5 g, 6.67 mmol) and **13** (1.4 g, 3.03 mmol) yielded 1.75 g of crude as a mixture of Boc-protected **19** and starting material. The crude product was purified by flash silica gel column (23 cm x 5.5 cm) chromatography using 400 mL MeOH/DCM (5 to 10%) affording 0.98 g (53% yield) of Boc-protected **19** and deprotection yielded **19** (0.61 g, 94% yield) as a white oil. ^1H NMR (D_2O, 400 MHz) δ 3.97 (t, *J* = 6.3 Hz, 1 H), 3.44 (t, *J* = 6.5 Hz, 2 H), 2.70 (t, *J* = 6.5 Hz, 2 H), 2.60 (t, *J* = 7.4 Hz, 2 H), 2.22 – 1.99 (m, 2 H); ^{13}C NMR (D_2O, 100 MHz) δ 172.3, 52.4, 50.2, 30.2, 29.8, 26.5; HRESI Calcd for $C_6H_{13}N_4O_2S$ ($[M+H]^+$) m/z 205.0754; measured m/z 205.0757.

***S*-benzyl-*L*-homocysteine TFA salt (20).** With benzyl bromide (0.5 mL, 4.27 mM) and **13** (1 g, 2.13 mmol) yielded 1.02 g (78% yield) of crude reaction. Deprotection of crude

afforded **20** (0.56 mg, 84 % yield) as an off-white solid. ^{1}H NMR (D_2O/TFA = 20/1, 500 MHz) δ 6.82 – 6-89 (m, 5 H), 3.65 (t, *J* = 6.4 Hz, 1 H), 3.30 (s, 2 H), 2.11 (t, *J* = 7.6 Hz, 2 H), 1.62 - 1.74 (m, 2 H); ^{13}C NMR (D_2O, 100 MHz) δ 171.3, 138.0, 128.8 (2 carbons), 128.7 (2 carbons), 127.2, 51.4, 34.6, 29.1, 25.5; HRESI Calcd for $C_{11}H_{16}NO_2S$ ($[M+H]^+$) m/z 226.0896; measured m/z 226.0891.

***S*-(4-vinylbenzyl)-*L*-homocysteine TFA salt (21).** With 4-vinylbenzyl chloride (0.6 mL, 4.27 mM) and **13** (1 g, 2.13 mmol) yielded 1.39 g (92% yield) of crude reaction. Deprotection afforded **21** (0.96 mg, 97% yield) as a white oil.^{1}H NMR (D_2O/TFA = 20/1, 500 MHz) δ 6.96 – 7.09 (m, 4 H), 6.38 (dd,1 H), 5.45 (d, *J* = 13.6 Hz, 1 H), 3.77 (t, *J* = 4.4 Hz, 1 H), 3.40 (s, 2 H), 2.2 (m, 2 H), 1.79 (m, 2 H); ^{13}C NMR (D_2O/TFA = 20/1, 125 MHz) δ 174.1, 131.6, 128.8, 119.5, 117.2, 121.8, 114.9, 53.9, 36.8, 31.6, 28.0; HRESI Calcd for $C_{13}H_{18}NO_2S$ ($[M+H]^+$) m/z 252.1052; measured m/z 252.1052.

3.4.8 2-(Methylthio)pyrimidin-4(3H)-one and 4-O-allyloxycarminomycin production and structure elucidation

Reactions (3 mL) containing thiouracil (**1**) acceptor for chemoenzymatic DnrK and carminomycin (CAR) acceptor in addition to *S*-allyl-*L*-homocysteine (**14**) donor for hMAT2A/DnrK coupled reaction were conducted under previously reported conditions[18,40] in a 10 mL sterile conical tube and the desired products from each reaction were subsequently purified using semi-preparative HPLC (Methods **B**, **Figure S3.1**) to afford **1a** and (Methods **C**, **Figure S3.7**) to afford 4-*O*-allyloxycarminomycin, respectively.

2-(methylthio)pyrimidin-4(3*H*)-one (1a). With 2 mg (0.015 mmol) of **1** yielded 1.2 mg (54% yield) of **1a** as a white solid. ^{1}H NMR (CD_3OD, 600 MHz): 7.85 (d, *J*=6.7 Hz, H-6), 6.12 (d, *J*=6.7 Hz, 1H, H-5), 2.56 (s, 3H, 2-SCH3); ^{13}C NMR (CD_3OD, 150 MHz): 165.2 (C-2), 163.1 (C-4), 154.6 (CH-6), 110.9 (CH-5), 13.5 (CH_3); HRESI Calcd for $C_5H_7N_2OS$ ($[M+H]^+$) m/z 143.0273; measured m/z 143.0273.

4-*O*-allyloxycarminomycin. With 1.1 mg (0.0021 mmol) of CAR and 2.64 mg (0.009 mmol) of **14** yielded 0.83 mg (70% yield) of 4-*O*-allyloxycarminomycin as a ruby solid. ^{1}H NMR (CD_3OD, 600 MHz): 8.03 (dd, *J*=7.7, 1.0 Hz, 1H), 7.84 (dd, *J*=8.5, 7.7 Hz, 1H), 7.58 (dd, *J*=8.6, 1.1 Hz, 1H), 6.16 (ddt, *J*=17.2, 10.7, 4.6 Hz, 1H), 5.72 (dg, *J*=17.3, 1.8 Hz, 2H), 5.49 (brd, *J*=3.8 Hz, 1H), 5.36 (dg, *J*=8.5, 10.7, 1.6 Hz, 2H), 5.16 (dd, *J*=5.4, 2.8 Hz, 1H), 4.82 (brm, 2H), 4.31 (m, 1H), 3.65 (brm, 1H), 3.60 (ddd, *J*=12.8, 4.7, 2.9 Hz, 1H), 3.09 (s, 2H), 2.35 (s, 3H), 2.34 (dd, *J*=14.7, 2.7 Hz, 2H), 2.21 (dd, *J*=14.6, 5.4 Hz, 2H), 2.05 (td, *J*=12.8, 3.9 Hz, 2H), 1.90 (dd, *J*=12.7, 4.7 Hz, 2H), 1.29 (d, *J*=6.6 Hz, 3H); ^{13}C NMR (CD_3OD, 150 MHz): 213.5 (C-13), 188.5 (C-12), 161.7 (C-4a), 157.7 (C-6), 156.5 (C-11), 136.9 (C-12a), 137.2 (CH-2), 136.2 (C-6a), 135.8 (C-10a), 133.9 (CH-2”), 122.3 (C-4a), 121.9 (CH-3), 120.9 (CH-1), 118.0 (CH_2-3”), 112.8 (C-5a), 112.6 (C-11a), 101.3 (CH-1’), 72.2 (CH-7), 71.2 (CH_2-1”), 68.2 (C-4’), 68.0 (CH-5’), 48.7 (CH-3’), 37.3 (CH_2-8), 33.3 (CH_2-10), 29.7 (CH_2-2’), 24.5 (CH_3-14); HRESI Calcd for $C_{29}H_{31}NO_{10}$ ($[M+H]^+$) m/z 554.2020; measured m/z 554.2020.

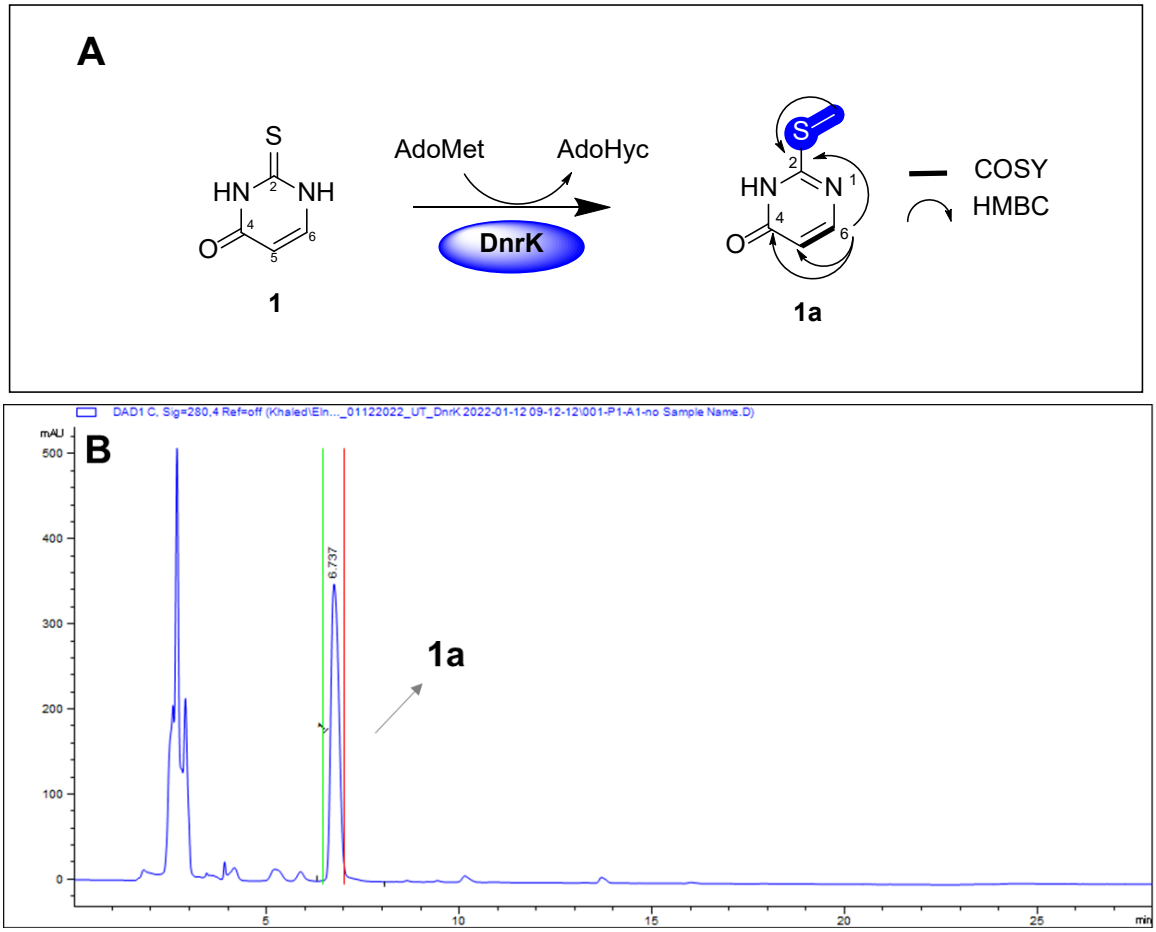

Figure S3.1. (A) General DnrK reaction with thiouracil (**1**) as substrate and DnrK reaction/methylated product 2-(methylthio)pyrimidin-4(3*H*)-one (**1a**). ^{1}H-^{1}H COSY (**—**) and key HMBC (→) correlations of **1a**. The methyl group installed by DnrK is highlighted in blue. **(B)** Semi-preparative HPLC profile of DnrK *S*-methylated product **1a** using HPLC (Method **B**).

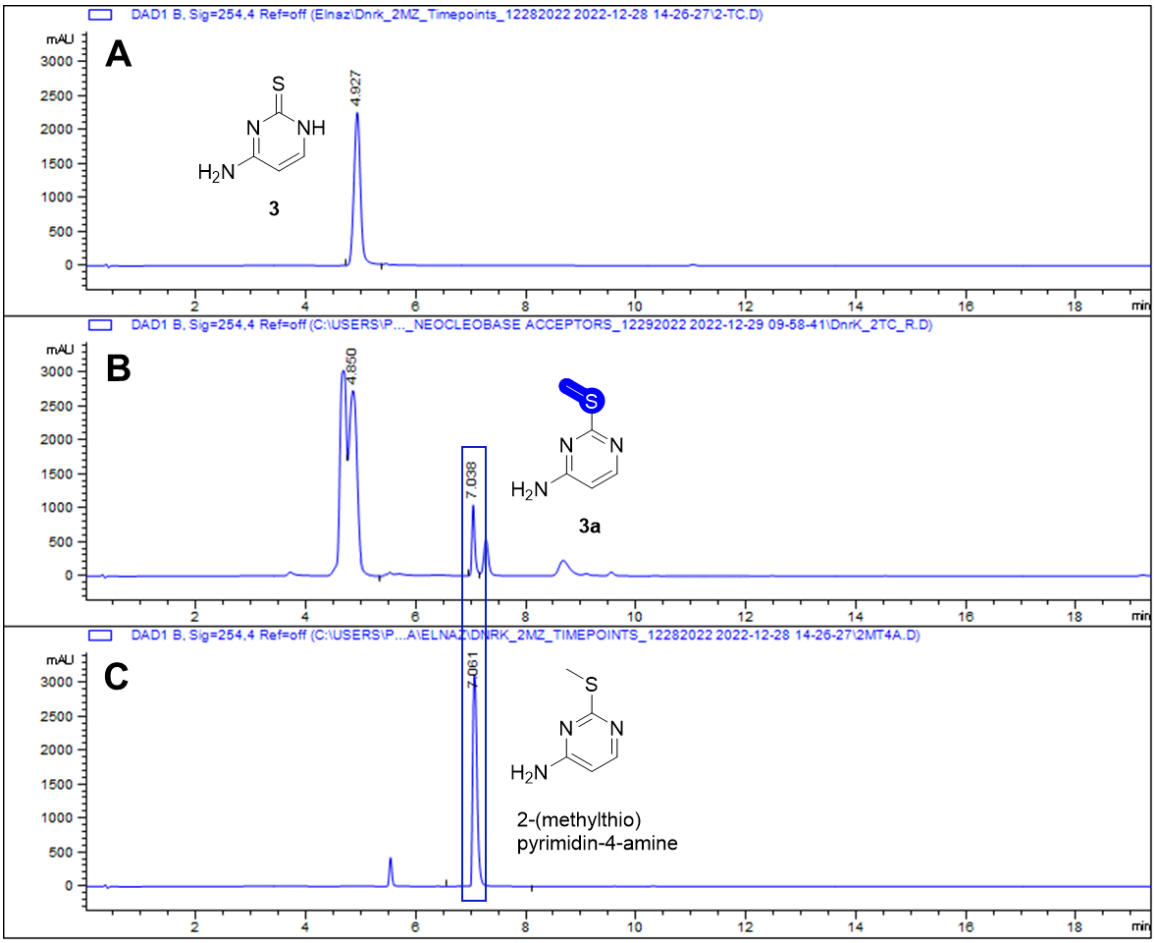

Figure S3.2. Test agent thiocytosine (**3**) in the **(A)** absence and **(B)** presence of DnrK. **(C)** Elution profile of of 2-(methylthio)pyrimidin-4-amine standard.

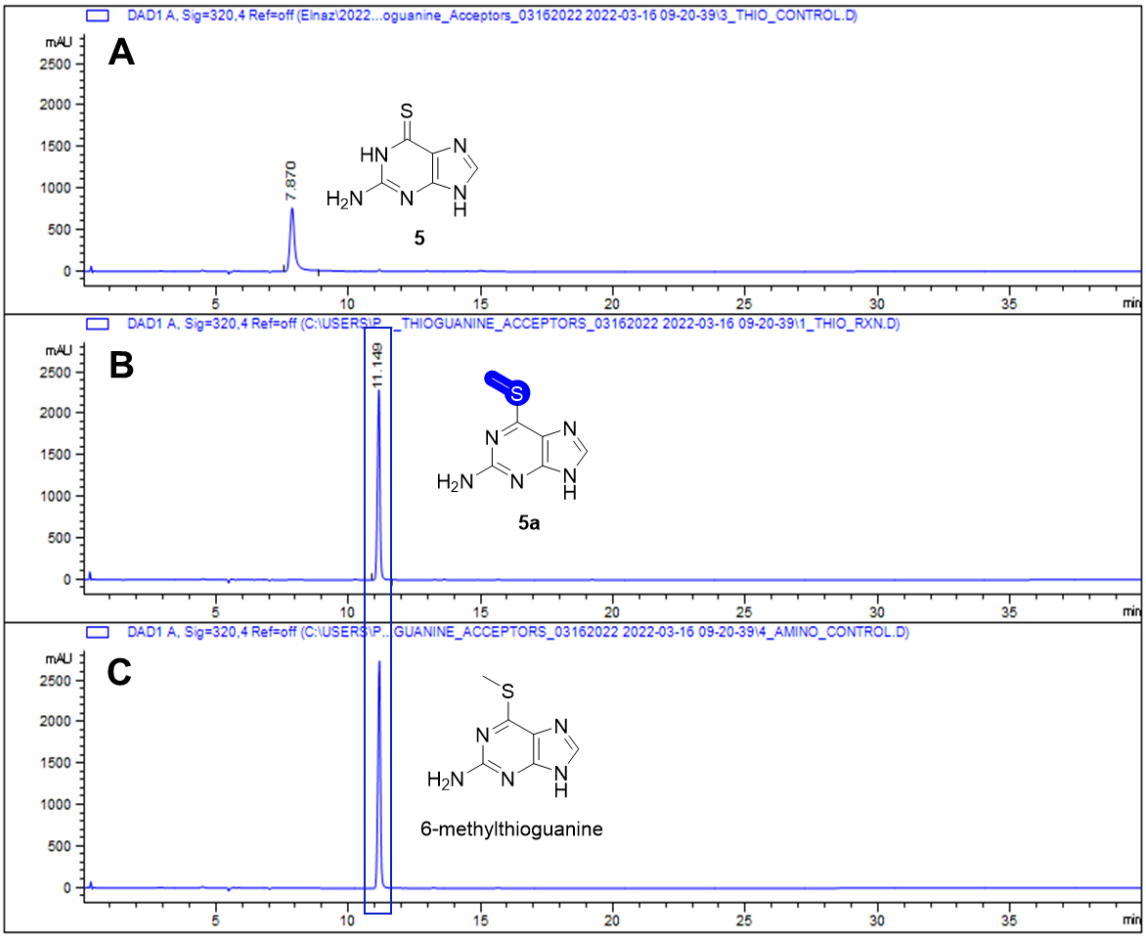

Figure S3.3. Test agent thioguanine (**5**) in the **(A)** absence and **(B)** presence of DnrK. **(C)** Elution profile of 6-methylthioguanine standard.

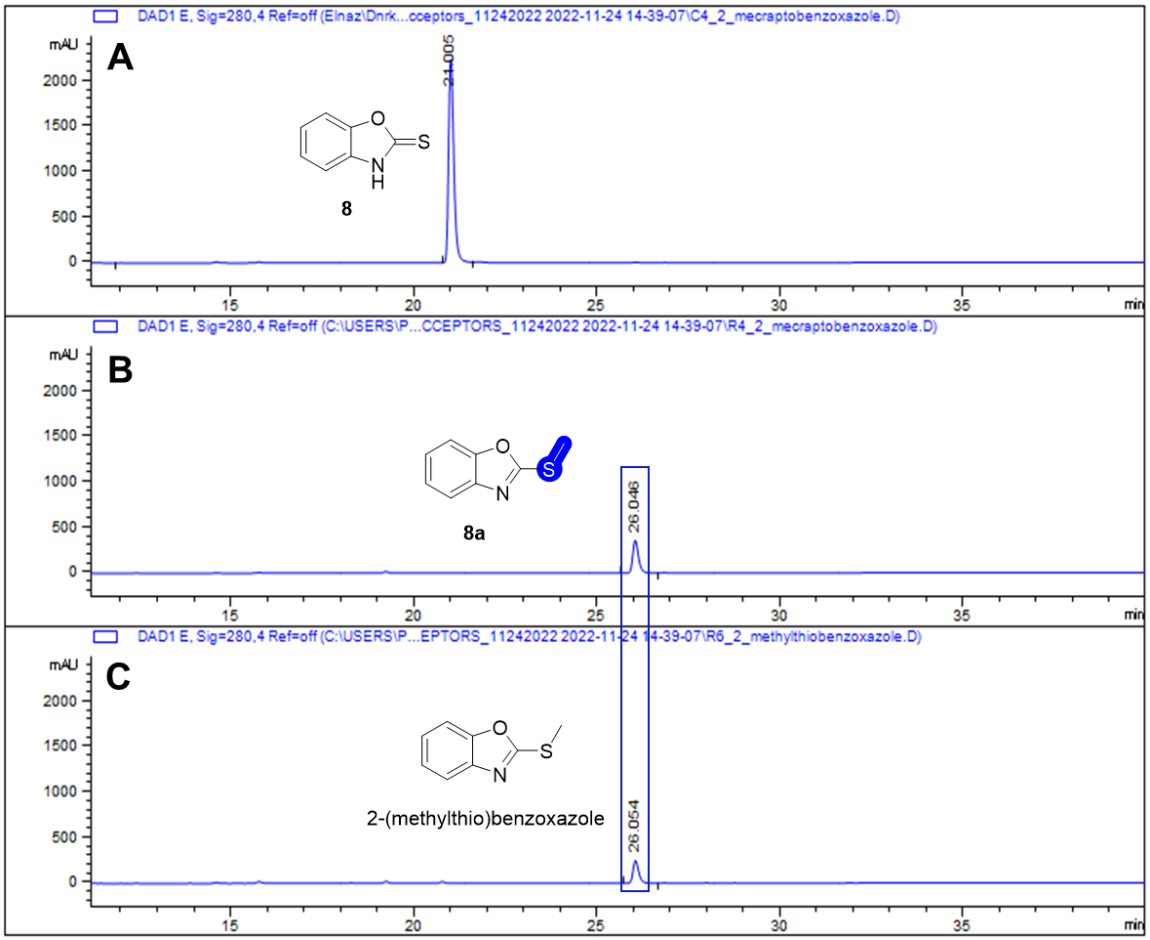

Figure S3.4. Test agent 2-mercaptobenzoxazole (**8**) in the **(A)** absence and **(B)** presence of DnrK. **(C)** Elution profile of of 2-(methylthio)benzoxazole standard.

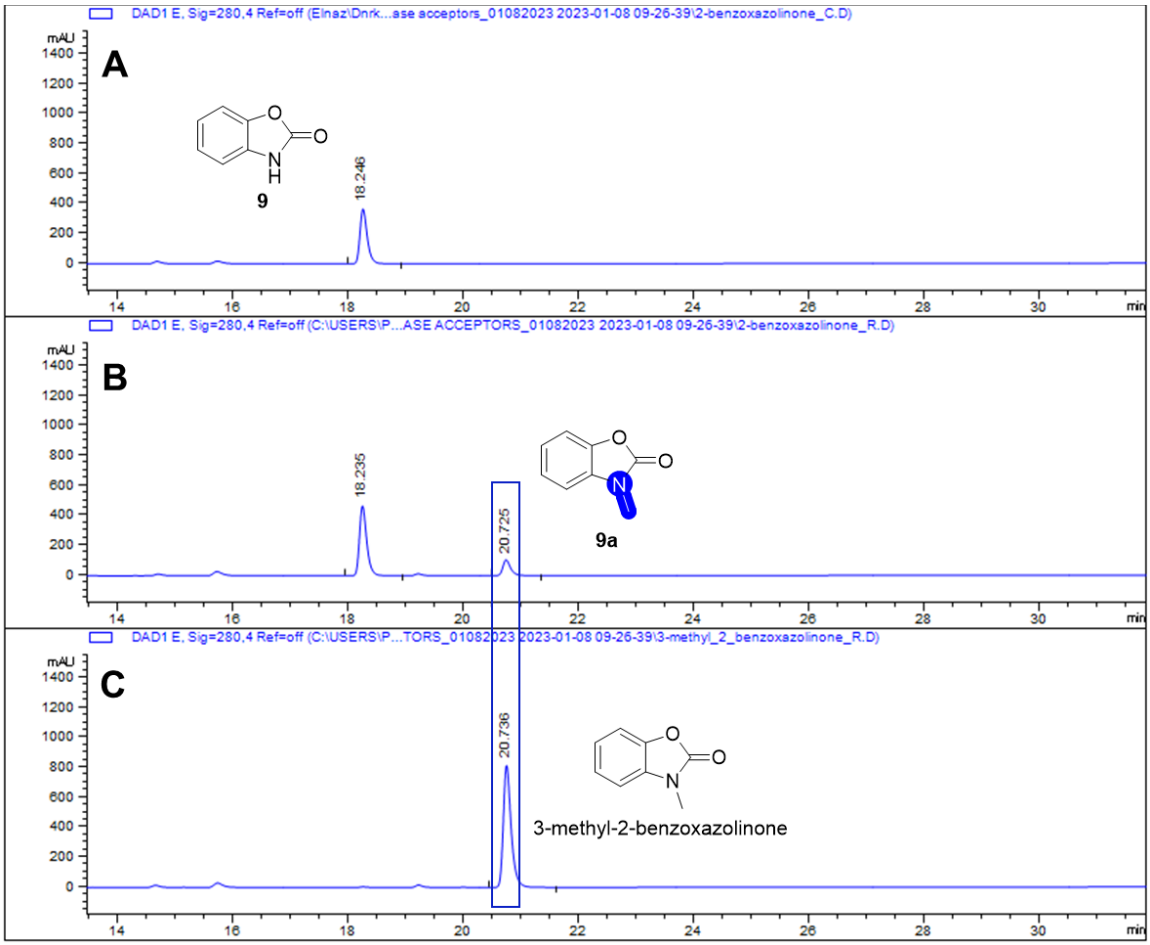

Figure S3.5. Test agent 2-benzoxazolinone (**9**) in the **(A)** absence and **(B)** presence of DnrK. **(C)** Elution profile of 3-methyl-2-benzoxazolinone standard.

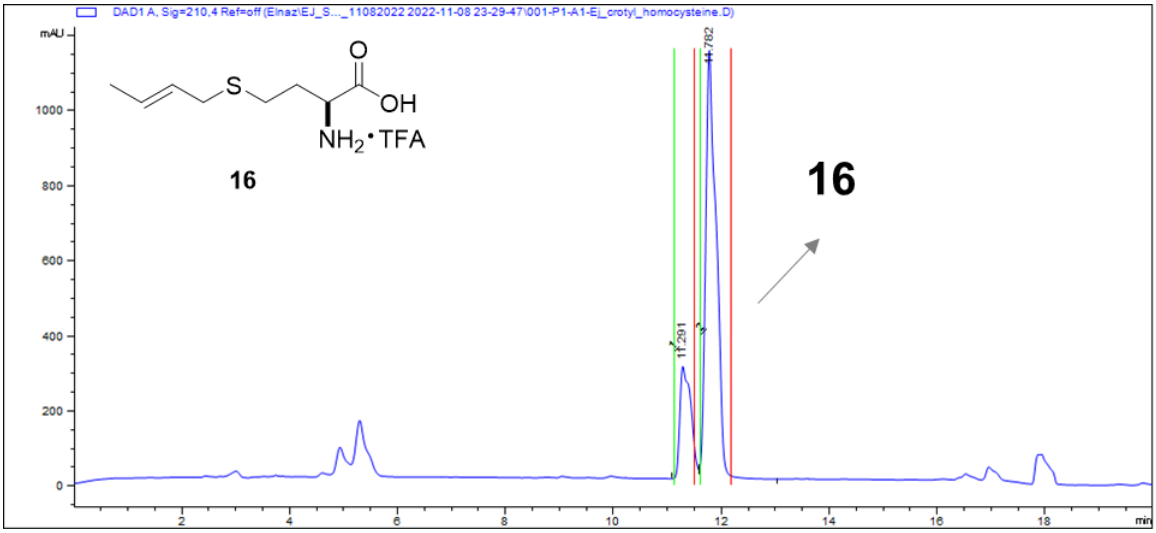

Figure S3.6. Semi-preparative HPLC profile of synthesized (*E*)-*S*-(but-2-en-1-yl)-*L*-homocysteine TFA salt (**16**) using HPLC (Method **D**).

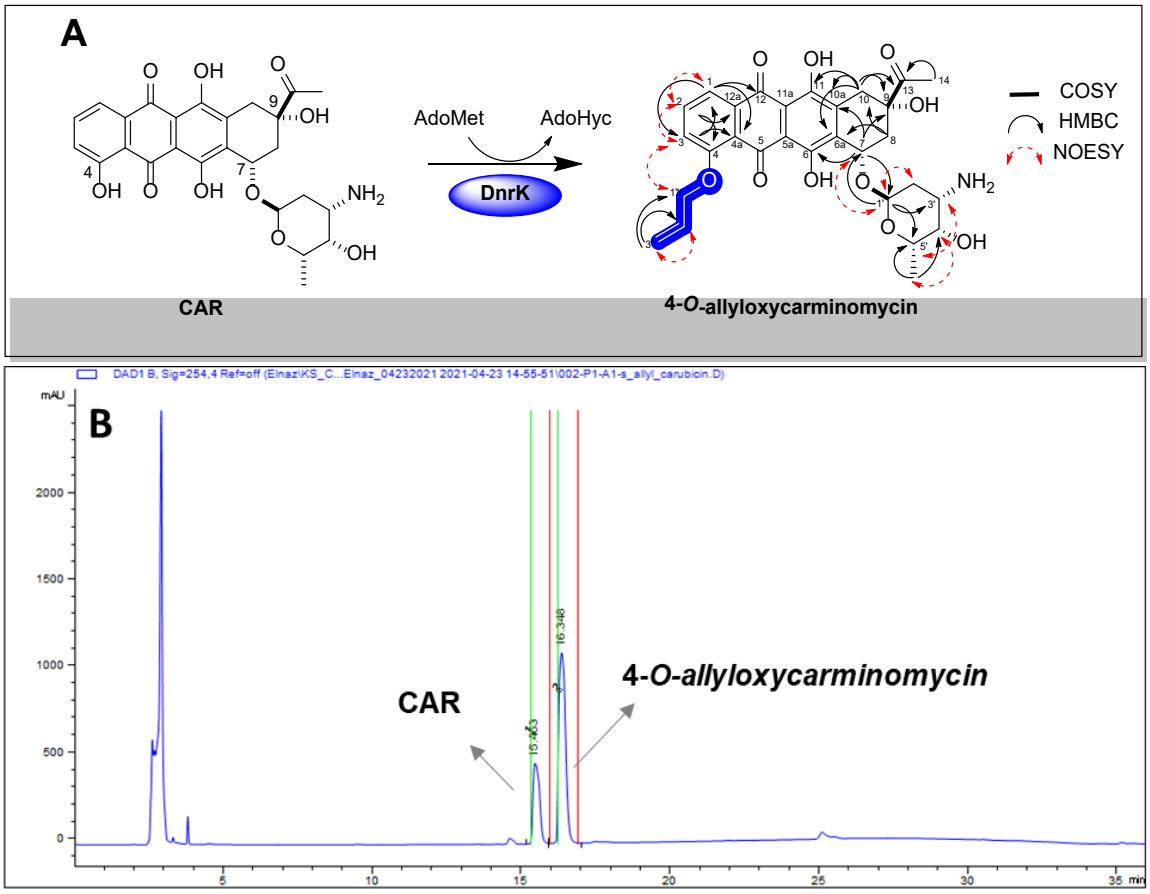

Figure S3.7. (A) General hMAT2A/DnrK coupled reaction using *S*-allyl-*L*-homocysteine 14 prep as a substrate for hMAT2A generating non-native donor that is used by DnrK to alkylate native substrate CAR affording 4-O-allyloxycarminomycin. ^{1}H,^{1}H-COSY (**—**), selected HMBC (→) and selected NOESY (⤾) correlations of 4-*O*-allyloxycarminomycin. The alkyl group installed by DnrK is highlighted in blue. (**B**) Semi-preparative HPLC profile of DnrK 4-*O*-allyloxycarminomycin using HPLC (Method **C**).

References for Chapter Three

(1) Zhang, C.; Weller, R.L.; Thorson, J.S.; Rajski, S.R. Natural product diversification using a non-natural cofactor analogue of *S*-adenosyl-L-methionine. *J. Am. Chem. Soc*. **2006**, *128*, 2760-2761.

(2) Struck, A.W.; Thompson, M.L.; Wong, L.S.; Micklefield, J. *S*-adenosyl-methionine-dependent methyltransferases: highly versatile enzymes in biocatalysis, biosynthesis and other biotechnological applications. *Chem. Bio. Chem.* **2012**, *13*, 2642-2655.

(3) Bennett, M.R.; Shepherd, S.A.; Cronin, V.A.; Micklefield, J. Recent advances in methyltransferase biocatalysis. *Current Opin Chem. Biol*. **2017**, *3*, 97-106.

(4) Sun, Q.; Huang, M.; Wei, Y. Diversity of the reaction mechanisms of SAM-dependent enzymes. *Acta. Pharm. Sin B*. **2020**, *11*, 632-650.

(5) Huber, T.D.; Clinger, J.A.; Liu, Y.; Xu, W.; Miller, M.D.; Phillips Jr, G.N.; Thorson, J.S. Methionine Adenosyltransferase Engineering to Enable Bioorthogonal Platforms for AdoMet-Utilizing Enzymes. *ACS Chem. Biol*. **2020**, *15*, 695-705.

(6) Jalali, E.; Thorson, J.S. Enzyme-mediated bioorthogonal technologies: catalysts, chemoselective reactions and recent methyltransferase applications. *Curr Opin Biotechnol*. **2021**, *69*, 290-298.

(7) Connors, N.C.; Bartel, P.L.; Strohl, W.R. Biosynthesis of anthracydines: enzymic conversion of aklanonic acid to aklavinone and ε-rhodomycinone by anthracycline-producing streptomycetes. *J. Gen. Microbiol.* **1990**, *136*, 1895-1898.

(8) Connors, N.C.; Strohl, W.R. Partial purification and properties of carminomycin 4-*O*-methyltransferase from *Streptomyces sp.* strain C5. *Microbiol*. **1993**, *139*, 1353-1362.

(9) Madduri, K.; Torti, F.; Colombo, A.L.; Hutchinson, C.R. Cloning and sequencing of a gene encoding carminomycin 4-*O*-methyltransferase from *Streptomyces peucetius* and its expression in *Escherichia coli*. *J. Bacteriol*. **1993**, *175*, 3900-3904.

(10) Madduri, K.; Hutchinson, C.R. Functional characterization and transcriptional analysis of a gene cluster governing early and late steps in daunorubicin biosynthesis in *Streptomyces peucetius*. *J. Bacteriol*. **1993**, *177*, 3879-3884.

(11) Jalali, E.; Wang, F.; Overbay, B.R. Miller, M.D. Shaaban, K.A. Ponomareva, L.V.; Ye, Q.; Bhardwaj, M.; Steele, A.D.; Teijaro, C.N.; Shen, B.; Van Lanen, S.G. She, Q.; Voss, R.; Phillips Jr, G.N.; Thorson, J.S. Biochemical and structural studies of the carminomycin 4-*O*-methyltransferase DnrK. *manuscript submitted.*

(12) Pacholec, M.; Tao, J.; Walsh, C.T. CouO and NovO: *C*-methyltransferases for tailoring the aminocoumarin scaffold in coumermycin and novobiocin antibiotic biosynthesis. *Biochemistry*. **2005**, *44*, 14969-14976.

(13) Stecher, H.; Tengg, M.; Ueberbacher, B.J.; Remler, P.; Schwab, H.; Griengl, H.; Gruber-Khadjawi, M. Biocatalytic Friedel-Crafts alkylation using non-natural cofactors. *Angew. Chem., Int. Ed.* **2009**, *48*, 9546-9548.

(14) Pavkov-Keller, T.; Steiner, K.; Faber, M.; Tengg, M.; Schwab, H.; Gruber-Khadjawi, M.; Gruber, K. Crystal structure and catalytic mechanism of CouO, a versatile *C*-methyltransferase from *Streptomyces rishiriensis*. *PLoS One*. **2017**, *12*, e0171056.

(15) Pljevaljcić, G.; Schmidt, F.; Weinhold, E. Sequence-specific methyltransferase-induced labeling of DNA (SMILing DNA). *Chem. Bio. Chem.* **2004**, *5*, 265-269.

(16) Dalhoff, C.; Lukinavičius, G.; Klimašauskas, S.; Weinhold, E. Synthesis of *S*-adenosyl-L-methionine analogs and their use for sequence-specific transalkylation of DNA by methyltransferases. *Nat. Protoc*. **2006**, *1*, 1879-1886.

(17) Zhang, C.; Weller, R.L.; Thorson, J.S.; Rajski, S.R. Natural Product diversification using a non-natural cofactor analogue of *S*-adenosyl-L-methionine. *J. Am. Chem. Soc.* **2006**, *128*, 2760–2761.

(18) Singh, S.; Zhang, J.; Huber, T.D.; Sunkara, M.; Hurley, K.; Goff, R.D.; Wang, G.; Zhang, W.; Liu, C.; Rohr, J.; Van Lanen, S.G.; Thorson, J.S. Facile chemoenzymatic strategies for the synthesis and utilization of *S*-adenosyl-(L)-methionine analogues. *Angew. Chemie., Int. Ed*. **2014**, *53*, 3965–3969.

(19) Huber, T.D.; Clinger, J.A.; Liu, Y.; Xu, W.; Miller, M.D.; Phillips Jr, G.N.; Thorson, J.S. Methionine adenosyltransferase engineering to enable bioorthogonal platforms for AdoMet-utilizing enzymes. *ACS Chem. Biol*. **2020**, *15*, 695-705.

(20) Michailidou, F.; Klöcker, N.; Cornelissen, N.V.; Singh, R.K.; Peters, A.; Ovcharenko, A.; Kümmel, D.; Rentmeister, A. Engineered SAM synthetases for enzymatic generation of AdoMet analogs with photocaging groups and reversible DNA modification in cascade reactions. *Angew. Chem., Int. Edit.* **2021**, *60*, 480-485.

(21) Davis, T.D.; Kunakom, S.; Burkart, M.D.; Eustaquio, A.S. Preparation, assay, and application of chlorinase SalL for the chemoenzymatic synthesis of *S*-adenosyl-L-methionine and analogs. *Methods Enzymol*. **2018**, *604*, 367-388.

(22) Tang, Q.; Grathwol, C.W.; Aslan-Üzel, A.S.; Wu, S.; Link, A.; Pavlidis, I.V.; Badenhorst, C.P.; Bornscheuer, U.T. Directed evolution of a halide methyltransferase enables biocatalytic synthesis of diverse SAM analogs. *Angew. Chem., Int. Ed.* **2021**, *60*, 1524-1527.

(23) Lin, S.; Yang, X.; Jia, S.; Weeks, A.M.; Hornsby, M.; Lee, P.S.; Nichiporuk, R.V.; Iavarone, A.T.; Wells, J.A.; Toste, F.D.; Chang, C.J. Redox-based reagents for chemoselective methionine bioconjugation. *Science*. **2017**, *355*, 597-602.

(24) Taylor, M.T.; Nelson, J.E.; Suero, M.G.; Gaunt, M.J. A protein functionalization platform based on selective reactions at methionine residues. *Nature*. **2018**, *562*, 563-568.

(25) Kim, J.; Li, B.X.; Huang, R.Y.C.; Qiao, J.X.; Ewing, W.R.; MacMillan, D.W.C. Site-Selective Functionalization of Methionine Residues via Photoredox Catalysis. *J. Am. Chem. Soc*. **2020**, *142*, 21260-21266.

(26) Knowles, O.J.; Johannissen, L.O.; Crisenza, G.E.; Hay, S.; Leys, D.; Procter, D.J. A Vitamin B2 -Photocatalysed Approach to Methionine Analogues. *Angew. Chem., Int. Ed.* **2022**, *61*, e202212158.

(27) Takehara, J.; Ichikawa, Sh.; Iwane, H. Method for producing homocystine. U.S. Patent 5847205A. **1998.**

(28) Hoffman, J.L. Chromatographic analysis of the chiral and covalent instability of *S*-adenosyl-L-methionine. *Biochem*. **1986**, *25*, 4444-4449.

(29) Iwig, D.F.; Booker, S.J. Insight into the polar reactivity of the onium chalcogen analogues of *S*-adenosyl-L-methionine. *Biochem*. **2004**, *43*, 13496-13509.

(30) Peters, W.; Willnow, S.; Duisken, M.; Kleine, H.; Macherey, T.; Duncan, K.E.; Litchfield, D.W.; Lüscher, B.; Weinhold, E. Enzymatic site-specific functionalization of protein methyltransferase substrates with alkynes for click labeling. *Angew. Chem., Int. Ed.* **2010**, *49*, 5170-5173.

(31) Wang, R.; Zheng, W.; Yu, H.; Deng, H.; Luo, M. Labeling substrates of protein arginine methyltransferase with engineered enzymes and matched *S*-adenosyl-L-methionine analogues. *J. Am. Chem. Soc.* **2011**, *133*, 7648-7651.

(32) Rudenko, A.Y.; Mariasina, S.S.; Sergiev, P.V.; Polshakov, V.I. Analogs of *S*-Adenosyl-L-Methionine in Studies of Methyltransferases. *Mol. Biol*. **2022**, *56*, 229-250.

(33) Mizutani, M.; Sanemitsu, Y.; Tamaru, Y.; Yoshida, Z. Palladium-catalyzed polyhetero-Claisen rearrangement of 2-(allylthio) pyrimidin-4 (3*H*)-ones. *J. Org. Chem*. **1985**, *50*, 764-768.

(34) Huang, L.K.; Cherng, Y.C.; Cheng, Y.R.; Jang, J.P.; Chao, Y.L.; Cherng, Y.J. An efficient synthesis of substituted cytosines and purines under focused microwave irradiation. *Tetrahedron*. **2007**, 63, 5323-5327.

(35) Bakherad, M.; Gholipoor, F. Regioselective syntheses of 3-benzyl-substituted 7H-thiazolo [3, 2-a] pyrimidine-7-ones through palladium-catalyzed heteroannulation of acetylenic compounds. *Org. Chem. Int*. **2012**, *2012*, 1-5.

(36) Tibiletti, F.; Simonetti, M.; Nicholas, K.M.; Palmisano, G.; Parravicini, M.; Imbesi, F.; Tollari, S.; Penoni, A. One-pot synthesis of meridianins and meridianin analogues via indolization of nitrosoarenes. *Tetrahedron*. **2010**, *66*, 1280-1288.

(37) Sadler, J.C.; Humphreys, L.D.; Snajdrova, R.; Burley, G.A. A Tandem enzymatic sp^2-*C*-methylation process: Coupling *in situ S*-adenosyl-L-methionine formation with methyl transfer. *Chem. Biochem*. **2017**, *18*, 992-995.

(38) Linares-Anaya, O.; Avila-Sorrosa, A.; Díaz-Cedillo, F.; Gil-Ruiz, L.Á.; Correa-Basurto, J.; Salazar-Mendoza, D.; Orjuela, A.L.; Alí-Torres, J.; Ramírez-Apan, M.T.; Morales-Morales, D. Synthesis, characterization, and preliminary *in vitro* cytotoxic evaluation of a series of 2-substituted benzo [*d*] [1,3] azoles. *Molecules.* **2021**, *26*, 2780.

(39) Wang Z.X.; Li S.M.; Heide, L. Identification of the coumermycin A(1) biosynthetic gene cluster of *Streptomyces rishiriensis* DSM 40489. *Antimicrob Agents Chemother*. **2000**, *44*, 3040-3048.

(40) Huber, T.D.; Wang, F.; Singh, S.; Johnson, B.R.; Zhang, J.; Sunkara, M.; Van Lanen, S.G.; Morris, A.J.; Phillips Jr., G.N.; Thorson, J.S. Functional AdoMet isosteres resistant to classical AdoMet degradation pathways. *ACS Chem. Biol*. **2016**, *11*, 2484-2491.

(41) Maiti, B.; Ng, G.; Abramov, A.; Boyer, C.; Díaz, D.D. Methionine-based carbon monoxide releasing polymer for the prevention of biofilm formation. *Polymer Chem*. **2021**,*12*, 3968-3975.

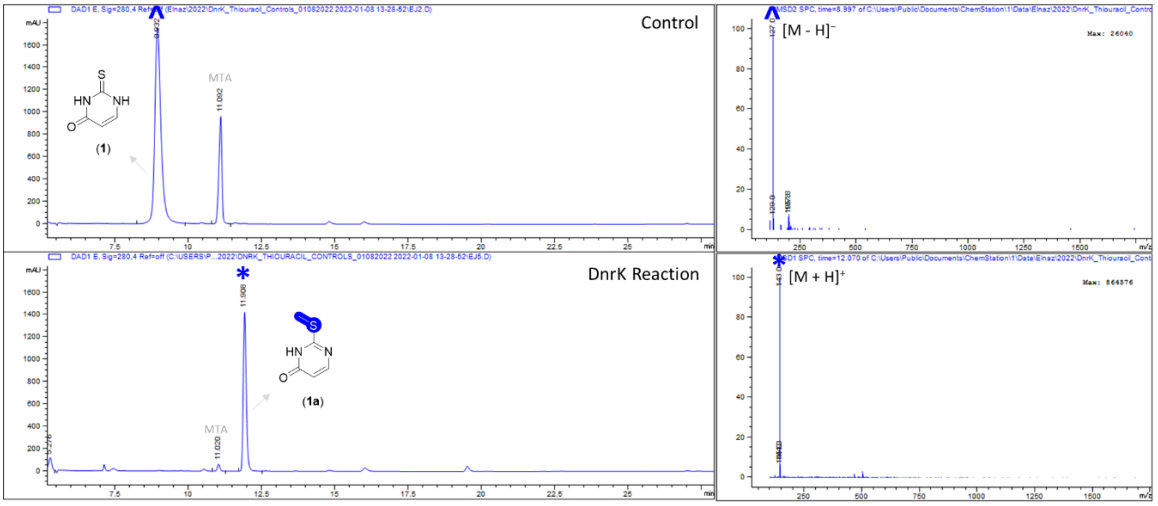

Figure S3.8. LC-MS analysis of thiouracil (**1**)^ and the corresponding DnrK-catalyzed reaction product **1a***. Determined DnrK regioselectivity is highlighted in blue.

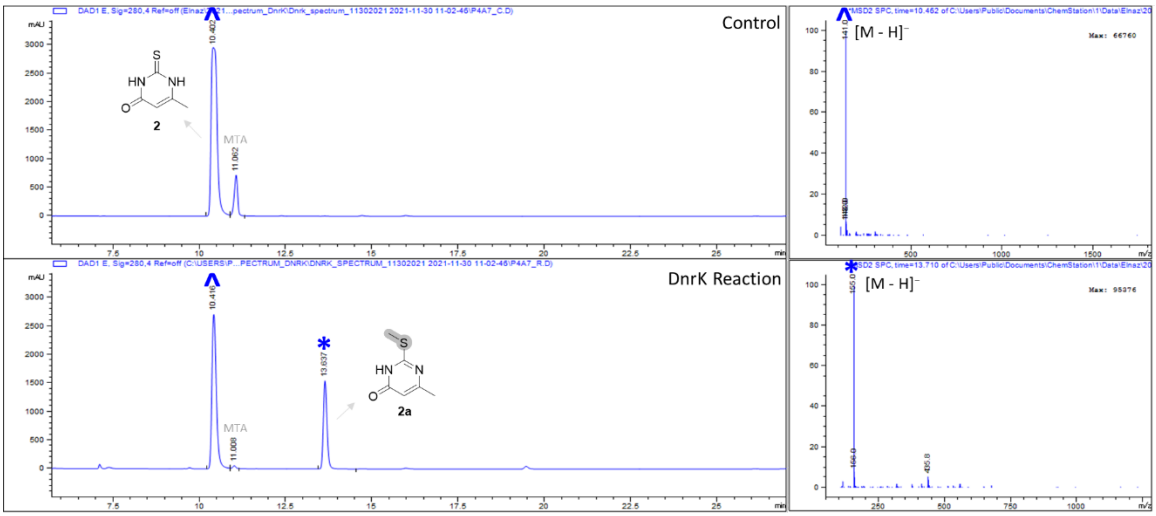

Figure S3.9. LC-MS analysis of 6-methyl-2-thiouracil (**2**)^ and the corresponding DnrK-catalyzed reaction product **2a***. Determined DnrK regioselectivity is highlighted in blue.

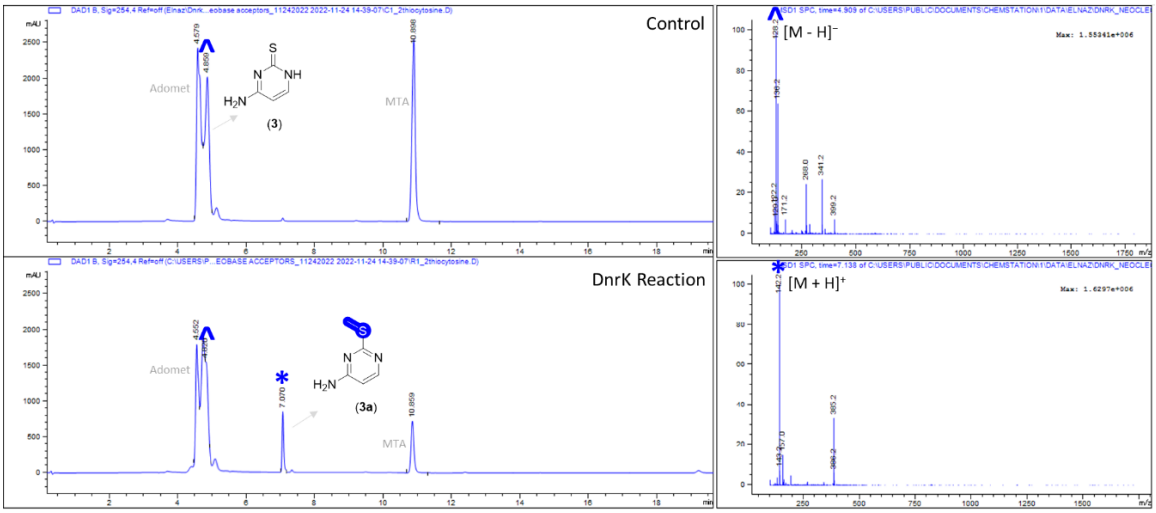

Figure S3.10. LC-MS analysis of thiocytosine (**3**)^ and the corresponding DnrK-catalyzed reaction product **3a***. Determined DnrK regioselectivity is highlighted in blue.

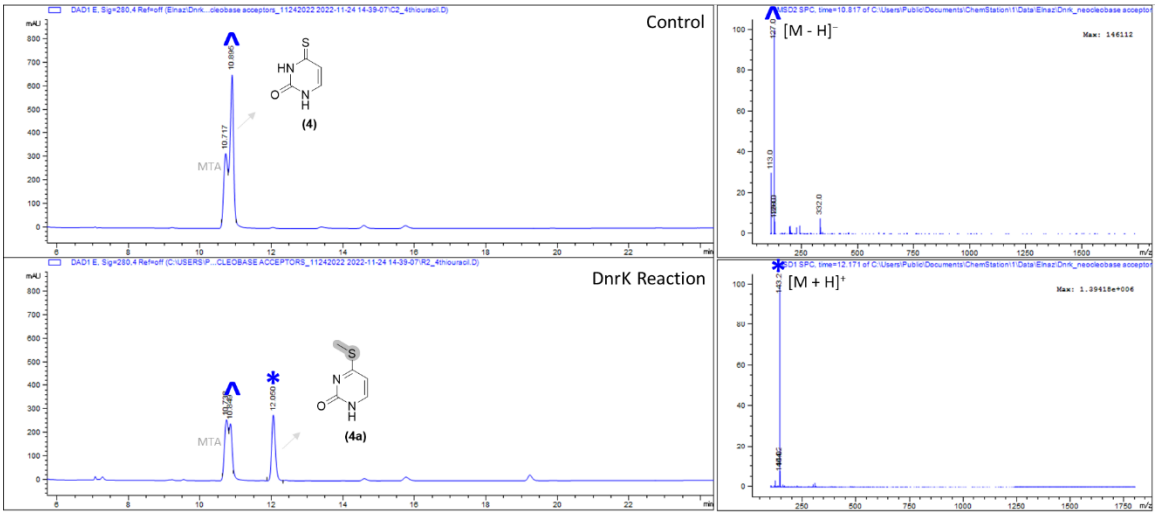

Figure S3.11. LC-MS analysis of 4-thiouracil (**4**)^ and the corresponding DnrK-catalyzed reaction product **4a***. Determined DnrK regioselectivity is highlighted in blue.

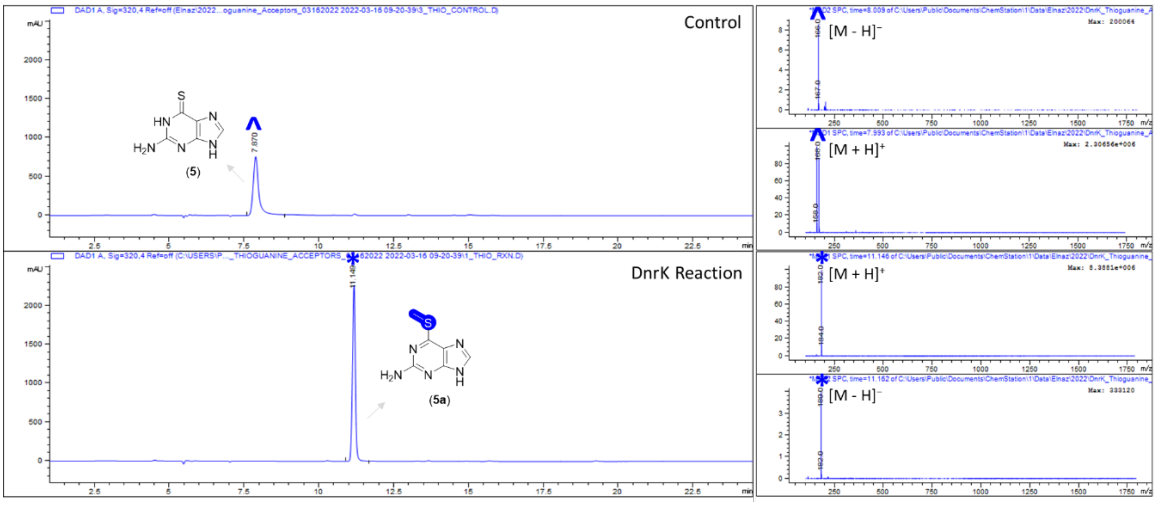

Figure S3.12. LC-MS analysis of thioguanine (**5**)^ and the corresponding DnrK-catalyzed reaction product **5a***. Determined DnrK regioselectivity is highlighted in blue.

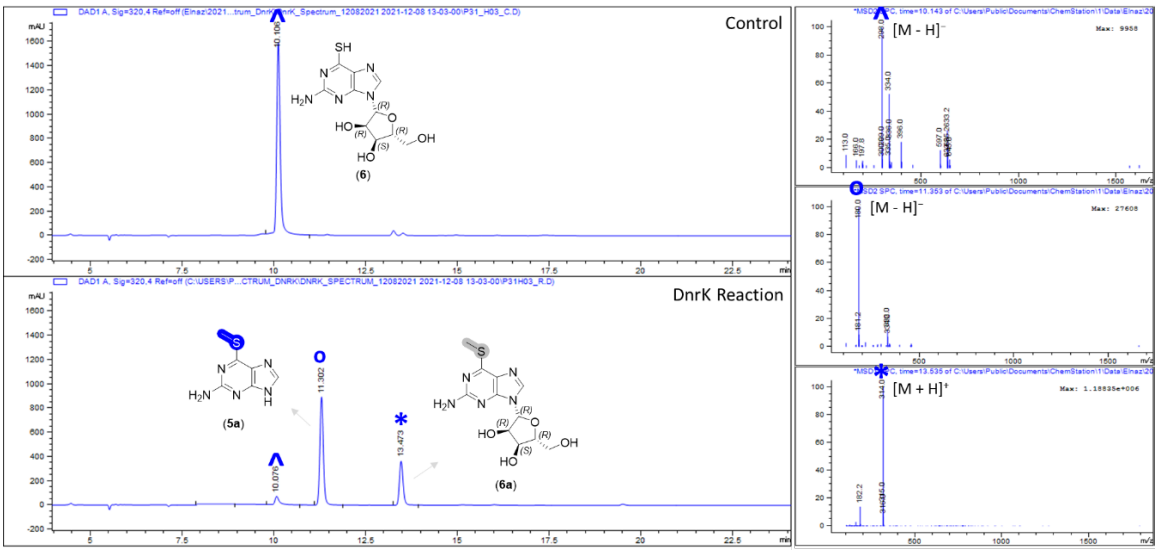

Figure S3.13. LC-MS analysis of thioguanosine (**6**)^ and the corresponding DnrK-catalyzed reaction product **6a***. Predicted DnrK regioselectivity is highlighted in grey and determined DnrK regioselectivity is highlighted in blue.

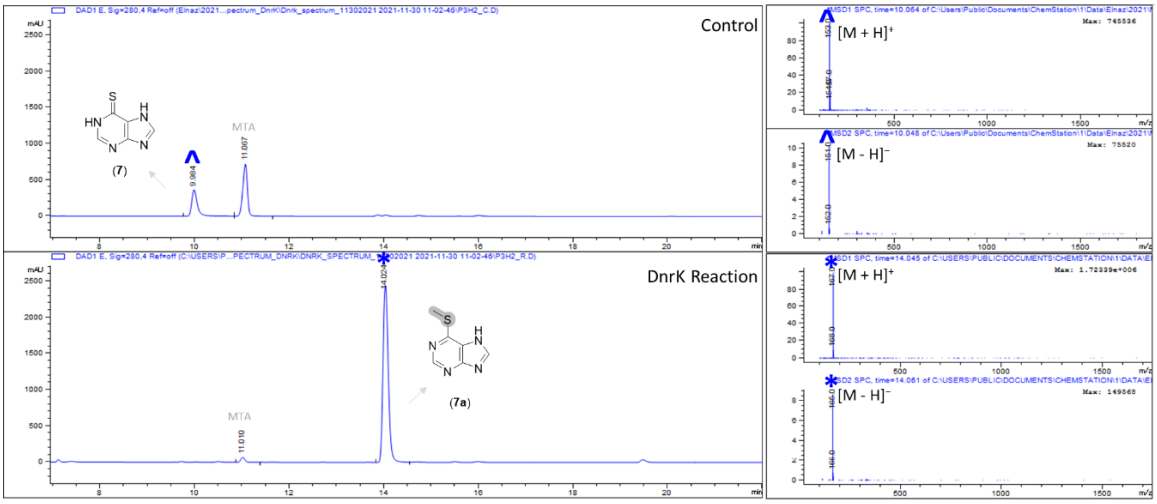

Figure S3.14. LC-MS analysis of 6-mercaptopurine (**7**)^ and the corresponding DnrK-catalyzed reaction product **7a***. Predicted DnrK regioselectivity is highlighted in grey.

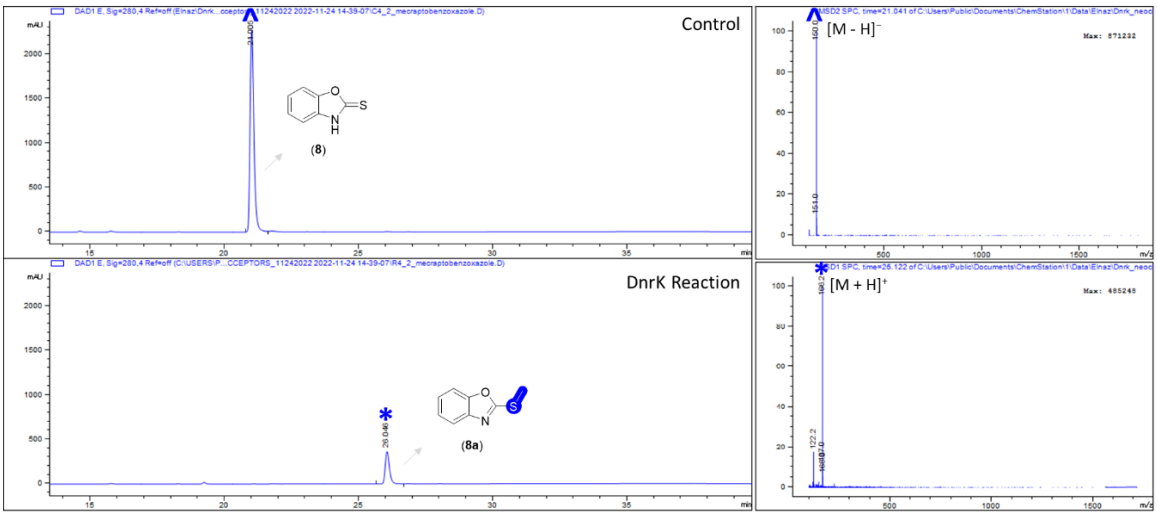

Figure S3.15. LC-MS analysis of 2-mercaptobenzoxazole (**8**)^ and the corresponding DnrK-catalyzed reaction product **8a***. Determined DnrK regioselectivity is highlighted in blue.

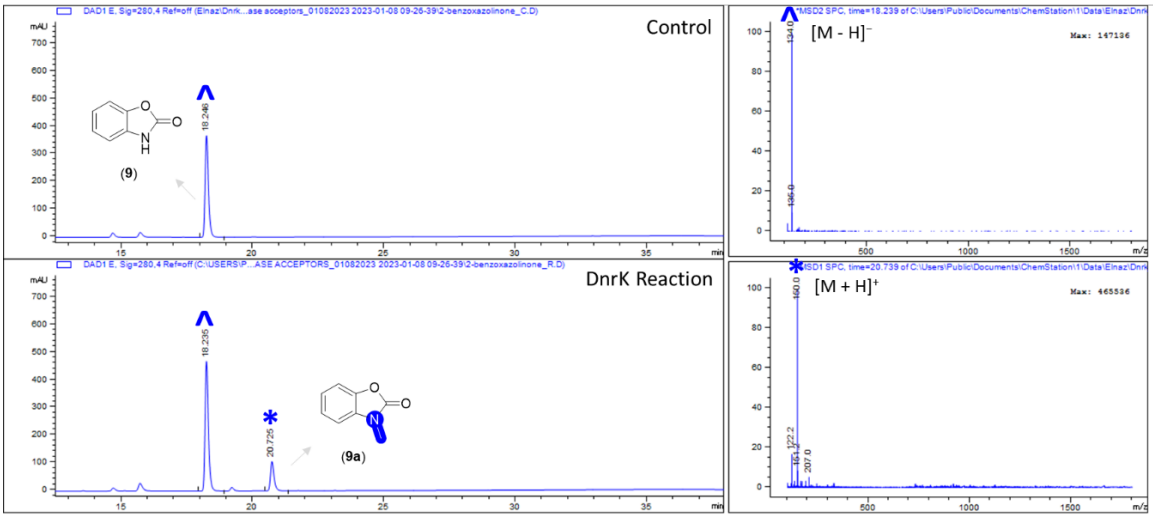

Figure S3.16. LC-MS analysis of 2-benzoxazolinone (**9**)^ and the corresponding DnrK-catalyzed reaction product **9a***. Determined DnrK regioselectivity is highlighted in blue.

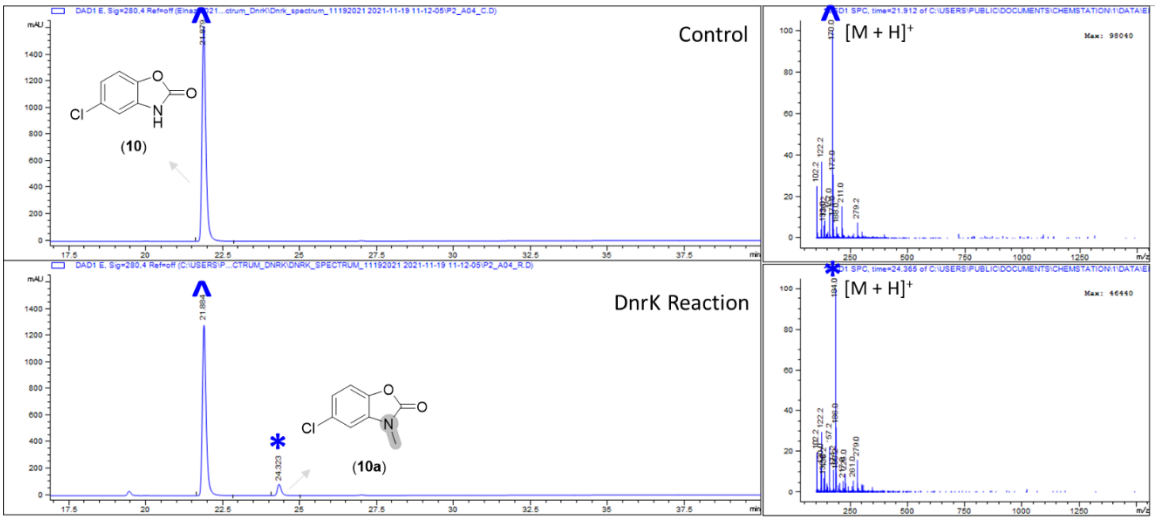

Figure S3.17. LC-MS analysis of chlorzoxazone (**10**)^ and the corresponding DnrK-catalyzed reaction product **10a***. Predicted DnrK regioselectivity is highlighted in grey.

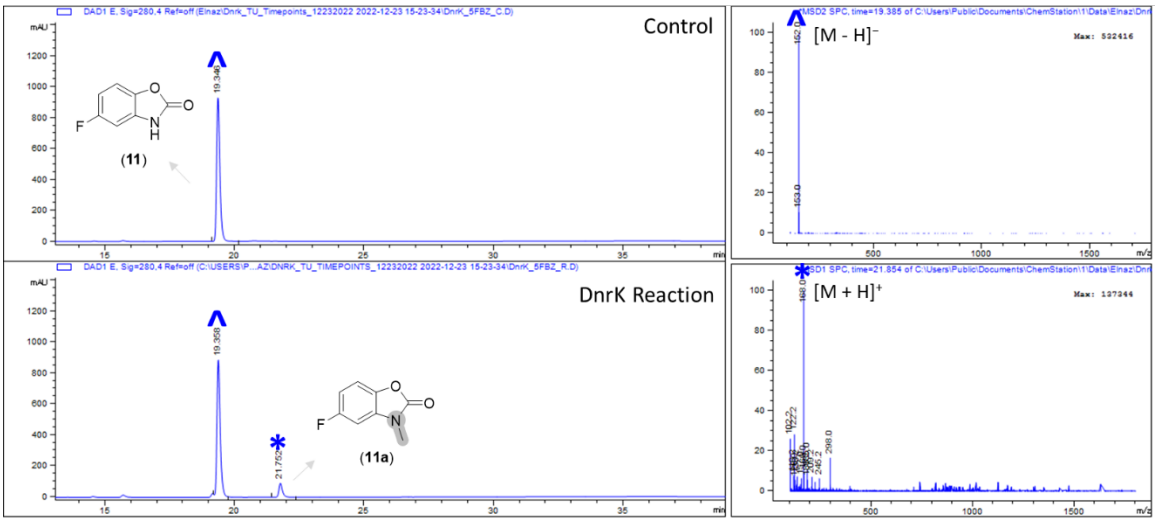

Figure S3.18. LC-MS analysis of 5-fluoro-2(3*H*)-benzoxazolone (**11**)^ and the corresponding DnrK-catalyzed reaction product **11a***. Predicted DnrK regioselectivity is highlighted in grey.

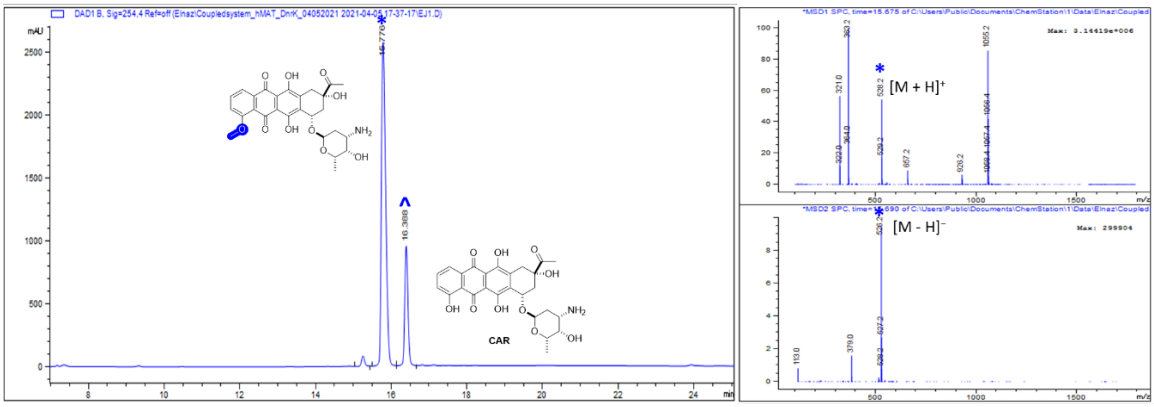

Figure S3.19. LC-MS analysis of the hMAT2/DnrK-catalyzed reaction of CAR^ and methylated product (DNR)* in the presence of AdoMet co-factor. Determined DnrK regioselectivity is highlighted in blue.

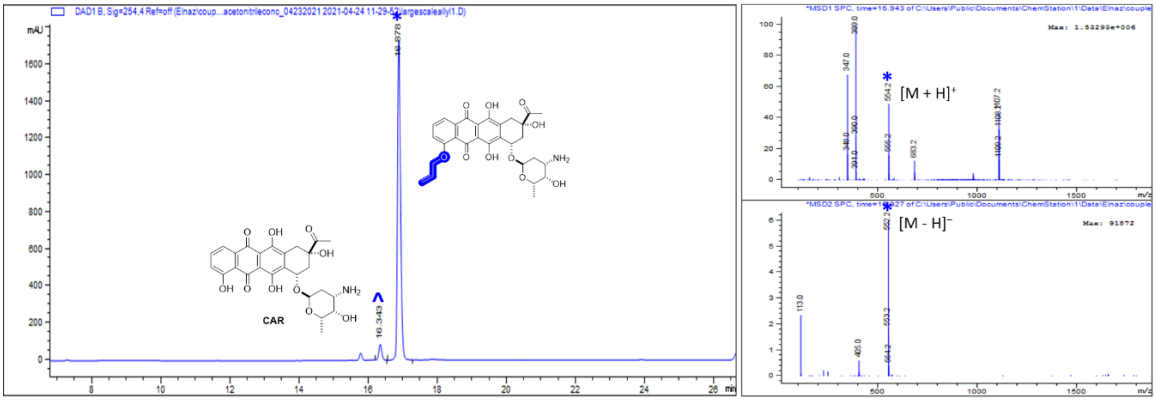

Figure S3.20. LC-MS analysis of the hMAT2/DnrK-catalyzed reaction of CAR^ and alkylated product (4-*O*-allyloxycarminomycin)* in the presence of **Ado14** co-factor. Determined DnrK regioselectivity is highlighted in blue.

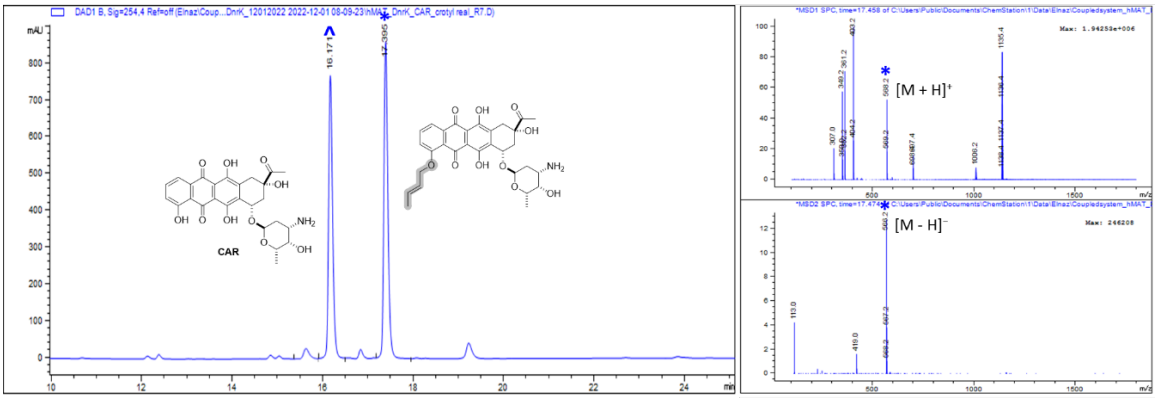

Figure S3.21. LC-MS analysis of the hMAT2/DnrK-catalyzed reaction of CAR^ and alkylated product* in the presence of **Ado16** co-factor. Predicted DnrK regioselectivity is highlighted in grey.

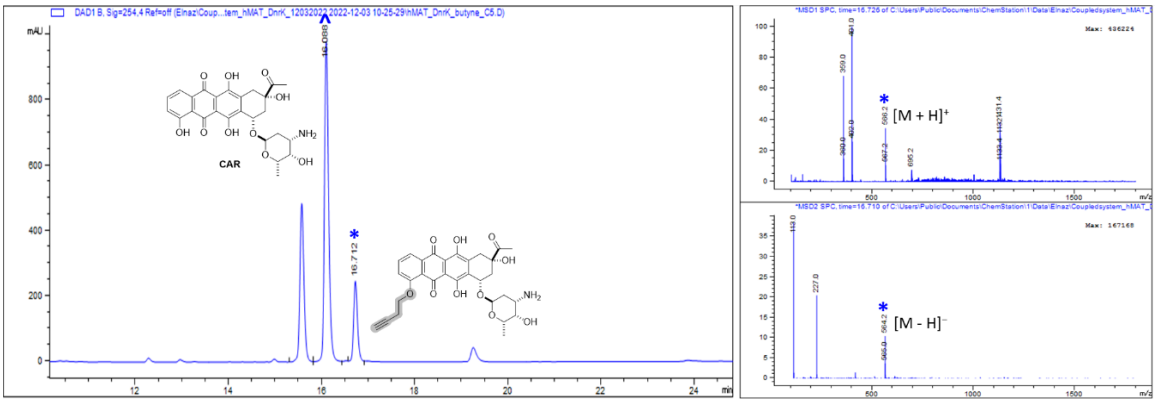

Figure S3.22. LC-MS analysis of the hMAT2/DnrK-catalyzed reaction of CAR^ and alkylated product* in the presence of **Ado17** co-factor. Predicted DnrK regioselectivity is highlighted in grey.

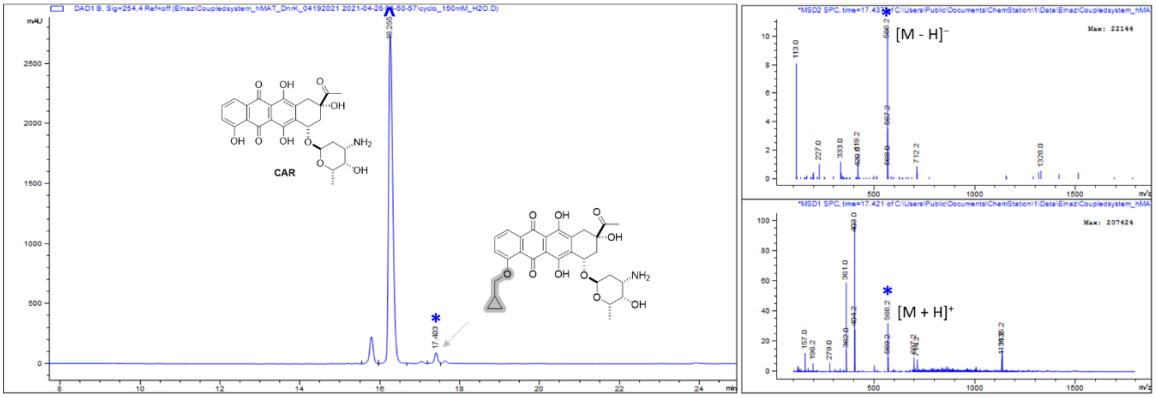

Figure S3.23. LC-MS analysis of the hMAT2/DnrK-catalyzed reaction of CAR^ and alkylated product* in the presence of **Ado18** co-factor. Predicted DnrK regioselectivity is highlighted in grey.

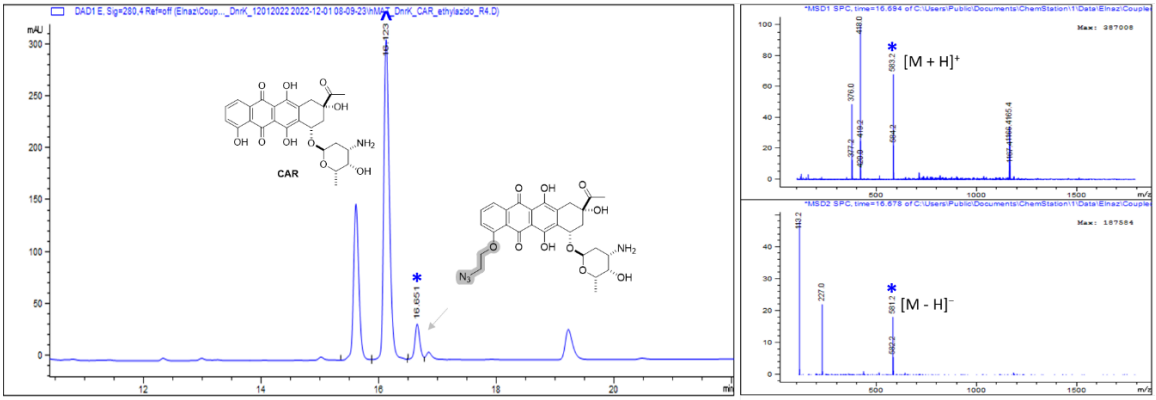

Figure S3.24. LC-MS analysis of the hMAT2/DnrK-catalyzed reaction of CAR^ and alkylated product* in the presence of **Ado19** co-factor. Predicted DnrK regioselectivity is highlighted in grey.

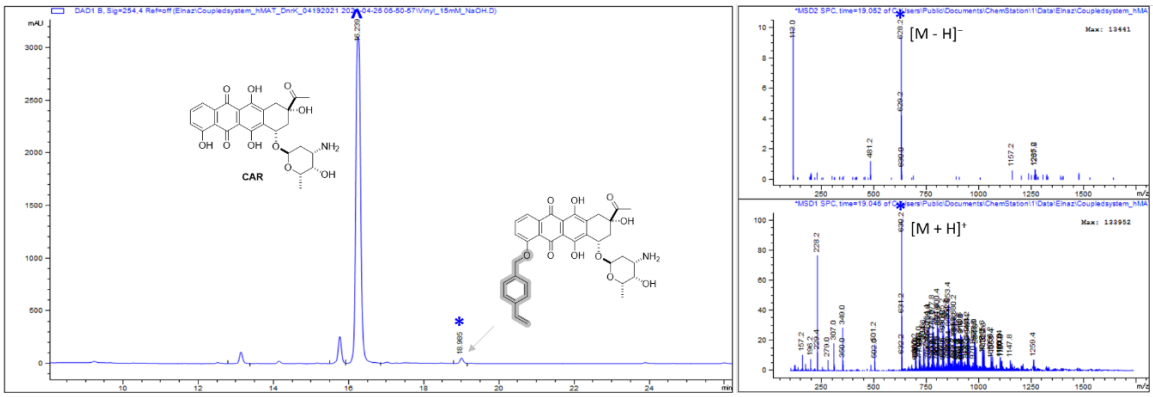

Figure S3.25. LC-MS analysis of the hMAT2/DnrK-catalyzed reaction of CAR^ and alkylated product* in the presence of **Ado21** co-factor. Predicted DnrK regioselectivity is highlighted in grey.

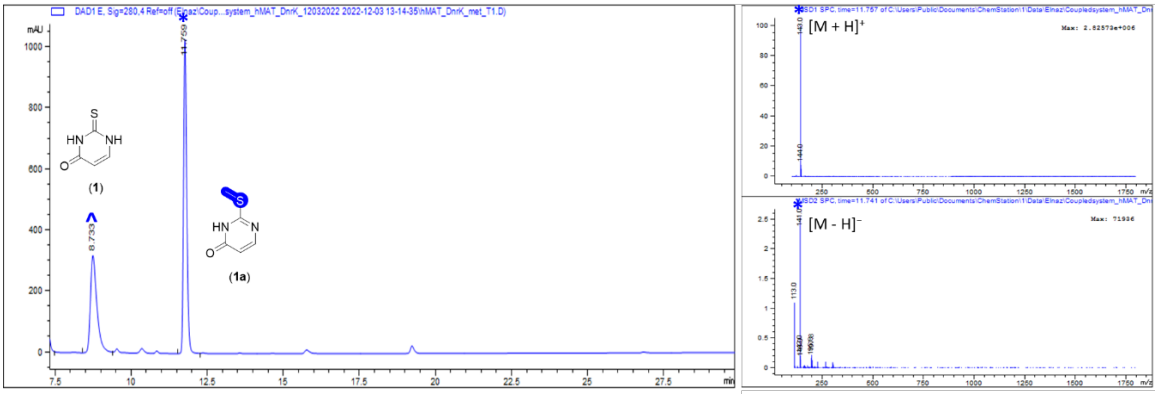

Figure S3.26. LC-MS analysis of the hMAT2/DnrK-catalyzed reaction of thiouracil (**1**)^ and methylated product 2-(methylthio)pyrimidin-4(3*H*)-one (**1a**)* in the presence of AdoMet co-factor. Determined DnrK regioselectivity is highlighted in blue.

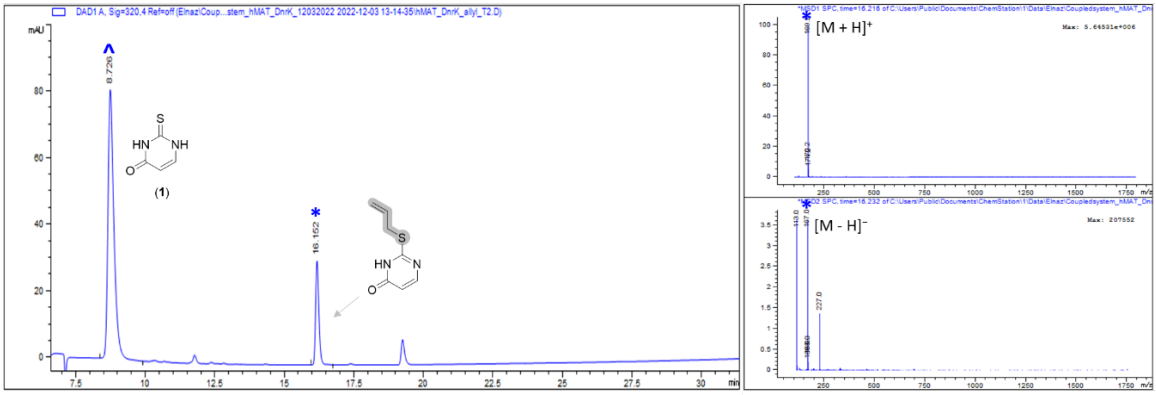

Figure S3.27. LC-MS analysis of the hMAT2/DnrK-catalyzed reaction of thiouracil (**1**)^ and alkylated product* in the presence of **Ado14** co-factor. Predicted DnrK regioselectivity is highlighted in grey.

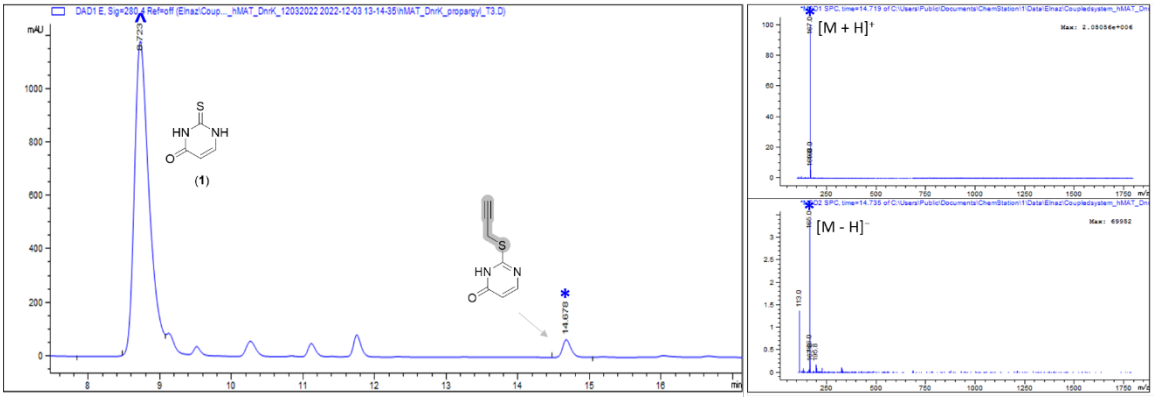

Figure S3.28. LC-MS analysis of the hMAT2/DnrK-catalyzed reaction of thiouracil (**1**)^ and alkylated product* in the presence of **Ado15** co-factor. Predicted DnrK regioselectivity is highlighted in grey.

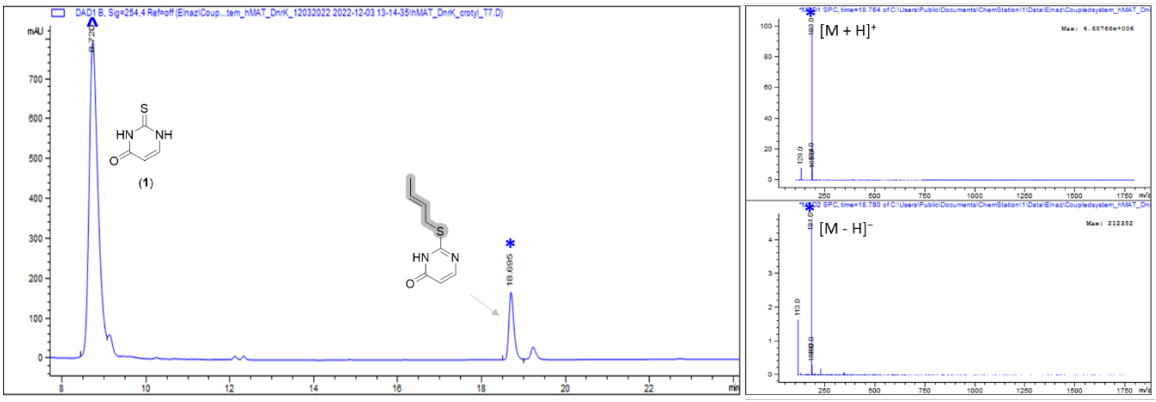

Figure S3.29. LC-MS analysis of the hMAT2/DnrK-catalyzed reaction of thiouracil (**1**)^ and alkylated product* in the presence of **Ado16** co-factor. Predicted DnrK regioselectivity is highlighted in grey.

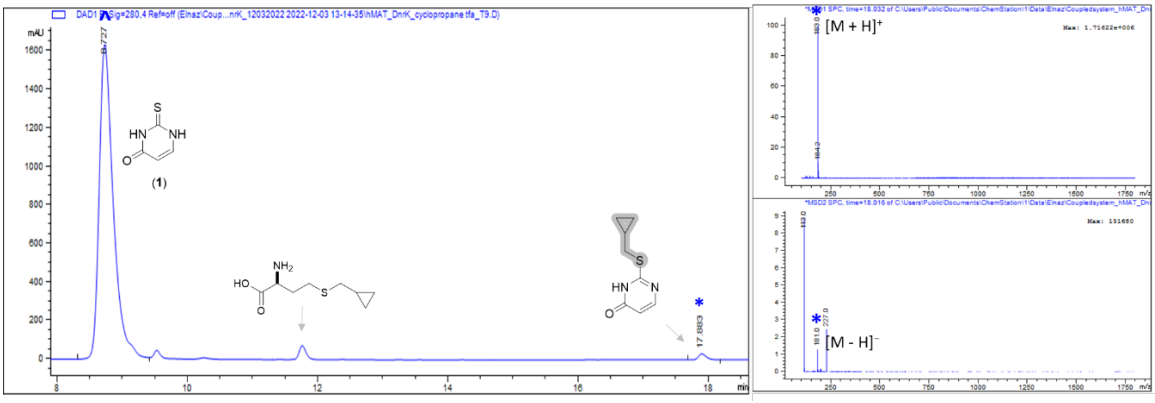

Figure S3.30. LC-MS analysis of the hMAT2/DnrK-catalyzed reaction of thiouracil (**1**)^ and alkylated product* in the presence of **Ado18** co-factor. Predicted DnrK regioselectivity is highlighted in grey.

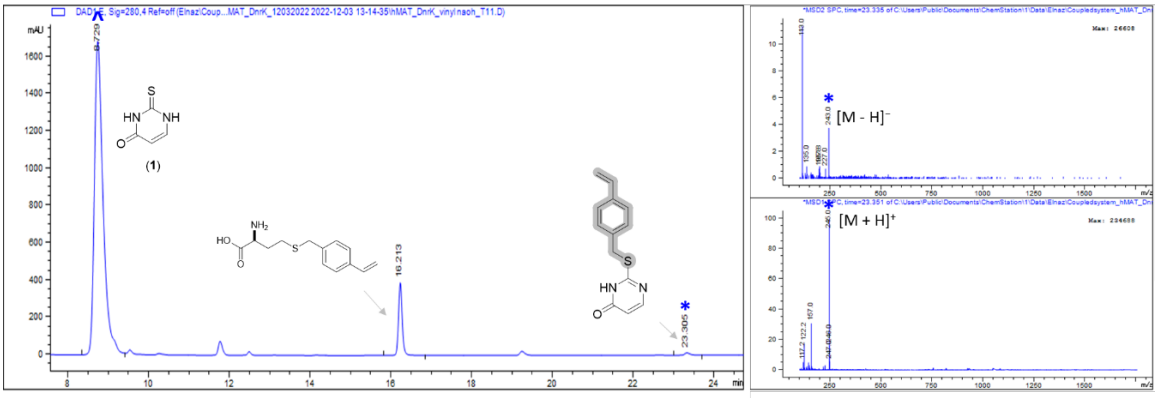

Figure S3.31. LC-MS analysis of the hMAT2/DnrK-catalyzed reaction of thiouracil (**1**)^ and alkylated product* in the presence of **Ado21** co-factor. Predicted DnrK regioselectivity is highlighted in grey.

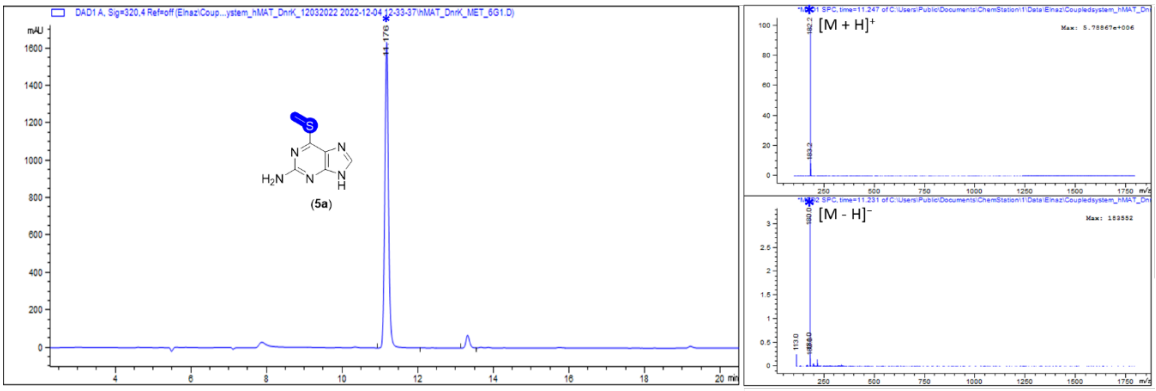

Figure S3.32. LC-MS analysis of the hMAT2/DnrK-catalyzed reaction of thioguanine (**5**)^ and methylated product 6-methylthioguanine (**5a**)* in the presence of AdoMet co-factor. Determined DnrK regioselectivity is highlighted in blue.

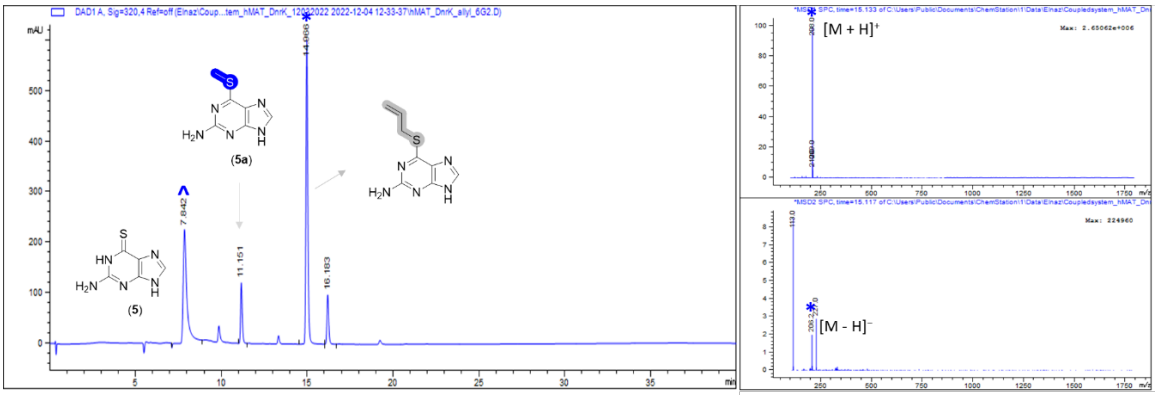

Figure S3.33. LC-MS analysis of the hMAT2/DnrK-catalyzed reaction of thioguanine (**5**)^ and alkylated product* in the presence of **Ado14** co-factor. Predicted DnrK regioselectivity is highlighted in grey.

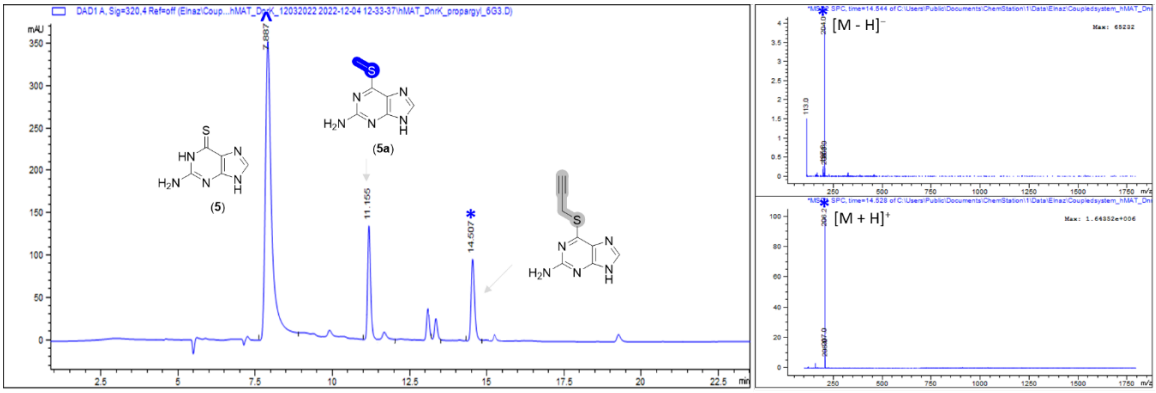

Figure S3.34. LC-MS analysis of the hMAT2/DnrK-catalyzed reaction of thioguanine (**5**)^ and alkylated product* in the presence of **Ado15** co-factor. Predicted DnrK regioselectivity is highlighted in grey.

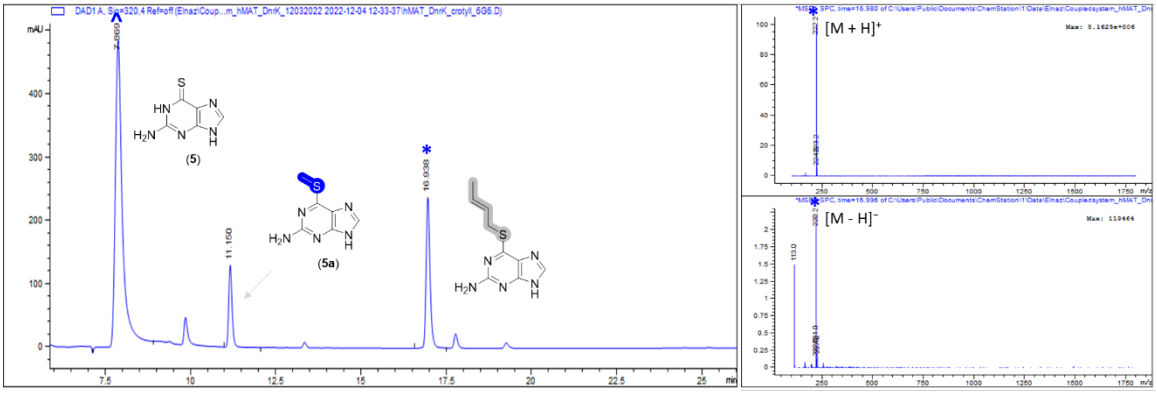

Figure S3.35. LC-MS analysis of the hMAT2/DnrK-catalyzed reaction of thioguanine (**5**)^ and alkylated product* in the presence of **Ado16** co-factor. Predicted DnrK regioselectivity is highlighted in grey.

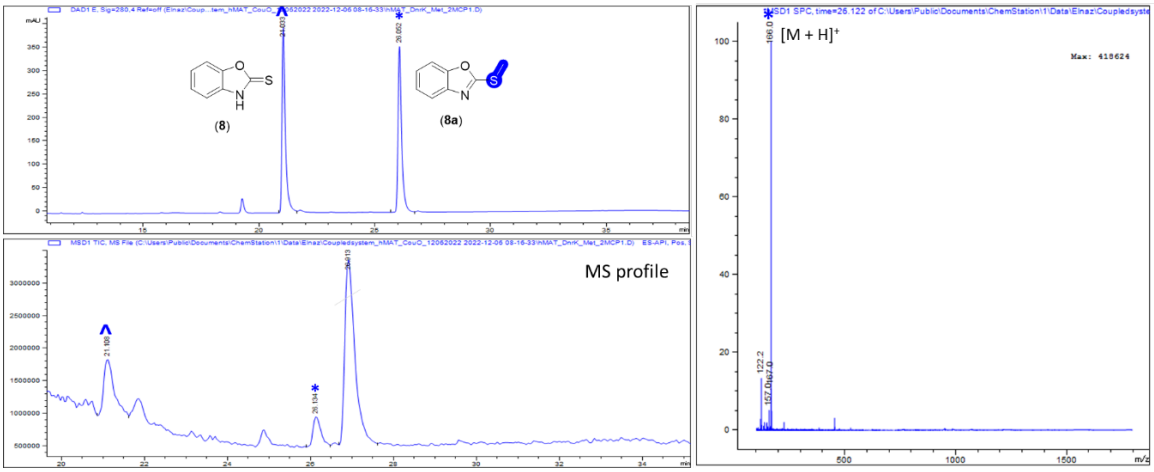

Figure S3.36. LC-MS analysis of the hMAT2/DnrK-catalyzed reaction of 2-mercaptobenzoxazole (**8**)^ and methylated product 2-(methylthio)benzoxazole (**8a**)* in the presence of AdoMet co-factor. Determined DnrK regioselectivity is highlighted in blue.

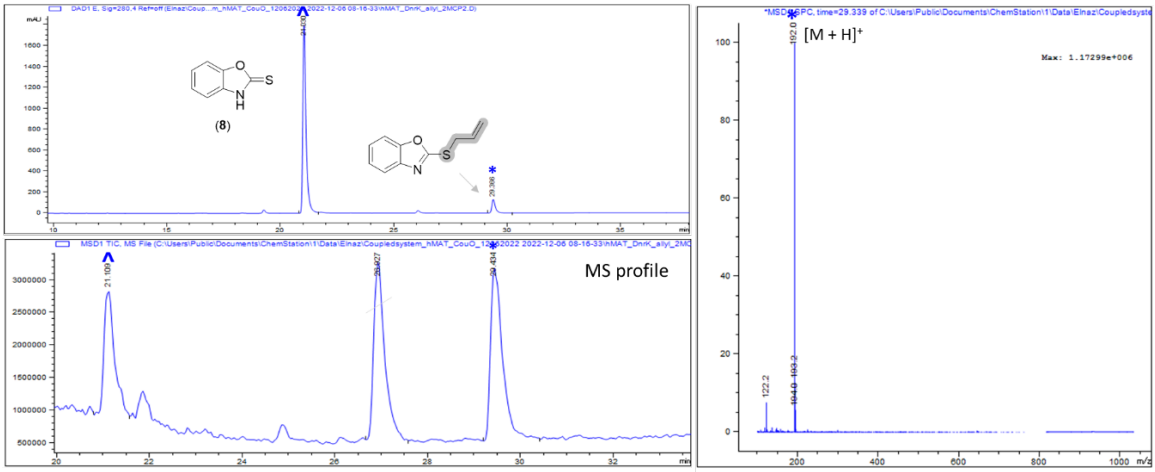

Figure S3.37. LC-MS analysis of the hMAT2/DnrK-catalyzed reaction of 2-mercaptobenzoxazole (**8**)^ and alkylated product* in the presence of **Ado14** co-factor. Predicted DnrK regioselectivity is highlighted in grey.

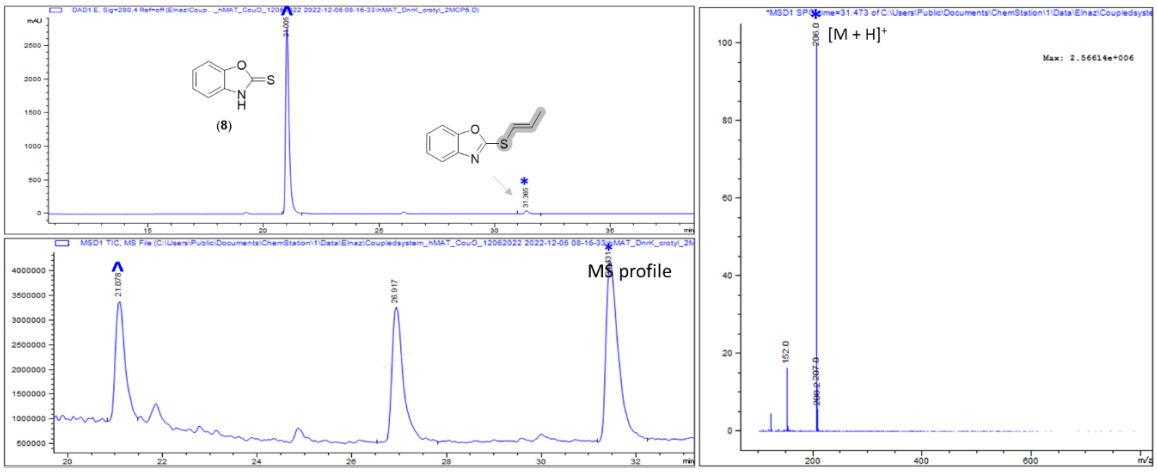

Figure S3.38. LC-MS analysis of the hMAT2/DnrK-catalyzed reaction of 2-mercaptobenzoxazole (**8**)^ and alkylated product* in the presence of **Ado16** co-factor. Predicted DnrK regioselectivity is highlighted in grey.

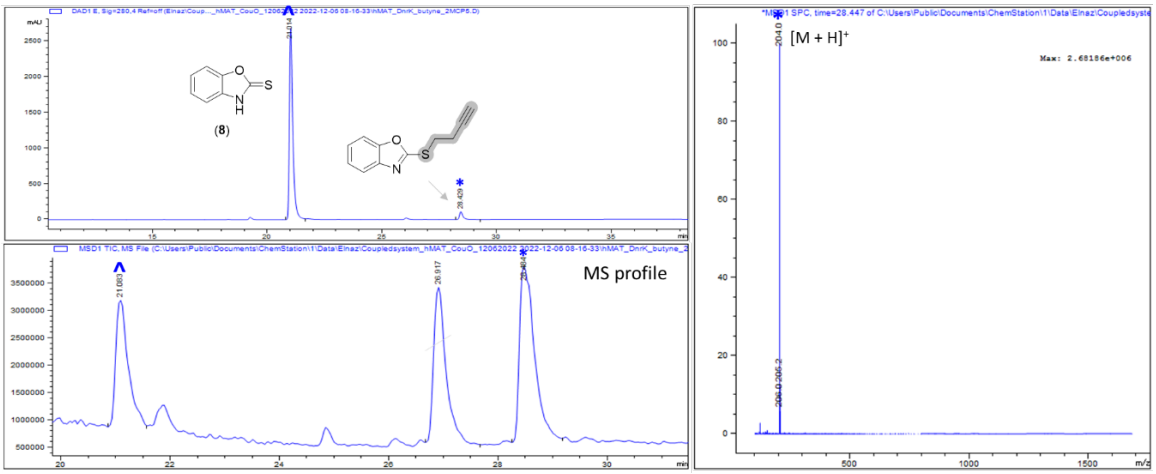

Figure S3.39. LC-MS analysis of the hMAT2/DnrK-catalyzed reaction of 2-mercaptobenzoxazole (**8**)^ and alkylated product* in the presence of **Ado17** co-factor. Predicted DnrK regioselectivity is highlighted in grey.

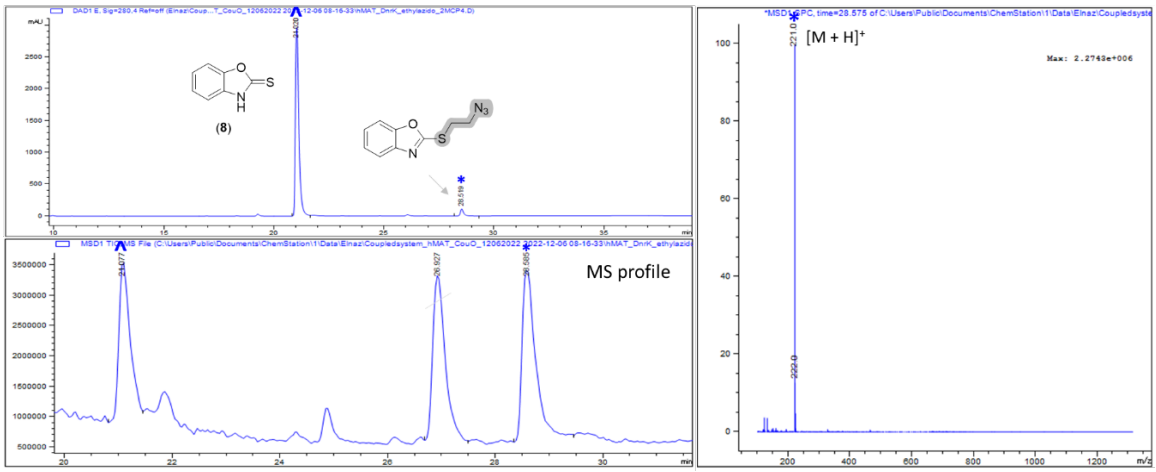

Figure S3.40. LC-MS analysis of the hMAT2/DnrK-catalyzed reaction of 2-mercaptobenzoxazole (**8**)^ and alkylated product* in the presence of **Ado19** co-factor. Predicted DnrK regioselectivity is highlighted in grey.

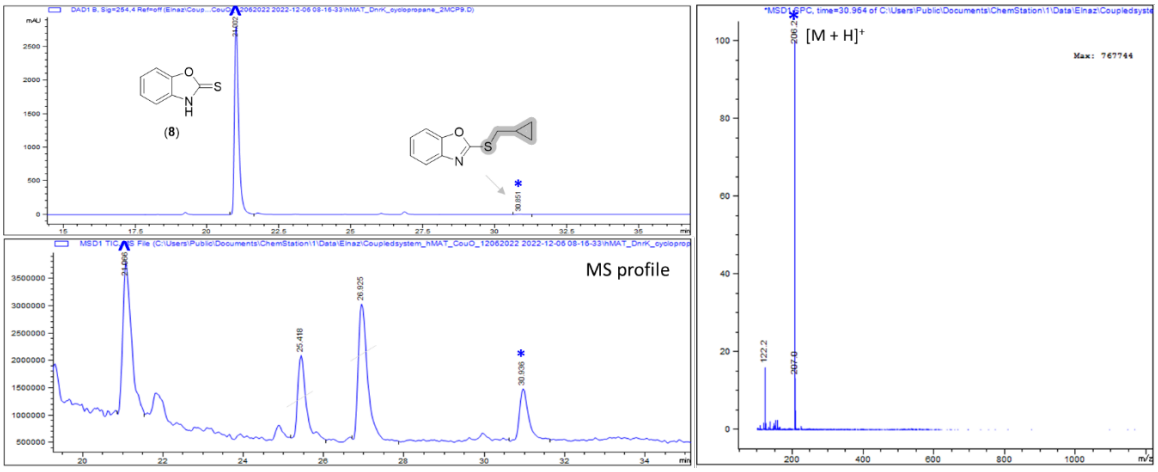

Figure S3.41. LC-MS analysis of the hMAT2/DnrK-catalyzed reaction of 2-mercaptobenzoxazole (**8**)^ and alkylated product* in the presence of **Ado18** co-factor. Predicted DnrK regioselectivity is highlighted in grey.

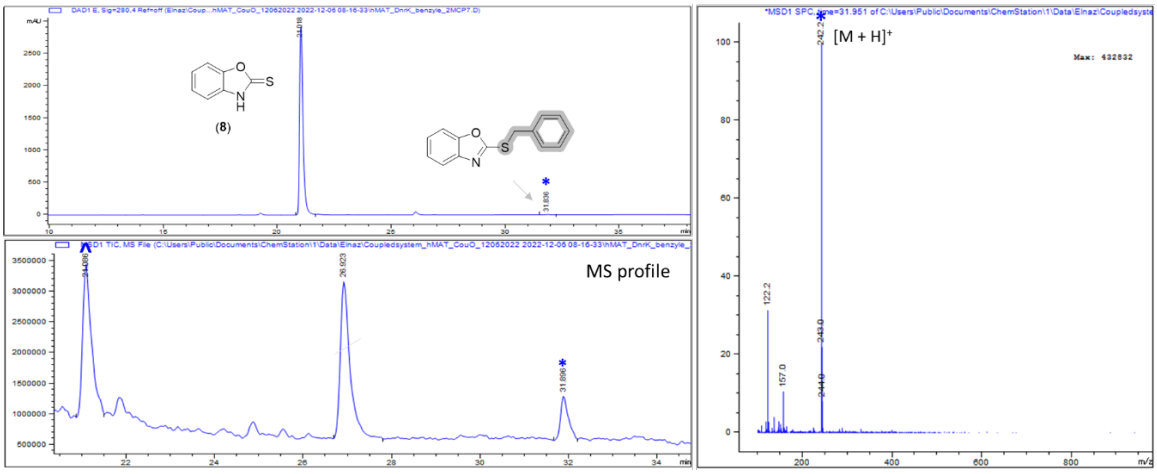

Figure S3.42. LC-MS analysis of the hMAT2/DnrK-catalyzed reaction of 2-mercaptobenzoxazole (**8**)^ and alkylated product* in the presence of **Ado20** co-factor. Predicted DnrK regioselectivity is highlighted in grey.

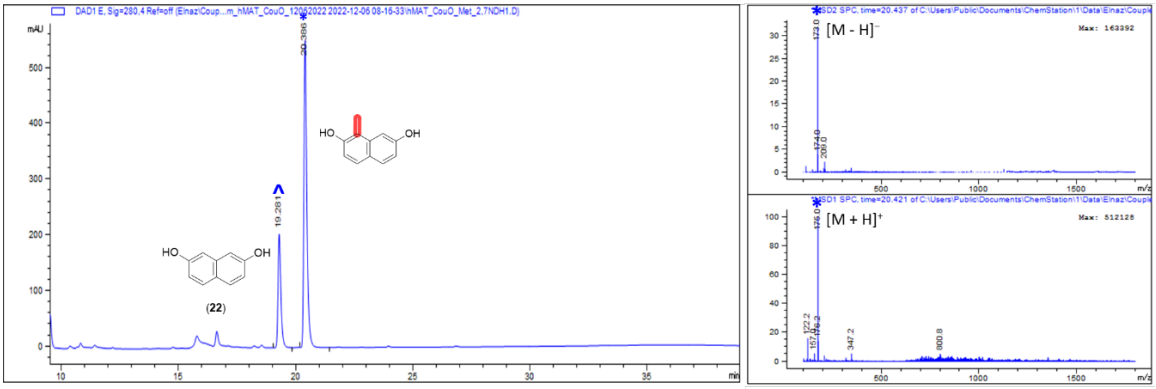

Figure S3.43. LC-MS analysis of the hMAT2/CouO-catalyzed reaction of 2,7-naphthalenediol (**22**)^ and methylated product* in the presence of AdoMet co-factor. Determined CouO regioselectivity is highlighted in red.

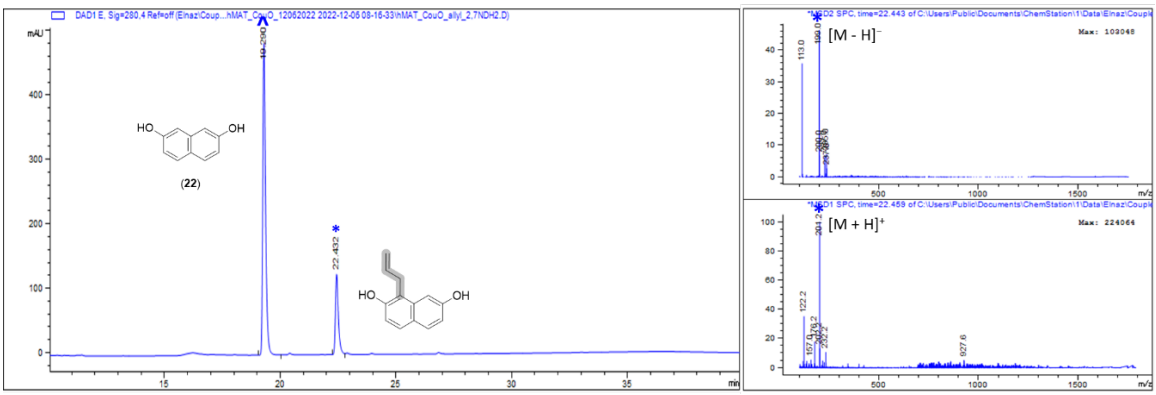

Figure S3.44. LC-MS analysis of the hMAT2/CouO-catalyzed reaction of 2,7-naphthalenediol (**22**)^ and alkylated product* in the presence of **Ado14** co-factor. Predicted CouO regioselectivity is highlighted in grey.

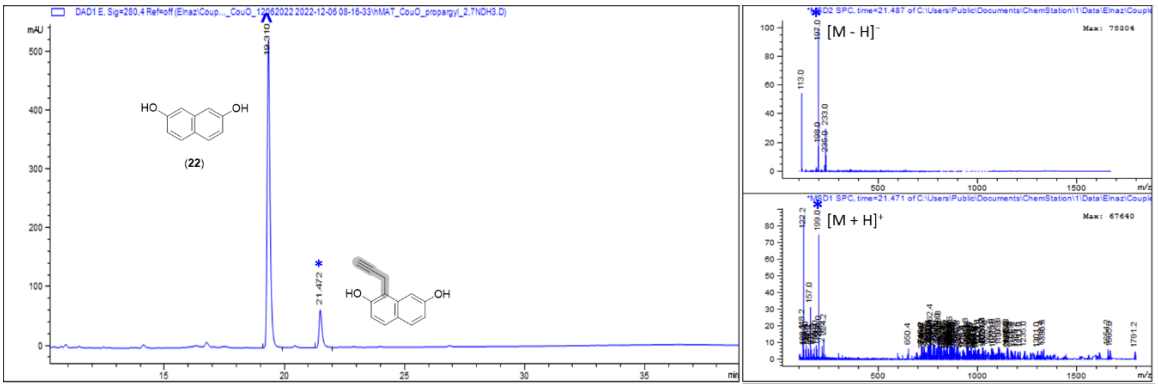

Figure S3.45. LC-MS analysis of the hMAT2/CouO-catalyzed reaction of 2,7-naphthalenediol (**22**)^ and alkylated product* in the presence of **Ado15** co-factor. Predicted CouO regioselectivity is highlighted in grey.

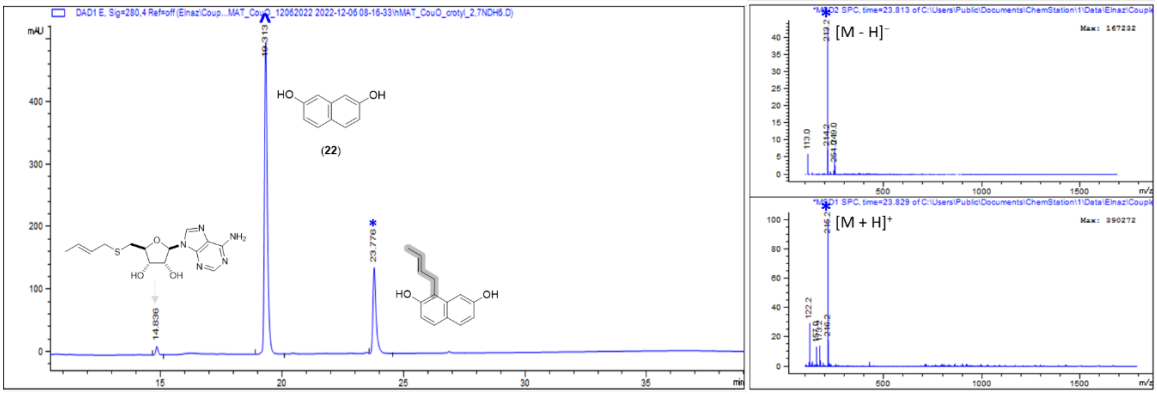

Figure S3.46. LC-MS analysis of the hMAT2/CouO-catalyzed reaction of 2,7-naphthalenediol (**22**)^ and alkylated product* in the presence of **Ado16** co-factor. Predicted CouO regioselectivity is highlighted in grey.

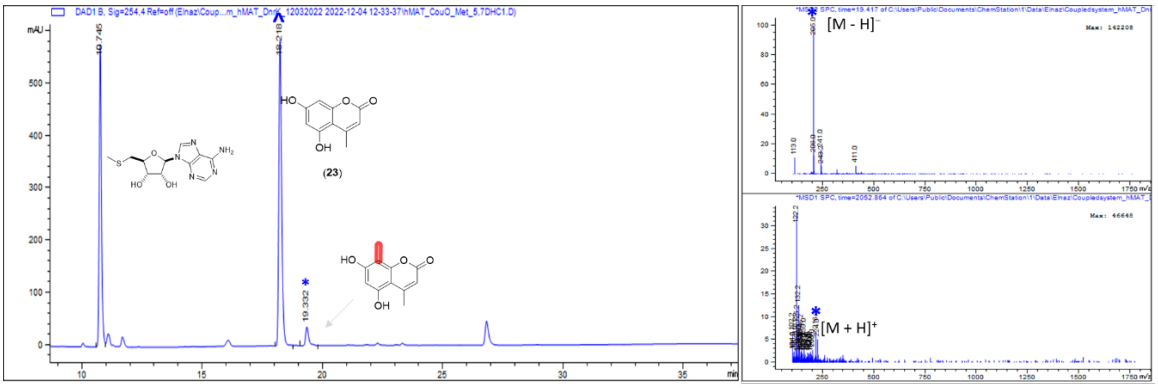

Figure S3.47. LC-MS analysis of the hMAT2/CouO-catalyzed reaction of 7-dihydroxy-4-methylcoumarin (**23**)^ and methylated product* in the presence of AdoMet co-factor. Determined CouO regioselectivity is highlighted in red.

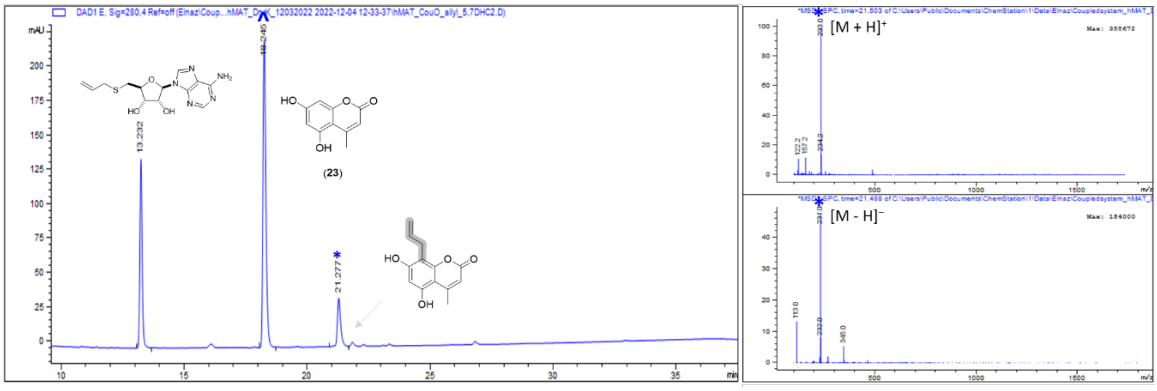

Figure S3.48. LC-MS analysis of the hMAT2/CouO-catalyzed reaction 7-dihydroxy-4-methylcoumarin (**23**)^ and alkylated product* in the presence of **Ado14** co-factor. Predicted CouO regioselectivity is highlighted in grey.

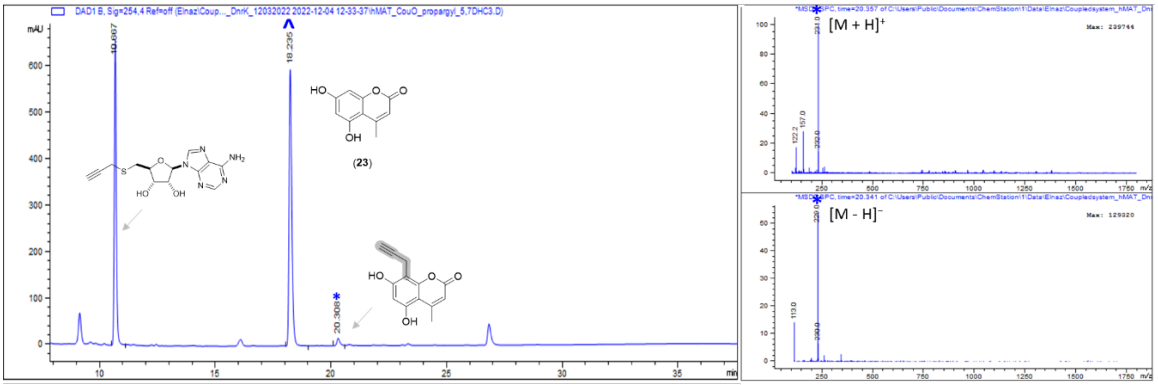

Figure S3.49. LC-MS analysis of the hMAT2/CouO-catalyzed reaction 7-dihydroxy-4-methylcoumarin (**23**)^ and alkylated product* in the presence of **Ado15** co-factor. Predicted CouO regioselectivity is highlighted in grey.

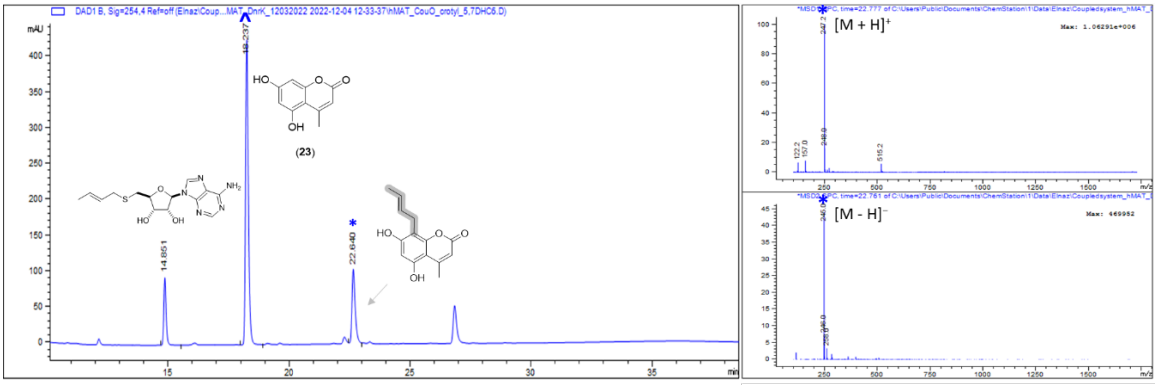

Figure S3.50. LC-MS analysis of the hMAT2/CouO-catalyzed reaction 7-dihydroxy-4-methylcoumarin (**23**)^ and alkylated product* in the presence of **Ado15** co-factor. Predicted CouO regioselectivity is highlighted in grey.

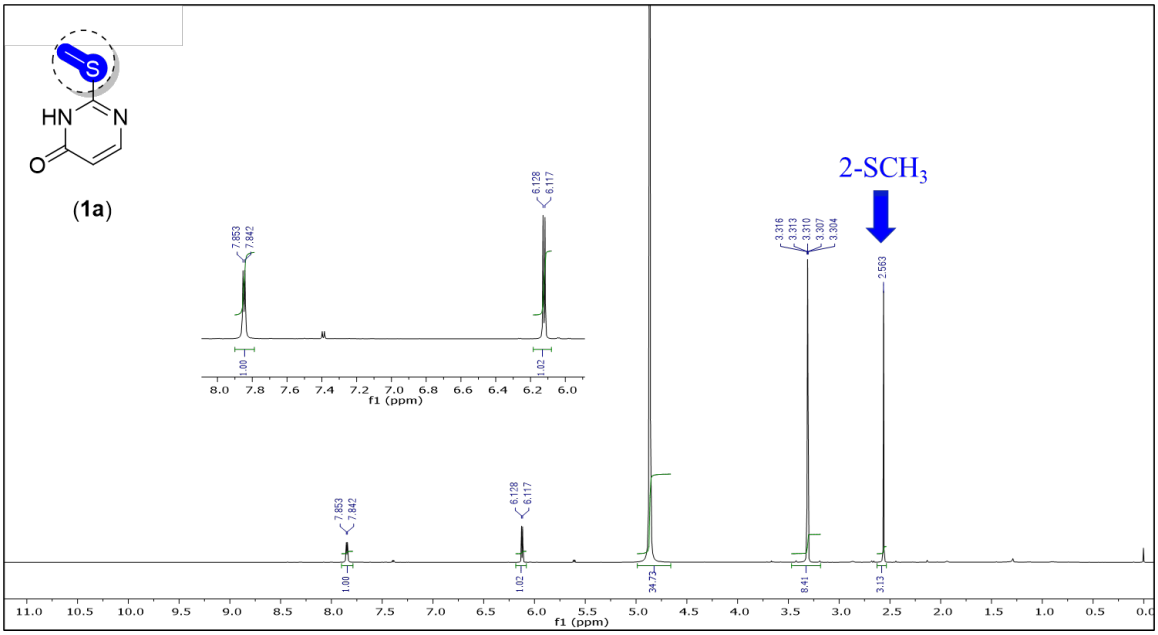

Figure S3.51. ^{1}H NMR spectrum (CD_3OD, 600 MHz) of **1a**.

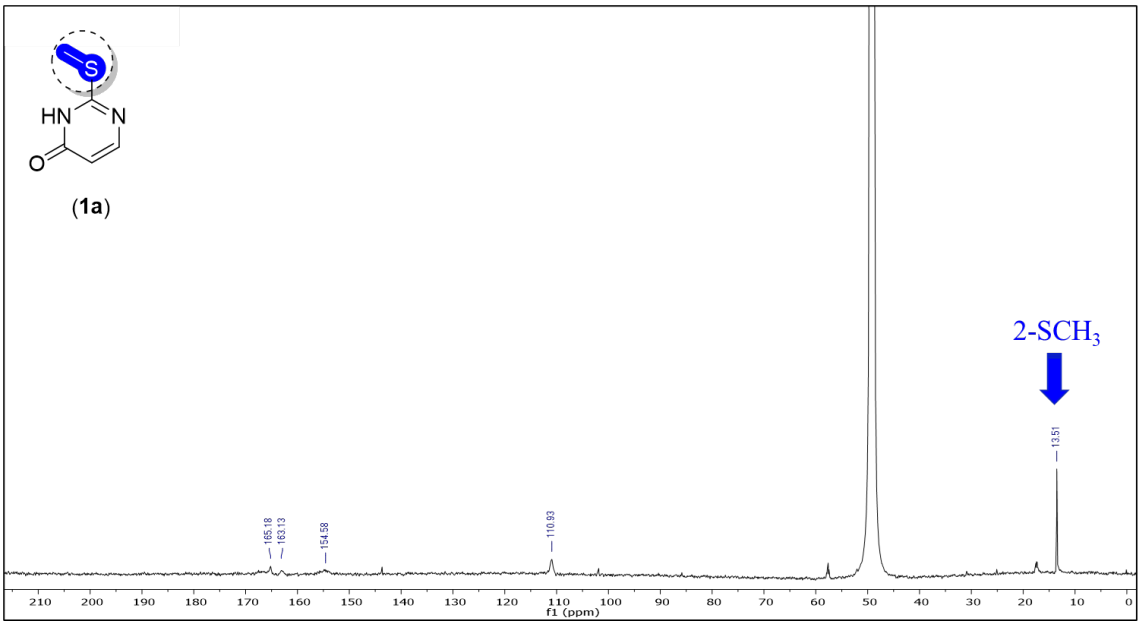

Figure S3.52. ^{13}C NMR spectrum (CD_3OD, 600 MHz) of **1a**.

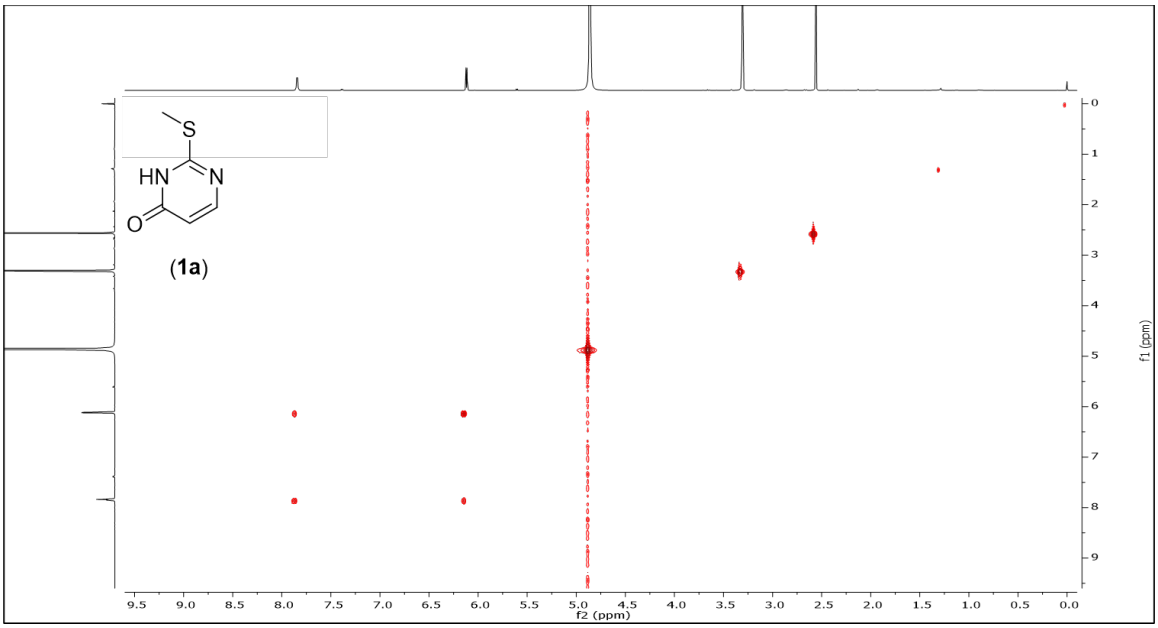

Figure S3.53. ^{1}H,^{1}H-COSY spectrum (CD_3OD, 600 MHz) of **1a**.

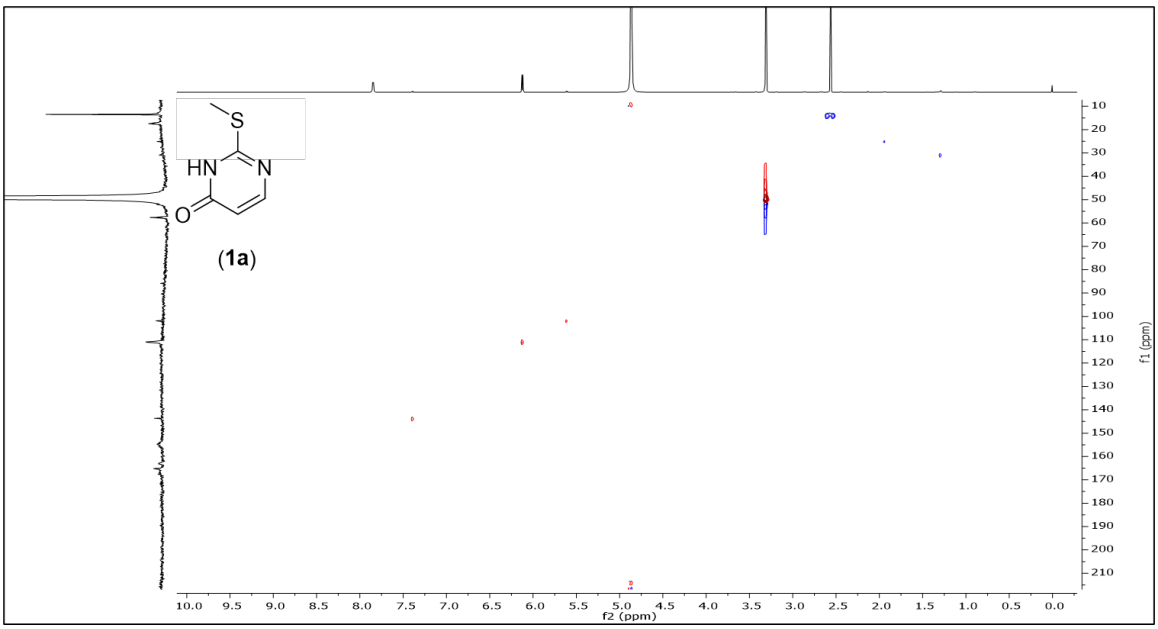

Figure S3.54. HSQC spectrum (CD_3OD, 600 MHz) of **1a**.

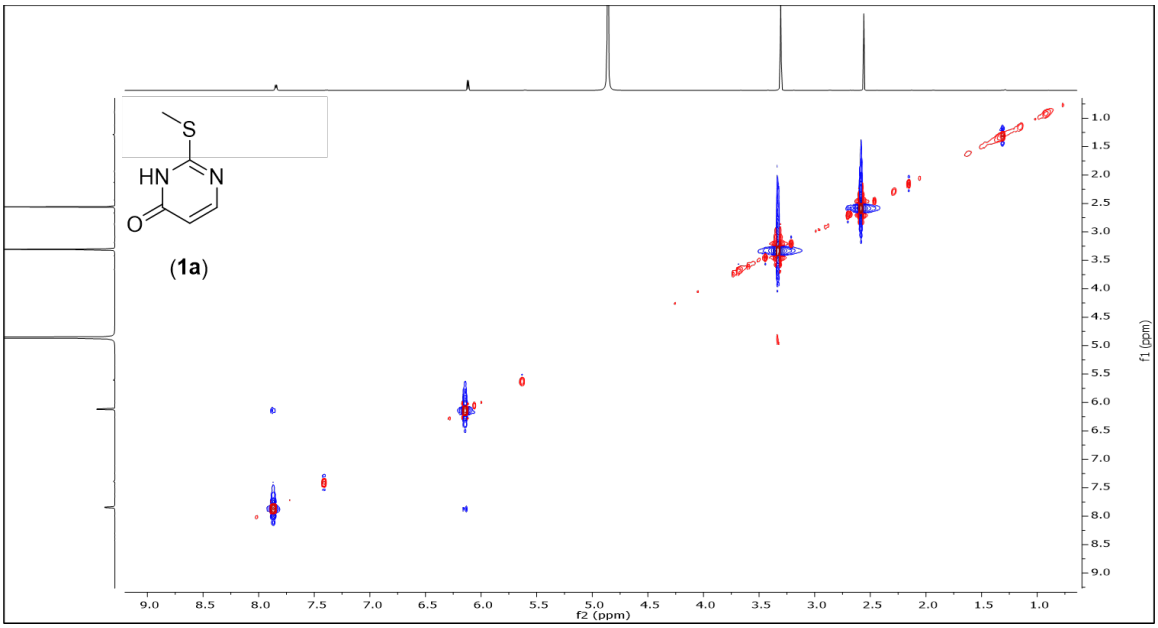

Figure S3.55. NOESY spectrum (CD_3OD, 600 MHz) of **1a**.

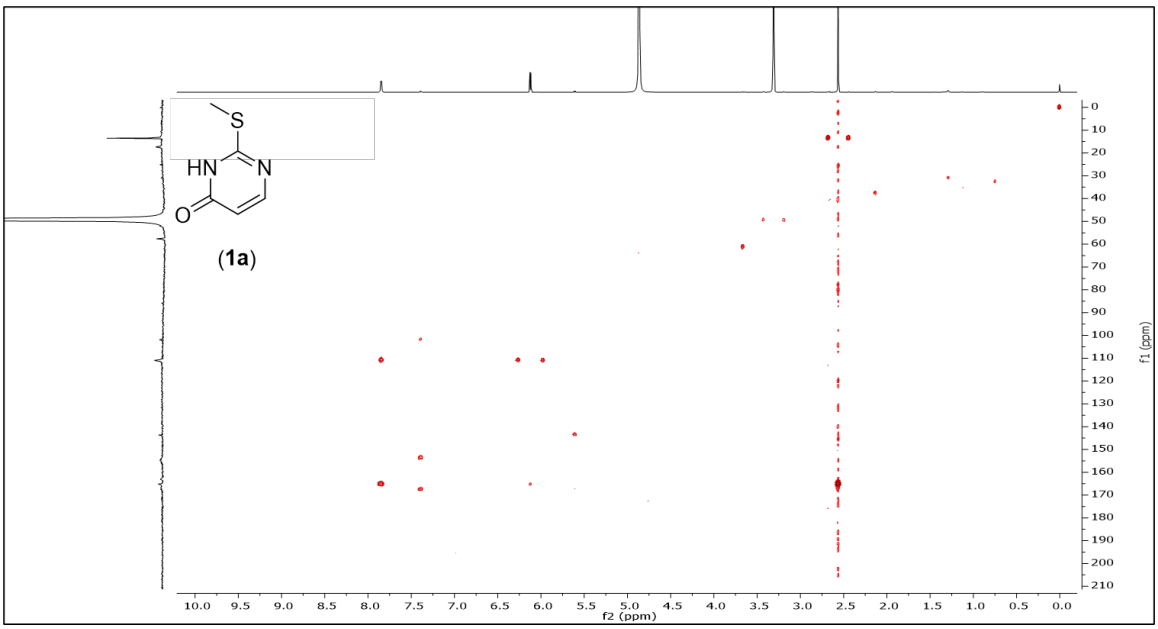

Figure S3.56. HMBC spectrum (CD_3OD, 600 MHz) of **1a**.

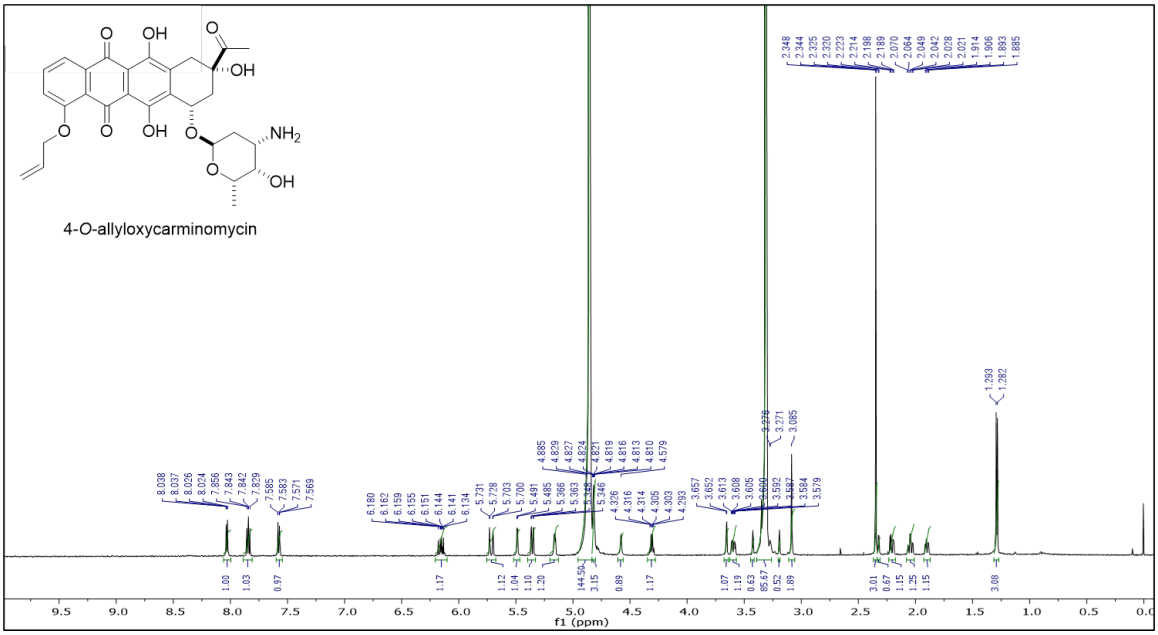

Figure S3.57. ^{1}H NMR spectrum (CD_3OD, 600 MHz) of 4-*O*-allyloxycarminomycin.

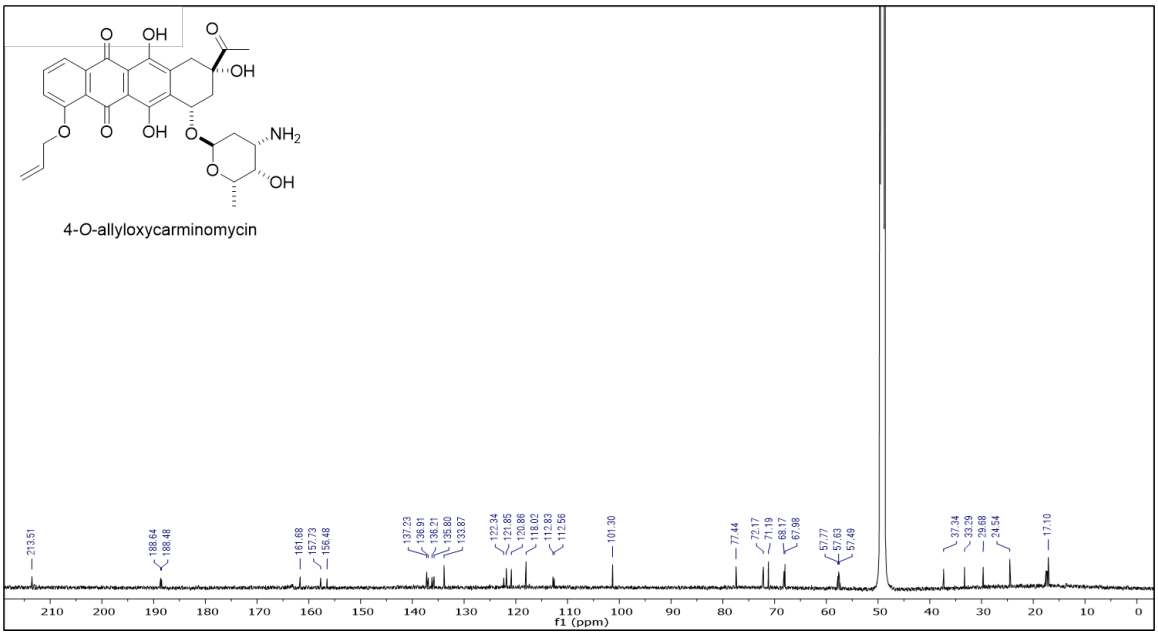

Figure S3.58. ^{13}C NMR spectrum (CD_3OD, 150 MHz) of 4-*O*-allyloxycarminomycin.

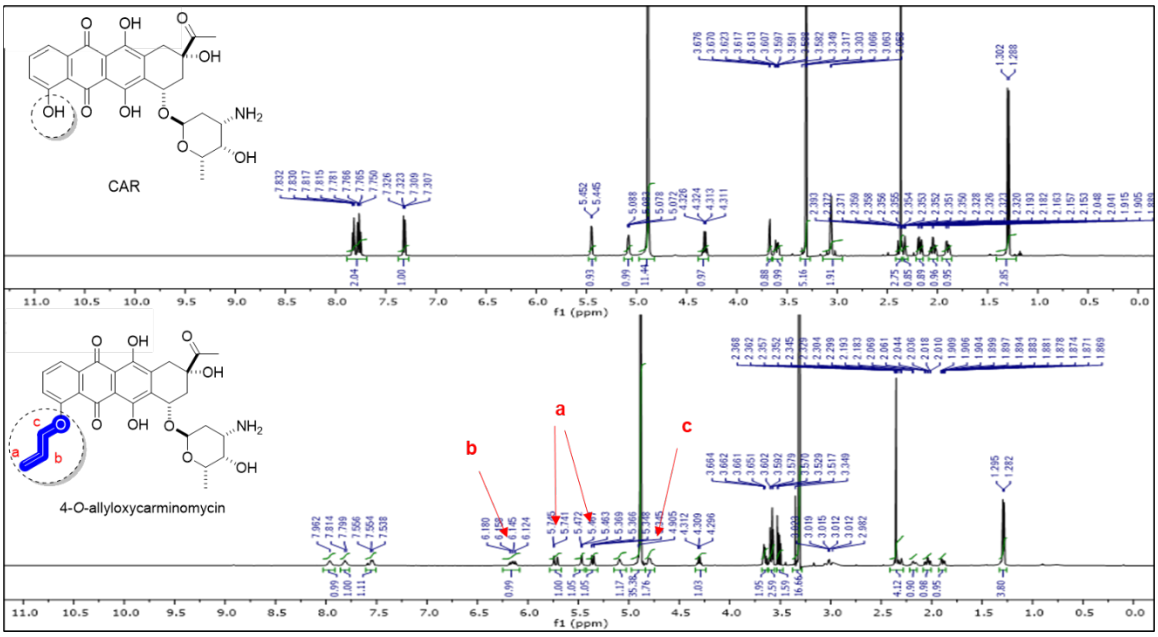

Figure S3.59. Comparison of the ^{1}H NMR spectrum (CD_3OD, 600 MHz) of CAR and coupled hMAT2A/DnrK product 4-*O*-allyloxycarminomycin.

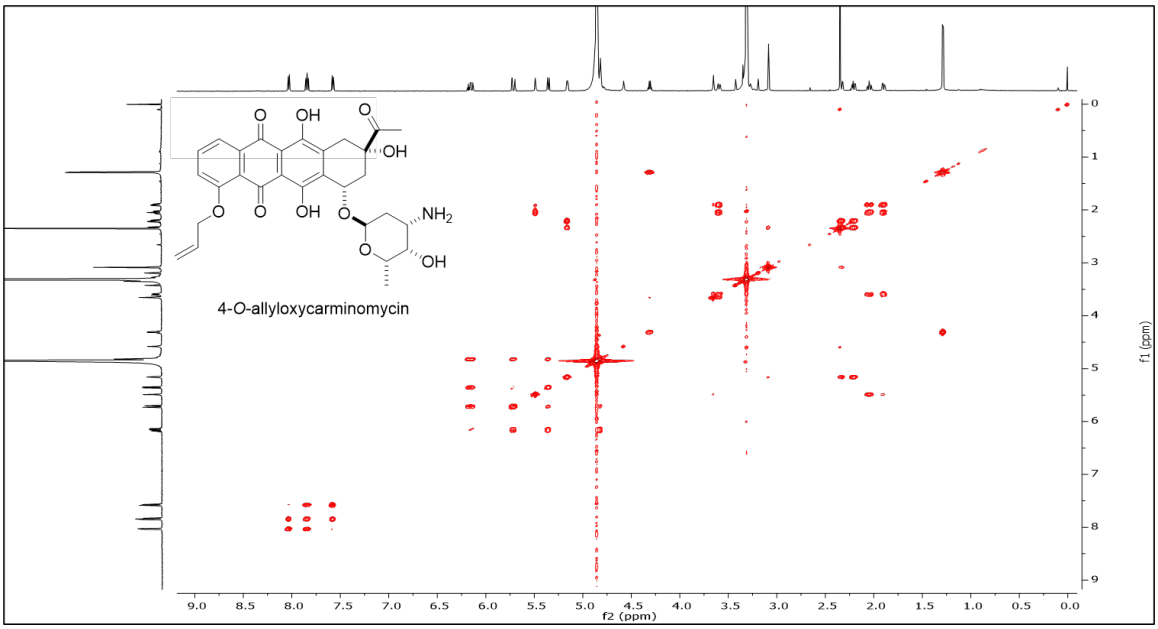

Figure S3.60. ^{1}H,^{1}H-COSY spectrum (CD_3OD, 600 MHz) of 4-*O*-allyloxycarminomycin.

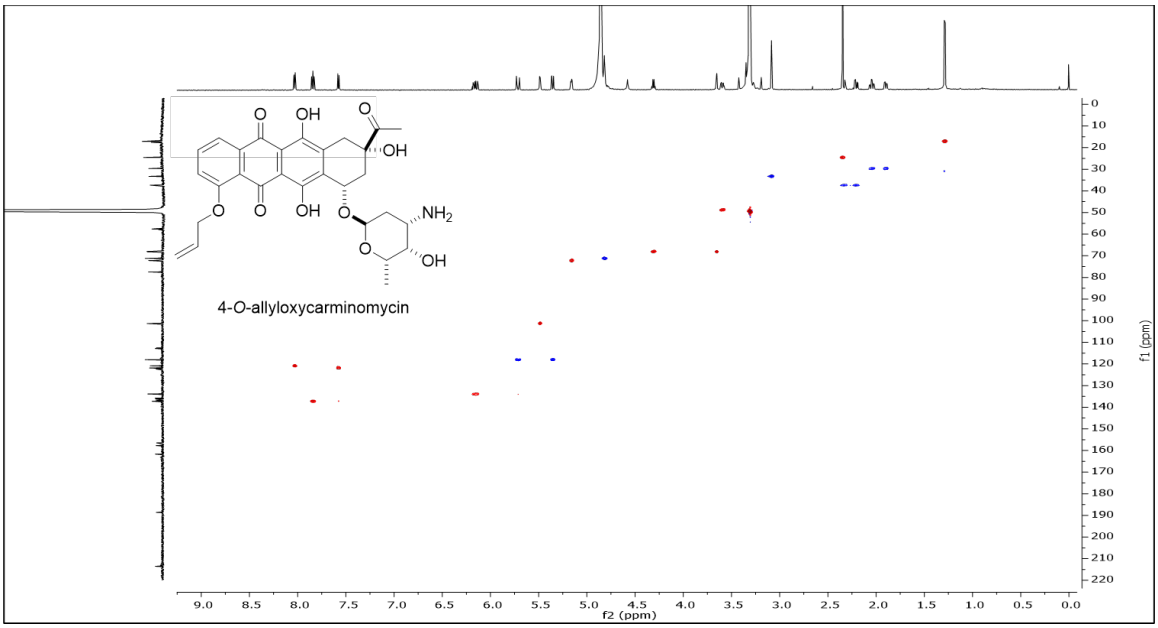

Figure S3.61. HSQC spectrum (CD_3OD, 600 MHz) of 4-*O*-allyloxycarminomycin.

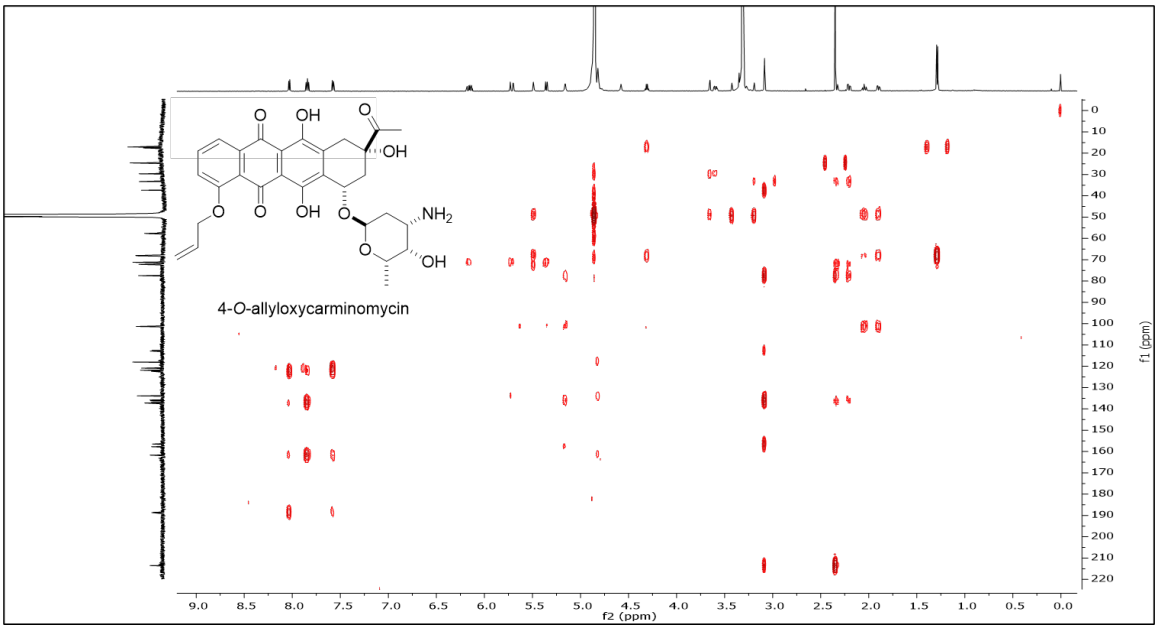

Figure S3.62. HMBC spectrum (CD_3OD, 600 MHz) of 4-*O*-allyloxycarminomycin.

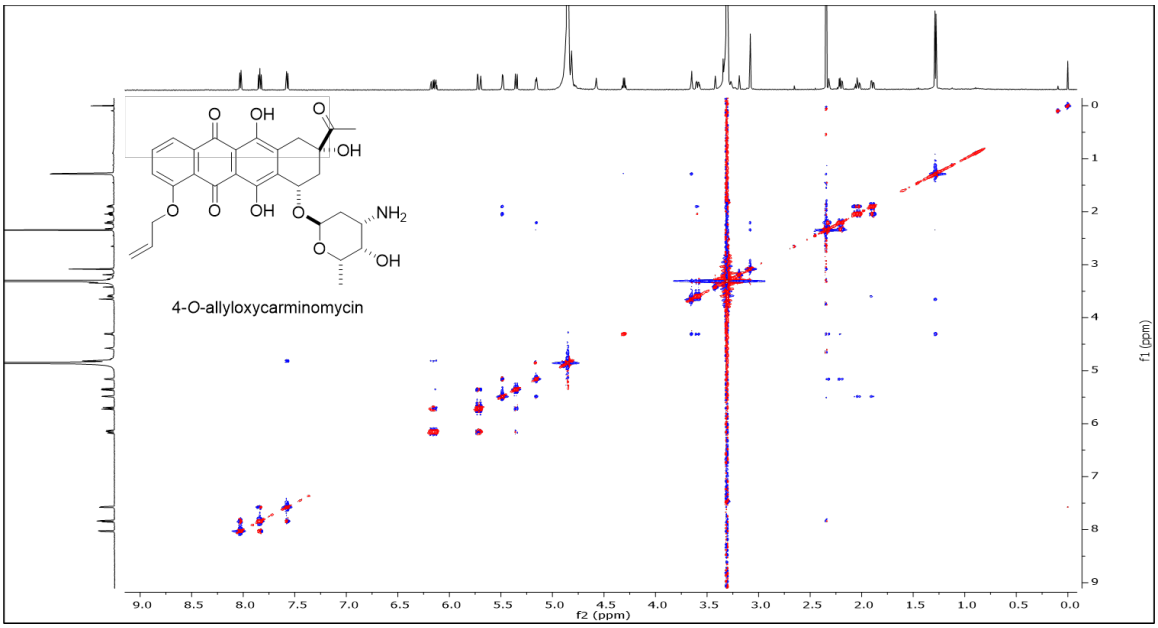

Figure S3.63. NOESY spectrum (CD_3OD, 600 MHz) of 4-*O*-allyloxycarminomycin.

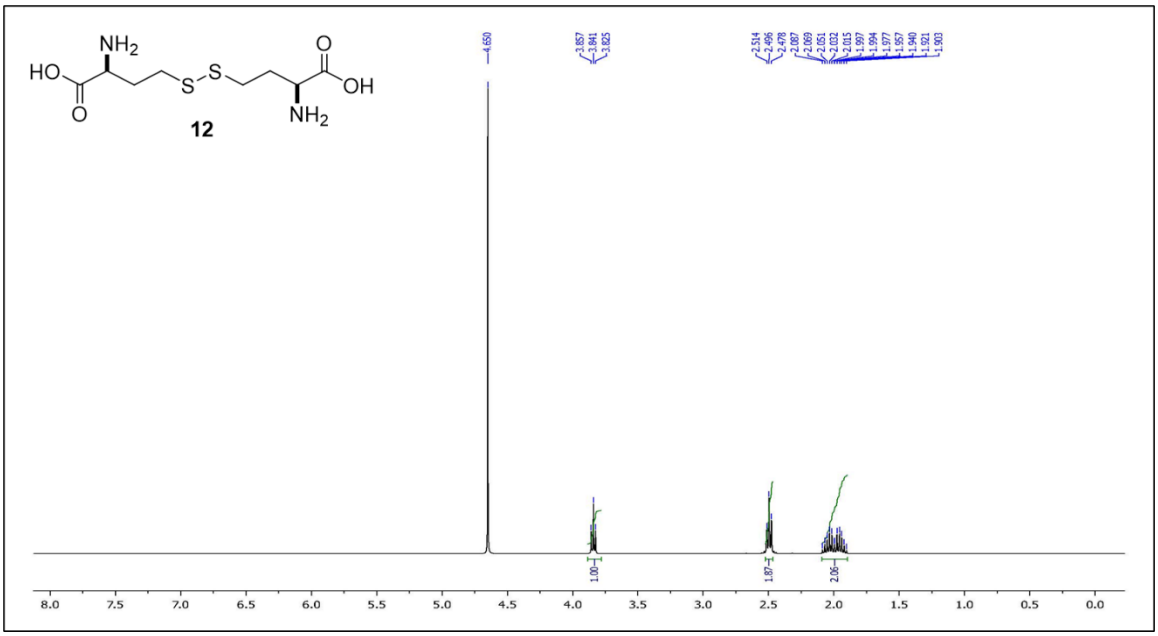

Figure S3.64. ^{1}H NMR spectrum (D_2O/TFA = 20/1, 400 MHz) of L,L-homocystine (**12**).

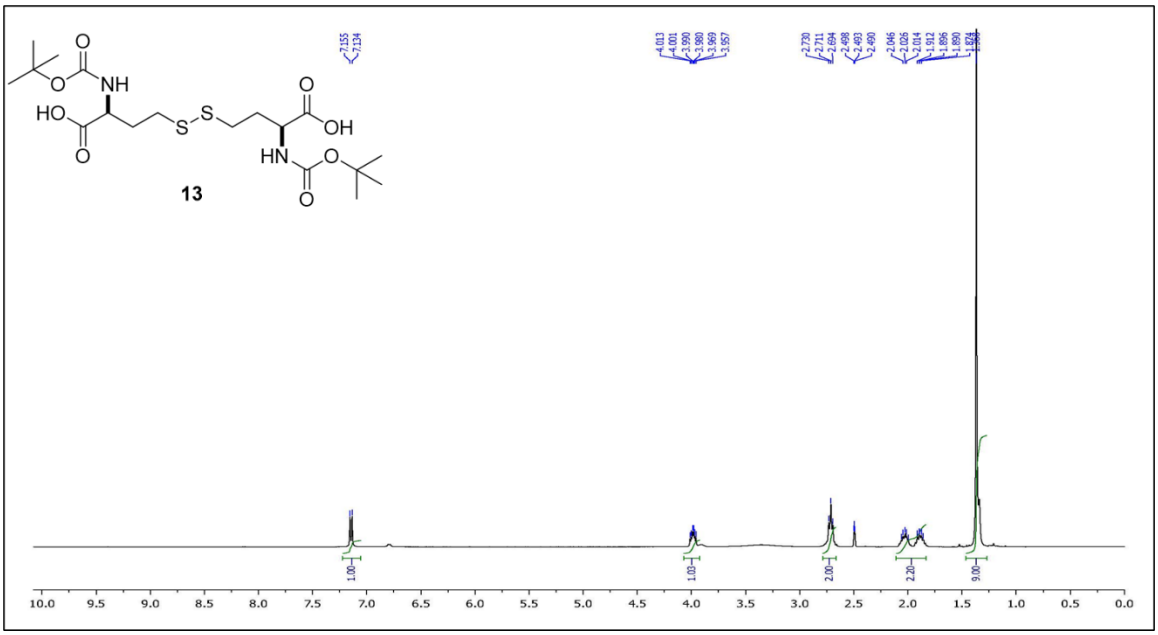

Figure S3.65. ^{1}H NMR spectrum (DMSO, 400 MHz) of *N*-Boc-L,L-homocystine (**13**).

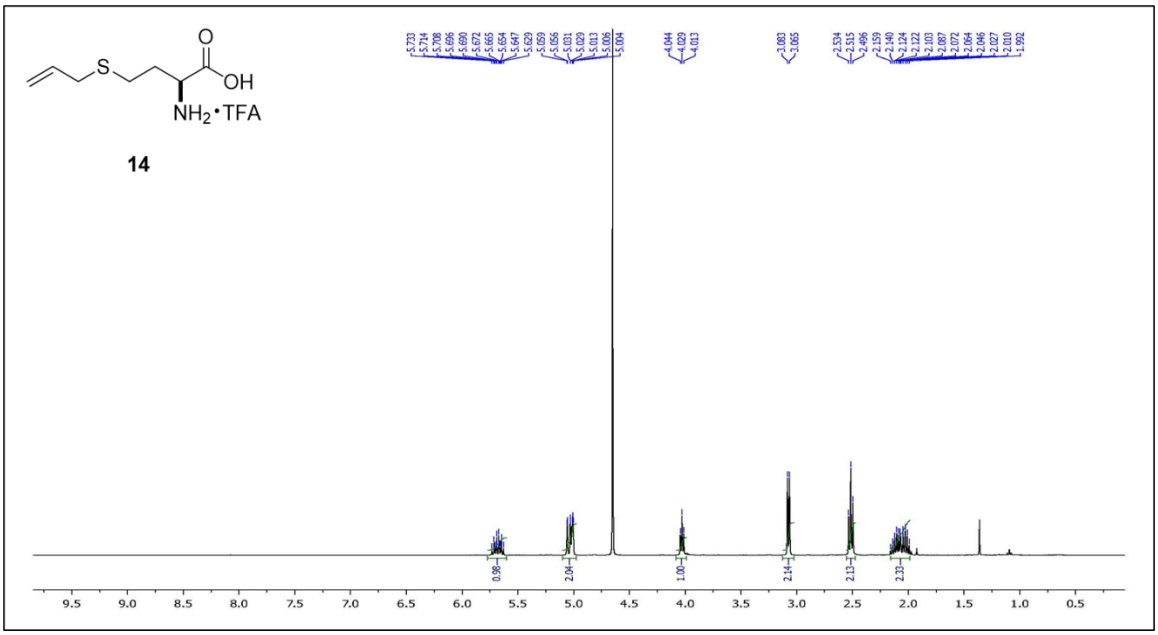

Figure S3.66. ^{1}H NMR spectrum (D_2O, 400 MHz) of *S*-allyl-*L*-homocysteine TFA salt (**14**).

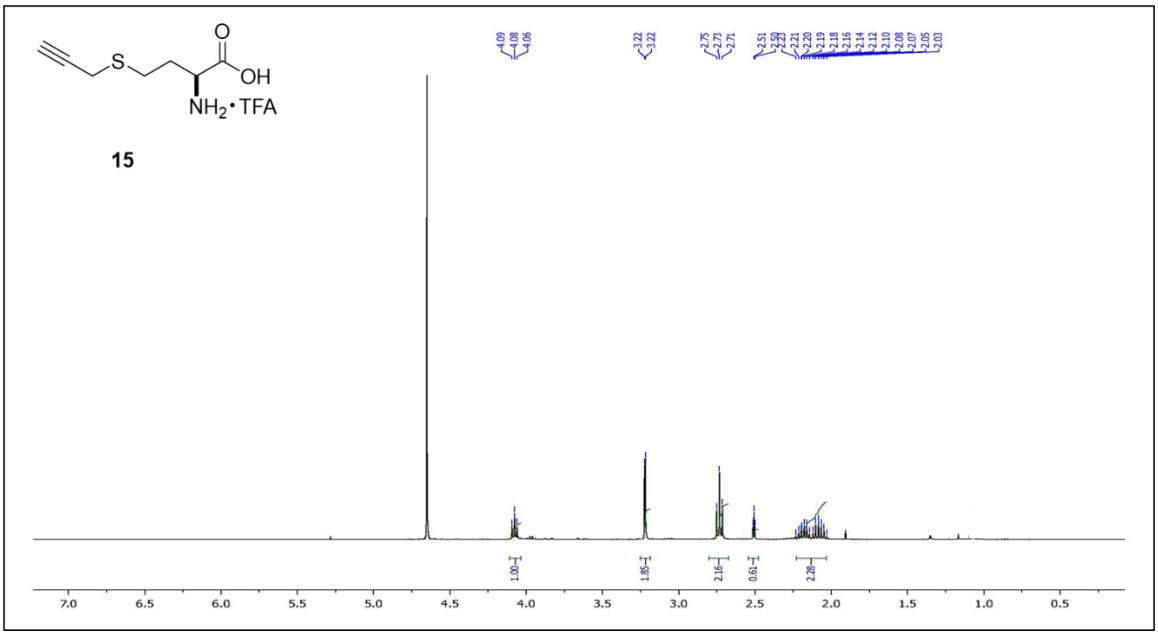

Figure S3.67. ^{1}H NMR spectrum (D_2O/TFA = 20/1, 400 MHz) of *S*-(prop-2-yn-1-yl)-*L*-homocysteine TFA salt (**15**).

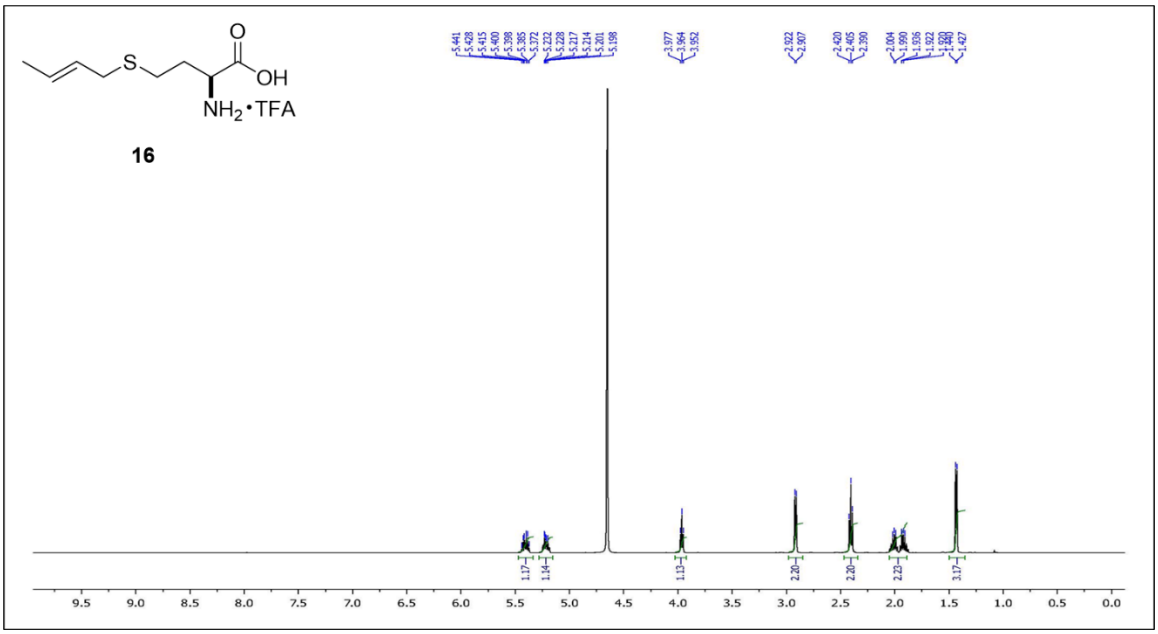

Figure S3.68. ^{1}H NMR spectrum (D_2O/TFA = 20/1, 500 MHz) of (*E*)-*S*-(but-2-en-1-yl)-*L*-homocysteine TFA salt (**16**).

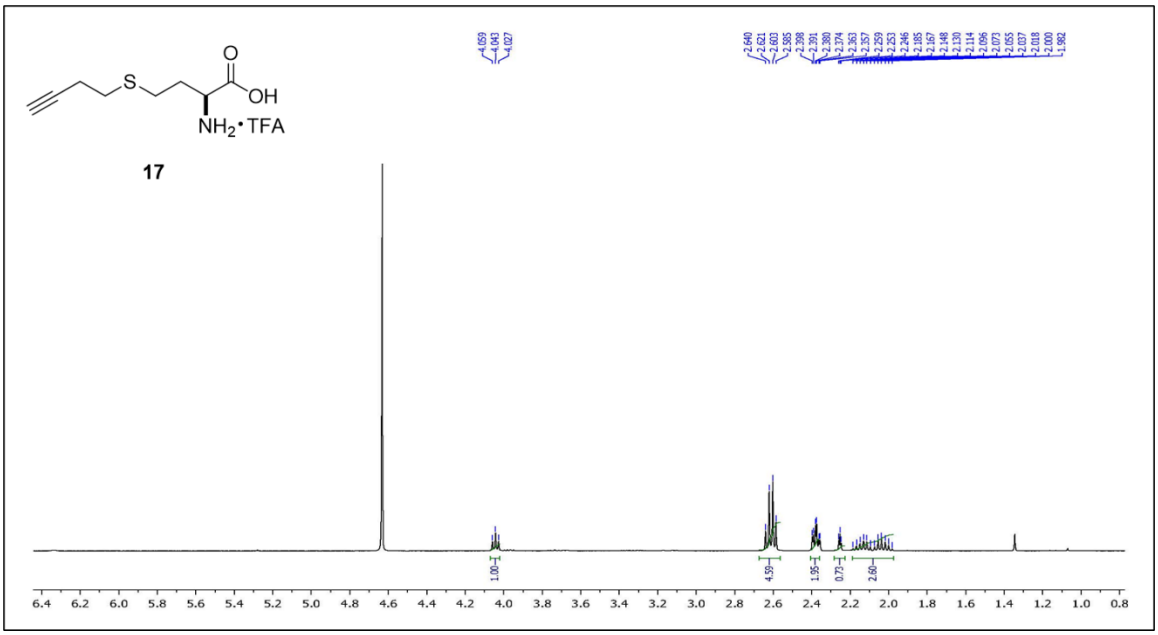

Figure S3.69. ^{1}H NMR spectrum (D_2O, 400 MHz) of S-(but-3-yn-1-yl)-*L*-homocysteine TFA salt (**17**).

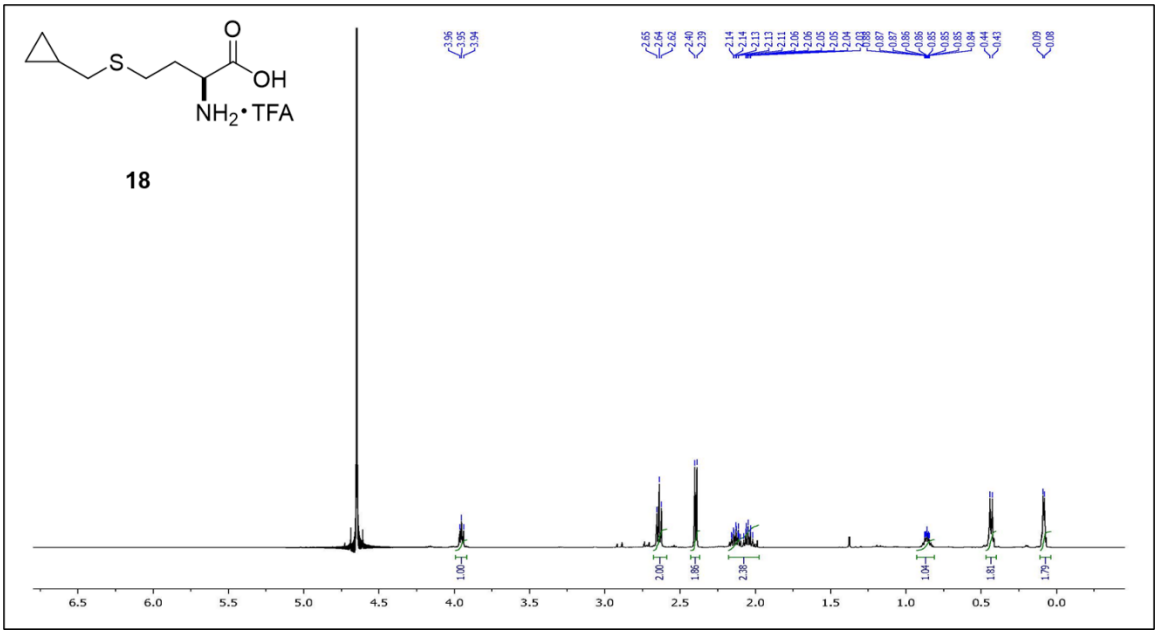

Figure S3.70. ^{1}H NMR spectrum (D_2O, 500 MHz) of *S*-(cyclopropylmethyl)-*L*-homocysteine TFA salt (**18**).

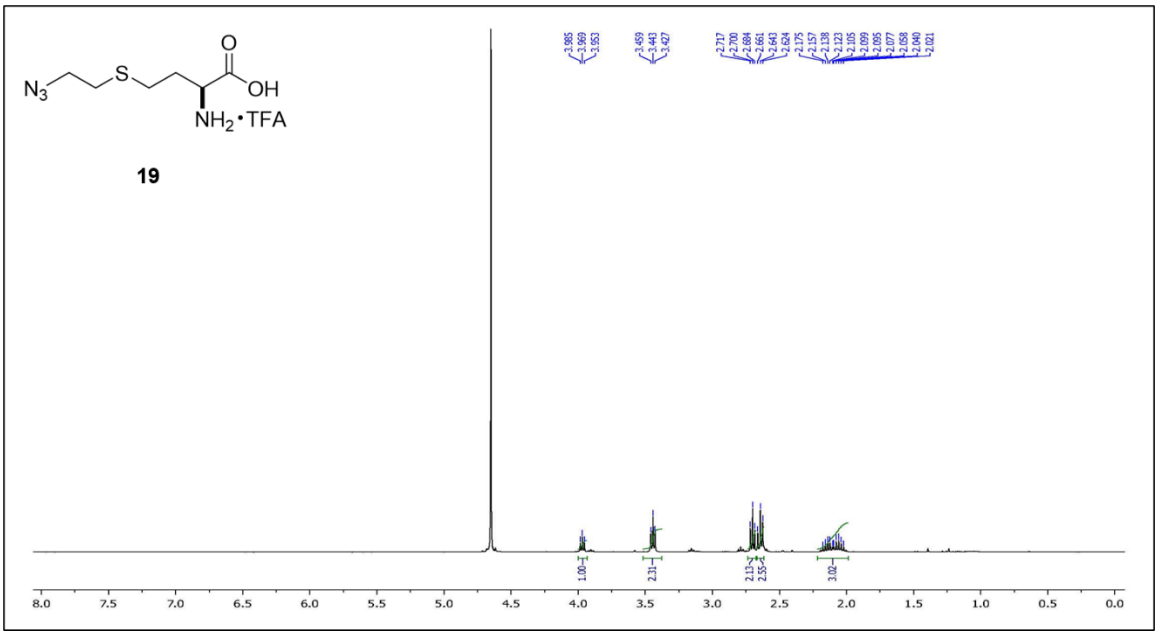

Figure S3.71. ^{1}H NMR spectrum (D_2O, 400 MHz) of *S*-(2-azidoethyl)-*L*-homocysteine TFA salt (**19**).

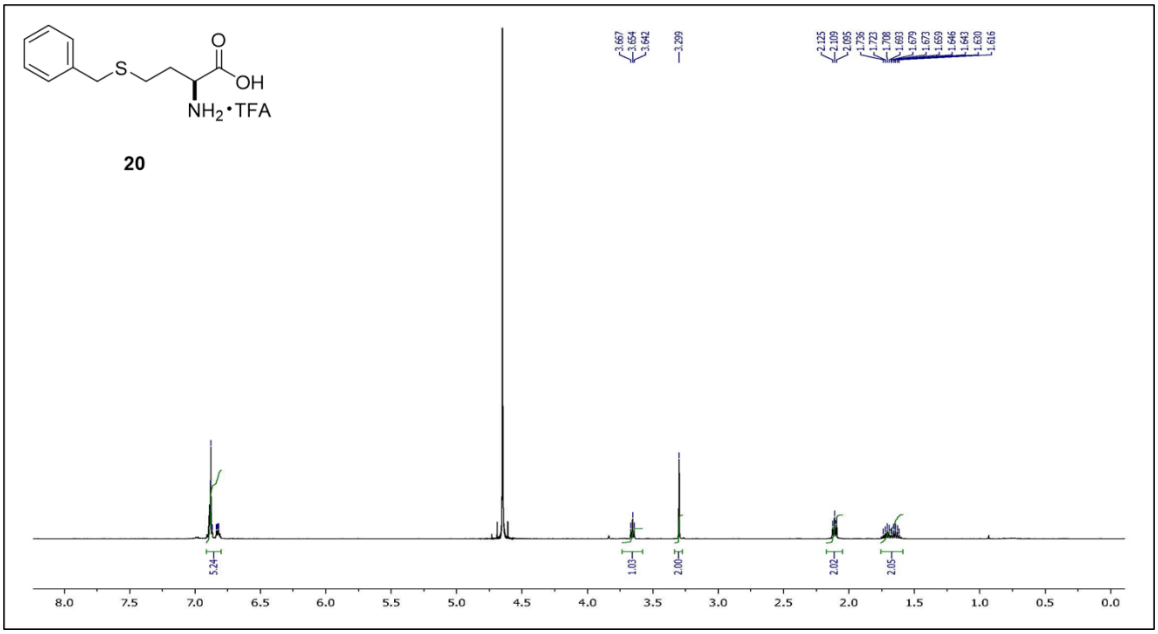

Figure S3.72. ^{1}H NMR spectrum (D_2O/TFA = 20/1, 500 MHz) of *S*-benzyl-*L*-homocysteine TFA salt (**20**).

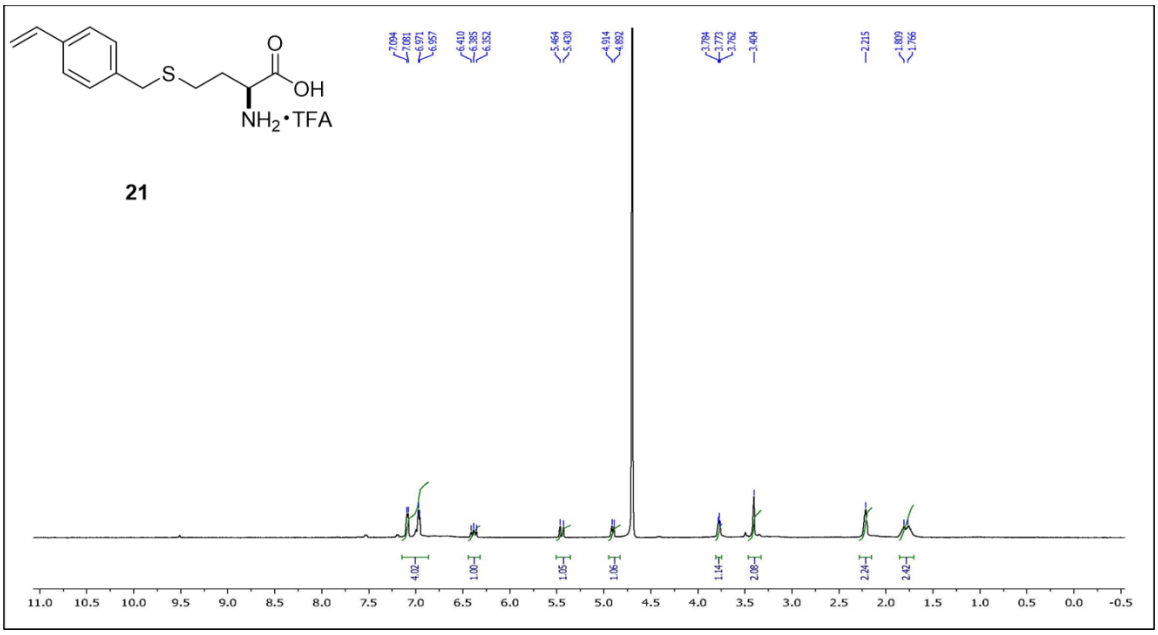

Figure S3.73. ^{1}H NMR spectrum (D_2O/TFA = 20/1, 400 MHz) of *S*-(4-vinylbenzyl)-*L*-homocysteine TFA salt (**21**).

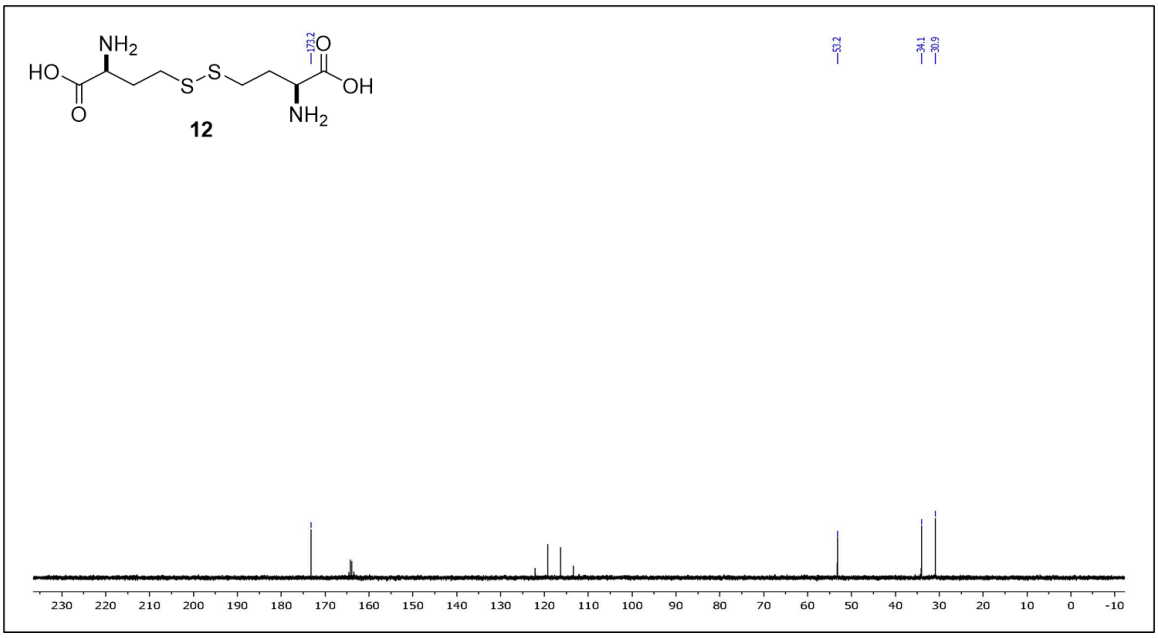

Figure S3.74. ^{13}C NMR spectrum (D_2O/TFA = 20/1, 100 MHz) of L,L-homocystine (**12**).

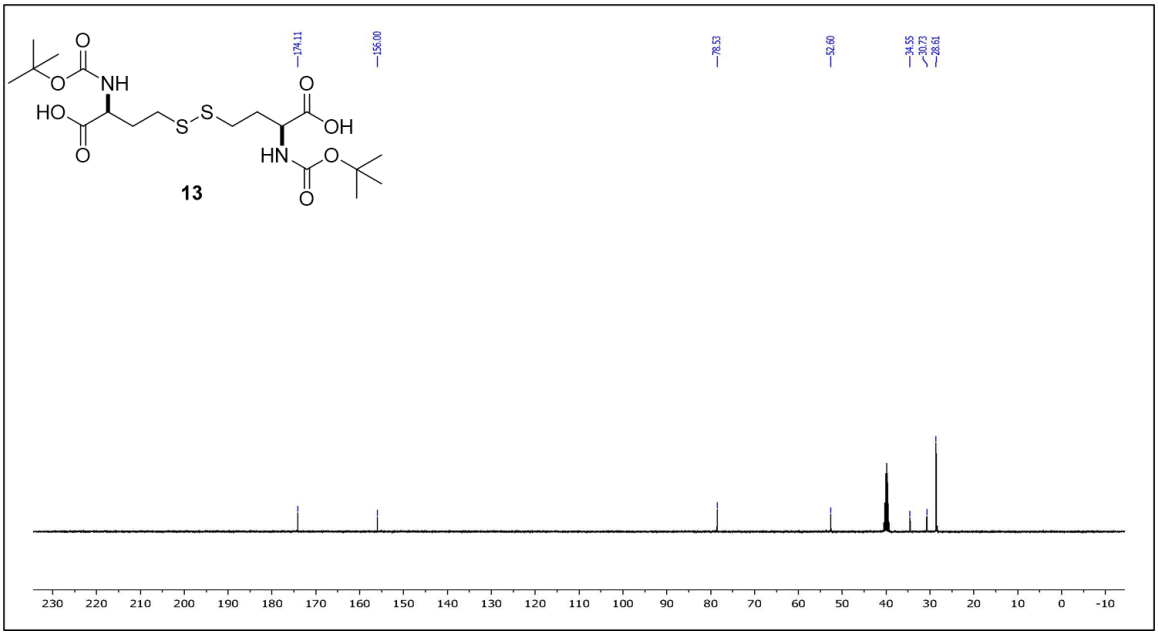

Figure S3.75. ^{13}C NMR spectrum (DMSO, 100 MHz) of *N*-Boc-L,L-homocystine (**13**).

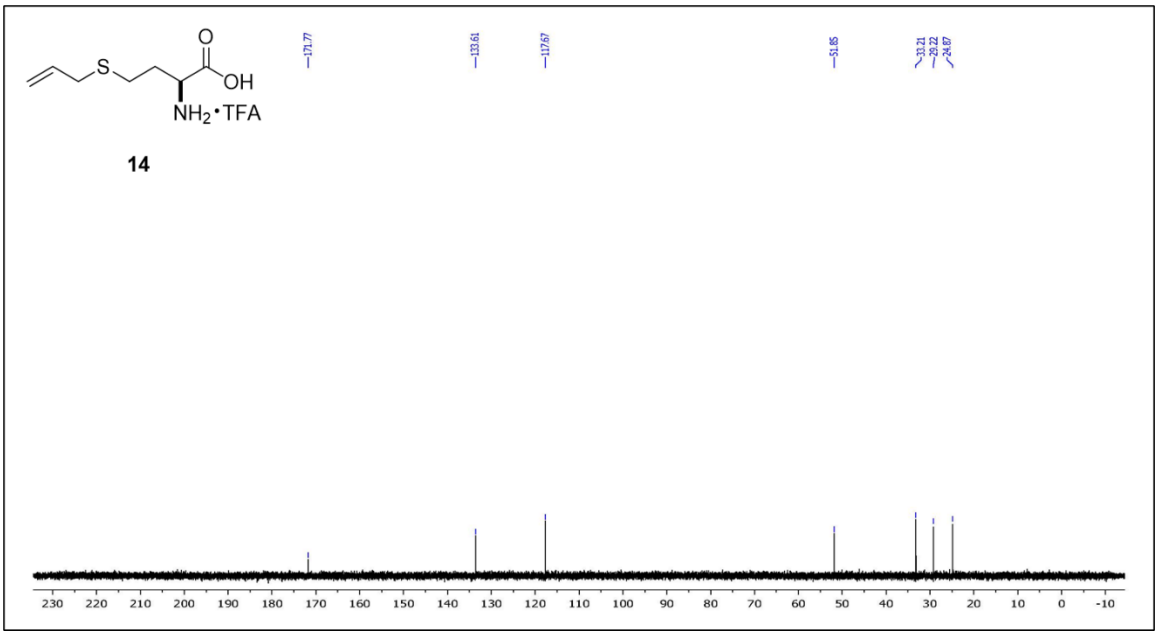

Figure S3.76. ^{13}C NMR spectrum (D_2O, 100 MHz) of *S*-allyl-*L*-homocysteine TFA salt (**14**).

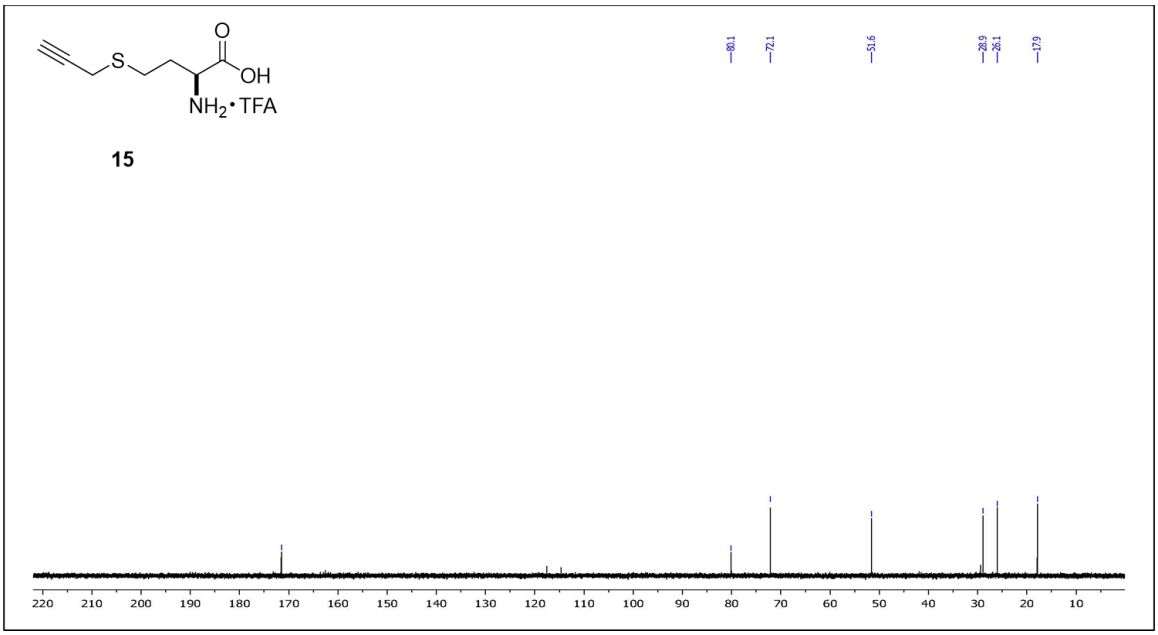

Figure S3.77. ^{13}C NMR spectrum (D_2O/TFA = 20/1, 100 MHz) of *S*-(prop-2-yn-1-yl)-*L*-homocysteine TFA salt (**15**).

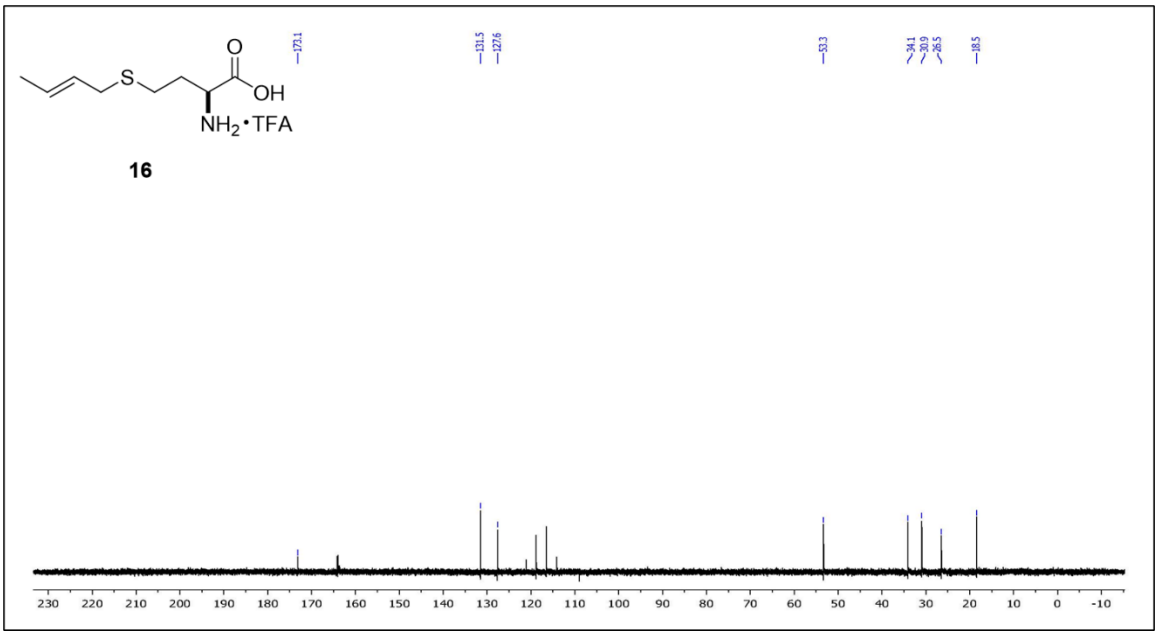

Figure S3.78. ^{13}C NMR spectrum (D_2O/TFA = 20/1, 125 MHz) of (*E*)-*S*-(but-2-en-1-yl)-*L*-homocysteine TFA salt (**16**).

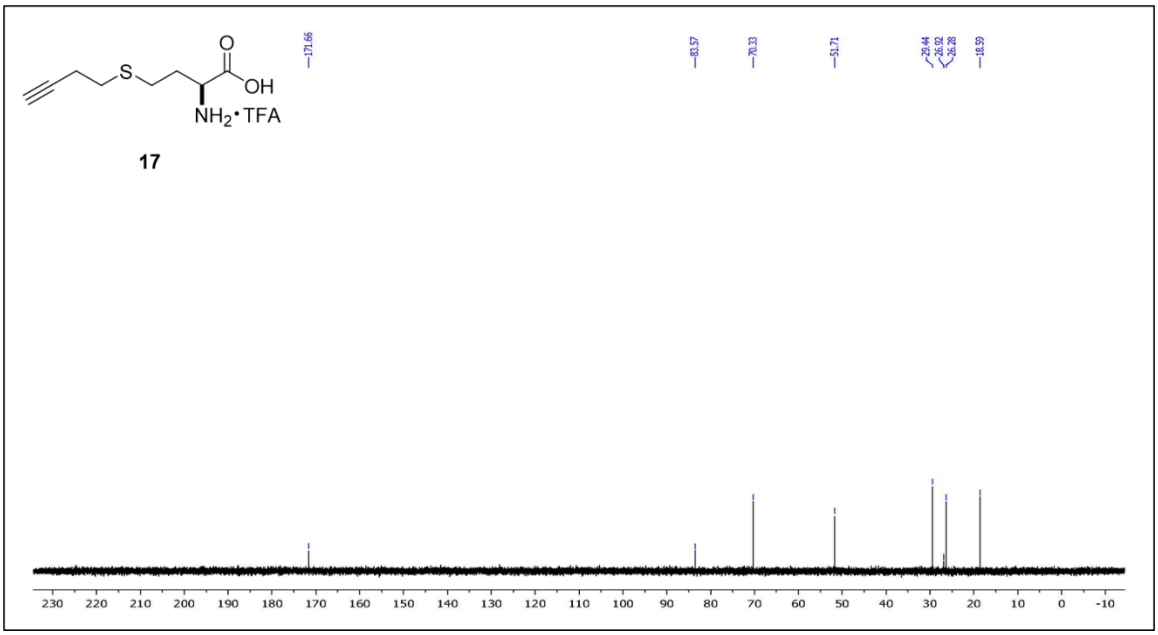

Figure S3.79. ^{13}C NMR spectrum (D_2O, 100 MHz) of S-(but-3-yn-1-yl)-*L*-homocysteine TFA salt (**17**).

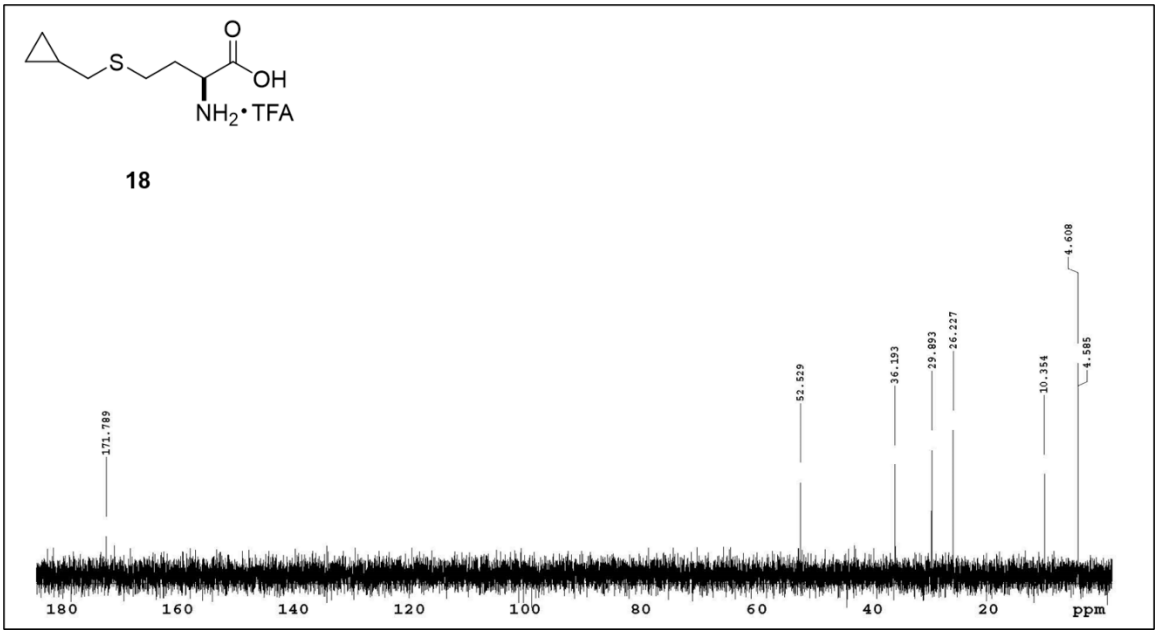

Figure S3.80. ^{13}C NMR spectrum (D_2O, 100 MHz) of *S*-(cyclopropylmethyl)-*L*-homocysteine TFA salt (**18**).

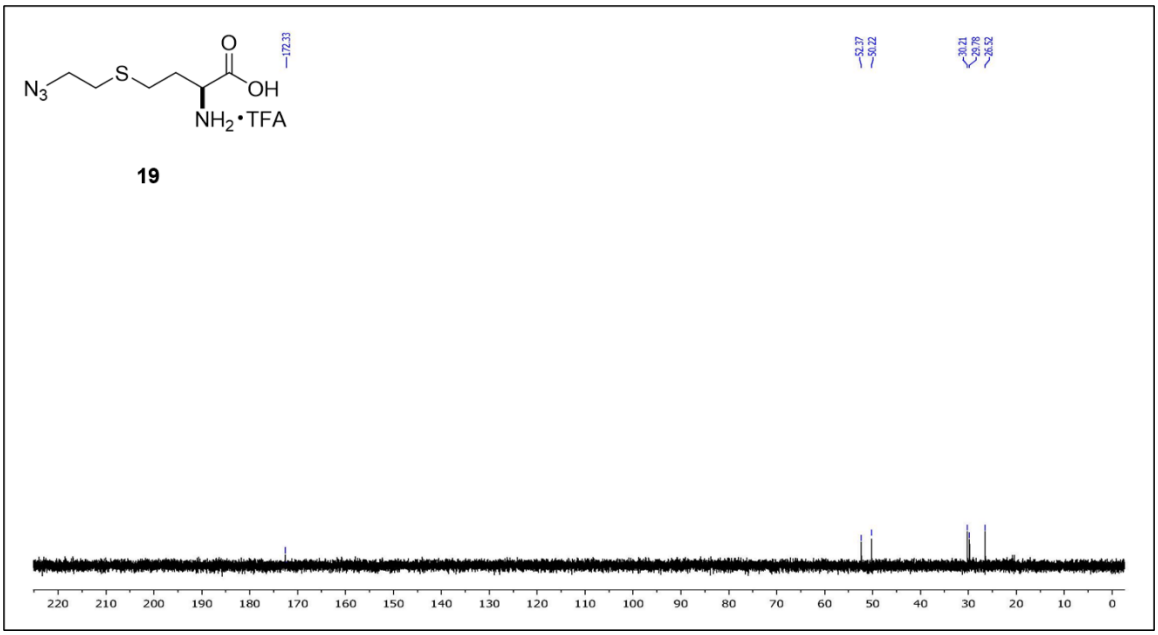

Figure S3.81. ^{13}C NMR spectrum (D_2O, 100 MHz) of *S*-(2-azidoethyl)-*L*-homocysteine TFA salt (**19**).

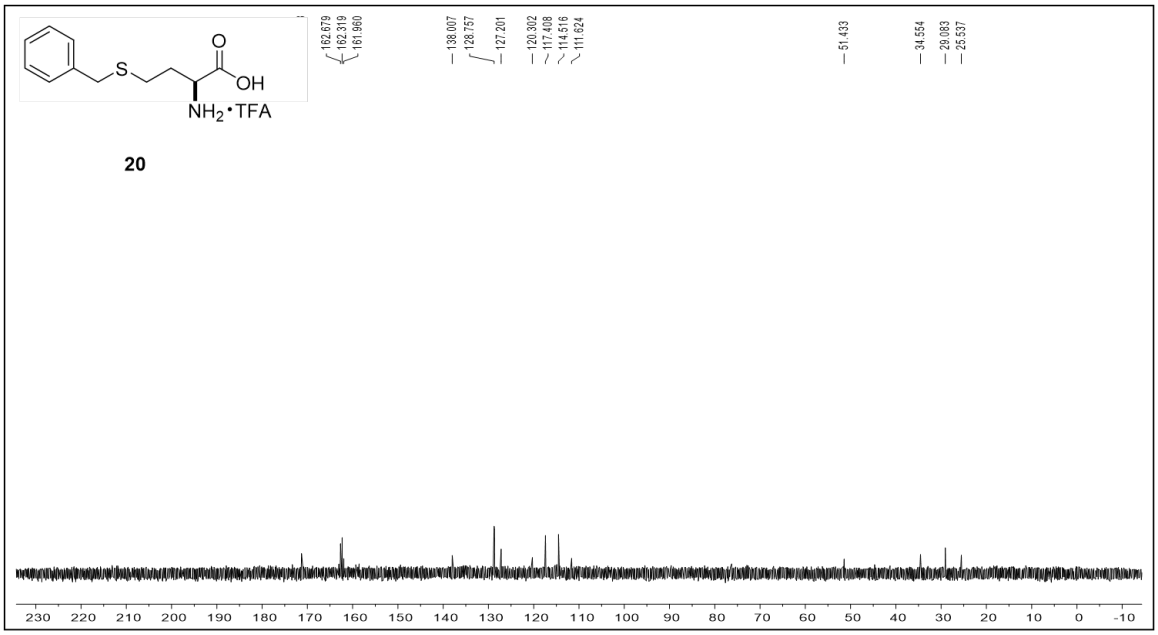

Figure S3.82. ^{13}C NMR spectrum (D_2O/TFA = 20/1, 100 MHz) of *S*-benzyl-*L*-homocysteine TFA salt (**20**).

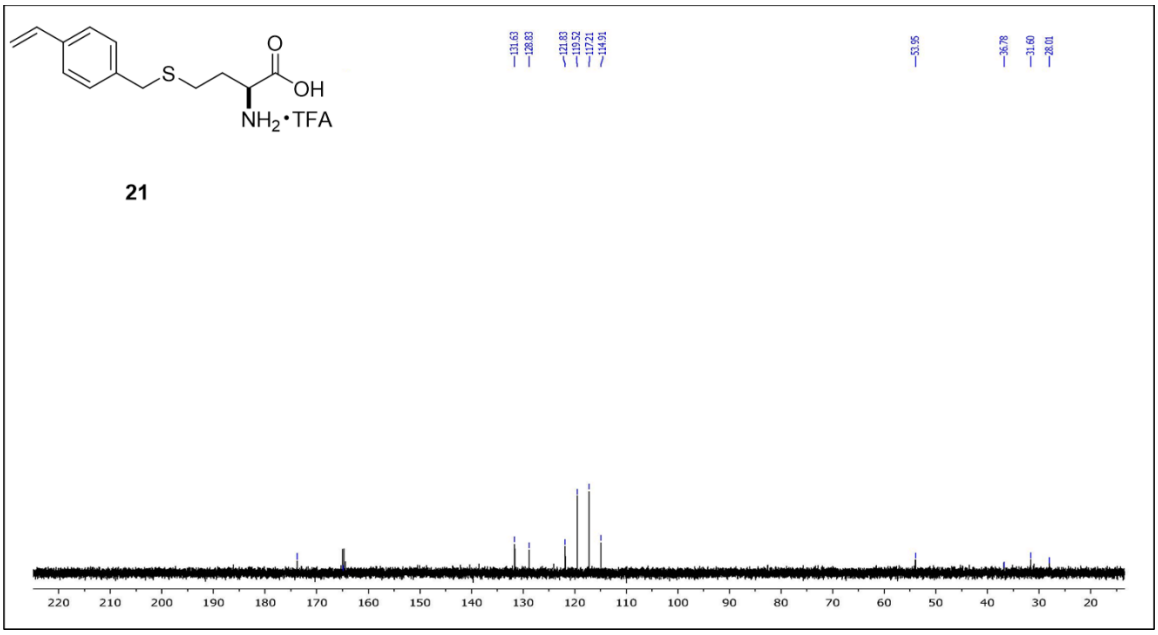

Figure S3.83. ^{13}C NMR spectrum (D_2O/TFA = 20/1, 125 MHz) of *S*-(4-vinylbenzyl)-*L*-homocysteine TFA salt (**21**).

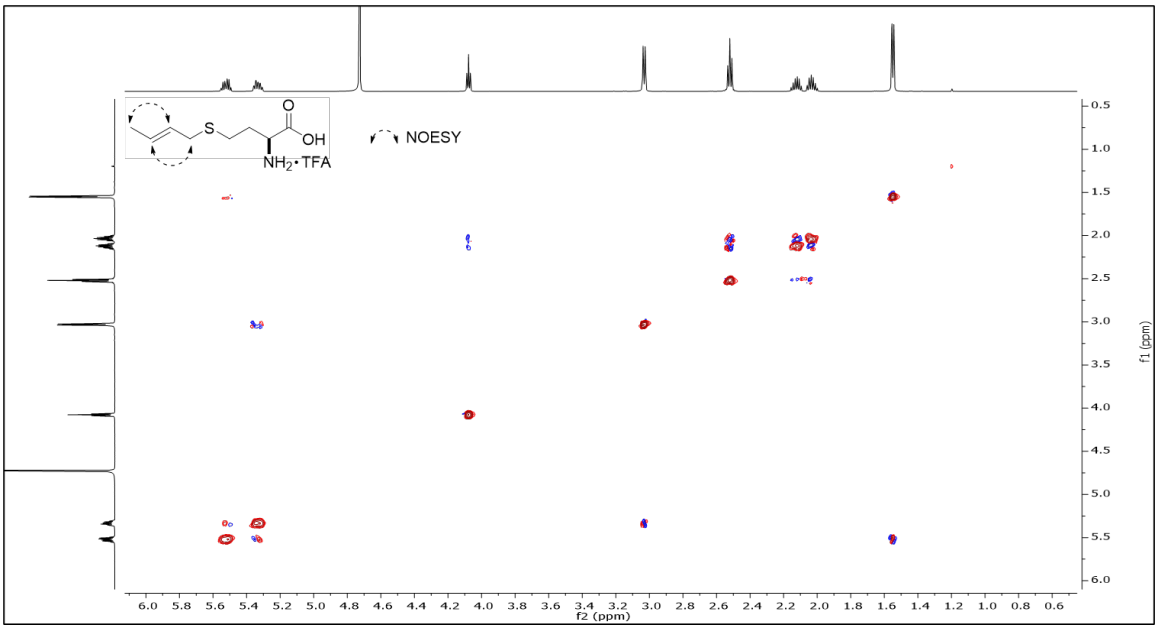

Figure S3.84. NOESY spectrum (CD_3OD, 600 MHz) of (*E*)-*S*-(but-2-en-1-yl)-*L*-homocysteine TFA salt (**16**).

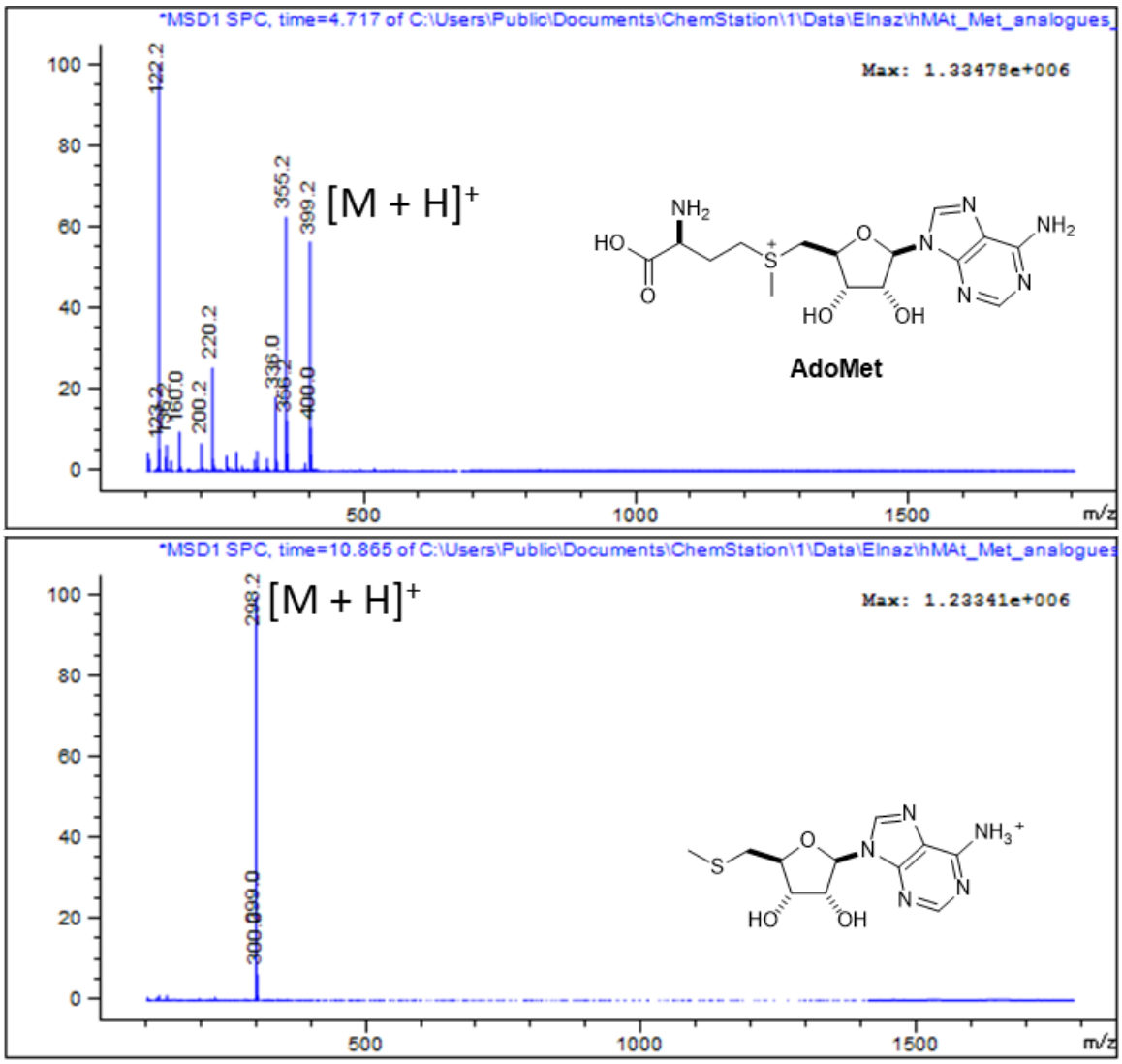

Figure S3.85. ESI-MS profile of AdoMet from hMAT2A-catalyzed reaction.

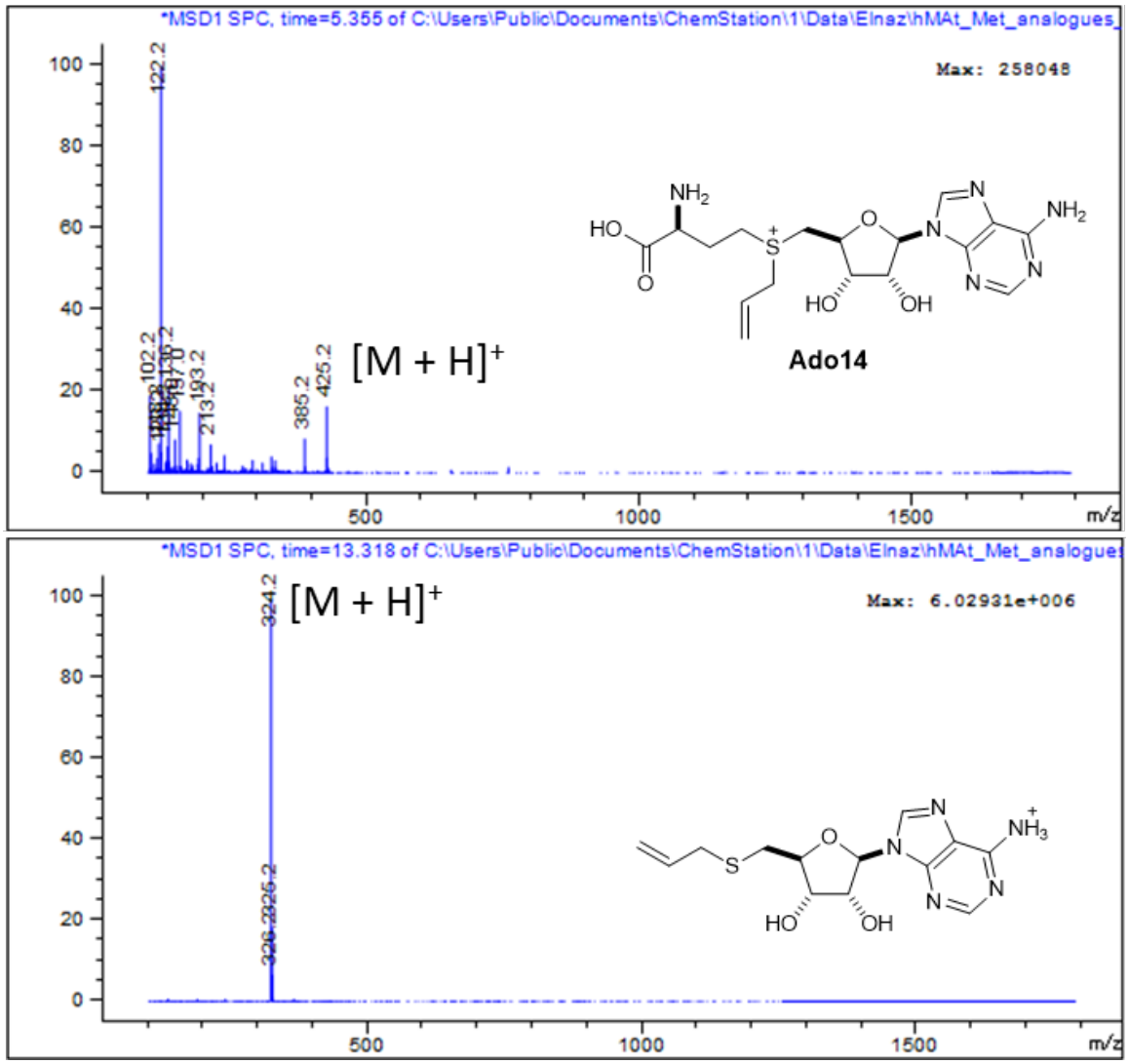

Figure S3.86. ESI-MS profile of **Ado14** from hMAT2A-catalyzed reaction.

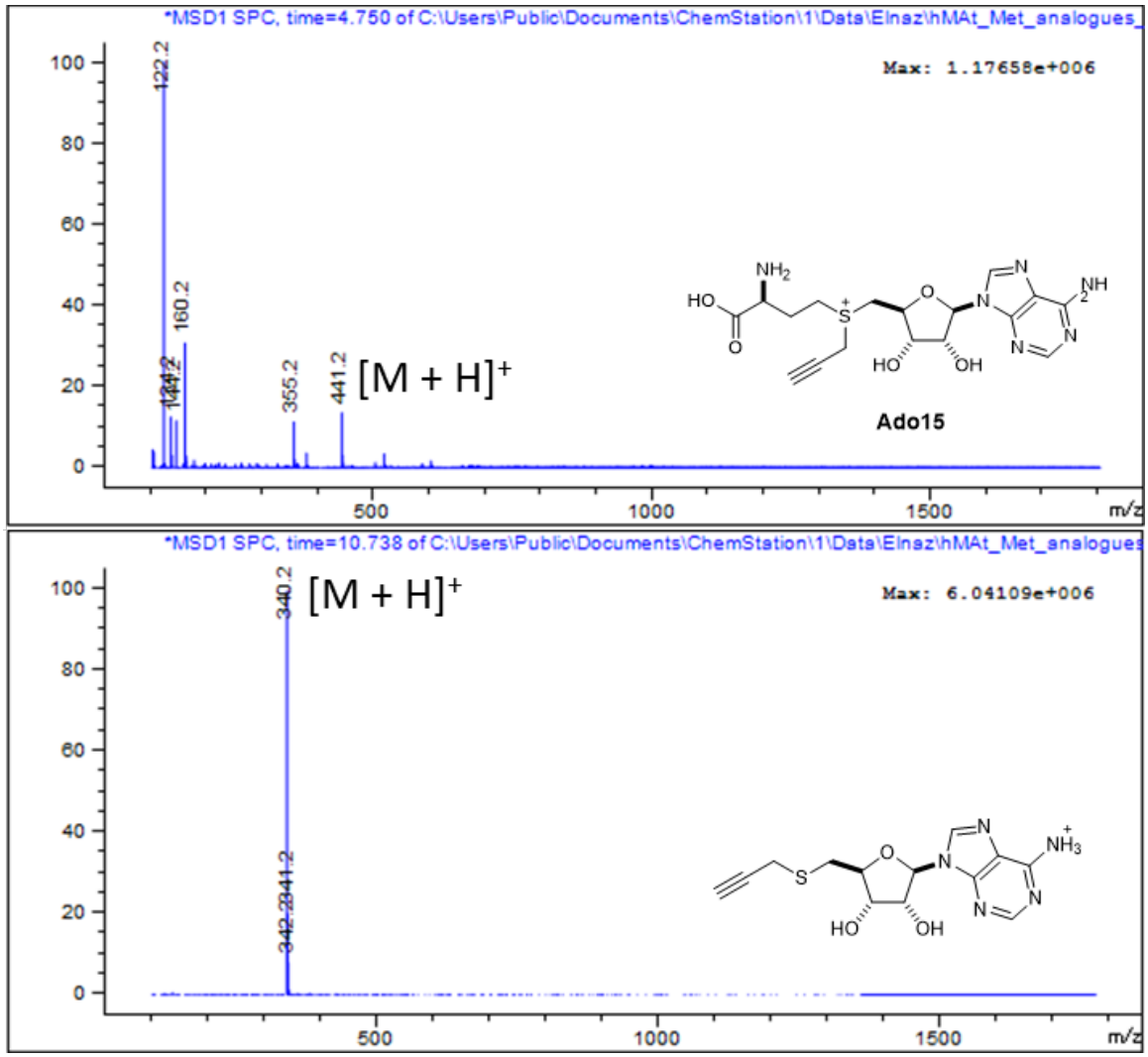

Figure S3.87. ESI-MS profile of **Ado15** from hMAT2A-catalyzed reaction.

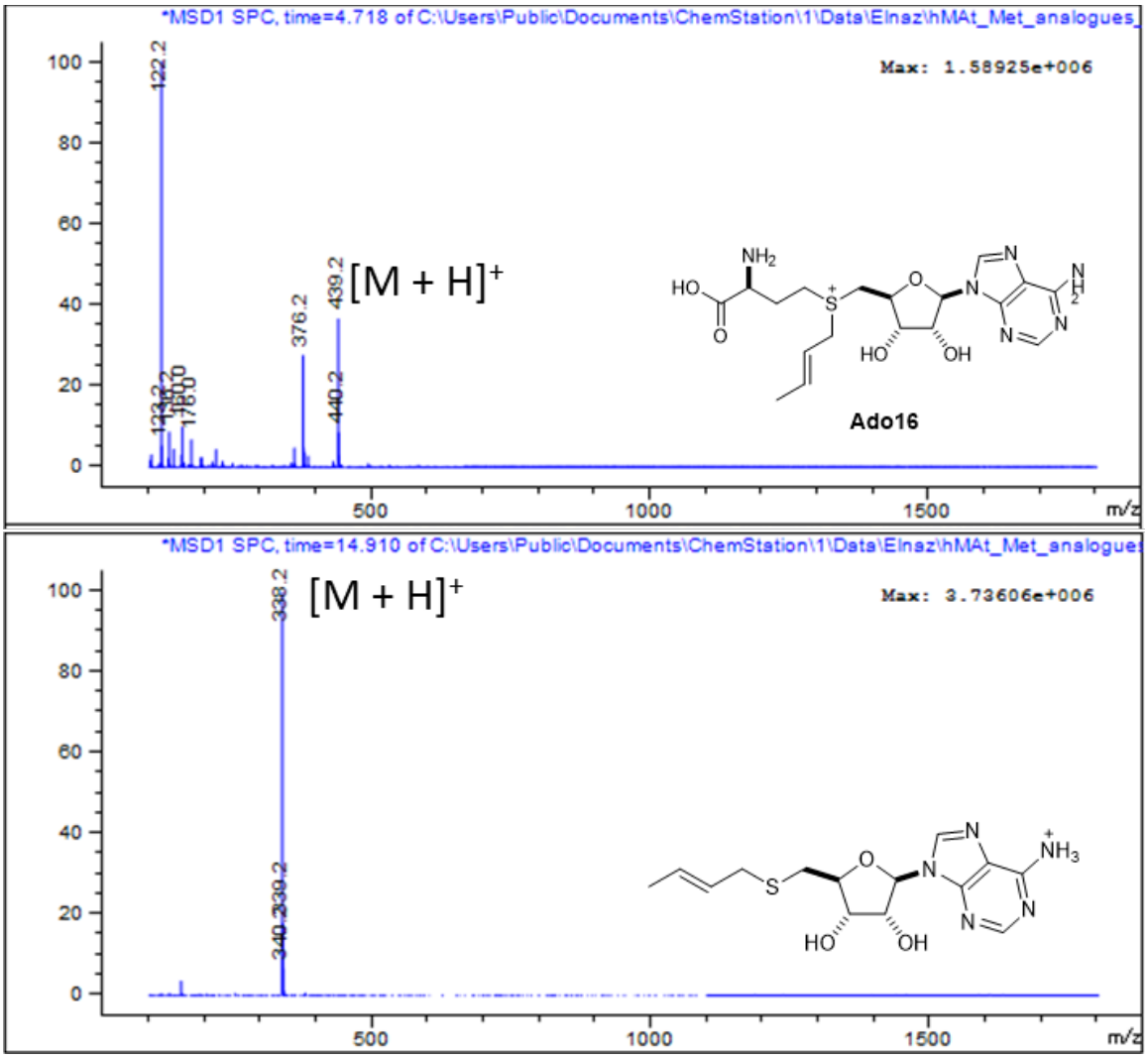

Figure S3.88. ESI-MS profile of **Ado16** from hMAT2A-catalyzed reaction.

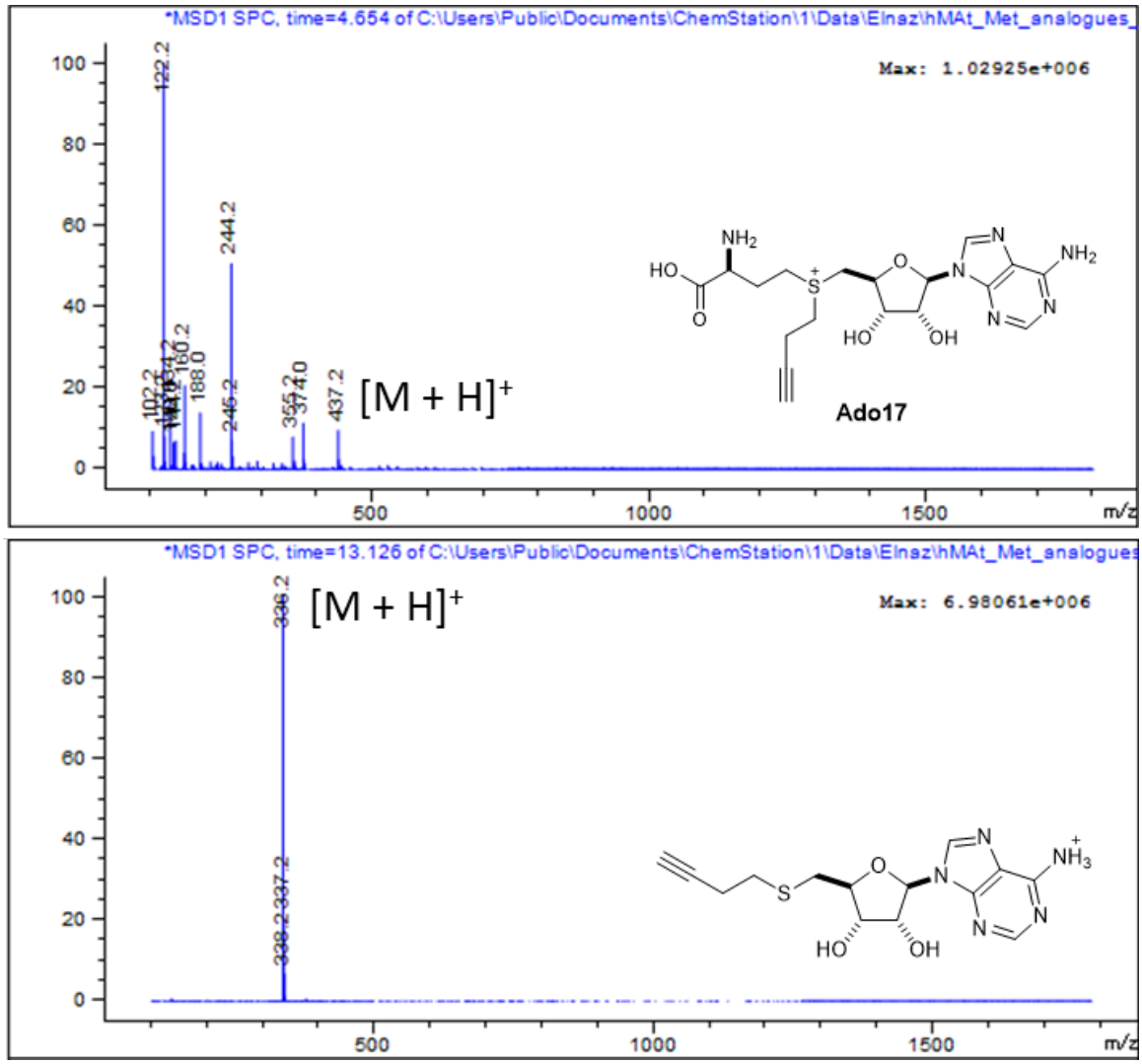

Figure S3.89. ESI-MS profile of **Ado17** from hMAT2A-catalyzed reaction.

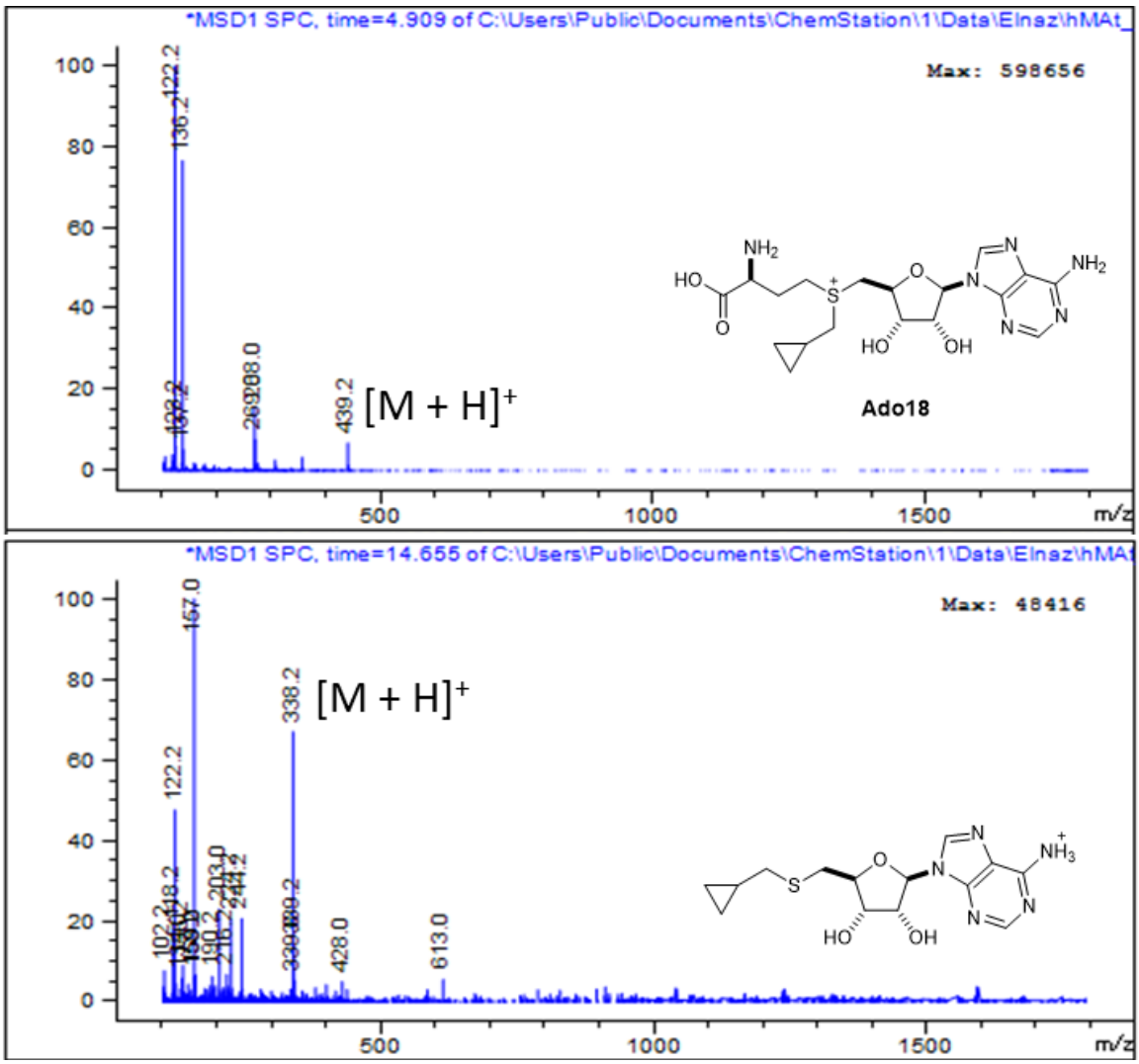

Figure S3.90. ESI-MS profile of **Ado18** from hMAT2A-catalyzed reaction.

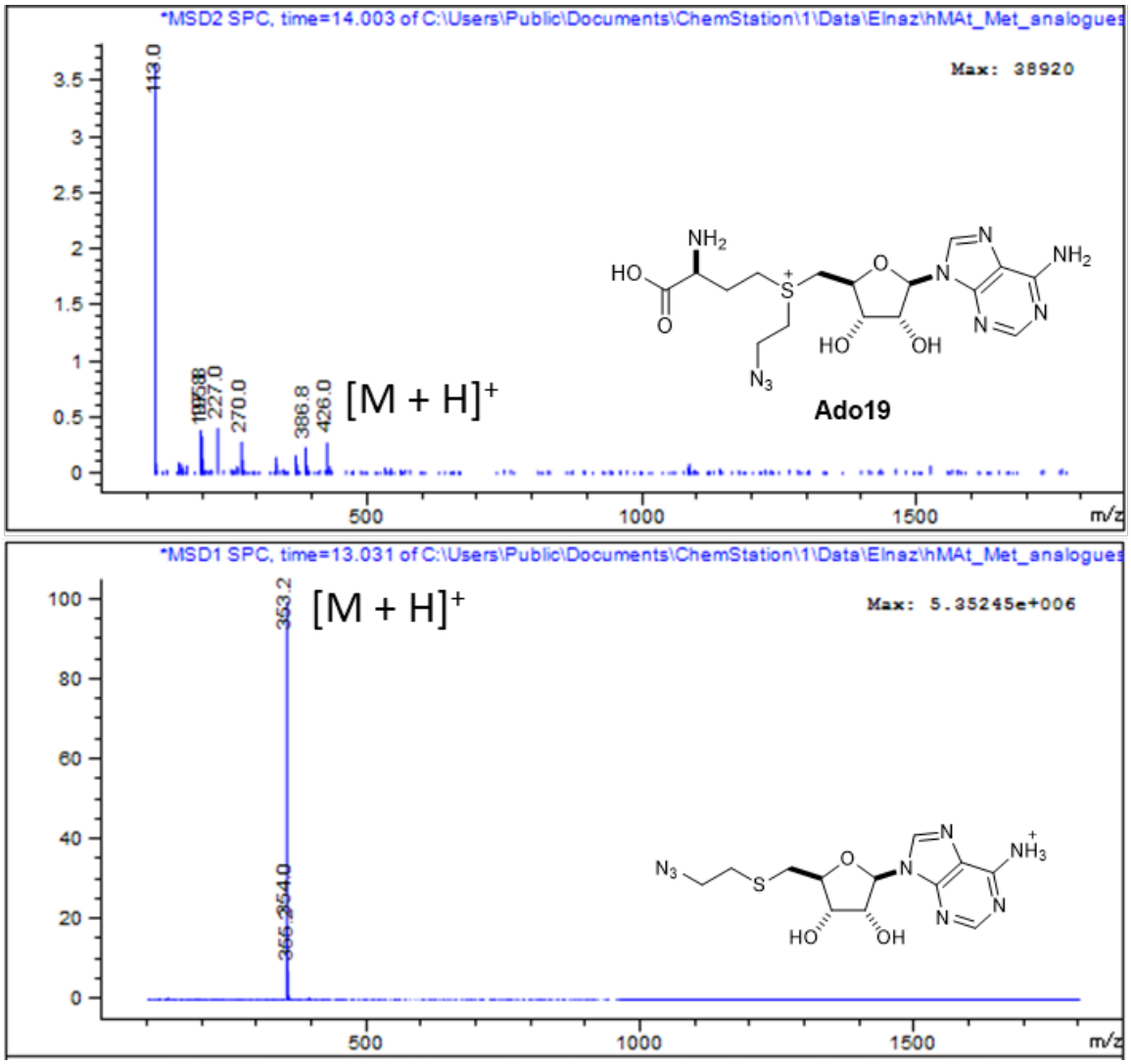

Figure S3.91. ESI-MS profile of **Ado19** from hMAT2A-catalyzed reaction.

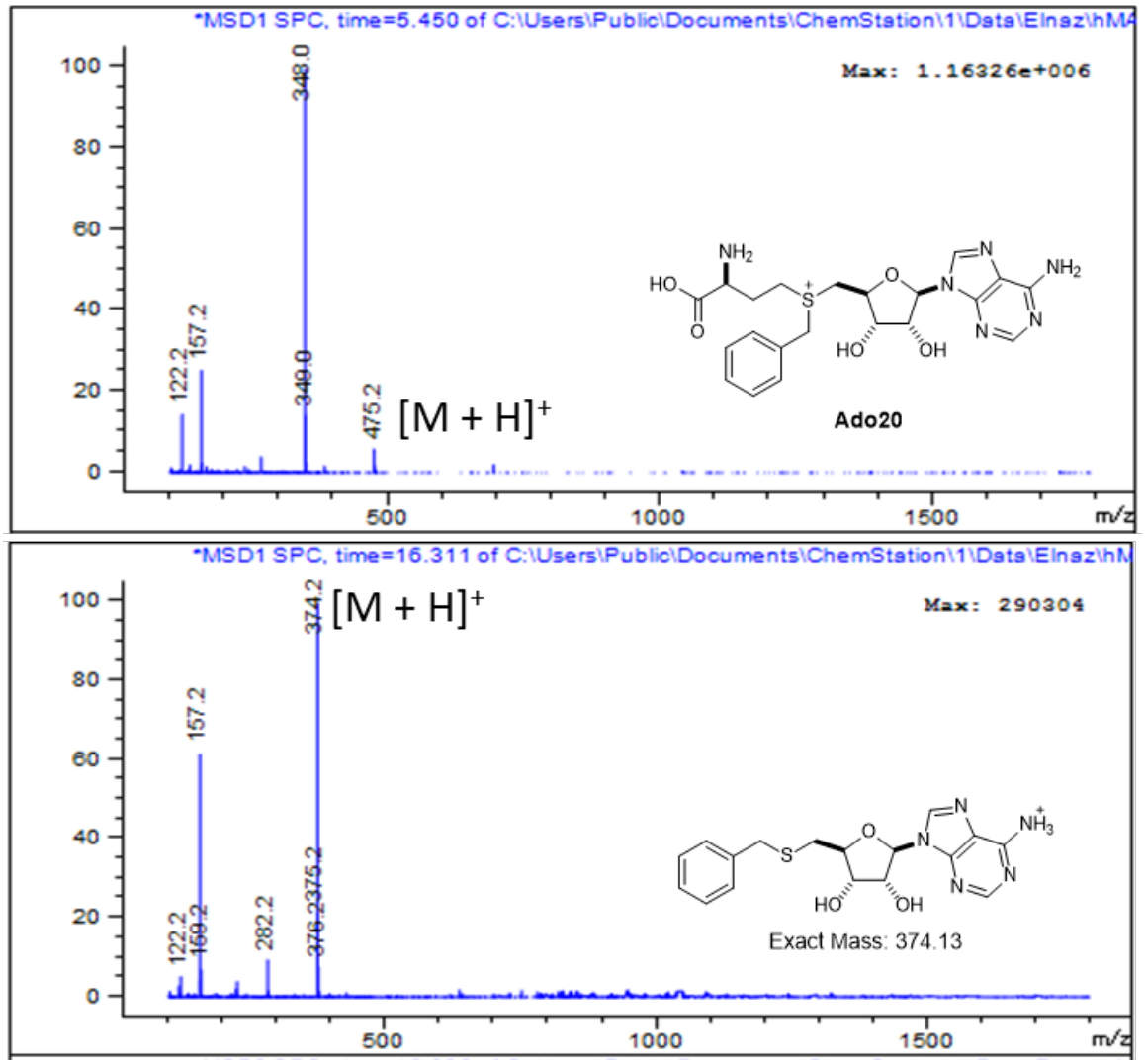

Figure S3.92. ESI-MS profile of **Ado20** from hMAT2A-catalyzed reaction.

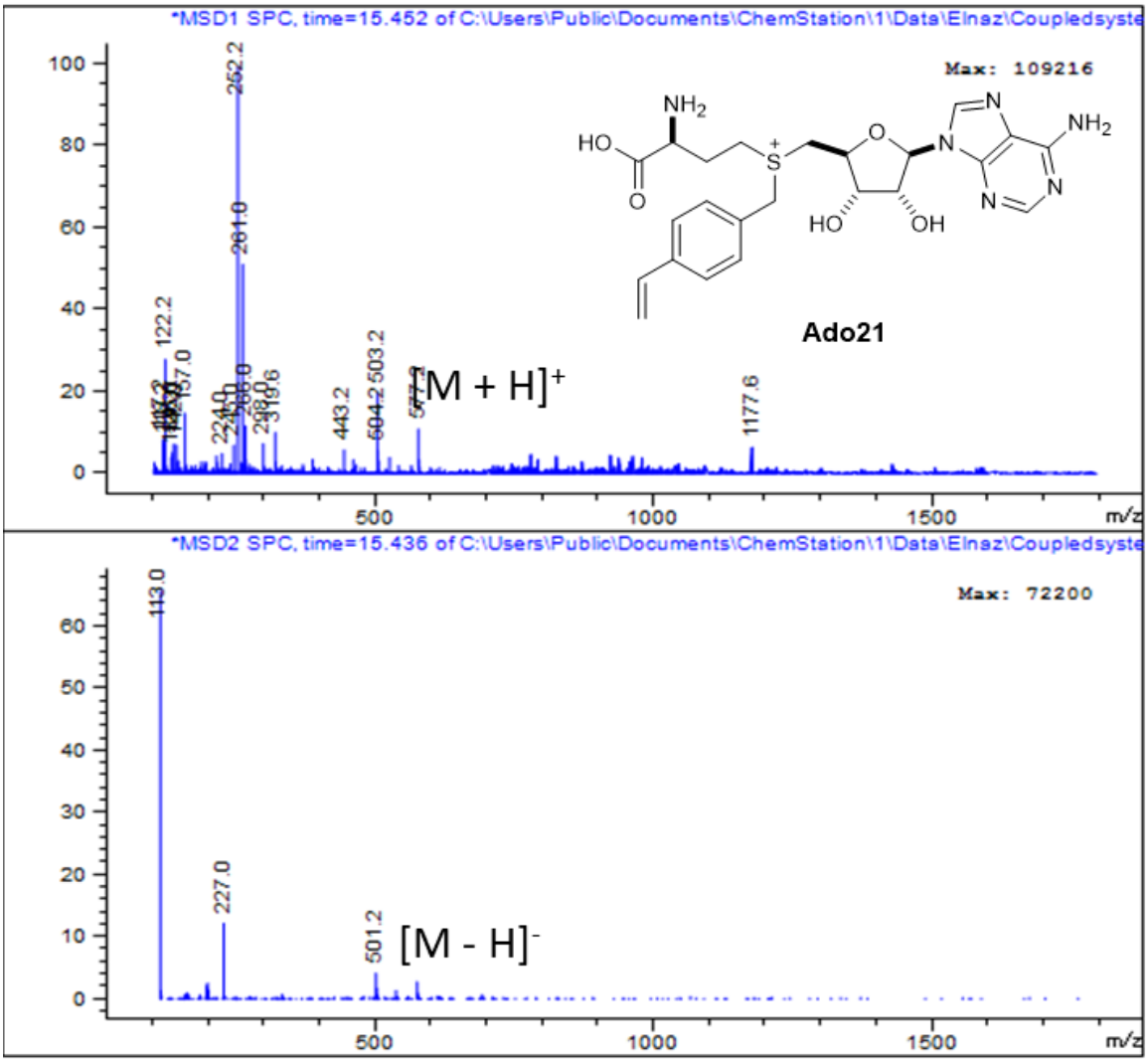

Figure S3.93. ESI-MS profile of **Ado21** from hMAT2A-catalyzed reaction.

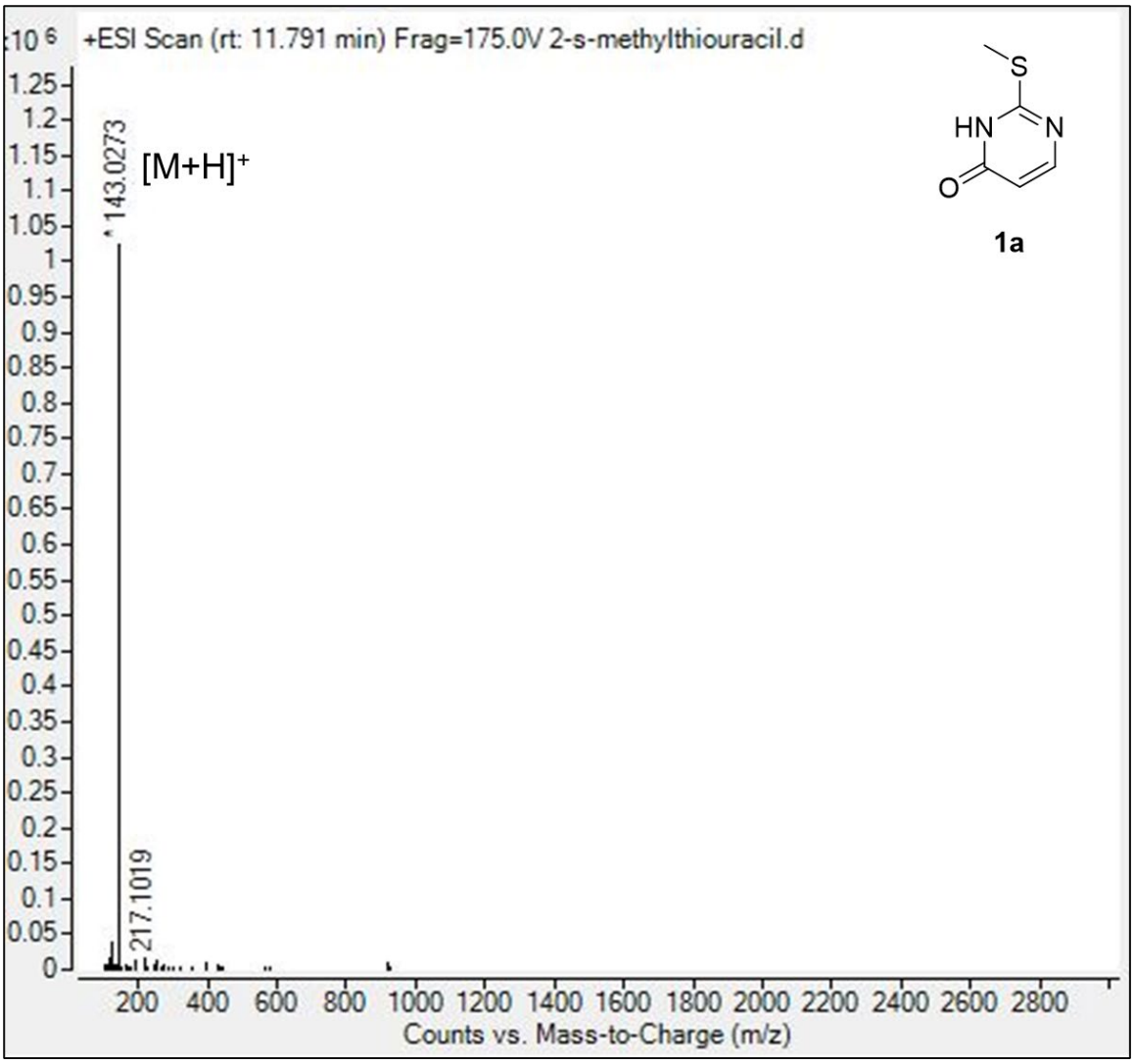

Figure S3.94. HRMS profile of 2-(Methylthio)pyrimidin-4(3*H*)-one (**1a**)

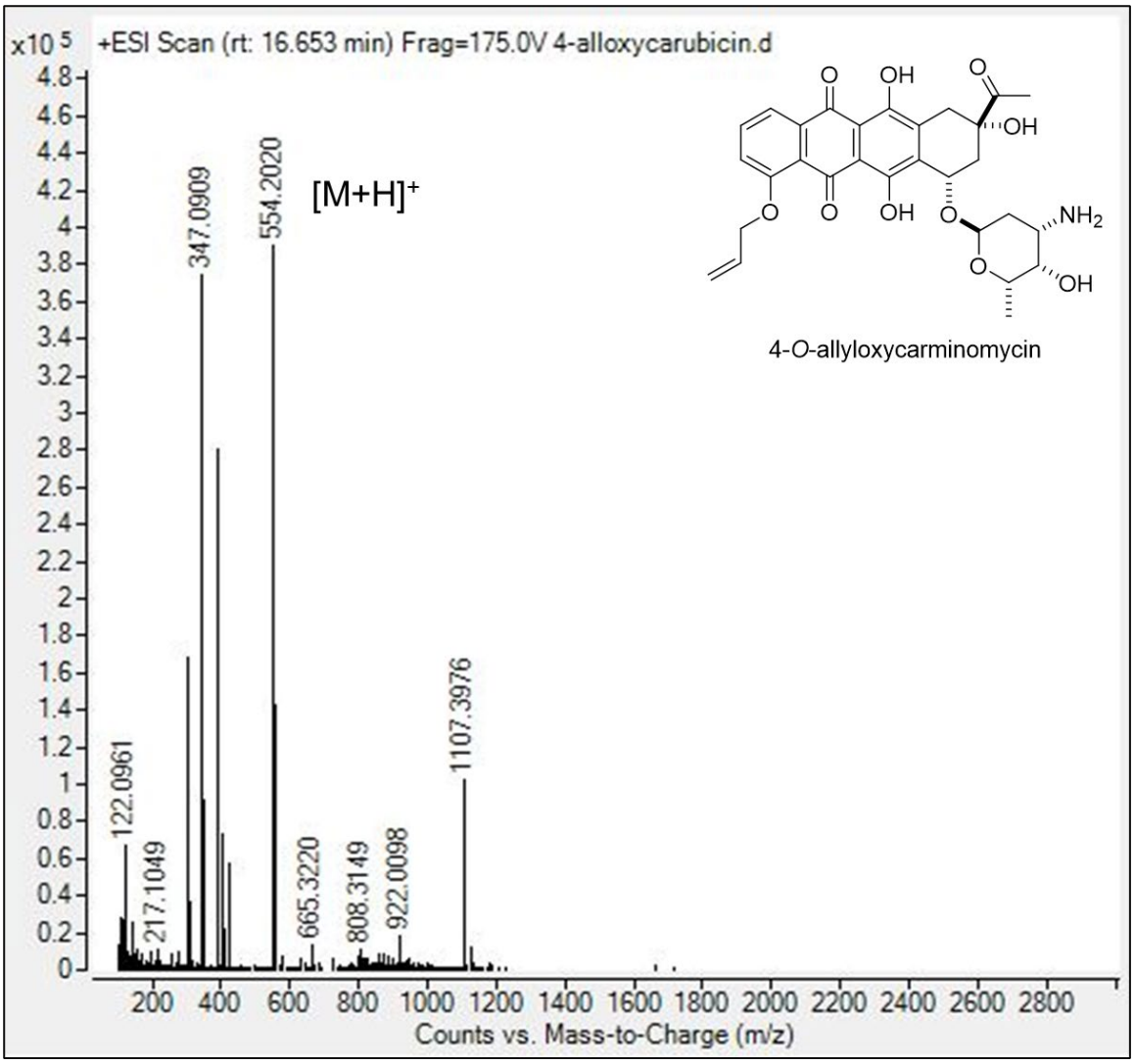

Figure S3.95. HRMS profile of 4-*O*-allyloxycarminomycin.

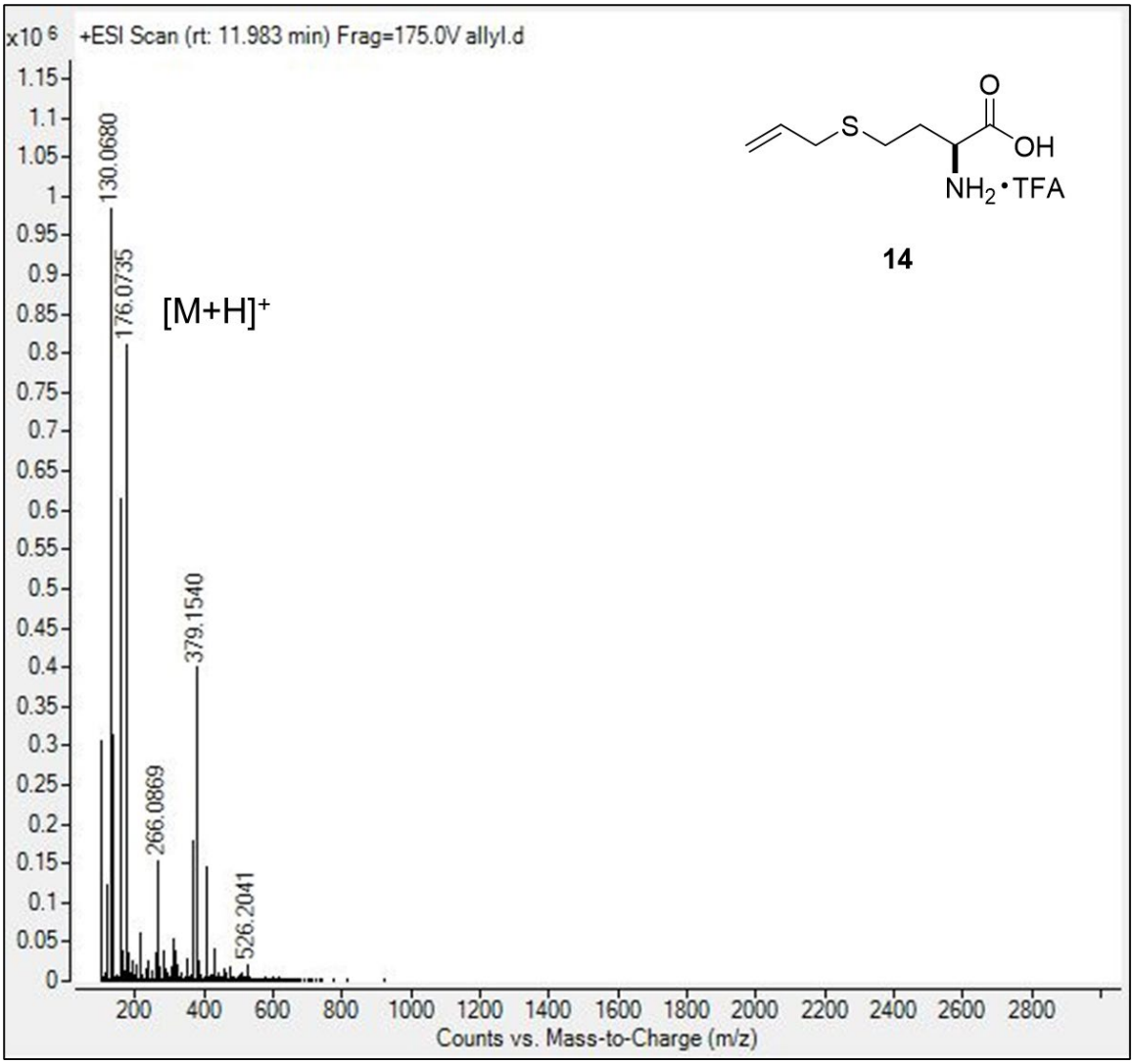

Figure S3.96. HRMS profile of *S*-allyl-*L*-homocysteine (**14**).

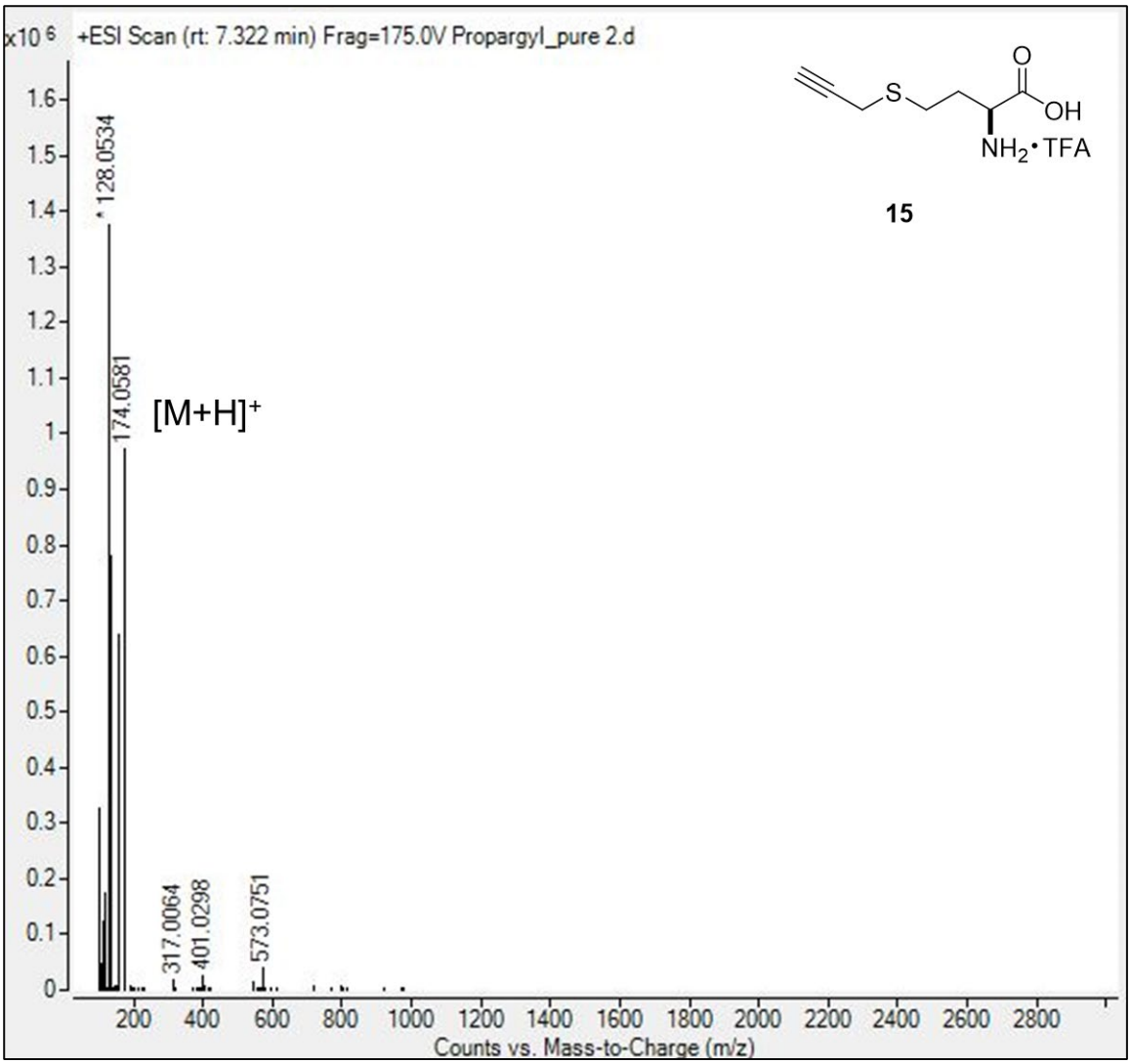

Figure S3.97. HRMS profile of *S*-(prop-2-yn-1-yl)-*L*-homocysteine (**15**).

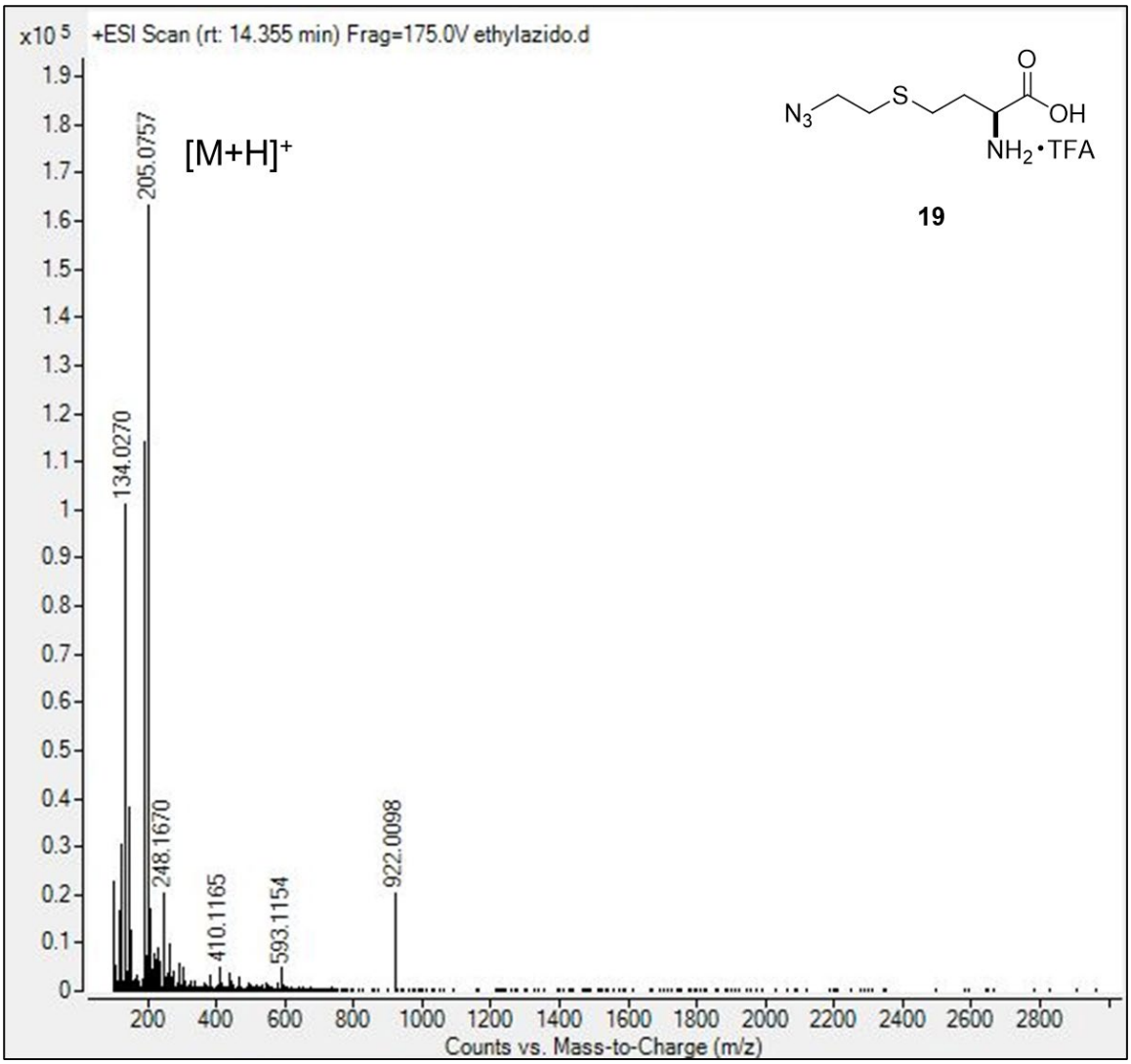

Figure S3.98. HRMS profile of (*E*)-*S*-(but-2-en-1-yl)-*L*-homocysteine (**16**).

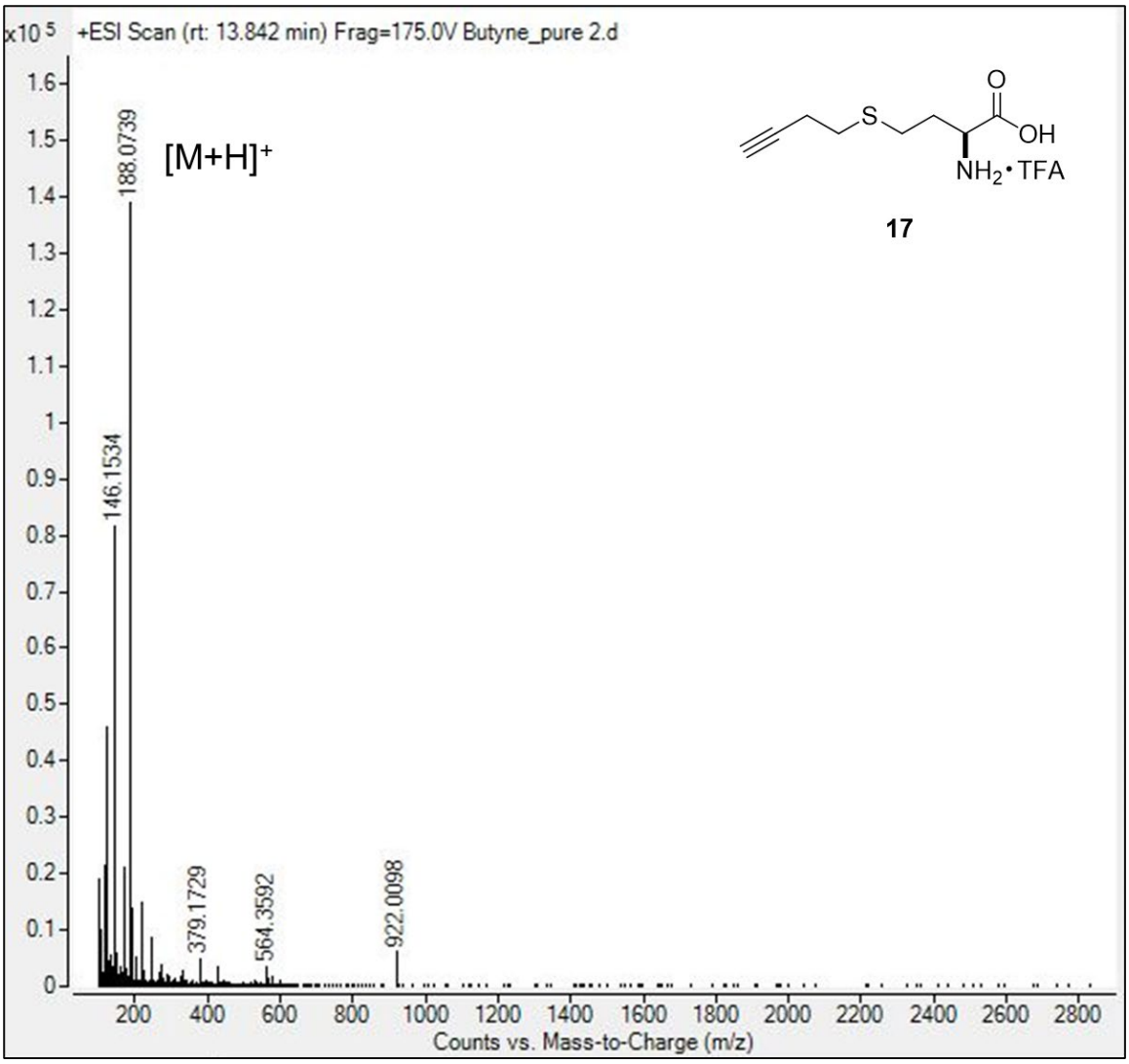

Figure S3.99. HRMS profile of *S*-(but-3-yn-1-yl)-*L*-homocysteine (**17**).

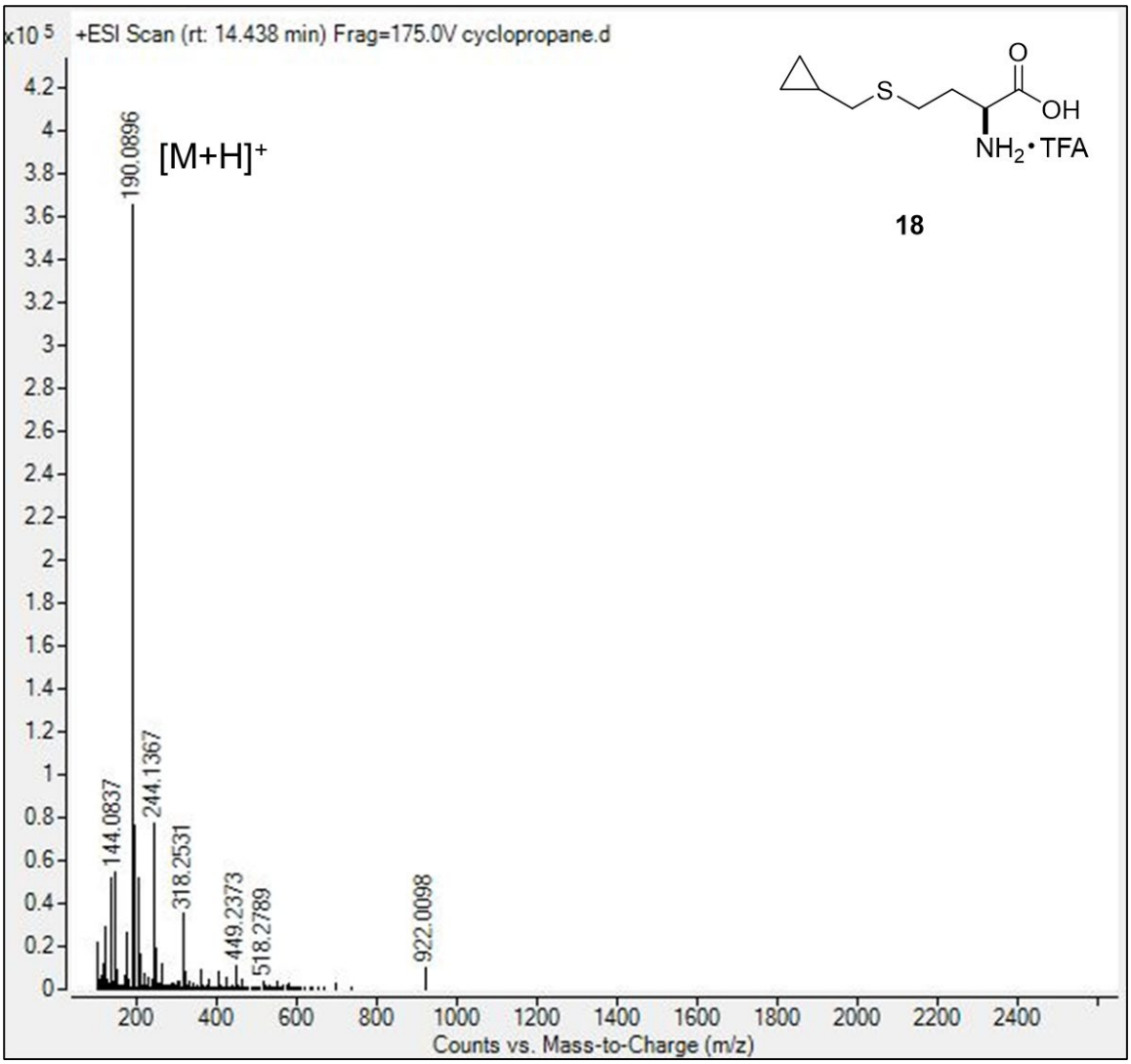

Figure S3.100. HRMS profile of *S*-(cyclopropylmethyl)-*L*-homocysteine (**18**).

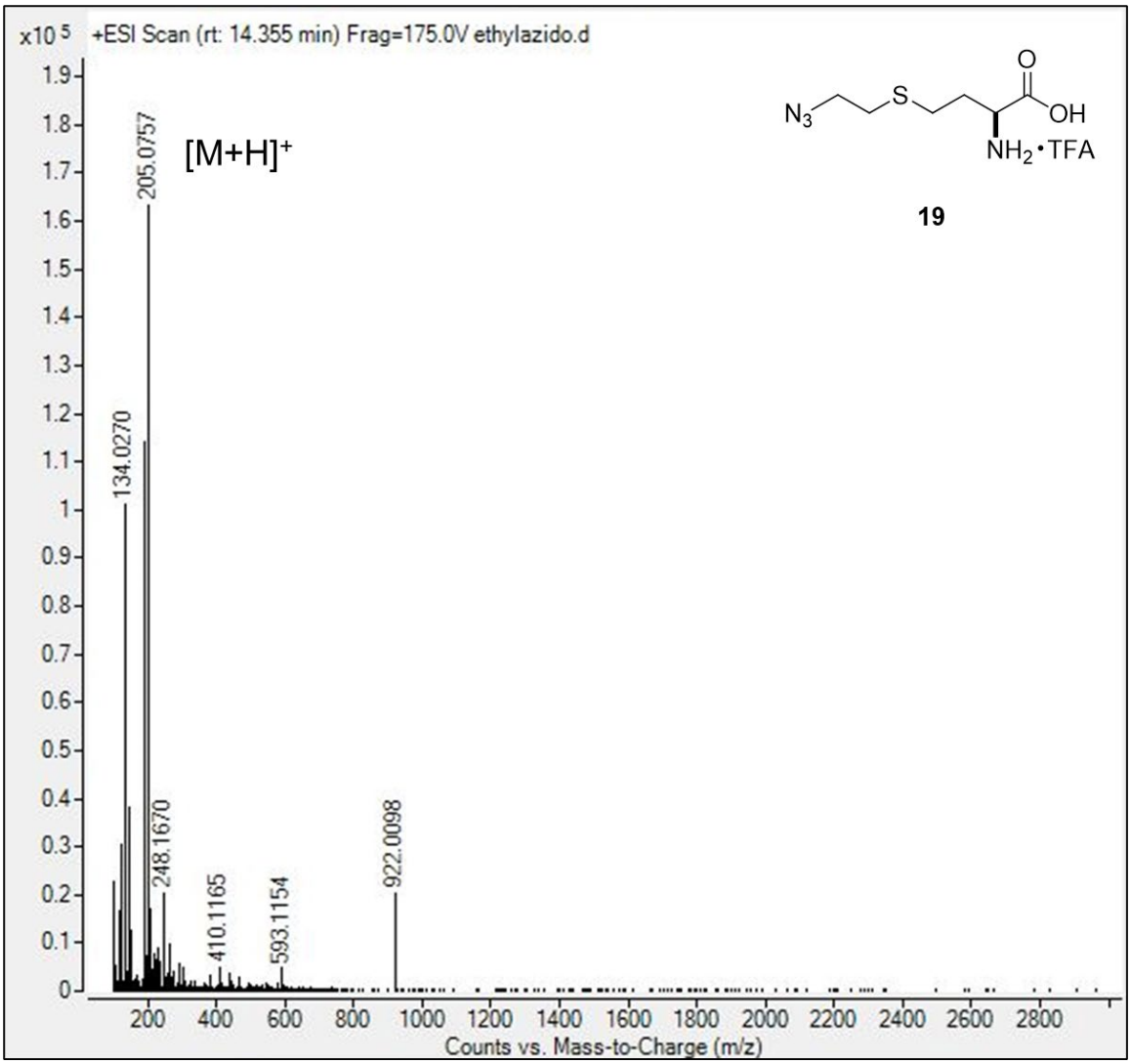

Figure S3.101. HRMS profile of *S*-(2-azidoethyl)-*L*-homocysteine (**19**).

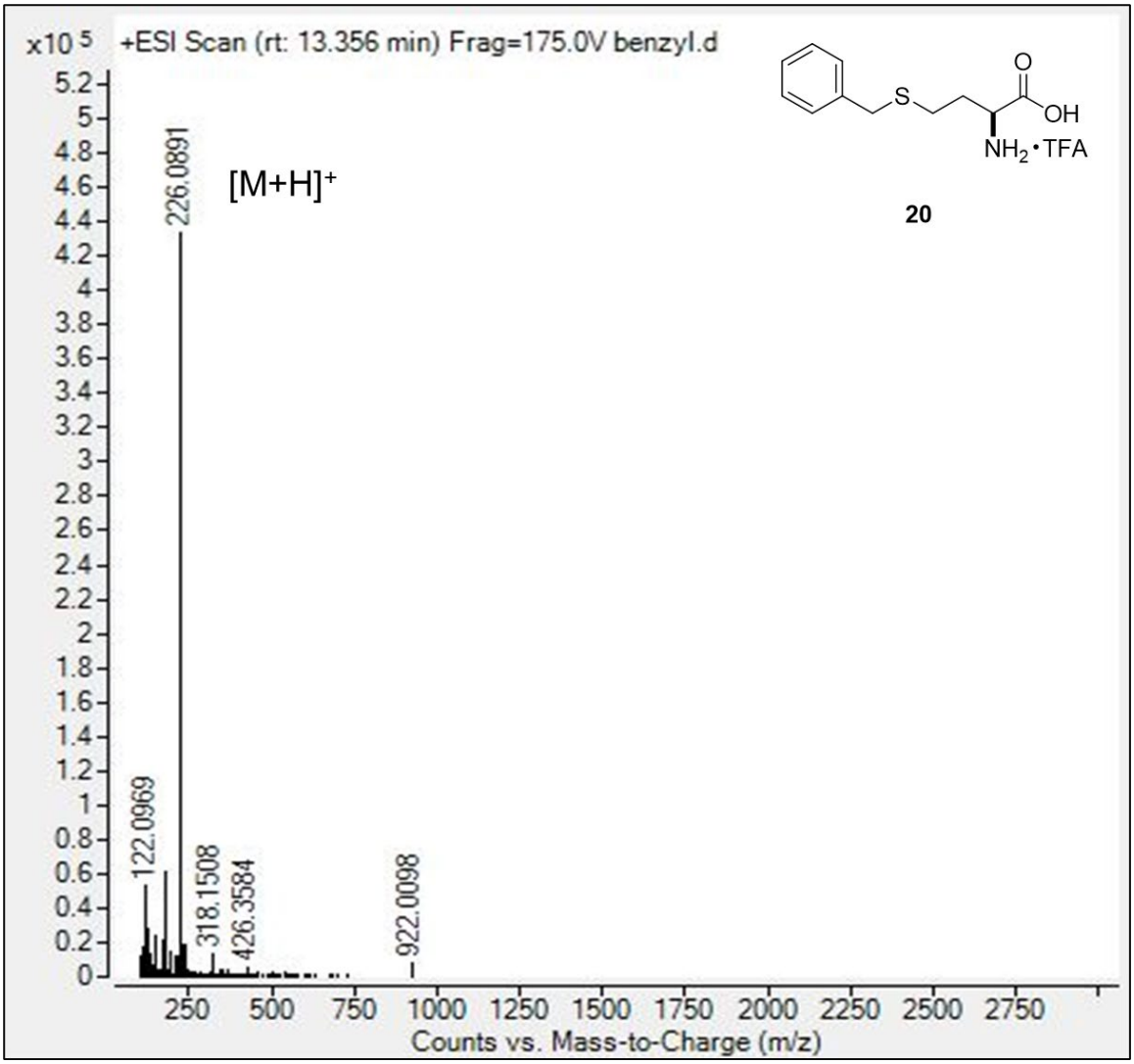

Figure S3.102. HRMS profile of *S*-benzyl-*L*-homocysteine (**20**).

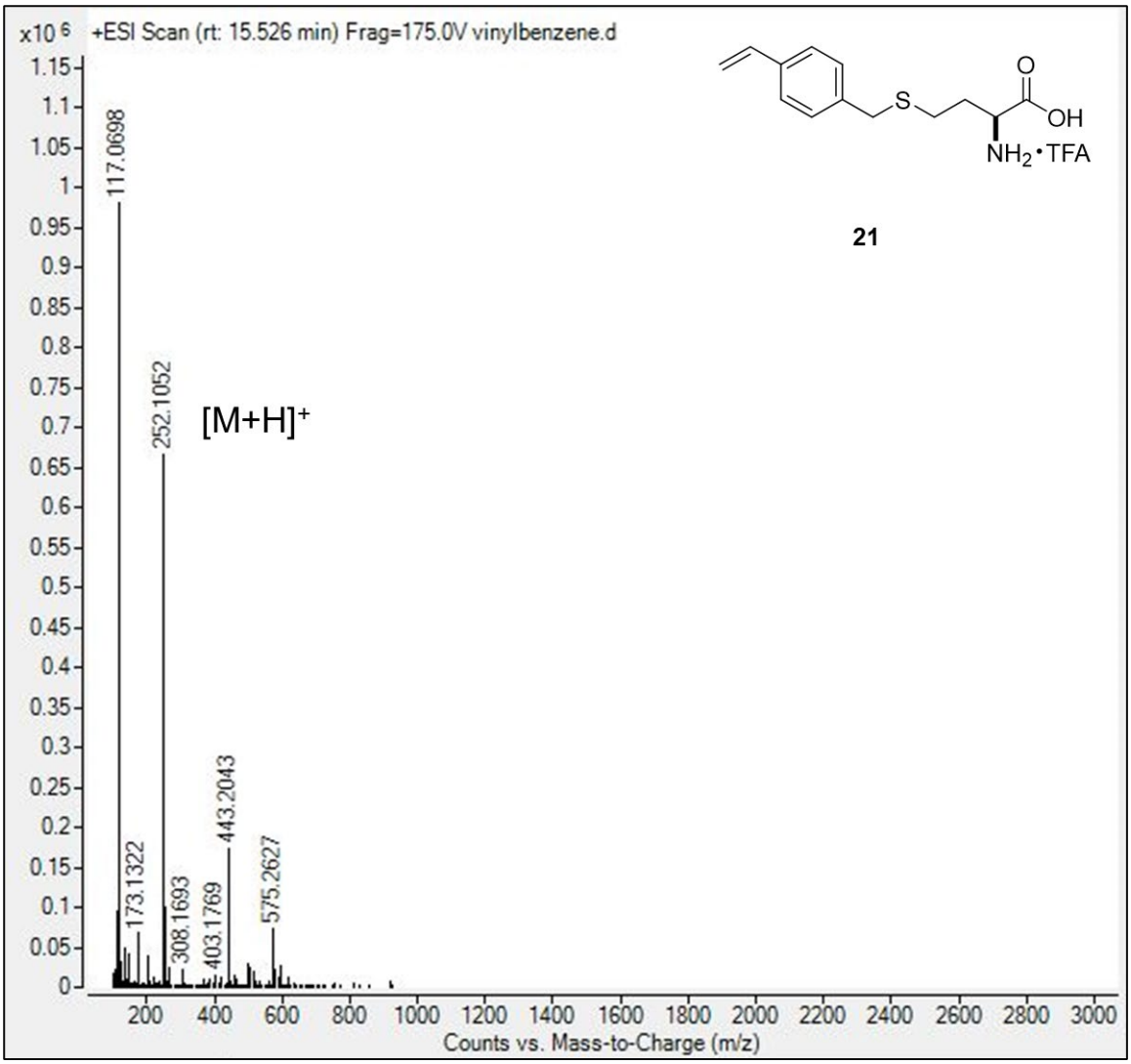

Figure S3.103. HRMS profile of *S*-(4-vinylbenzyl)-*L*-homocysteine (**21**).

Chapter Four: Conclusions and Prospectus

4.1 Conclusions

An overarching goal of this thesis project was to advance new strategies, tools and reagents to facilitate the (1) study of methylation in biology/disease and (2) diversification of complex natural product (NP)-based pharmacophores. The significance of this work stems from (1) the potential impact new tools and reagents may have on advancing our fundamental understanding of the extensive role MTs play in drug development and disease and (2) facile access to new chemical diversity, with emphasis on complex bioactive natural NP and NP-inspired molecules. At the start of this dissertation work, three broad Specific Aims were put forth: (1) Develop robust high-throughput MT assays/screens for the discovery of novel MT substrates to enable MT directed evolution/engineering; (2) Develop a robust, scalable chromatography-free synthetic method for the synthesis of non-native methionine precursors, a foundational reagent for the proposed chemoenzymatic strategies; (3) Demonstrate tandem systems for enzyme-driven intramolecular cyclization reactions within the context of a NP scaffold. While much of this dissertation's aspirations were realized, the final Specific Aim 3 objective of a successful tandem reaction remains elusive.

4.1.1 Develop robust high-throughput MT assays/screens for the discovery of novel MT substrates and to enable MT directed evolution/engineering.

Transferases have emerged as among the best catalysts for enzyme-mediated bioorthogonal functional group installation to advance innovative *in vitro*, cell-based and *in vivo* chemical biology applications.[1] In Chapters Two and Three of this work, structural and functional studies of the NP carminomycin 4-*O*-MT DnrK were extensively studied, with an emphasis on interrogating the acceptor substrate scope of DnrK. Specifically, the evaluation of 100 structurally and functionally diverse natural products revealed an array of pharmacophores as productive DnrK substrates including anthracyclines, angucyclines, enediynes, flavonoids, pyranonapthoquinones and polyketides. To further explore DnrK's biocatalytic potential, we described the novel *S*- and *N*-chemical activity of DnrK with a representative set of thionucleobases, thionucleosides and benzoxazole derivatives which exhibits a very novel mechanistic feature of this enzyme among transferases. LC-MS as the central moderate throughput assay employed for this work. However, during the course of this thesis effort, multiple alternative assays were validated as feasible high-throughput assays including the commercially available MTase Glo assay (Promega Corporation), a real-time fluorescent assay based on the non-native fluorescent hydroxycoumarin acceptor 4-methylumbelliferone (Chapter Two)[2] and a real-time colorimetric assay based on the colorimetric substrate 2-chloro-4-nitrophenol (ClNP).[3] This work also included the ligand-bound structure of DnrK bound to a non-native fluorescent hydroxycoumarin acceptor 4-methylumbelliferone, which along with the corresponding structural comparisons to TnmH and TcmO and the many other publicly available ligand-bound MT structures, serve as a strong basis for future structure-based directed evolution/engineering.

4.1.2 Robust, scalable, and chromatography-free synthetic method for the synthesis of methionine analogues

User-friendly robust access to non-native AdoMet analogues remains a fundamental bottleneck to broader adoption of these tools by the research community. There has been considerable interest in utilizing *S*/*Se*-alkylated L-*S*/*Se*-Met analogues and MATs to chemoenzymatically synthesize the corresponding *S*/*Se*-alkylated AdoMet analogues because of all the aforementioned liabilities of chemically synthesized and chemical instability of AdoMet analogues.[4-8] The simple advances in non-native *S*-alkyl-Met synthesis described in Chapter 3 are significant as it represents the first efficient, scalable and chromatography-free method reported. As such, this method is expected to ease access to these key reagents and thereby facilitate work in this field by both specialists and non-specialists alike.

4.1.3 Establish in vitro model systems for tandem chemoselective reactions

A primary objective of this work was to establish a robust chemoenzymatic tandem system to eventually enable natural product scaffold expansion. A first priority toward this goal was to establish *in vitro* systems to assess the feasibility of the multi-enzyme tandem combinations of tailoring enzymes [MTs and/or glycosyltransferases (GTs)]. If successful, the second step was to accomplish chemoselective intramolecular cyclization of enzyme-installed selectively-reactive functional groups (**Figure 4.1. A**), subsequent ring system installation can be explored. Thus, the fundamental functional transferase/substrate pairing from an array of transferases and substrates was assessed. Specifically, a subset of four

permissive model transferases were selected - *O*-MT DnrK, *C*-MT CouO, oleandomycin GT OleD[9] and the engineered *Mangifera Indica C*-MT MiCGTb-GAGM.[10] This effort focused on optimizing common buffer parameters for all four model enzymes, assessing, and circumventing any potential co-substrate/co-product inhibition issues and ultimately identifying a set of substrates common to multiple target transferases (**Figure 4.1 B**). While no major crossover substrate/product inhibition was observed, buffer composition had a notable impact on enzyme efficiency and all 'universal' buffers led to some reduction in turnover. Importantly, the major restriction to tandem reaction stemmed from the inability of transferase 2 to act on the product of transferase 1 (*i.e.*, installation of a methyl/glycosyl by the first transferase prohibited the ability of the second transferase to recognize the new product as a substrate). Consistent with this, all single vessel tandem reactions led to mixtures of single catalytic products (*e.g.*, a combined DnrK/MiCGTb reaction led to a mixture of DnrK product and MiCGTb product). In the case of *C*-MTs/GTs, these studies were also consistent with the need for a free-OH adjacent to the site of *C*-alkylation/glycosylation.

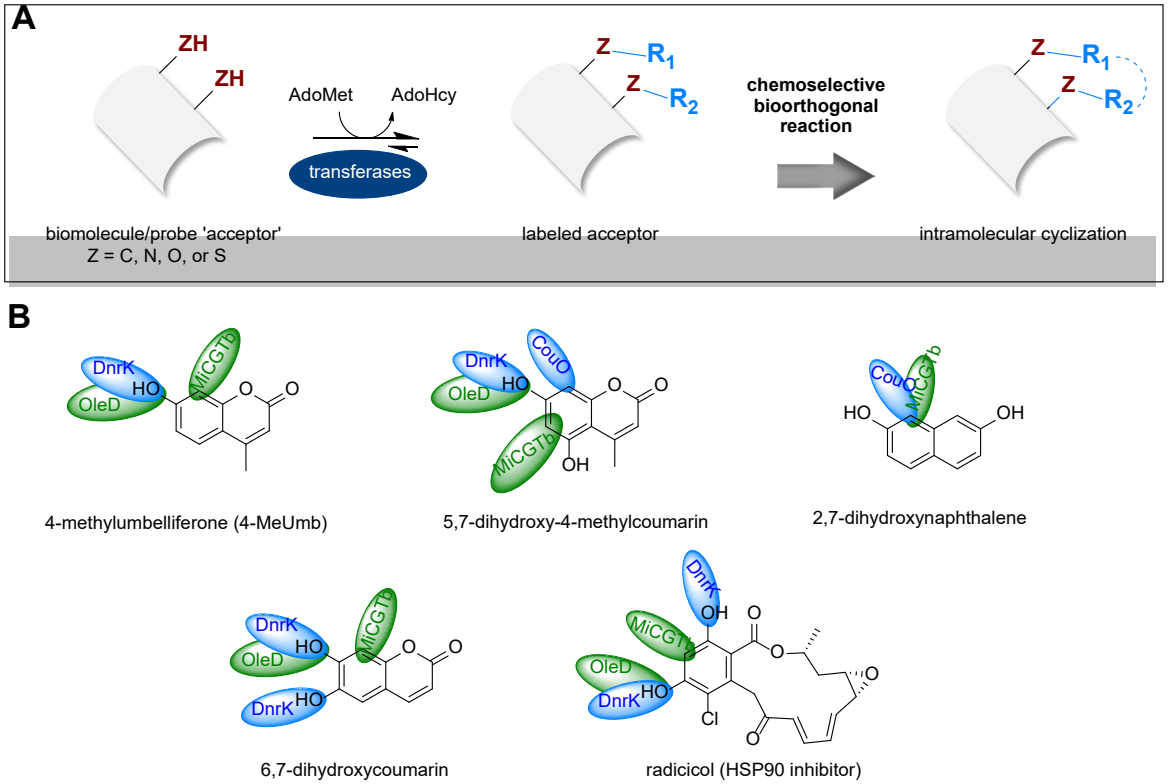

Figure 4.1. (A) The proposed chemoenzymatic tandem platform for target NPs diversification **(B)** Target substrate models that undergo multiple enzymatic reactions including DnrK *O*-methylation, CouO *C*-methylation, OleD *O*-glycosylation and MiCGTB C-glycosylation. Target substrate models. MT reactions are highlighted in blue; GT reactions are highlighted in green.

4.2 Prospectus

4.2.1 Develop robust high-throughput MT assays/screens for the discovery of novel MT substrates and to enable MT directed evolution/engineering.

The work advanced in this thesis in conjunction with previous work clearly set the stage for high throughput substrate/catalyst discovery. Multiple robust assays are in place and there is an extensive array of structural model from which to base structure-based evolution/engineering campaigns.

4.2.2 Robust, scalable, and chromatography-free synthetic method for the synthesis of methionine analogues

Three additional near-term refinements are recommended to further streamline this new methodology. First, increasing the size and hydrophobicity of the Boc protecting group and/or integrating a hyperfluorinated protecting group may further improve the requisite extraction/precipitation steps. Second, while the use of the crude TFA salts in the subsequent enzyme-catalyzed reactions was notably successful and efficient, systematic neutralization prior to use may improve solubility/turnover in some cases. This is based on the observed improvements in solubility of certain analogues in the present of 150 mM NaOH noted in Chapter 3. Third, expansion of this method to *Se*-Met analogues is also an important next step. A unique chemical feature of *Se*-AdoMet analogues is their longer and weaker *Se*-C bond in comparison with the equivalent sulfonium analogues. As such *Se*-AdoMet analogues were thus expected to be better alkyl donors in MT-catalyzed reactions. However, to date there are conflicting reports on both the catalytic advantages and the relative stabilities of *S*- versus *Se*-AdoMet analogues.[11] A proposed general strategy for *Se*-

L-Met analogues synthesis would parallel that described in Chapter 3 but starting from L-selenomethionine via metallic sodium in liquid ammonia (in -78 °C). The corresponding L-selenohomocysteine would be air-oxidized to the desired di-selenide compound and advanced as described for the *S*-alkyl Met analogues.

4.2.3 Establish in vitro model systems for tandem chemoselective reactions

Two restrictions prohibited the success of the tandem reactions – substrate specificity (major) and buffer compatibility (minor). Of these, substrate specificity is the primary concern, the solutions for which include evolving an enzyme pairing to overcome this restriction and/or identifying alternative enzyme pairings that are not limited by this barrier. A near-term alternative here that would enable assessment of downstream feasibility of the intramolecular cyclization reaction would be to introduce the first chemoselective functional group enzymatically and introduce the second chemically. As noted, buffer compatibility is relatively minor and can be addressed via improving the universal buffer employed or conducting a simple buffer exchange between reaction 1 and reaction 2. Chapter 1 highlights the range of chemoselective reactions currently available as a foundational guide for the proposed studies.

References for Chapter Four

(1) Jalali, E. and Thorson, J.S. Enzyme-mediated bioorthogonal technologies: catalysts, chemoselective reactions and recent methyltransferase applications. *Curr. Opin. Biotechnol*. **2021**, *69*, 290-298.

(2) Williams, G.J., Zhang, C., and Thorson, J.S. Expanding the promiscuity of a natural-product glycosyltransferase by directed evolution. *Nat. Chem. Biol*. **2007**, *3*, 657-662.

(3) Huber, T.D., Wang, F., Singh, S., Johnson, B.R., Zhang, J., Sunkara, M., Van Lanen, S.G., Morris, A.J., Phillips Jr, G.N. and Thorson, J.S. Functional AdoMet isosteres resistant to classical AdoMet degradation pathways. *ACS. Chem. Biol*. **2016**, *11*, 2484-2491.

(4) Singh, S., Zhang, J., Huber, T.D., Sunkara, M., Hurley, K., Goff, R.D., Wang, G.,Zhang, W., Liu, C., Rohr, J., Van Lanen S.G., Morris A.J., Thorson J.S. Facile chemoenzymatic strategies for the synthesis and utilization of *S*-adenosyl-L-methionine analogues. *Angew. Chemie., Int. Ed.* **2014**, *53*, 3965-3969.

(5) Wang, R., Islam, K., Liu, Y., Zheng, W., Tang, H., Lailler, N., Blum, G., Deng, H. and Luo, M., Profiling genome-wide chromatin methylation with engineered posttranslation apparatus within living cells. *J. Am. Chem. Soc.* **2013**, *135*, 1048-1056.

(6) Michailidou, F., Klöcker, N., Cornelissen, N.V., Singh, R.K., Peters, A., Ovcharenko, A., Kümmel, D., Rentmeister, A. Engineered SAM synthetases for enzymatic generation of AdoMet analogs with photocaging groups and reversible DNA modification in cascade reactions. *Angew. Chem. Int. Ed.* **2021**, *60*, 480-485.

(7) Muttach, F., Rentmeister, A.A. A biocatalytic cascade for versatile one-pot modification of mRNA starting from methionine analogues. *Angew. Chemie., Int. Ed*. **2016**, *55*, 1917-1920.

(8) Huber, T.D., Clinger, J.A., Liu, Y., Xu, W., Miller, M.D., Phillips Jr, G.N., Thorson, J.S. Methionine adenosyltransferase engineering to enable bioorthogonal platforms for AdoMet-utilizing enzymes. *ACS Chem Biol*. **2020**, *15*, 695-705.

(9) Gantt, R.W., Peltier-Pain, P., Cournoyer, W.J., and Thorson, J.S. Using simple donors to drive the equilibria of glycosyltransferase-catalyzed reactions. *Nat Chem Biol.* **2011**, *7*, 685-691.

(10) Chen, D., Chen, R., Xie, K., Yue, T., Zhang, X., Ye, F., and Dai, J. Biocatalytic *C*-glucosylation of coumarins using an engineered *C*-glycosyltransferase. *Org Lett.* **2018**, *20,* 1634-1637.

(11) Huber, T.D., Johnson, B.R., Zhang, J., and Thorson, J. S. AdoMet analog synthesis and utilization: current state of the art. *Curr Opin Biotechnol.* **2016**, *42,* 189-197.

VITA

Elnaz Jalali

EDUCATION

Ph.D. in Pharmaceutical Sciences, University of Kentucky, Lexington, KY 2017-2023

M.S. in Organic Chemistry, Western Kentucky University, Bowling Green, KY 2015-2017

B.S. in Chemistry, University of Tehran, Tehran, Iran 2009-2013

AWARDS

Pharmaceutical Sciences Excellence in Graduate Achievement Fellowship Award, University of Kentucky, College of Pharmacy, Lexington, KY 2022

PUBLICATIONS

Jalali, E.; Wang, F.; Overbay, B.R.; Miller, M.D.; Shaaban, K.A.; Ponomareva, L.V.; Ye, Q.; Bhardwaj, M.; Steele, A.D.; Teijaro, C.N.; Shen, B.; Van Lanen, S.G.; She, Q.; Voss, R.; Phillips Jr, G.N.; Thorson, J.S. (2023) Biochemical and Structural Studies of the Carminomycin 4-*O*-Methyltransferase DnrK. *submitted*.

Jalali, E.; Karim, UI.; Huber, T.; Overbay, B.R.; Ponomareva, L.V.; Shaaban, K.A.; Thorson, J.S. (2023). Studies on DnrK methyltransferase unnatural acceptors and donors *submitted*.

Jalali, E.; Thorson J. S. (2021) Enzyme-mediated bioorthogonal technologies: Catalysts, chemoselective reactions and recent methyltransferase applications. *Curr Opin Biotechnol*. 69, 290-298.